Universitat Autònoma de Barcelona

Photoresponse of Ferroelectric BaTiO3 Thin Films

Fanmao Liu

Universitat Autònoma de Barcelona

Photoresponse of Ferroelectric $BaTiO_3$ Thin Films

Fanmao Liu

SUPERVISORS

Prof. Josep Fontcuberta Griñó
Dr. Ignasi Fina Martínez

Institut de Ciència de Materials de Barcelona ICMAB-CSIC
Laboratory of Multifunctional Oxides and Complex Structures

TUTOR

Prof. Jordi Sort Viñas

Universitat Autònoma de Barcelona
Department of Physics, Faculty of Science

This dissertation is submitted for the degree of Doctor of Philosophy
June 2017

ICMAB
INSTITUT DE CIÈNCIA DE MATERIALS DE BARCELONA
EXCELENCIA SEVERO OCHOA
CSIC
CONSEJO SUPERIOR DE INVESTIGACIONES CIENTÍFICAS

Prof. Josep Fontcuberta Griñó and **Dr. Ignasi Fina Martínez**, research professor and research fellow at the Institut de Ciència de Materials de Barcelona – Consejo Superior de Investigaciones Científicas, and **Prof. Jordi Sort Viñas**, ICREA research professor at Universitat Autònoma de Barcelona

CERTIFY

that **Fanmao Liu** carried out the research work "**Photoresponse of ferroelectric $BaTiO_3$ thin films**" under their supervision. This work has been developed within a PhD program in Materials Science at the Department of Physics of Universitat Autònoma de Barcelona.

For that record they sign the certificate.

Prof. Josep Fontcuberta Griñó   Dr. Ignasi Fina Martínez   Prof. Jordi Sort Viñas

Bellaterra, June 2017

To Mom

Acknowledgements

First of all, I would like to present my greatest gratitude to my PhD supervisors, Prof. Josep Fontcuberta and Dr. Ignasi Fina, for invaluable guidance, assistance, revelation and patience they give to me in this four-year research. Prof. Josep Fontcuberta provide me the opportunity to start the PhD study and taught me the way to hypothesize boldly, to testify rigorously in science. Dr. Ignasi Fina taught me enormous methodologies in specific research, in daily working, in scientific expression, etc. All these complete my understanding of the academic world.

I express my great sincere gratitude to Dr. Diego Gutiérrez for guiding me at the first months and lead me from zero to the area of ferroelectrics and optoelectronics step by step. In particular, I would like to thank Dr. Carlos Frontera, for helping me much better understanding X-ray diffraction. I also acknowledge Rafael Cichelero for all help in optics, Mengdi Qian for assistance in experimental setups, Mathieu Mirjolet for aid in scientific software. I would like to thank Dr. Gervasi Herranz, Dr. Florencio Sánchez, Dr. Mateusz Ścigaj, Prof. Vladimir Laukhin and Dr. Vassil Skumryev for valuable discussion in ferroelectrics. Also I would like to appreciate Dr. Guillaume Sauthier for professional suggestions and discussions in XPS analysis, Dr. Qian Wu for selfless support in AFM characterization. And many thanks to Prof. Peng Niu for giving me suggestions in ferroelectrics and opportunities to express my work. Moreover, I want to extend gratitude to Blai Casals, Yu Chen, Jike Lyu for making me feel like home in the group.

Furthermore, greatest thanks go to China Scholarship Council (CSC) for financial support during my doctoral study.

Last but not least, I give the deepest gratitude to my family, my mom and my sister, without their support, their sacrifice, their suffering and their love, I would not persist in neither the study of PhD, nor the completion of this thesis.

Abstract

$BaTiO_3$ is a lead-free ferroelectric oxide material. $BaTiO_3$ thin films have been widely studied for memory applications due to its charge memory effect resulting from its ferroelectric nature. Nowadays, the scientific community has renewed its interest on $BaTiO_3$, because it holds characteristics that is interesting for rapidly developing areas such as photovoltaics, photoelectric sensing and photocatalysis. The main goal of the present thesis is to study the photoelectric effects on $BaTiO_3$ thin films and to give light on the relevant mechanisms that control them.

Ferroelectric materials show intrinsic, unavoidable and exclusive internal electric fields: imprint electric field (E_{imp}) and depolarization electric field (E_{dep}). Thus distinct photoelectric effects can be obtained due to E_{imp} and E_{dep}. In the present thesis we have studied in detail the role of E_{imp} and E_{dep} on photoelectric effects of $BaTiO_3$ films. In particular, it is shown that appropriate measurement configuration can be used to disclose and isolate their contribution. As a result, different transient and constant photoresponses can be obtained as wish. By the same token, their contribution to the ferroelectric switching dynamics are also analyzed. The transient photoresponse finds its origin on the screening of surface charge (photoscreening). In order to modulate its magnitude detailed characterization has been performed. It is concluded that the polarization photoscreening is governed by the presence of water adsorbed at the surface, allowing it to be controlled. However, the photoelectric efficiency has been found to be limited by the low generation of carriers by light, that is the reason why the effect of O substituted by N in $BaTiO_3$ lattice, which should result in band-gap narrowing, hence improving the photoelectric efficiency, has been studied. Interestingly, it is found that ammonia treatments are efficient to improve photoelectric responses, without having any clear evidence of N substitution.

Resumen

$BaTiO_3$ es un material de óxido ferroeléctrico sin plomo. $BaTiO_3$ películas delgadas han sido ampliamente estudiados para aplicaciones de memoria debido a su efecto de memoria de carga resultante de su naturaleza ferroeléctrica. Hoy en día, la comunidad científica ha renovado su interés en $BaTiO_3$, ya que posee características que son interesantes para áreas de rápido desarrollo como la fotovoltaica, la detección fotoeléctrica y la fotocatálisis. El objetivo principal de la presente tesis es estudiar los efectos fotoeléctricos de las películas delgadas $BaTiO_3$ y dar luz sobre los mecanismos relevantes que las controlan.

Los materiales ferroeléctricos muestran campos eléctricos internos intrínsecos, inevitables y exclusivos: campo eléctrico de impresión (E_{imp}) y campo eléctrico de despolarización (E_{dep}). Así se pueden obtener distintos efectos fotoeléctricos debido a E_{imp} y E_{dep}. En la presente tesis hemos estudiado en detalle el papel de E_{imp} y E_{dep} en los efectos fotoeléctricos de películas $BaTiO_3$. En particular, se muestra que se puede usar una configuración de medición apropiada para revelar y aislar su contribución. Como resultado, pueden obtenerse diferentes foto respuestas transitorias y constantes según se desee. De igual modo, se analiza su contribución a la dinámica de conmutación ferroeléctrica. La foto respuesta transitorio tiene su origen en el cribado de la carga superficial (fotograbado). Para modular su magnitud se ha realizado una caracterización detallada. Se concluye que la polarización de las fotos se rige por la presencia de agua adsorbida en la superficie, lo que permite su control. Sin embargo, se ha encontrado que la eficiencia fotoeléctrica está limitada por la baja generación de portadores por la luz, por lo que el efecto de O sustituido por N en la red $BaTiO_3$, lo que debería dar lugar a un estrechamiento de banda, mejorando así la eficiencia fotoeléctrica , ha sido estudiado. Curiosamente, se encuentra que los tratamientos de amoníaco son eficientes para mejorar las respuestas fotoeléctricas, sin tener ninguna evidencia clara de la sustitución de N.

Contents

Chapter 1. Introduction

1.1 Main objective

The main objective of this thesis is to build a comprehensive understanding of how various factors influence photoresponses in $BaTiO_3$ thin films, and to essay feasible methods to tune the photoresponses. Acquired knowledge can be useful to obtain expected photoresponses from optimized material designing, deposition parameters, electrode configurations and post-preparation treatments in $BaTiO_3$ thin film for photoelectric applications. Moreover, it is expected the learnt physical sciences behind observed phenomena can be helpful for discovering novel properties in photoelectric ferroelectrics.

We have carried out a systemic study on the influence of internal electric field, electrode configuration, electrode/$BaTiO_3$ interface, microstructure, surface adsorbates to photoresponses of $BaTiO_3$ thin film, and made efforts on surface adsorbates modifying and nitrogen doping to tune photoresponses of $BaTiO_3$ thin film. The route of researches made in this thesis starts from film growing by pulsed laser deposition (PLD) and Pt electrodes growing by radio frequency sputtering (RF sputtering), to multi-characterization technologies including ferroelectric, transportation and impedance analysis by electric method, structural analysis by X-ray diffraction (XRD), surface chemicals analysis by X-ray photoelectron spectroscopy (XPS), surface topography characterization by atomic force microscopy (AFM), transmittance analysis by uv-vis-nir spectrophotometer. Characterizations are combined with illumination, temperature and atmosphere control. Furthermore, post-sample-preparation treatment including high-vapor-pressure environment exposing and ammonia annealing are employed for tuning photoresponses to complete this study on $BaTiO_3$ thin film.

1.2 Project MOSES

Major research work carried out in this thesis was in the framework of and granted by Spanish Ministry of Economy and Competitiveness with project title “Metals and Oxides for a Sustainable Electronics (MOSES)” and reference MAT2014-56063-C2-1-R, active for the period 2014 − 2017.

1.3 Thesis outline

State of the art of the specified research area and motivation are depicted in the introduction section of each chapter.

Chapter 2 describes the methodologies used in the thesis. It includes principles of materials preparation and characterization technologies and experimental setups.

To achieve the objectives described in section 1.1, following research work are carried out:

In Chapter 3, the contribution of the imprint field E_{imp} *in different electrode configuration, especially top-top, is studied.* A series of $BaTiO_3$ thin film grown on different substrates a piece of $BaTiO_3$ single crystal are used. Ferroelectric *P*-*E* loops are measured from low to high frequency. The reason why E_{imp} shows up only at particular frequency in top-top configuration are discussed. Blue laser illumination is introduced and its influence on switching process of top-top configuration is analyzed. At the end an experiment showing how illumination enhances the retention behavior of $BaTiO_3$ is performed.

In Chapter 4, the contribution of. E_{imp} *and* E_{dep} *to determine the direction and magnitude of short-circuit photocurrent are analyzed.* Two $BaTiO_3$ thin films deposited on $SrTiO_3$ are used. Distinct *P*-*E* loops and retention behavior of bottom-top and top-top are displayed first. Then discussion on the driving force between E_{imp} and E_{dep} is carried out base on results from polarization dependence of short-circuit photocurrents measurement. At the end the difference in short-circuit photocurrents and photoscreening behavior between bottom-top and top-top is explained by different electrode/$BaTiO_3$ interfaces via band diagram analysis.

In Chapter 5, the polarization photoscreening effect revealed in Chapter 4 is studied. A series of $BaTiO_3$ films on $SrTiO_3$ and $DyScO_3$ with thickness from ~30 to ~110 nm are used. Structural and surface chemical analysis are firstly performed and various interpreting to results are employed aiming to determine the controlling factor of photoscreening which can be dramatically different among samples. A treatment that expose $BaTiO_3$ films in the environment with high vapor pressure called *stream-treatment* is introduced for testifying the controlling factor, meanwhile examine the possibility of enhancing the photoscreening.

In Chapter 6, a relative independent study on strain states of $BaTiO_3$ thin film by synchrotron X-ray radiation are carried out. A series of $BaTiO_3$ films on $SrTiO_3$ and $DyScO_3$ with thickness from ~4 to ~110 nm are used. Reciprocal space maps are built to access both in-plane and out-of-plane lattice parameters and to manifest the strain relaxing process in $BaTiO_3$ thin film. Lattice parameters are compared among films with different thickness or deposited on different substrate, as the purpose of understanding how different factors influence the relaxation. Grazing incidence diffraction is also performed to learn the depth distribution of $BaTiO_3$ phases with different stain state. At the end temperature dependence of lattice parameters are carried out to define the phase transition temperature in different strain states.

In Chapter 7, ammonia annealing is performed on $BaTiO_3$ thin film aiming to narrow its band-gap. In this chapter the results obtained are listed but the data analysis is undergoing. A series of identical $BaTiO_3$ thin film grown on $SrTiO_3$ or Nb doped $SrTiO_3$ are used. Annealing parameters are optimized to obtain narrowed band-gap and preserved polarization at the same time. Structural and surface chemical analysis are firstly performed after annealing to trace the possible doped nitrogen. Measurement of transmittance spectroscopy and photocurrents are applied afterwards to test the change in band-gap after annealing. Control group that annealing $BaTiO_3$ in N_2 is carried out for study the possible influence from oxygen vacancies created during NH_3 annealing.

Ammonia annealing on $BaTiO_3$ grown on Nb doped $SrTiO_3$ is executed at the end aiming to exclude the influence from bottom electrodes.

The final conclusions are summarized in Chapter 8.

Some interesting results and works that are not discussed in detail or not closely correlating to the main idea of the thesis are listed in Appendix.

Chapter 2. Method

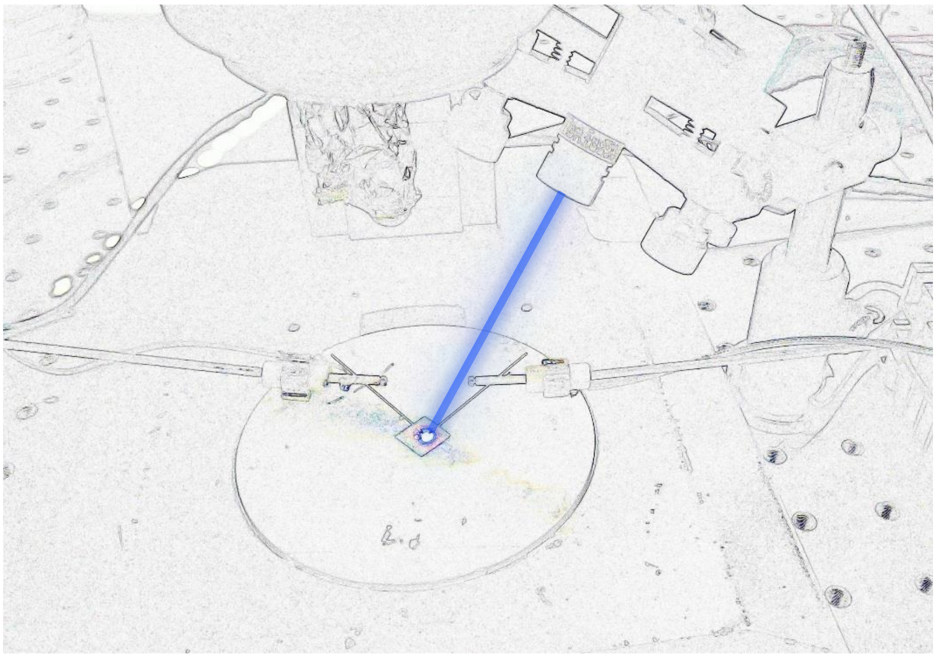

In this chapter, the main technologies of characterization used in this thesis are introduced, starting from growing $BaTiO_3$ thin films and Pt electrodes, moving to the most important ferroelectric properties characterization with the participation of illumination, to surface analysis technologies, to crystal structure studies, to post-preparation treatments and finishing with optic measurement.

2.1 Sample preparation

2.1.1 Pulsed laser deposition (PLD)

$BaTiO_3/La_{2/3}Sr_{1/3}MnO_3$(LSMO) and $BaTiO_3/SrRuO_3$(SRO) epitaxial bilayers have been grown by pulsed laser deposition (PLD) on (001) oriented $SrTiO_3$ (STO), (110 oriented $DyScO_3$ (DSO) and $(LaAlO_3)_{0.3}(SrAl_{0.5}Ta_{0.5}O_3)_{0.7}$ (LSAT) single crystal substrates.

PLD is a physical vapor deposition (PVD) technique. In the experimental setup of PLD, a high-power pulsed laser (excimer) beam is focused inside the vacuum chamber though transparent window to strike the target of materials to be deposited. The chamber is commonly with background oxygen when depositing oxide thin films. Due to the high energy density of the laser, the target is ablated and emits materials under the condition far away from equilibrium, resulting in plasma creation perpendicular to the surface of the target. The plasma plume composed of stoichiometric composition of target material approaches the substrate placed at certain distance which is heat up to a certain temperature aiming to achieve epitaxial growth. Atoms rearrange, nucleates and order themselves on the surface of the substrate, and react physically and chemically with oxygen on the way reaching the substrate. A picture of the PLD setup taken during deposition and a sketch illustrating the PLD setup of ICMAB is plotted in Figure 2.1.

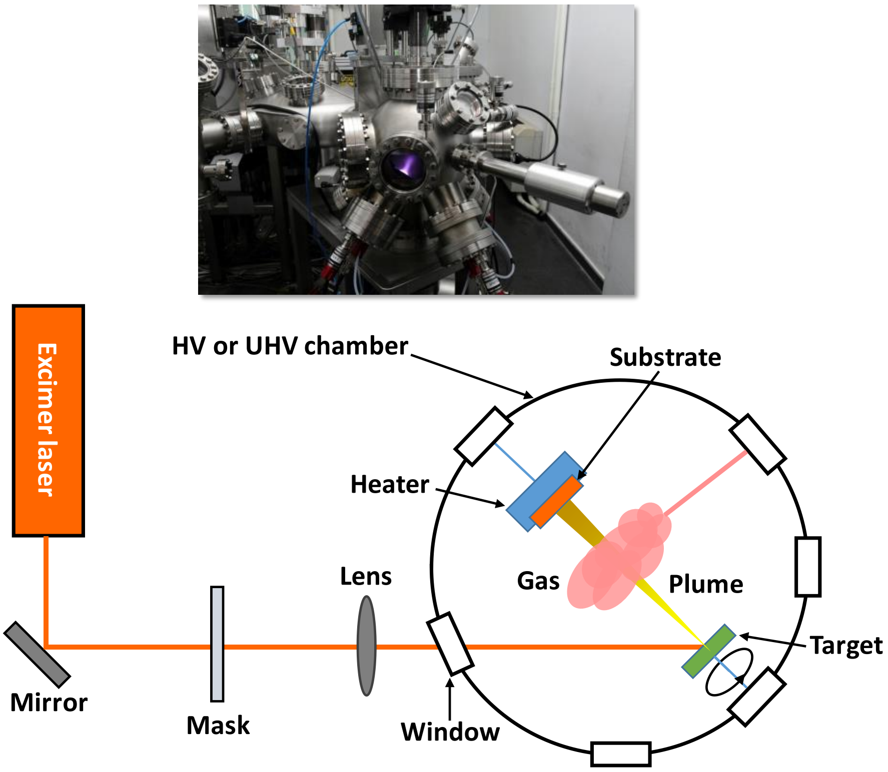

Figure 2.1. Top: deposition is in process. Bottom: sketch of PLD system located at the ICMAB.

$BaTiO_3$ thin films in the thesis are grown at PLD service of ICMAB, managed by Dr. Florencio Sánchez. A KrF excimer laser (λ = 248 nm) is used. The LSMO/SRO film was grown at 725 °C under an oxygen pressure of 0.2 mbar and a laser repetition rate of 2 Hz. The growth of BTO was performed at 700 °C and with an oxygen pressure of 0.02 mbar and 2 Hz of laser frequency. No annealing is performed after deposition. Growth and optimization conditions had been previously determined by Dr. Florencio Sánchez.

Although most of films described in this thesis were grown at ICMAB using the setup just described, the $BaTiO_3$ thin films used in Chapter 4 are grown at Dipartimento di Fisica del Politecnico di Milano, managed by Prof. R. Bertacco. A quadrupled Q-Switched Nd:YAG laser (λ = 266 nm) is used with a fluence of 1.3 J cm^{-2} for LSMO deposition process and 0.4 J cm^{-2} for BTO deposition process and a repetition rate of 2 Hz. LSMO films were grown at a deposition temperature of 730 °C and an oxygen pressure of 0.22 Torr. The subsequent growth of BTO, performed at 640 °C and with an oxygen pressure of 0.02 Torr, was followed by 30 min annealing at 600 °C in a high oxygen pressure (760 Torr).

2.1.2 Electrodes sputtering

After PLD process, Platinum contacts are *ex-situ* deposited by radio frequency (RF) sputtering on the surface of $BaTiO_3$ as top electrodes. Pt is chosen because its noble metal nature, very stable in a wide temperature range, difficult to be oxidized, hardest noble metal not easy to be scratched and found to be appropriate top electrode for ferroelectricity characterization[1]. In RF sputtering, there are a cathode (the Pt target here) and an anode (the $BaTiO_3$ thin film sample here) in a vacuum chamber previously evacuated up to high vacuum (~10^{-6} Torr), the power supply is a high voltage RF source fixed at 13.56 MHz. With flowing gas (Argon) in the chamber, gas atoms are ionized due the potential applied and form a plasma bombarding the target, then atoms of target are emitted and deposited on the sample. To allow efficient target erosion, magnetron sources are commonly used. In our case, to deposit Pt electrodes, a *PLASSYS* magnetron sputtering system located at the ICMAB is used. The sketch of sputtering chamber is shown in Figure 2.2.

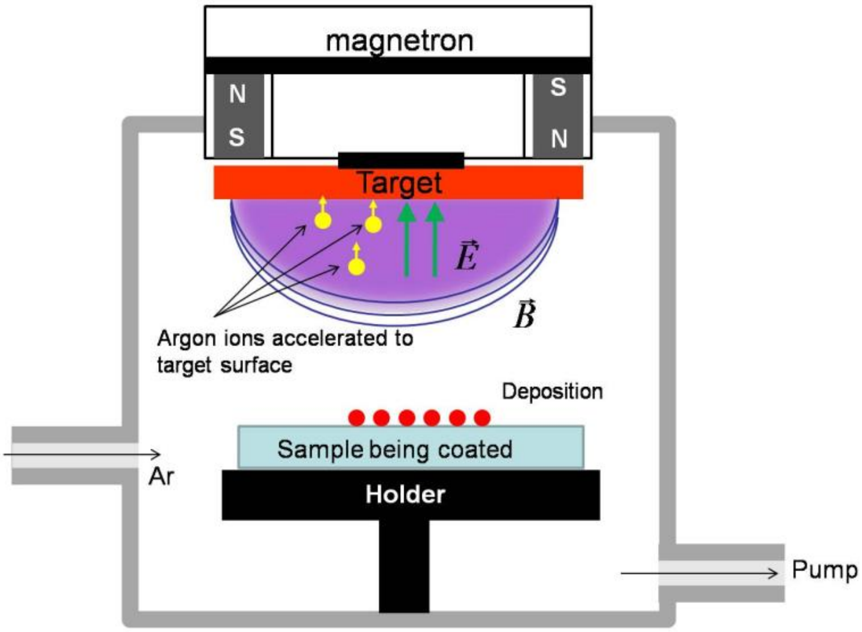

Figure 2.2. Sketch of the chamber of *PLASSYS* magnetron sputtering system[2] (schematic diagram courtesy of Dr. Diego Gutiérrez).

Before Pt deposition, samples are cleaned with acetone and ethanol, and subsequent 20 minutes in Ozone + UV Cleaner to reduce surface organic adsorbates. In most cases of the thesis, a 300 mesh TEM grid is used as mask allowing to deposit about 600 electrodes (60 × 60 μm^2, 15 μm distance apart) simultaneously. The sputtering is performed at room temperature with base pressure of 10^{-6} Torr, sputtering power is typically 20 Watts, the flux of Argon is 10 sccm, and distance from target to sample is 5 cm. 3 min sputtering is performed and ~20 nm Pt is deposited. Figure 2.3 shows the deposited Pt electrodes imaged by optic microscope and the transparency to visible light of a piece of glass with ~20nm Pt deposited.

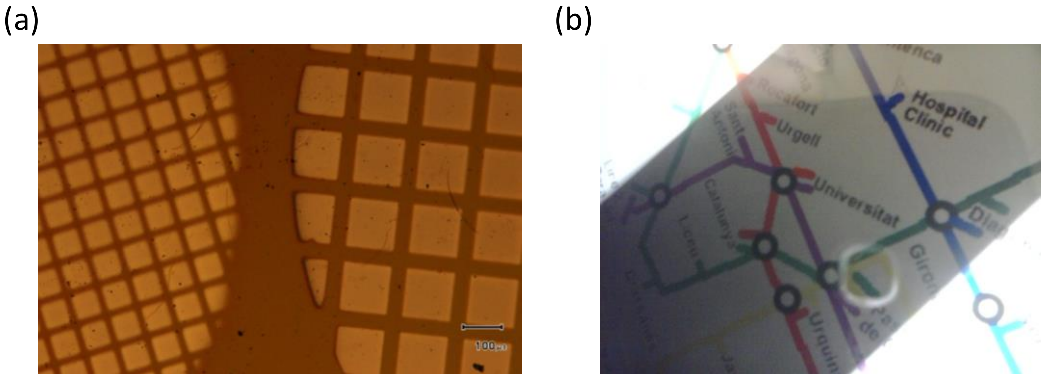

Figure 2.3. (a) Two different size of Pt electrodes images by optic microscope. Left: 60 × 60 μm^2, right: 120 × 120 μm^2. (b) Transparency manifest of a piece of glass with ~20 nm thick Pt deposited. Darker region is the view of Barcelona Metro map through the glass (photograph courtesy of Dr. Diego Gutiérrez).

2.2 Electric characterization of ferroelectric thin films

2.2.1 Ferroelectric characterization

Ferroelectric characterization is performed using an *aixACCT* TFAnalizer2000 system with coaxial cable connected to a probe station having micrometer tips. In this thesis, we use two different electrodes configuration, bottom-top (*b-t*) and top-top (*t-t*) as Figure 2.4 a,b show. Bottom-top is to apply electric field on the top electrode and ground the bottom electrodes (LSMO layer typically) which is most widely used in ferroelectric study, as measuring a ferroelectric capacitor. But in most cases, asymmetric results will be obtained using *b-t* due to different BTO/metal interface, strain gradient and defects in BTO, etc., thus *t-t* configuration which applies electric field on one top electrode and ground another one that could avoid these problems and provide symmetric results is employed. In the *t-t* configuration, due to the large difference of resistivity of BTO and LSMO or SRO (10^6~10^7 Ω·cm^{-1} vs. 10^{-3} Ω·cm^{-1}), most electric field will apply on the out-of-plane direction in BTO as the black dashed line in Figure 2.4c thus the equivalent circuit is two ferroelectric capacitors in serial. Detailed discussion on differences between *b-t* and *t-t* will be conducted in Chapter 3. The Pt electrodes used in *t-t* configuration are adjacent, unless otherwise stated.

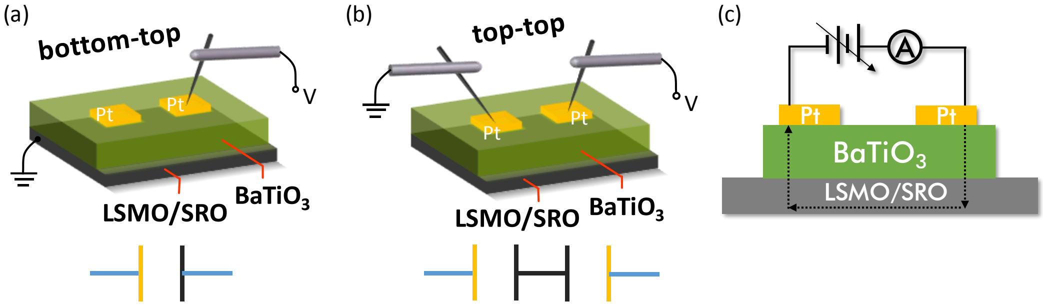

Figure 2.4. Electrodes configuration and equivalent circuits: (a) bottom-top, (b) top-top. (c) Electric field distribution in BTO while measuring.

In this thesis, ferroelectric loops are recorded by applying triangular voltage waveform *V*(*t*) and measuring current (*I*) using virtual ground method[3], then the value of polarization (*P*) is calculated by integrating *I*(*t*) the *I* into charge *Q* and normalizing by the area of electrode *A*, as indicated by equation 2.1:

$$P \approx D = Q/A = \int I(t)dt \tag{2.1}$$

where *D* is electric displacement. *I* typically consists of 3 contributions: leakage current

(I_{leakage}) coming from electrons flowing though the material, dielectric current (I_{ε}) corresponding to charging and discharging current of the capacitor, and ferroelectric current (I_{FE}) caused by ferroelectric domain switching. By properly selecting the amplitude and frequency of applied voltage, and local area (electrode) with relative smaller leakage, measured I_{FE} can be the dominating contribution to measured I, then reliable determination of ferroelectric properties of BTO can be achieved. A method called Dynamic Leakage Current Compensation (DLCC) developed by Meyer[3,4] which minimize the influence of I_{leakage} by assuming displacement current (I_{ε} + I_{FE}) varies linearly with the frequency and I_{leakage} varies just by the voltage applied. However, when I_{leakage} is modulated by illumination this method cannot be safely used as I_{leakage} will not be compensated by DLCC method. Therefore DLCC is avoided to prevent introducing artifacts on photoresponses.

- **Dynamic hysteresis measurement (DHM)**

Most polarization-electric field hysteresis loops (P-E) in the thesis are obtained in DHM method, where $E = V/t$ and t is the thickness. The measurement is completed by four consecutive voltage pulses with fixed 1 second time-interval between each other, as Figure 2.5a shows. The first one is the prepolarization pulse, the third pulse is changing negative remanent polarization state (P_{r-}) to positive one (P_{r+}), both pulses are without sampling data. The obtained P-E loop is the combination of data from negative branch of the second pulse (green region) and positive branch of the fourth pulse (blue region). Sketches of typical I-V loop and integrated P-E loop measured by DHM mode are also plotted in Figure 2.5b and 2.5c.

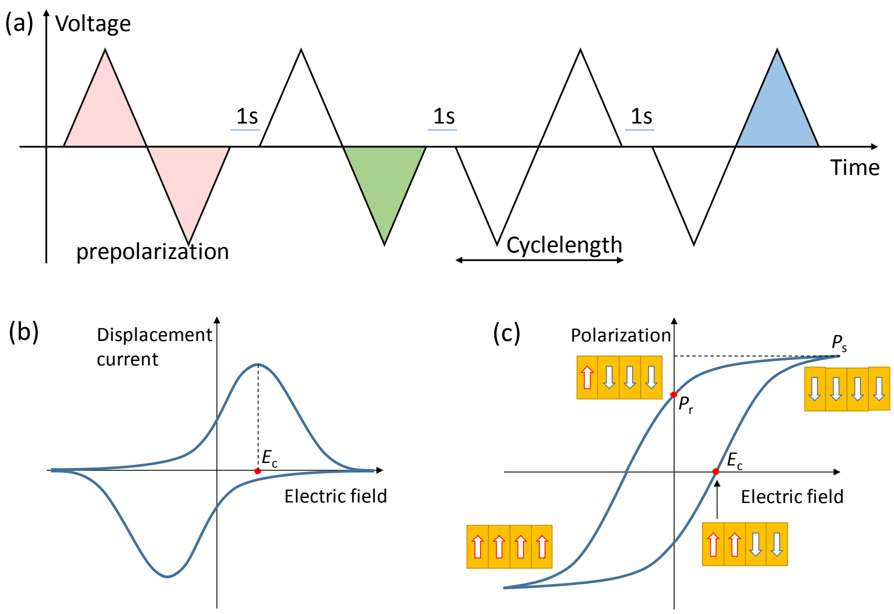

Figure 2.5. (a)Excitation signal for the DHM mode hysteresis measurement. (b) *I*-*V* loop of a standard ferroelectric material. (c) A typical *P*-*E* loop integrated from the *I*-*V* loop. Ferroelectric domain configurations at different polarization states are sketched.

- **Pulse measurement (PUND)**

Another method to characterize polarization with more flexibility than DHM mode is also used in the thesis, called PUND (p̲ositive u̲p̲ n̲egative d̲own), especially in occasions of specific prepolarization state is needed. As the waveform displayed in Figure 2.6, PUND measurement start with a write pulse, after a certain delay time (0.2 - 1000s by the limitation of TFAnalizer2000 system), one to four reading pulses can be applied to determine properties such as remanent polarization (P_r). The time gap τ between each reading pulses is identical and can be tuned from 2.5 ns to 1000s.

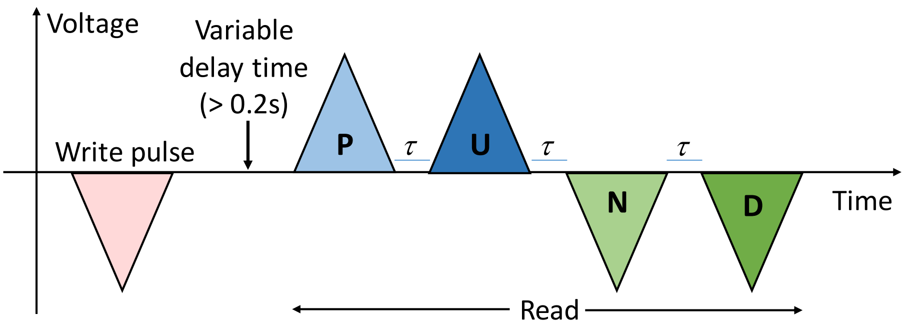

Figure 2.6. Typical excitation waveform of a PUND measurement.

- **Retention measurement**

Retention is a crucial property of ferroelectric materials. It describes the phenomenon that remanent polarization decays with time after polarization. The essence of retention measurement is to detect P_r with a certain delay time τ_FE after prepol. TFAnalizer2000 system provide the retention mode. It starts with a writing pulse, then after set delay time, a read pulse is applied to measure the remanent switchable polarization P_sw. Subsequently, several reference pulses are applied to determine total switchable polarization P_max, thus the remanent polarization P_r equals to $P_\mathrm{max} - P_\mathrm{sw}$. Repeating this procedure and change the delay time, we can obtain the plot of retention behavior, which actually is delay time dependence of P_r.

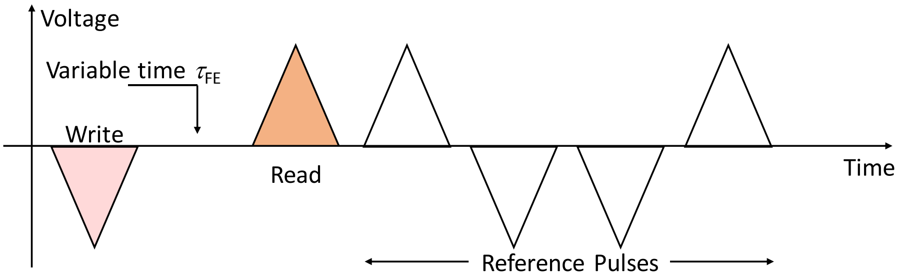

Figure 2.7. Signal sequence used in retention measurement.

2.2.2 Laser illumination

Photo-induced effects of $BaTiO_3$ thin films will be explored in this thesis. In chapter 3-5, a blue laser (405 nm) and a green laser (532 nm) feed by a CPX400SA DC power source (*AimTTi* Co.) and focusable lens are used. Laser spot is tuned to about 300 μm diameter that ensures a homogeneous illuminating on two adjacent 60 × 60 μm^2 Pt electrodes separated about 15 μm. Incident angle of the laser light (> 60°) varies in a small range (< 2°) to adapt different samples or electrodes. In this condition, the power density is about 10 $W \cdot cm^{-2}$ with negligible fluctuation. Figure 2.8 shows the sketch of illuminating setup.

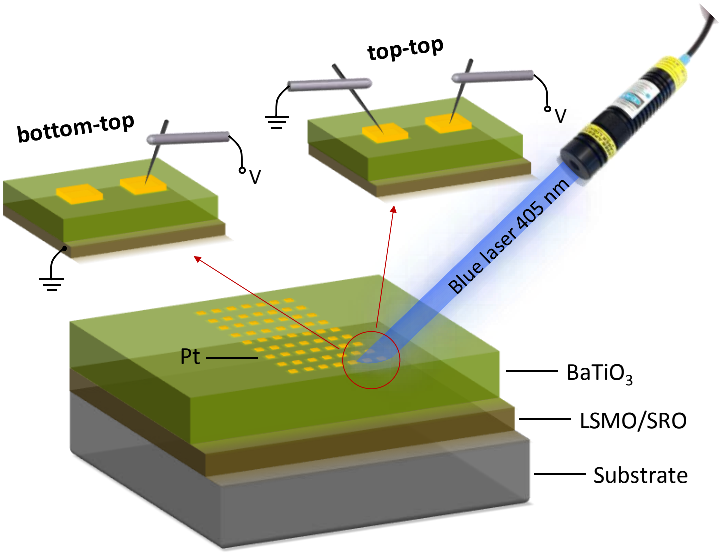

Figure 2.8. Sketch of measurement under blue laser illumination. The bitmap of the laser is the one used in experiments.

The laser used in chapter 7 is a *Blue Sky Research* STEC multi-wavelength system with fixed parallel laser beam and tunable output energy. It provides ~1 mm diameter illumination at $\lambda = 638$ nm, 520 nm, 450 nm and 405 nm with maximum power density from 1.5 to 2.8 W/cm^2. In chapter 7, a fixed 1.5 W/cm^2 power density is used among different λ towards comparable results. Figure 2.9 shows a sample measured under 4 different wavelengths.

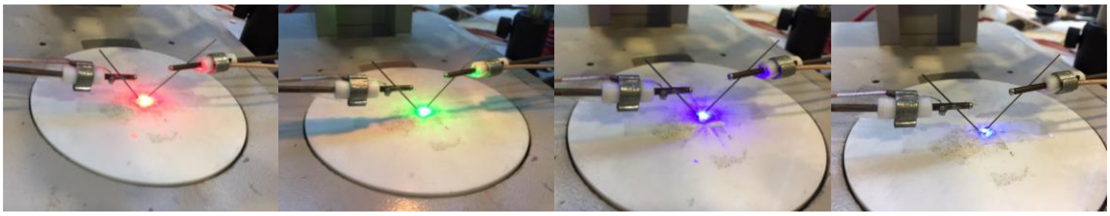

Figure 2.9. Sample measured on probe station under 4 λ illumination. Left to right, λ = 638, 520, 450 and 405 nm respectively.

The most used laser wavelength in the thesis is 405 nm, with 3.06 eV photon energy, which is of sub-bandgap energy of BTO single crystal (3.3 eV)[5]. It is known that oxygen deficiencies (or other point defects) in $BaTiO_3$ introduce donor states, either shallow or deep[6-8] in the bandgap and thus significant photon absorption, even for sub-bandgap incoming photons, can be anticipated[7,9,10]. Indeed, light absorption experiments reveal an enhanced absorption at 3.06 eV as Figure 2.10 shows. In Figure 2.10 we show the absorption spectra of a BTO/LSMO//STO(001) sample. For comparison data collected on a bare STO substrate is included. To emphasize changes in absorption close to the band edge, data are normalized at the corresponding values at energies well below the band edge. It can be observed an enhanced absorption (see STO spectrum for comparison) at energies similar to the used blue laser (405 nm, 3.06 eV) light.

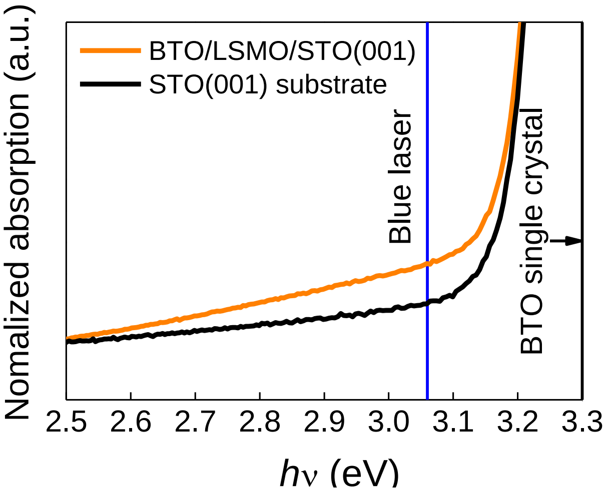

Figure 2.10 Absorption spectra normalized to their value at 2.5 eV of a BTO/LSMO//STO sample and of a bare STO (001) substrate.

2.2.3 Resistivity characterization

To determine the resistivity of thin films, van der Pauw method is used. It was first reported in 1958 by L. J. van der Pauw[11] with the ability of accurately measuring the resistivity of a sample of any arbitrary shape, in the case that the sample is approximately two-dimensional, namely one dimension of the sample should be much smaller than other dimensions. The procedure to determine the resistivity ρ of thin film used in this thesis which usually have a 5 × 5 μm dimension by van der Pauw method is as follows.

a) Place small drops of silver paste at the four corners of the film as electrodes, mark as electrodes A, B, C, D, as the sketch in Figure 2.11 shows.

b) Inject current though electrodes A and B, and measure the voltage at electrodes D and C. Then a resistance $R_{\mathrm{AB,DC}}$ can be calculated. The amplitude of injecting current depends on the materials checked. For LSMO or SRO that is used as bottom electrode, the current about 1 mA should be a proper scale. While for BTO that is very insulating, the current used should be at the scale of nA or even smaller, thus controlling the noise in the signal is crucial. Van der pawn test on BTO film is generally performed in the chamber of *Lakeshore* EMPX-HF probe station (see section 2.2.6) to enhance the signal-to-noise ratio, which provides a completely electromagnetic shielding.

c) Repeat the test in b) but change the sign of injecting current, then obtain $R_{\mathrm{BA,CD}}$. The purpose of doing this is to cancel out any offset voltages.

d) Repeat similar test as b) and c) but rotate the sample 90°, 180° and 270°. Then $R_{\mathrm{DA,CB}}$, $R_{\mathrm{AD,BC}}$, $R_{\mathrm{CD,BA}}$, $R_{\mathrm{DC,AB}}$, $R_{\mathrm{BC,AD}}$, $R_{\mathrm{CB,DA}}$ are obtained.

e) Calculate ρ:

$$R_{\mathrm{vertical}} = (R_{\mathrm{AB,DC}} + R_{\mathrm{BA,CD}} + R_{\mathrm{CD,BA}} + R_{\mathrm{DC,AB}}) / 4 \tag{2.2}$$

$$R_{\mathrm{horizontal}} = (R_{\mathrm{DA,CB}} + R_{\mathrm{AD,BC}} + R_{\mathrm{BC,AD}} + R_{\mathrm{CB,DA}}) / 4 \tag{2.3}$$

$$\rho = \frac{\pi d}{ln2} \cdot \frac{R_{vertical}+R_{horizontal}}{2} \cdot f(\frac{R_{vertical}}{R_{horizontal}}) \tag{2.4}$$

where $f(\frac{R_{vertical}}{R_{horizontal}})$ is the van der Pauw correction factor, its deduction and value can be found in van der Pauw's work[11].

In the practical operation, excepting measuring ρ of BTO or LSMO on the single layer, ρ of LSMO can also be measured on BTO/LSMO bilayers, due to the huge difference of resistivity between BTO (10^6~10^7 $\Omega\cdot\mathrm{cm}^{-1}$) and LSMO ($10^{-3}$ $\Omega\cdot\mathrm{cm}^{-1}$). Although electrodes connect to BTO and LSMO simultaneously, the vast majority of injected current flows though LSMO so that measured resistance is for LSMO.

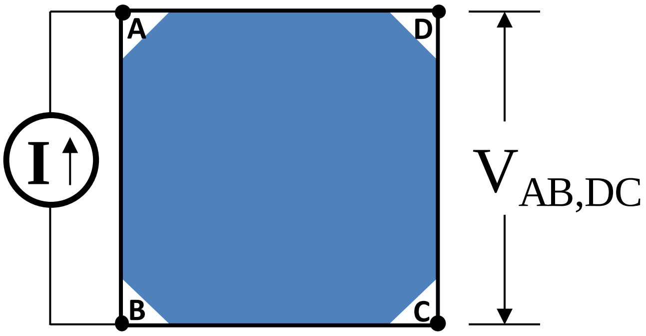

Figure 2.11. Sketch of electrodes and measuring configuration of van der Pauw method.

2.2.4 Impedance spectroscopy

Impedance spectroscopy is recorded using an *Agilent* HP4192A impedance analyzer. The purpose of obtaining impedance properties is to extract the permittivity of the material. The ferroelectric thin films can be considered as parallel capacitors, where

$$C = \varepsilon_0 \varepsilon_r A/t \tag{2.5}$$

ε_0, ε_r, A and t is vacuum permittivity, relative permittivity of the material, electrode area and thickness respectively. And capacitance can be calculated from the measured impedance:

$$\tilde{C} = \frac{1}{i\omega\tilde{Z}} \text{where} \tag{2.6}$$

$$\tilde{V}(\omega) = \tilde{Z}(\omega)\tilde{I}(\omega) \tag{2.7}$$

And it is a complex number with real part (Z') and imaginary part (Z''), equivalent to resistance R in DC circuit.

The HP4192A impedance analyzer provides measurable frequency range from 5 Hz to 13 MHz, oscillation voltage V_0 from 50 mV to 1 V. To obtain a frequency dependence spectroscopy of impedance, the device scan from low frequency to high frequency, generally in logarithm scale. At each frequency, AC oscillation $\tilde{V}(\omega) = V_0 e^{i\omega t}$ is applied and $\tilde{I}(\omega)$ is measured then $\tilde{Z}(\omega)$ is obtained.

Notice extrinsic influences on the impedance characterization of thin film materials should not be ignore. Due to the nanometer thickness scale of thin film, any influence such as circuit impedance, contact resistance, electrode/film interface capacitance, Maxwell-Wagner effect, etc. can lead inconsiderable deviation[12-18], even larger than the amplitude of thin film itself, especially at relative low frequency. In the case of BTO, due to its large resistivity, impedance at low frequency (typically < 1 kHz) is over the range of device, thus impedance recorded at higher frequency is used, avoiding these artifacts to a certain extent.

2.2.5 Measurement in vacuum

All previous mentioned electric characterization of $BaTiO_3$ can be performed by the open-air probe station shown in Figure 2.9, and can also be performed in vacuum or specific atmosphere at different temperature. A *Lakeshore* EMPX-HF multifunctional probe station provides these feasibilities. Samples can be measured in vacuum up to 10^{-6} mbar or other atmosphere such as N_2, Ar, synthetic air, etc., and in a temperature range 4 - 650 K. A window on the vacuum chamber allows illuminating the sample by lasers. The sketch of the system is plotted in Figure 2.12 and the picture on top right shows the measurement performed in the vacuum chamber and under illumination simultaneously.

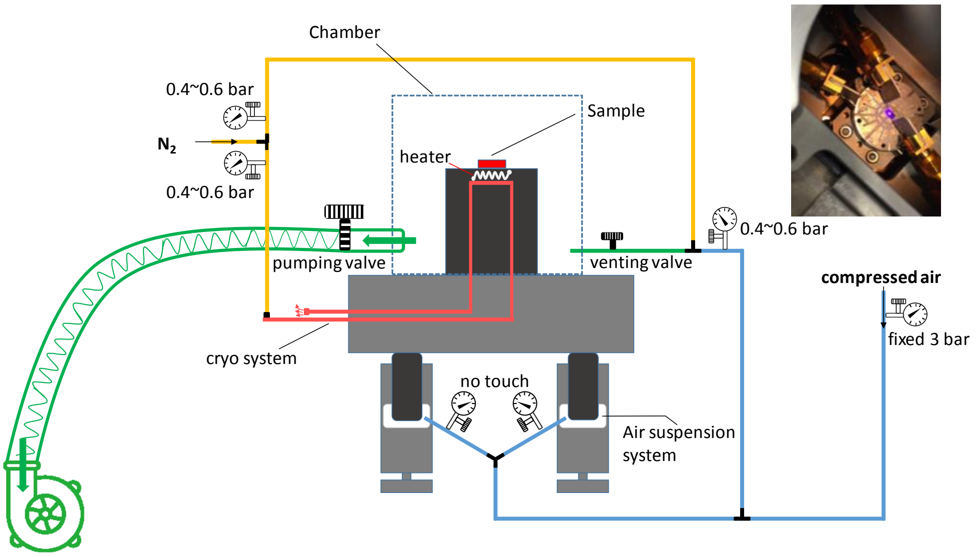

Figure 2.12. Sketch of *Lakeshore* EMPX-HF system. Picture on top right shows a sample measured in vacuum chamber and under illumination.

2.3 Surface characterization of ferroelectric thin films

2.3.1 X-ray photoelectron spectroscopy (XPS)

- **History**

X-ray photoelectron spectroscopy (XPS) is one of most powerful surface chemistry analysis technology which providing qualitative and quantitative information of elemental composition, chemical state and electronic state for all elements in principle. In practical, XPS can detects elements with atomic number of 3 (Li) and above, cannot easily detect H and He. Its history can trace back to 1880's that Heinrich Rudolf Hertz discovered the photoelectric effect, and later explained by Albert Einstein by Planck's concept of energy quantization in 1905 (Nobel Prize in Physics 1921). After half a century, during 1950's and 1960's, Kai Siegbahn's team in Sweden greatly improve the energy resolution and sensitivity of electron spectrometer that was prototypically developed by P.D. Innes in 1907. High resolution XPS spectrum was obtained and Siegbahn called the technology ESCA (Electron Spectroscopy for Chemical Analysis) in the publication. Then the first commercial monochromatic XPS system is produced by Hewlett-Packard cooperating with Siegbahn. His excellent work on XPS honors him the Nobel Prize in Physics at 1981.

Modern XPS system is greatly improved. For example, it can be combined with ultraviolet photoelectron spectroscopy (UPS) system, integrated into synchrotron light source, it can obtain depth profile by ion beam etching or tilting the sample, and it can analyze samples in ambient-pressure (tens of mbar) instead of high or ultra-high vacuum (10^{-8} to 10^{-9} mbar).

- **Principle**

Electrons in a material are with different levels of bonding energy E_B, and they can be excited from their initial states when they absorb external energy from photons with energy hv larger than E_B. In solid state materials, transition from excited electrons to photoemissions can be depicted by a 3-step model[19]. The first step is photo-excitation. Electrons from core levels or valence band are excited to empty states above Fermi level E_F. The second step is transportation towards the surface. In this process the excited electrons may encounter scattering on the route and only those elude inelastic collision can reach the surface without losing the E_B information on their initial states. The third step is the emission. Due to the existing of work function ϕ in solid state materials, only those with kinetic energy $E_k > \phi$ can escape from the surface and become photoelectrons. Electrons that already encounter inelastic scattering and still able to shake off the constraint of surface work function, will contribute to the secondary electron background of spectrum obtained[20].

E_k of photoelectrons is detected by electron spectrometer in XPS system. Then E_B can be determined by the conservation of energy equation based on the work of Ernest Rutherford (1914):

$$E_B = hv - (E_k + \phi) \tag{2.8}$$

where ϕ depends on the work function of both the spectrometer (usually called "analyzer work function") ϕ_a and the material ϕ_s. In practical XPS, ϕ_s is cancelled out by electrically connecting the sample surface (fixed on the sample holder by metallic clamp) and the spectrometer so that their Fermi levels are equilibrated. And ϕ_a is already calibrated and compensated in commercial XPS systems. Therefore, equation 2.8 can be simplified as:

$$E_B = hv - E_k \tag{2.9}$$

and E_B is easily obtained so long as knowing the energy of incident X-ray and measured kinetic energy. Due to each atom species has specific core level E_B, and variation of E_B caused by surrounding coordination atoms is small enough to be confused with other atom species, XPS spectrum can provide explicitly identification of each element of the surface and near-surface region.

Figure 2.13 is an illustration of the how X-rays interact with electrons in the material, how electrons finally reach electron spectrometer and contribute to the specific peaks of energy levels of the element.

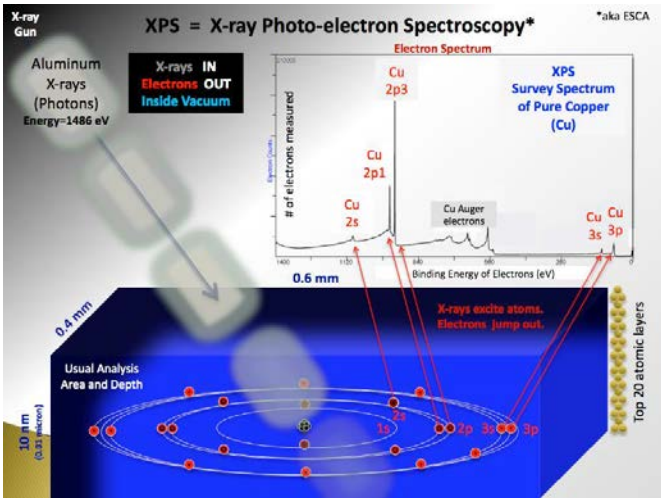

Figure 2.13. Schematic diagram of the process of electrons excited by X-rays and contribute to the spectrum. (Figure released by its author Dr. B. Vincent Crist into the public domain)

- **Experimental setup and sample preparation**

XPS measurements are performed with a Phoibos 150 analyzer (*SPECS* GmbH, Berlin, Germany) in ultra-high vacuum conditions (base pressure 4×10^{-10} mbar) with a monochromatic aluminum K_α X-ray source (1486.74 eV). The energy resolution as measured by the FWHM of the Ag 3d5/2 peak for a sputtered silver foil was 0.62 eV. Samples are cleaned by ethanol and ethanol then 20 min in UV + Ozone cleaner before measurement. Samples are fixed on the sample holder by metallic screws (contacting the upper surface of sample, namely the surface of BTO) that were grounded. Because samples have been exposed to air between when transferred to the XPS chamber, a clear C contamination was found in all spectra obtained in the thesis (see Figure A-1 in Appendix). The takeoff angle is always 90°. A sketch and a photograph of the XPS system used are displayed in Figure 2.14

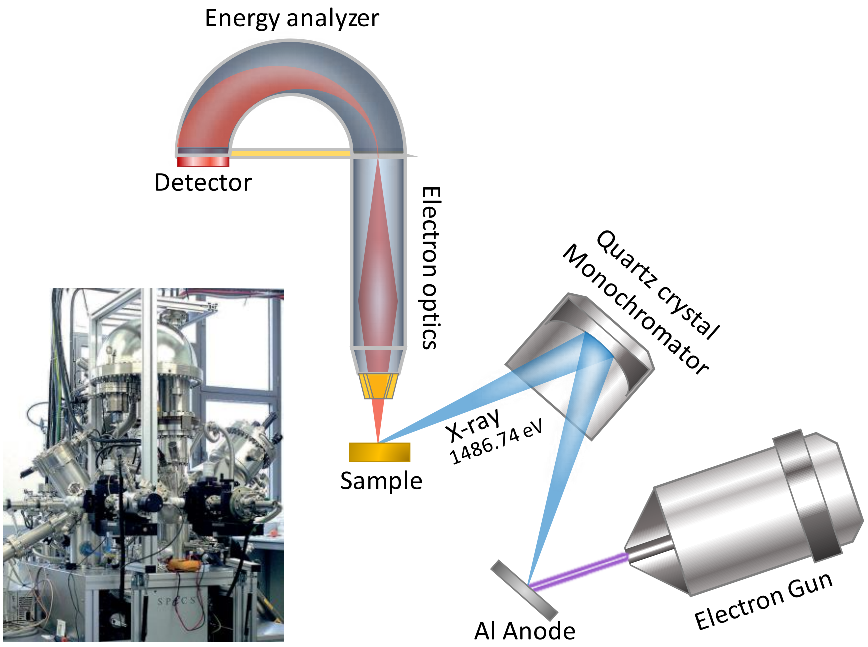

Figure 2.14. Sketch of basic components of XPS system (schematic diagram reproduced from *Physical Electronics*[21]).

- **Data analysis**

The data are analyzed by the software CasaXPS[22]. The binding energy is corrected by using the C-1s line at 284.6 eV as the reference. Curve fitting is performed using Gaussian/Lorentzian (70/30) ratio for all peaks with strict constrains. Full width at half maximum (FWHM) is constrained at the same value with ±0.2 eV fluctuation in a certain energy level of one element, e.g. 1.5±0.2 eV for O 1s and Ba 3d spectrum. And peak position is constrained to ±0.1 eV fluctuation. Shirley algorithm was used to subtract the background before data fitting.

2.3.2 Atomic force microscopy (AFM)

Atomic force microscopy (AFM) is a scanning probe technique based on measuring forces interacting between a sharp tip and the surface of the sample when the distance between them at nanometric scale. An AFM system basically consists of a cantilever where the tip mounted at the end, a photodetector that detect the motion of the cantilever through the reflection of laser light, a piezoelectric tube which controls the position of scanning and the distance between AFM tip and the sample. A simplified sketch is plotted in Figure 2.15. When performing the measuring, the AFM tip is positioned close to the sample till the force from surface atoms applied to the tip, then a deflection Δx is applied to the flexible cantilever, which is proportional to the force according Hooke's law $F = -k\Delta x$, where k is the spring constant of the cantilever. This deflection is detected by a 4-quadrant photodetector, which senses the position variation of laser beam reflected from the back of the cantilever, and finally be outputted as topography signal. To perform a scan on a selected area, a piezoelectric tube bonded to the sample holder is used to control the movement on x and y direction. And continuously electronic feedback by applying required voltage on the piezoelectric tube is used to corrects the z position for ensuring constant the tip-to-sample distance and force applied to the tip. Typically, the resolution of an AFM system can be 2-10 nm in x and y direction and 0.1 nm in z direction^{23}.

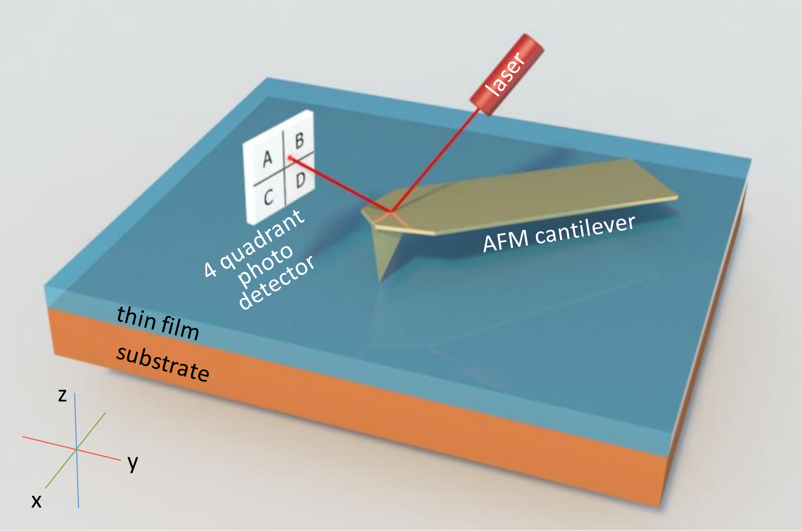

Figure 2.15. Sketch of atomic force microscope.

2.4 Structural characterization of ferroelectric thin film

2.4.1 X-ray diffraction (XRD)

X-ray diffraction is a widely-used technology in crystal structure analysis. Its principle is based on Bragg's law:

$$2d_{hkl}\sin\theta = n\lambda \qquad (2.10)$$

where d_{hkl} is the interplanar distance of crystal planes shows in Figure 2.16, θ is the incident angle, n is the order of diffraction and λ is the wavelength of the X-ray. While X-ray incident on crystal planes, photons are scattered by crystal planes and when the difference of light path length between two adjacent crystal planes, $2d_{\mathrm{hkl}}\sin\theta$, equals to n (n = 1, 2, 3···) times of λ, the Bragg's law is satisfied. Then the amplitude of diffracted wave is maximum superimposed. Diffractometer is used to record these specific high-intensity diffraction signals and corresponding θ. Then lattice parameter d_{hkl} is obtained.

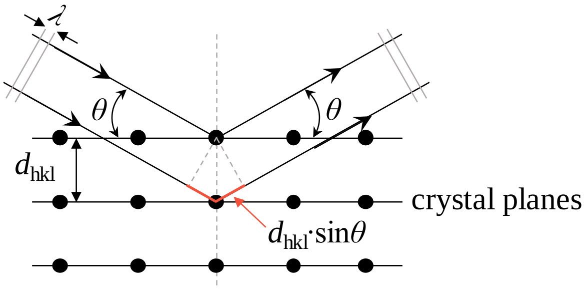

Figure 2.16. Scheme of Bragg condition (reproduced from the thesis of Dr. Diego Gutiérrez[2]).

- ***θ*-2*θ* theta scan**

θ-2θ scan is a method of XRD used in this thesis to check the out-of-plane lattice parameter of BTO(001) thin films, bottom electrodes and substrates. The motion of the detector (2θ angle) and the incident angle on BTO surface (θ) keep coupled during the scan. The scan at range 2θ = 10° – 120° can obtain 4 orders of diffraction peaks of BTO/LSMO(SRO)//substrate multilayers: (001), (002), (003) and (004). By these 4 orders of diffraction peaks one can correct the deviation between measured and real θ which is caused by small misalignment of sample mounting or the non-flat sample bottom. Assuming the deviation is a small angle δ, the Bragg's law will become:

$$2d_{hkl}\sin(\theta_{00l}+\delta)=\mathrm{n}\lambda \tag{2.11}$$

where θ_{00l} is the measured θ at each order of diffraction. With knowing n, λ and at least 2 groups of θ_{00l}, d_{hkl} and δ can be solved. θ of the substrate is chose to perform this correction, because the diffraction peaks of the substrate are well defined due to their high intensity and sharp peaks, also its real d_{hkl} is known that can be used to compare.

The θ-2θ scans in Chapter 3-5 and Chapter 7 are measured by a *Siemens* D500-2 circle diffractometer with Cu target, and the X-ray is two main lines: $k_{\alpha 1}$ = 1.5406 Å and $k_{\alpha 2}$ = 1.5444 Å with relative intensity 2:1. The θ-2θ scans in Chapter 6 are performed using a *Bruker* D8 Discover A25 high resolution diffractometer with Cu target and graphite monochromator thus $k_{\alpha 2}$ line is filtered.

- **X-ray reflectivity (XRR)**

X-ray reflectivity (XRR) is the method used in the thesis to determine the thickness of BTO thin films. And it can also reflect the flatness of the film. In the XRR measurement, diffractometer works by means of θ-2θ but at very low angles (2θ = 0.5° to 6.0° used in this thesis). In this case diffraction effect depicted by Bragg's low takes place at the top and bottom surface (interface with the substrate) of thin film instead of crystal planes. Thus d in equation (2.10) becomes the thickness of the film and refractive effects, which is negligible at high angle diffraction, must be took into account. Recorded spectrum starts below the critical angle of the materials which all incident radiation is reflected. Afterwards oscillations along with intensity decreasing named Kiessig fringes appears, which their period relies inversely on the film thickness.

A *Rigaku* Rotaflex RU-200B diffractometer with Cu target X-ray source is used for XRR measurement.

- **Reciprocal space map**

Reciprocal space map (RSM) in an important analysis method for epaxial films that allows accessing the in-plane lattice parameters. In crystallography, reciprocal space represents the Fourier transform of the real space crystal lattice. For example, diffraction patterns obtained in X-ray diffraction or electron diffraction are images in reciprocal space, and structure information of real space can be deduced from them. Ewald sphere as shown in Figure 2.17a is used to demonstrate the relationship between real space and reciprocal space. The position of X-ray diffracted by (hkl) plane in a sample, O, is set as the origin of coordinate of real space. Constructing a sphere with radius of $1/\lambda$, which cut the incident vector at point A and O^* and the diffraction vector

(2.12)

at point G. Set $\overrightarrow{OO^*} = \vec{K}$, $\overrightarrow{OG} = \overrightarrow{K'}$ and $\overrightarrow{O^*G} = \vec{g}_{hkl}$, in right triangle AOG

$$sin\theta = \frac{O^*G}{O^*A} = \frac{|\vec{g}_{hkl}|}{2/\lambda}$$

As diffraction geometry must conforming Bragg's law, from equation 2.11 we can obtain:

$$\sin\theta = \frac{1/d_{hkl}}{2/\lambda} \tag{2.13}$$

comparing equation 2.12 and 2.13, one can find $|\vec{g}_{hkl}| = 1/d_{hkl}$. $\vec{g}_{hkl}$ is defined as the reciprocal vector: $\vec{g}_{hkl} = h\bar{a}^* + k\bar{b}^* + l\bar{c}^*$. The origin of coordinate $O*$, basis vector $\overrightarrow{a^*}$, $\overrightarrow{b^*}$ and $\overrightarrow{c^*}$ construct the reciprocal space, as the grid in Figure 2.16a shows, where each point in reciprocal space represents a family of planes in real space. For orthorhombic lattice, $\bar{a}^* = 1/\vec{a}$, $\bar{b}^* = 1/\vec{b}$, $\bar{c}^* = 1/\vec{c}$, where $\vec{a}$, $\vec{b}$, $\vec{c}$ are basis vectors of real space, i.e. the lattice parameters. The diffracted X-ray is finally recorded by the detector as diffraction pattern that brings the coordinate information of $\vec{g}_{hkl}$ allowing accessing to lattice parameters. This diffraction pattern is called reciprocal space map in X-ray diffraction technology. It can be built by certain geometry and scanning mode of the Diffractometer.

RSMs in Chapter 4,5 are obtained using a *Bruker* D8 General Area Detector Diffraction System (GADDS) with a 4-axis sample stage, measurement geometry is shown in Figure 2.16b. First, an asymmetric crystal family $\{hkl\}$ is selected. Then φ and χ are moved to and fixed at positions making the $\{hkl\}$ family of planes horizontal. Afterwards 2θ and ω are moved to achieve the new diffraction geometry. A serial of 2θ scans are performed at various ω and converted into RSM at the end.

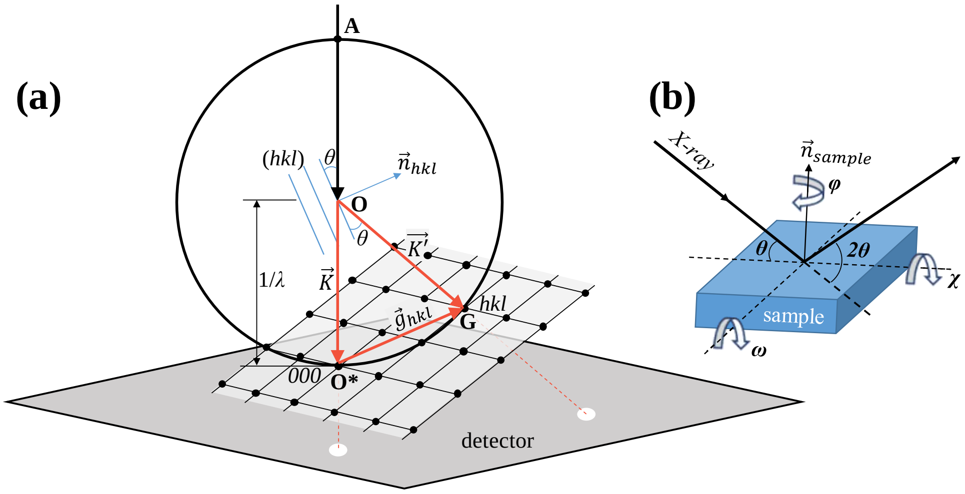

Figure 2.17. (a) Ewald sphere. (b) Geometry of sample measured in *Siemens* D500-2 circle diffractometer.

RSMs in Chapter 6 are results from KMC-2 beamline at HZB BESSY II synchrotron light source, which has a more complex goniometer. RSMs are obtained by fixing δ, η and χ at geometry of Bragg's law and performing φ scan (rotating sample on its surface normal, see Figure 2.20). RSMs built by synchrotron X-ray are with much higher spatial resolution and provide more detailed information of crystal structure, e.g. biaxial strain state, than normal diffractometer. Details are described in the next section.

2.4.2 Synchrotron radiation of X-ray diffraction

Synchrotron radiation is the electromagnetic radiation produced when charged particles with velocity v close to the speed of light are deflected in electromagnetic field. The frequency of synchrotron radiation can cover the entire electromagnetic spectrum. Typically, in a synchrotron facility, electrons are accelerated then injected into the storage ring. The radiation emits tangential to electron bunches and are contracted to a narrow fan shape due to the effect of relativity, as shown in Figure 2.18, then captured by beamlines. Synchrotron radiation can provide X-ray with intensity million times higher than that of conventional X-ray tube. And tuned by slits, attenuators, crystal monochromators and mirrors, the bandwidth, photon flux, beam dimensions, focus and collimation of the X-ray can be precisely controlled. Therefore, with high intensity, high stability and highly collimated X-ray, synchrotron light source is ideal for high-spatial-resolution crystal microstructure study.

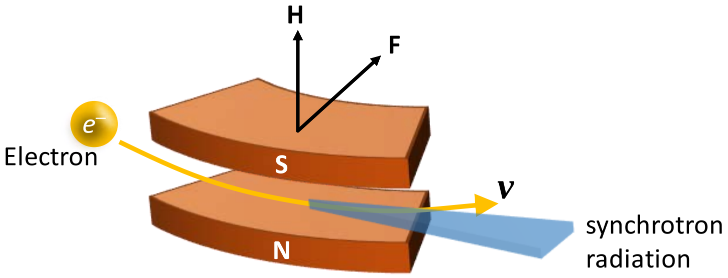

Figure 2.18. Sketch of synchrotron radiation produced by electrons in storage ring.

RSMs of BTO thin films in Chapter 6 are built by X-ray diffraction performed at KMC-2 beamline at HZB BESSY II synchrotron light source located at Berlin, Germany, as Figure 2.19 shows. The diffraction station of KMC-2 beamline is basically equipped by a 6-circle psi-geometry goniometer (*Huber*) with open Eulerian cradle, a motorized *x*-*y*-*z* sample stage (Huber), a scintillation point detector (Cyberstar) with motorized apertures and an area detector (*Bruker* Våntec 2000 MikroGap) that provides 250 µm spatial resolution. The sample was mounted on the *x*-*y*-*z* sample stage and 4 circles of goniometer were used: δ, η, χ and φ, the other 2 circles μ and v used for non-coplanar scattering are not applied in this work. See Figure 2.20 for the sketch of the sample stage and goniometer. To keep the conformity with results of θ-2θ scans, the wavelength of X-ray was tuned to 0.154056 nm by the monochromator. Temperature dependence of lattice parameters was characterized by RSMs from room temperature to 750°C, which was performed by heating up the sample via a domed hot stage (*Rigaku* Anton Paar DHS 1100) mounted on the *x*-*y*-*z* sample stage. For avoiding introducing oxygen vacancies, BTO film was heated in ambient atmosphere and the graphite dome was used to guarantee thermal stability in this case as Figure 2.21 shows. Double thermal couples, one adjacent to the heater and another underneath the sample, and sufficient waiting time after temperature reached set-points were employed to ensure the temperature accuracy. See the reference[24] and online manual[25] of KMC-2 beam line for more technical details.

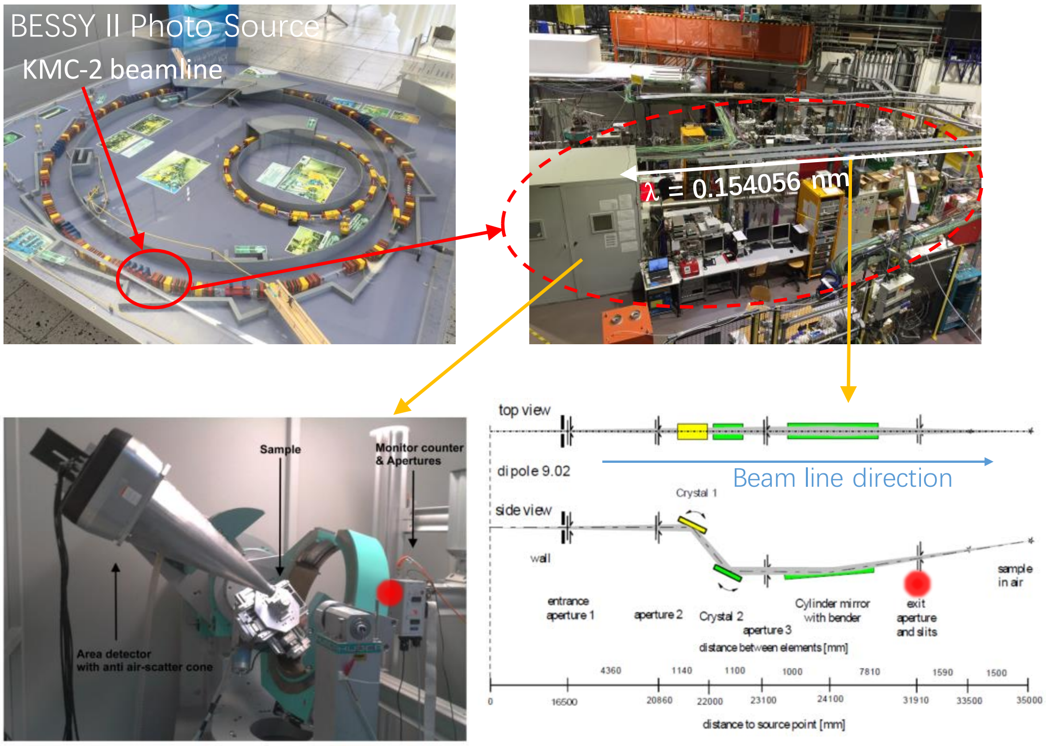

Figure 2.19. Top: Location of KMC-2 beamline in BESSY II synchrotron light source. Bottom left: experimental setup for diffraction measurement. Bottom right: sketch of the beamline. (Two bottom photographs reproduced from reference[24].) The red spot mark the position of incident slit of X-ray.

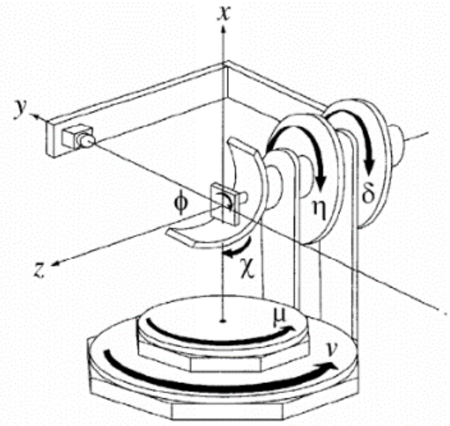

Figure 2.20. Sketch of the *x*-*y*-*z* sample stage and the 6-circle psi-geometry goniometer (schematic diagram reproduced from KMC-2 online manual [25]).

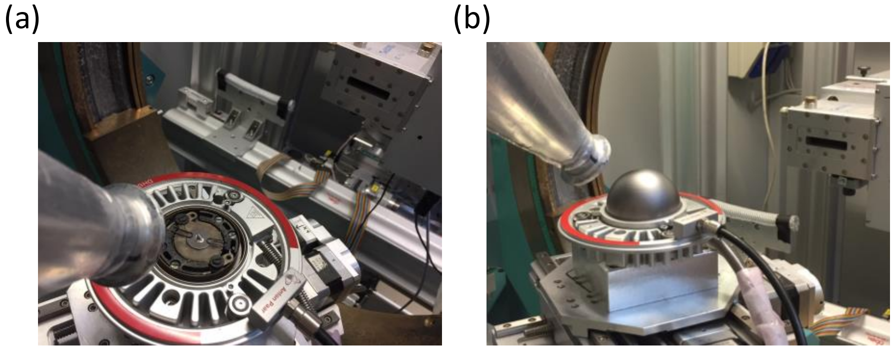

Figure 2.21. Photographs of *Rigaku* Anton Paar DHS 1100 domed hot stage. (a) Sample mounted. (b) Graphite dome mounted.

- **Grazing incidence diffraction**

Grazing incidence is a type of diffraction geometry with incident angle very close to critical angle of the sample and incident beam is diffracted almost in the plane of sample surface. Thus, grazing incidence X-ray diffraction (GIXD) is a surface sensitive analysis methodology due to the limit of X-ray penetration, changing the incident angle in a small range is able to build up depth profile of RSM. Figure 2.22 shows an example of measuring (111) diffraction of BTO(001) film by GIXD in practical. 3 circles of the goniometer, δ, χ and φ (see Figure 2.20), are fixed to meet the Bragg's law in grazing incidence geometry. And η is tuned to very small values (typically < 1°) to perform GIXD. The real incident angle γ can be calculated by equation: $sin\gamma = sin\eta \times sin\chi$ in experimental setup used in this thesis. Then one can obtain:

$$\lim_{\gamma \to 0, \eta \to 0} \frac{\sin\gamma}{\sin\eta} = \lim_{\gamma \to 0, \eta \to 0} \frac{\gamma}{\eta} = \sin\chi$$

where $sin\chi$ is a constant value here. That means γ is proportional to η when both of them are small. Therefore, we can use η instead of γ in the results' discussion to simplify the digits. (2.14)

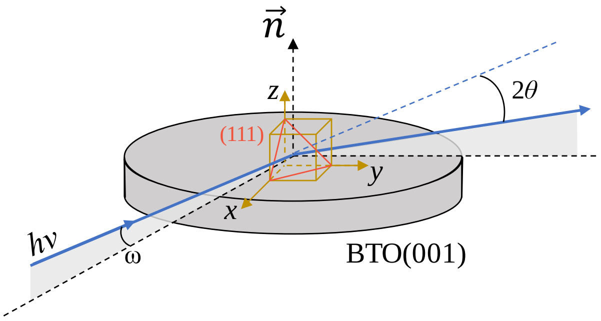

Figure 2.22. Illustration of GIXD performed on (111) plane of BTO(001) thin film.

2.5 Steam treatment

Steam-treatment experiment performed in chapter 5 is to enforce more water molecules and hydroxyl groups bonding on BTO surface via long time exposing BTO in steam from boiling water. The experiment setup is as Figure 2.23 shows. Deionized water keeps boiling in the bottle heating by a *YiDu* PTC heater at ambient pressure and room temperature surroundings. The sample is hanged above the water with surface parallel to steam flux. This process consists on placing the film at 100°C and in a jet of water vapour (800 cm^3/min) at atmospheric pressure for various time lengths.

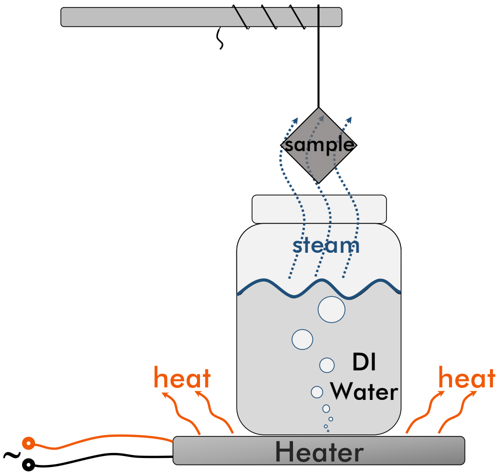

Figure 2.23. Schematic diagram of the steam exposure experiment.

2.6 NH$_3$ annealing experiment

NH$_3$ annealing treatment in Chapter 7 is performed by heating up the BTO sample in a tube furnace with controlled NH_3 flow. Once the sample is located into the center of the quartz tube, N_2 is purged into the cube and keeps flowing for sufficient time to evacuate the air. Then NH_3 flow replaces N_2 and stays at set flux during all the warming, annealing and cooling procedures. This experiment is cooperated with the Solid State Chemistry group in ICMAB and managed by Prof. Amparo Fuertes and Ashley Black. Figure 2.24 shows the sketch and photograph of experimental setup.

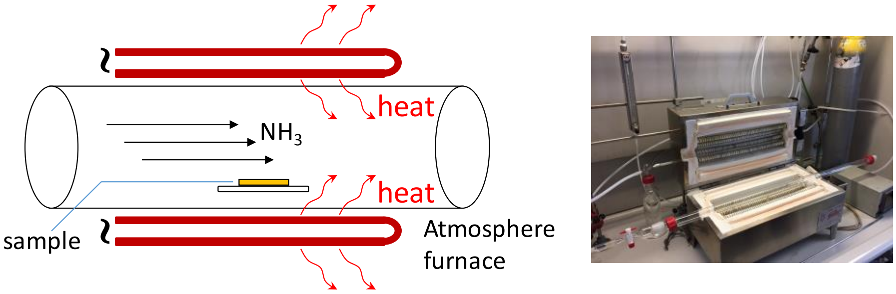

Figure 2.24. Sketch and photograph of the experimental setup for NH_3 annealing.

2.7 Transmittance spectroscopy

Transmittance spectra of thin films or single crystals in this thesis are obtained by an *Agilent* Cary 5000 UV-Vis-NIR (ultraviolet-visible light-near infrared) spectrometer. It can provide transmittance spectra in the range of λ = 200 nm to 1200 nm. Basic components and light path during measuring are plotted in Figure 2.25. Back side of samples are polished before measurement to remove the attached silver paste during PLD process and cleaned by acetone and ethanol. At first, two identical shadow masks with a hole slightly smaller than the sample are mounted at positions of “sample” and “reference” as the sketch show. Then the device make a scan and set obtained spectrum as the background which means 100% transmittance since no sample mounted. Afterwards the sample is mounted on the mask plate located at the position of “sample” and completely covers the hole. Finally, the transmittance spectrum of the sample is obtained through an identical scan with the background subtracted.

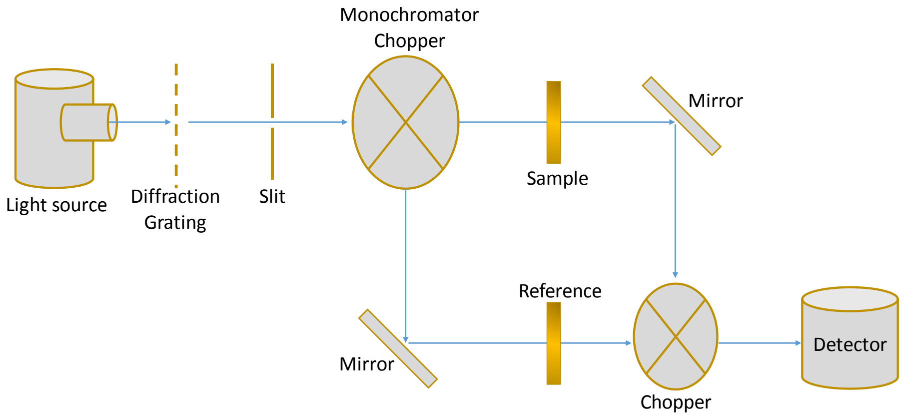

Figure 2.25 Experimental setup of Cary 5000 UV-Vis-NIR spectrometer.

Chapter 3. Influence of electrodes configuration on imprint and ferroelectric characterization

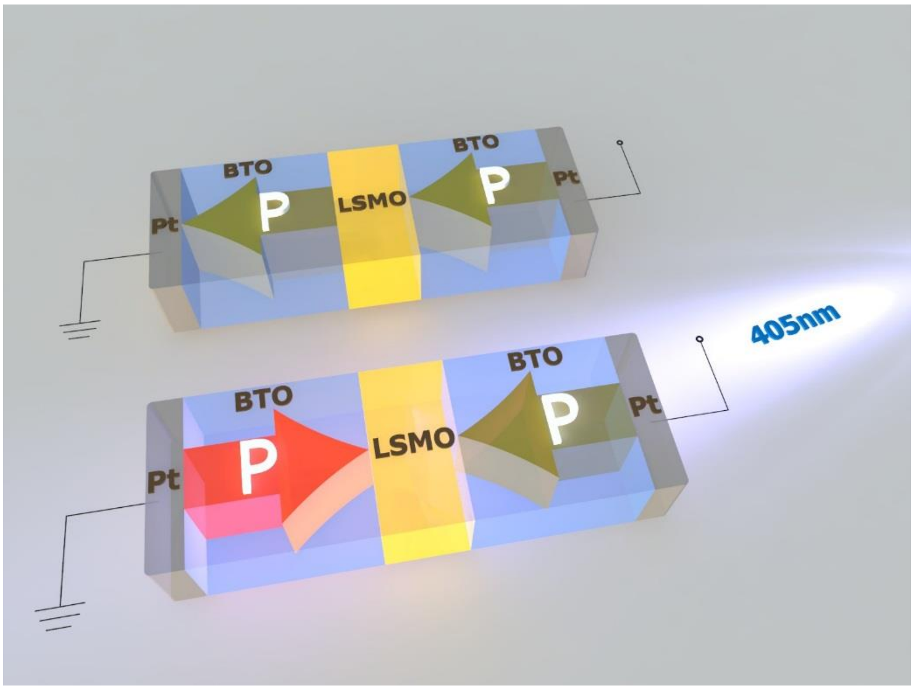

ABSTRACT

Ferroelectric materials have a spontaneous polarization that can point along energetically equivalent, opposite directions. However, when ferroelectric layers are sandwiched between different metallic electrodes, asymmetric electrostatic boundary conditions may induce the appearance of an electric field (imprint field, E_{imp}) that breaks the degeneracy of the polarization directions, favoring one of them. This has dramatic consequences on functionality of ferroelectric-based devices such as ferroelectric memories or photodetectors. Therefore, to cancel out E_{imp}, ferroelectric components are commonly built and tested using symmetric contact configuration. Indeed, in this symmetric contact configuration, when measurements are done under time-varying electric fields of relatively low frequency, symmetric single-step switching process is observed, indicating $E_{\mathrm{imp}} \approx 0$. However, we report here on the discovery that when measurements are performed at high frequency, a well-defined double-step switching is observed, indicating the presence of E_{imp}. We argue that this frequency dependence originates from short-living head-to-head or tail-to-tail ferroelectric capacitors in the device. We demonstrate that we can modulate E_{imp} and the life-time of head-to-head or tail-to-tail polarization configurations by adjusting the polarization screening charges by suitable illumination. These findings are of relevance to understand the effects of internal electric fields on pivotal ferroelectric properties, such as memory retention and photoresponse.

3.1 Introduction

Ferroelectric materials are receiving an enormous attention due to a plethora of already real and potential applications[26]. Most of these applications are based on their excellent piezoelectric properties or on their charge storage capability as exploited in non-volatile memory applications[27,28]. Nowadays, a flurry of research is focused on ferroelectric tunnel junctions for novel memory applications[29-34] and on photo-effects in ferroelectrics for their integration in solar cells[35-38]. In both applications, the role of internal electric fields is very important. In the former, internal fields determine the memory retention[39], and in the latter internal electric fields determine the magnitude and direction of the photocurrents[40-46]. Two types of internal electric fields can be identified: the depolarizing field (E_{dep}) and the imprint field (E_{imp}). The former (E_{dep}) is opposite to the direction of the polarization, is responsible of the film depolarization. The latter (E_{imp}) drives ferroelectric polarization towards a preferential direction when biasing electric fields are removed.

Imprint fields can have different origins, such as asymmetric metal-dielectric interfaces, which may give rise to unequal Schottky barriers, or graded defect concentration[47,48]. Consequently, to reduce E_{imp}, electrode-ferroelectric-electrode structures should be made as symmetric as possible[49]. When dealing with ferroelectric thin films, a common approach is the use of a symmetric contact configuration in which the ferroelectric film is grown on a bottom metallic electrode and two identical top electrode pads are contacted. In this so-called, top-top measurement configuration, the two pads and the ferroelectric layer form a two capacitors series circuit connected via a common bottom electrode. As a result, symmetric polarization-vs-electric field loops can be obtained[46,50]. When applying an electric field ($\boldsymbol{E}$) to the sample using the top-top configuration, the polarization $\boldsymbol{P}$ under each electrode points towards opposite directions. If an $\boldsymbol{E}_{\mathbf{imp}}$ exists across the ferroelectric layer, under one electrode $\boldsymbol{P}$ is parallel to $\boldsymbol{E}_{\mathbf{imp}}$ whereas under the other $\boldsymbol{P}$ is antiparallel to $\boldsymbol{E}_{\mathbf{imp}}$. Similarly, $\boldsymbol{E}_{\mathbf{imp}}$ is parallel to the applied electric field $\boldsymbol{E}$ in one capacitor but antiparallel in the other. As the switching of every ferroelectric capacitor is dictated by the actual field acting on it, their switching should occur at different $\boldsymbol{E}$ values and thus fingerprints of E_{imp} on *P-E* loops must be observable. However, as mentioned, data collected using top-top configuration typically display symmetric *P-E* loops, suggesting a virtual cancellation of E_{imp}. To decipher the ultimate reasons for the absence of imprint signatures in these devices is crucial for their performance optimization and understanding.

Here we study in detail the role of the E_{imp} on the switching process in devices formed by ferroelectric films [$BaTiO_3$ (150 nm), BTO] grown on a metallic bottom electrode [$La_{2/3}Sr_{1/3}MnO_3$ (50 nm), LSMO] using $SrTiO_3$ (STO) substrates. Measurements are performed using an asymmetric contact configuration (bottom-top, sketched in Figure 1a) and compared to those obtained in symmetric contact configuration constituted by two identical top metallic electrodes (top-top, Figure 1b). It is found that when using top-top, no signatures of E_{imp} in current-field *J-E* and polarization-field *P-E* loops are observed if measurements are performed at relatively low frequencies, thus indicating the E_{imp} does not show up. However, when loops are recorded at higher frequency, a two-step ferroelectric switching becomes visible, which signals the presence of $E_{\mathrm{imp.}}$ We argue that these results indicate that the absence of E_{imp} fingerprints in $P(E)$ loops recorded using in symmetric top-top configuration, is the result of a dynamic charge polarization screening process rather than an equilibrium property of the device. Consistently, we show that single or two-step *P-E* loops can be obtained in a given device at a given frequency, by on-purpose modification of the screening of the polarization by using photogenerated carriers. We claim that the commonly observed symmetric *P-E* loops in top-top symmetric electrode configuration is the result of a *simultaneous* switching of the polarization of the ferroelectric layers of each capacitor to avoid unfavorable head-to-head/tail-to-tail domain configuration, while the E_{imp} is still present. These conclusions, which have been verified by experiments performed on a variety of $BaTiO_3$ films grown on different substrates and using different bottom electrodes and also on $BaTiO_3$ single crystals, should help to the better understanding of the response of ferroelectric-based memories and of photo-effects arising in ferroelectric materials.

3.2 Materials

$BaTiO_3$ (150 nm)/$La_{2/3}Sr_{1/3}MnO_3$(50 nm) bilayers were grown by pulsed laser deposition on (001) $SrTiO_3$ substrates. 20 nm thick Pt top electrodes with dimension of 60×60 μm^2 and 15 μm apart (see Methods), were deposited ex-situ on the BTO surface by RF-sputtering. For comparison purposes, $BaTiO_3$ thin films on other substrates [$DyScO_3$ (DSO) and $(La,Sr)(Al,Ta)O_3$ (LSAT)], or using other metallic bottom electrodes [$SrRuO_3$ (SRO)] have also been tested, Consistent results have been obtained in all cases. We have also measured a $BaTiO_3$ single crystal (1 mm thick). In bottom-top (*b*-*t*) configuration (Figure 3.1a), the bias voltage (V) was applied to one of the top electrodes and the bottom electrode was grounded. In top-top (*t*-*t*) configuration (Figure 3.1b), one top electrode was biased and the other was grounded. Ferroelectricity was characterized by measuring the dynamic I-V hysteresis loop to determine the switchable polarization P (see Chap. 2 for details).

3.3 Results and discussion

3.3.1 Polarization switching in symmetric and asymmetric capacitors

Figure 3.1c,e,g and Figure 3.1d,f,h show the J-E loops (arrows indicate the sense of the electric field excursion) recorded at various frequencies using *b*-*t* and *t*-*t* configurations, respectively. The corresponding P-E loops are shown in Figure 3.2. In *b*-*t* configuration (Figure 3.1c,e,g), it can be observed that, irrespective of the measurement frequency, the current switching peaks (indicated by dashed lines for increasing voltage) occurring at the coercive field (E_c), are shifted along the positive electric field axis. This is a signature of the presence of E_{imp} that, in the present case, is pointing away from LSMO. A similar imprint direction has been determined by other authors on similar heterostructures[51]. From loops measured at 15 Hz we derive: $E_{imp} = (E_{c+} + E_{c-}) / 2$ is ~121.5 kV·cm^{-1} and a coercive field $E_c = (E_{c+} - E_{c-}) / 2$ of about ~100 kV·cm^{-1}. $E_{c\pm}$ are the coercive fields measured at positive and negative fields, respectively. As mentioned, it is known that E_{imp} can originate from a variety of effects, the most obvious one being a difference of work functions of the used electrodes; in the *b-t* configuration: LSMO and Pt, respectively. Although other mechanisms could play a role, the important point here is that E_{imp} is well visible and points away from LSMO. Tests performed on other *b-t* contacts yield similar E_{imp} values. The same orientation of E_{imp} had also been found in similar Pt/BTO/LSMO heterostructures and it was shown to be compatible with the different of screening ability of LSMO and Pt electrodes[52].

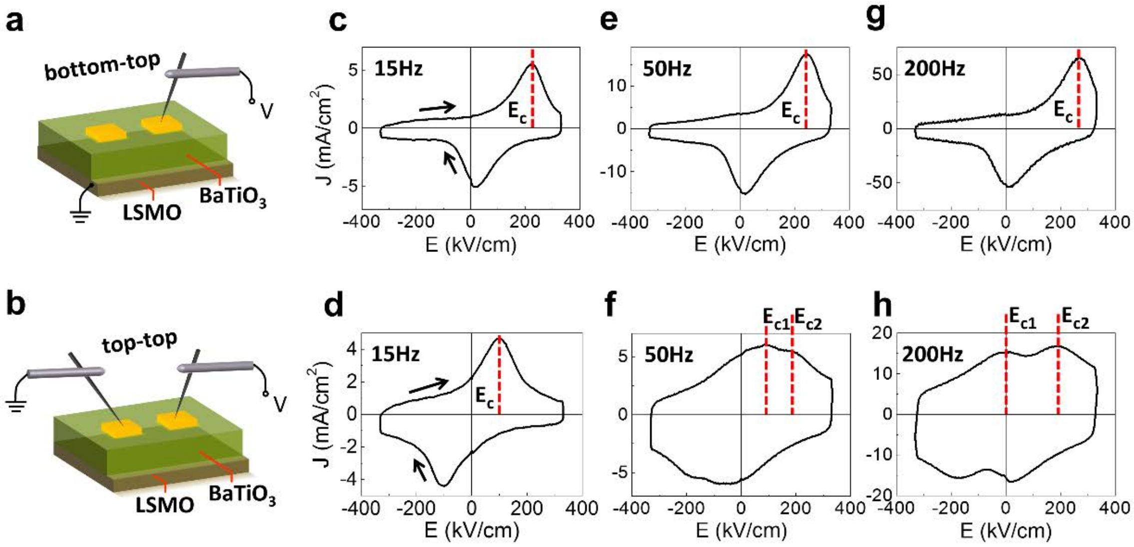

Figure 3.1. (a) Sketch of bottom-top (*b-t*) electrodes configuration for BTO (150 nm)/LSMO (50 nm)//STO sample. Top electrodes (yellow) represent the Pt top electrodes. (b) Sketch of top-top (*t-t*) electrodes configuration. (c,e,g) *J-E* loops measured in *b-t* at 15, 50 and 200 Hz, respectively. (d,f,h) *J-E* loops measured in *t-t* at 15, 50 and 200 Hz, respectively. The coercive field of single-switching-peak loops (E_c) and the corresponding E_{c1}, E_{c2} of double-switching-peaks loops are indicated by the (red) dashed lines. Coercive fields are only depicted for the branches of increasing applied E-field.

The results obtained using *t-t* contacts are radically different. Indeed, in Figure 3.1d it can be appreciated that in the *J-E* loop measured at 15 Hz, the current switching peaks appear at symmetric electric field values thus indicating that E_{imp} has seemingly disappeared. This observation implies that the polarization directions of the two in-series ferroelectric capacitors have switched at the same electric field. The coercive field E_c ($\approx$ 100 kV·cm^{-1}) is identical to that determined in the *b-t* configuration.

In Figure 3.2, the *P-E* loops of BTO/LSMO//STO sample at three different frequencies recorded using *b-t* and *t-t* configurations, corresponding to the *J-E* loops of Figures 3.1c,e,g (*b-t*) and Figures 3.1d,f,h (*t-t*) respectively, are shown. The presence of imprint is well visible producing a noticeable shift of *P-E* loops towards positive E-field. The coercive fields do not vary appreciably with frequency. The *P-E* loops recorded in *t-t* configuration are symmetric and shrink dramatically as the frequency increases. The features visible in the *J-E* loops of Figure 3.1d,f,h, referred as double-switching peaks, are not clearly apparent in *P-E* loops because the current switching peaks are relatively small compared with the displacive current background, producing a less apparent contrast after the integration to obtain the polarization.

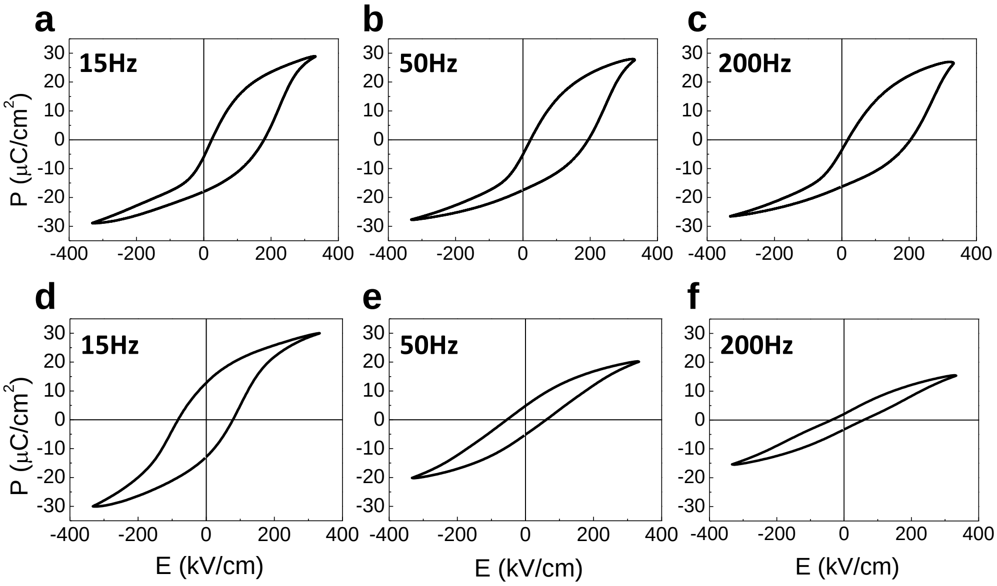

Figure 3.2. *P-E* loops of sample BTO/LSMO//STO measured in *b-t* (a,b,c) and *t-t* (d,e,f) configurations, at 15, 50, 200 Hz respectively, corresponding to the *J-E* loops in Figure 3.1c,e,g by *b-t* and Figure 3.1d,f,h by *t-t*, respectively.

A hint to identify the underlying mechanism for the absence of E_{imp} signatures in the low-frequency *J-E* loop recorded in *t-t* configuration can be obtained by inspecting the corresponding *J-E* loops recorded at higher frequencies (Figure 3.1f,h). At 50 Hz (Figure 3.1f) the ferroelectric switching current peak becomes broader and a tiny *additional* current peak appears (both signaled by dashed lines for increasing electric field). At even higher frequency (200 Hz) the presence of two switching peaks and their splitting are more evident (Figure 3.1h). This implies that the polarization switching in the two in-series capacitor device occurs as a two-step process, controlled by two at first sight, different coercive fields. In brief, two switching peaks in Figure 3.1f,h appear at different *E*-fields and their separation increases when increasing the measuring frequency. The fact that a double-switching current peak is clearly observable in the *t-t* but not in *b-t* measurements, indicates that it results from the measurement configuration rather than from an intrinsic property of the ferroelectric layer.

Similar experiments have been performed on other $BaTiO_3$ thin films grown on different substrates [$SrTiO_3$, $DyScO_3$ and $(La,Sr)(Al,Ta)O_3$] and/or using different bottom electrodes ($La_{2/3}Sr_{1/3}MnO_3$ and $SrRuO_3$). A $BaTiO_3$ single crystal where different electrodes have been deposited on opposite faces has been also tested. In all cases, consistent results have been obtained as described below.

Figure 3.3 shows a number of *J-E* loops measured on sample $BaTiO_3$(105 nm)/$La_{2/3}Sr_{1/3}MnO_3$(30 nm)//$DyScO_3$(DSO) using the *t-t* configuration at various frequencies. Similarly, to the results reported for BTO/LSMO//STO (Figure 3.1) double switching peaks shows up at relative high measuring frequency and they merge into one single peak at lower frequency.

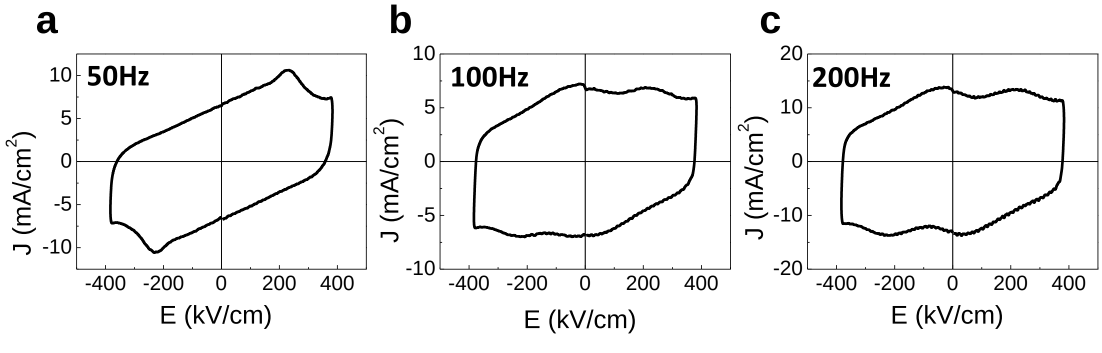

Figure 3.3. (a,b,c) The *J-E* loops of the sample BTO/LSMO//DSO measured in *t-t* configuration at 50, 100 and 200 Hz respectively, in dark (black curves) and under the

illumination of a blue laser (blue curves).

A (001) cut $BaTiO_3$ single crystal (Mateck Gmbh.) with dimension 1 cm × 1 cm × 1 mm, has also been similarly characterized. Two Ag electrodes with diameter 1.5 mm were prepared by silver paste on one of the crystal (001) faces. The opposite surface was fully coated with conductive carbon paste (bottom electrode). Therefore *t-t* and *b-t* measurements can be performed, mimicking the electrode configuration of Figure 3.1a,b.

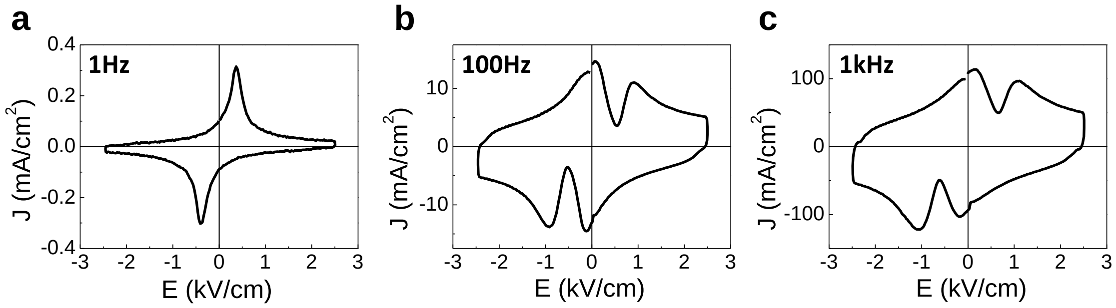

Figure 3.4. (a,b,c) The *J-E* loops recorded (in dark conditions) on a BTO single crystal measured in *t-t* configuration, at 1, 100 and 1000 Hz respectively.

Ferroelectric measurements on the single crystal were ran by using a similar setup as the thin film samples but by using a Trek 2205 voltage amplifier combined with the TFAnalyzer 2000, to allow reaching up to 500 V. Therefore, the maximum electric field than can be applied on the BTO single crystal (2.5 kV·cm^{-1} for *t-t*) is high enough to saturate its polarization. In Figure 3.4 we show the corresponding *J-E* data recorded in *t-t* at various frequencies. Obvious double switching current peaks and their variation when changing the measuring frequency are readily visible. These results are fully consistent with those recorded in BTO/LSMO//STO (Figure 3.1) and BTO/LSMO//DSO (Figure 3.3). The large lateral size of the sample does not allow performing measurements under illumination due to the smaller spot size of the laser.

3.3.2 Mechanism of double switching in symmetric double capacitors

Summarily, when using *t-t* configuration, the *J-E* loops recorded at low frequency display a single-switching current peak whereas at high frequency, two switching peaks splits are visible. In order to understand these results, we sketch in Figure 3.5a-c the expected voltage-dependent polarization of two ferroelectric capacitors connected in series through a common LSMO bottom electrode. In agreement with *b-t* experiments (Figure 3.1 c,e,g), the imprint field E_{imp} is depicted (small empty arrow) pointing away from LSMO. We sketch the ferroelectric polarization (P) direction (large solid arrow) for the two ferroelectric capacitors for different values of decreasing applied electric field (from V^+ to V^-). In Figure 3.5a, we show the situation occurring when an electric field ($V^+ > 0$) large enough ($E^+ >> E_{\mathrm{c}}$, E_{imp}) to saturate the ferroelectric with the polarization pointing towards the ground, defined as negative (pointing towards the left in the figure), is applied. The polarization in both capacitors will point to the direction imposed by E^+; note that the electric imprint is parallel to the polarization in one capacitor (left), but antiparallel in the other (right). When the electric field intensity reverses polarity (E^-), at some $E^- = E_{\mathrm{c1-}} = E_{\mathrm{c}} - E_{\mathrm{imp}}$, the polarization in the right capacitor will switch; notice that $|E_{\mathrm{c1}}| < |E_{\mathrm{c}}|$ because E_{imp} adds to help in the switching of the polarization (Figure 3.5b). When the electric field is further increased (in modulus), at $E_{\mathrm{c2-}} = E_{\mathrm{c}} + E_{\mathrm{imp}}$ (Figure 3.5c) the polarization in the left capacitor would switch as well; notice that $|E_{\mathrm{c2}}| > |E_{\mathrm{c}}|$ because now E_{imp} is opposite to the applied electric field and thus a larger E-field is required to induce its switching. As a consequence, if imprint were to act, a “two-step” switching would occur and it will produce distinctive features at $E_{\mathrm{c}} - E_{\mathrm{imp}}$ and $E_{\mathrm{c}} + E_{\mathrm{imp}}$ in the *J-E* hysteresis loop. Thus as sketched in Figure 3.5d, the *J-E* hysteresis loop should display two ferroelectric switching peaks. In the experimental loops of Figure 1(f,g,h), these double peaks are well visible. They are superimposed to the displacive current (i_{d}) resulting from the fact that the capacitors are charging/discharging upon voltage cycling ($i_{\mathrm{d}} = -\mathrm{d}Q/\mathrm{d}t = -\mathrm{d}Q/\mathrm{d}V \cdot \mathrm{d}V/\mathrm{d}t = -C \cdot \mathrm{d}V/\mathrm{d}t$).

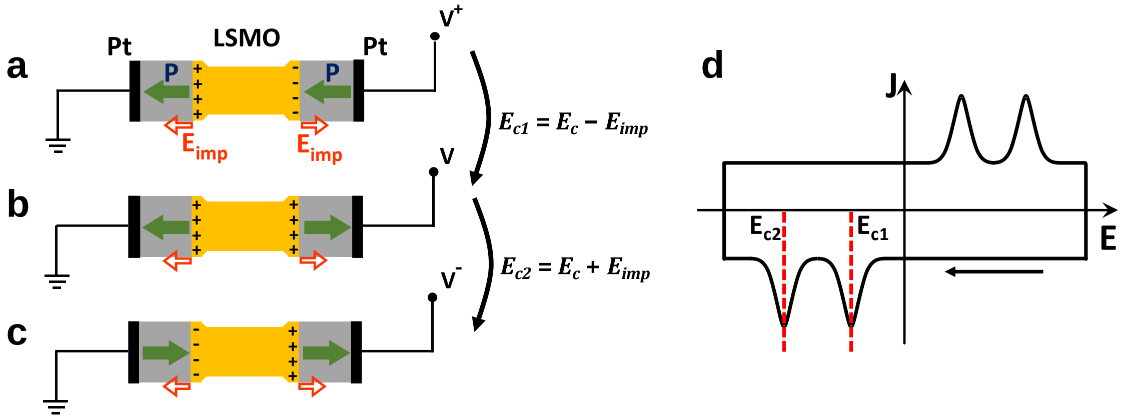

Figure 3.5. Sketches of the polarization state of the series connection of the ferroelectric capacitors of the *t-t* configuration, during switching in presence of E_{imp}. Solid (green) arrows indicate the direction of P, and empty (red) arrows the direction of E_{imp}. (a) Electric field smaller than $E_{\mathrm{c}} - E_{\mathrm{imp}}$: P in both capacitors point towards the same direction, negative. (b) Electric field slightly larger than $E_{\mathrm{c}} - E_{\mathrm{imp}}$: P in the right capacitor switches resulting in a "tail-to-tail" domain configuration. (c) Electric field slightly larger than $E_{\mathrm{c}} + E_{\mathrm{imp}}$: the domains in the left capacitor flip, P in both capacitors point towards the same direction positive. (d) Schematic diagram of the corresponding J-E loop recorded while applying a triangular voltage pulse to the device. The pair of switching-peaks and the position of two coercive fields E_{c1}, E_{c2} on the return (V^{+} to V^{-}) part of the loop are marked by dashed lines.

It can be observed in Figure 3.1h that $E_{\mathrm{c1+}} = -25$ kV·cm^{-1}, and $E_{\mathrm{c2+}} = +200$ kV·cm^{-1} at 200 Hz. These "effective" coercive field values are in good agreement with those that can be derived from the experimental E_{c} and E_{imp} determined from J-E loops recorded in *b-t* configuration (Figure 3.1c,e,g): $E_{\mathrm{c1}} = E_{\mathrm{c}} - E_{\mathrm{imp}} = -21.5$ kV·cm^{-1} and $E_{\mathrm{c2}} = E_{\mathrm{c}} + E_{\mathrm{imp}} = +221.5$ kV·cm^{-1}, confirming that the scenario depicted in Figure 3.5a,b collects the physics behind. A similar analysis has been performed in other samples and coherent with results obtained. In Table 3.1 we collect: the E_{imp} and E_{c} values extracted from *b-t* and *t-t* configurations, respectively, at low frequency regime; the estimated values of E_{c1} and E_{c2}; and experimental values of E_{c1} and E_{c2} at high frequency regime. See corresponding *J-E* loops in Figure 3.6.

Sample	E_{imp} (kV·cm^{-1})	E_c (kV·cm^{-1})	**Estimated** (kV·cm^{-1})		**Experimental** (kV·cm^{-1})	
			E_{c1}	E_{c2}	E_{c1}	E_{c2}
BTO(150)/LSMO(50)//STO	+121.5	±100	∓21.5	±221.5	∓25	±200
BTO(90)/SRO(25)//STO	+140	±80	∓60	±220	∓18	±210
BTO(105)/LSMO(30)//DSO	+216	±219	∓3	±435	∓50	±218
BTO(90)/SRO(25)//DSO	+150	±136	∓14	±286	∓28	±328
BTO(50)/LSMO(15)//LSAT	+192	±160	∓32	±352	∓45	±388

Table 3.1. Experimental and estimated values of E_{c1}, E_{c2} of five different BTO thin film samples, grown on different substrates and using different bottom electrodes. Numbers in brackets indicate the thicknesses (nm) of the different layers. The E_{imp} values of *b-t* and E_c values of *t-t* are extracted from the low frequency measurements; the experimental E_{c1}, E_{c2} are extracted from *J-E* loops recorded at high frequencies (values from loops at frequencies higher than 500 Hz, 200 Hz, 200 Hz, 1000 Hz, and 1000 Hz for sample BTO/LSMO//STO, BTO/SRO//STO, BTO/LSMO//DSO, BTO/SRO//DSO, BTO/LSMO//LSAT respectively).

The two-step switching is signaled by the corresponding double current peaks observed in the high frequency *t-t* measurements; it reveals that even in the *t-t* configuration the E_{imp} is acting. However, it is not apparent in the low frequency *J-E* measurements. To rationalize this observation, it is worth to notice that if two-step switching process would occur, the ferroelectric capacitors would be connected head-to-head and tail-to-tail through the common bottom electrode (LSMO) as shown in Figure 3.5b, which is floating, i.e. it is not grounded nor connected to a charge reservoir. This entails a poor polarization screening efficiency by the bottom electrode. Consequently, head-to-head/tail-to-tail configuration is energetically unfavorable and should revert to the stable head-to-tail/tail-to-head configurations. That is plausibly the reason why one can only indirectly observe the presence of this unfavorable domain configuration at high measurement frequencies. Switching from head-to-head (tail-to-tail) to tail-to-head (head-to-tail) occurs in the time scale of the measurement because a single current switching peak observed at low frequency. This indicates that the characteristic time for charge redistribution to screen unfavorably oriented domains is of about $\tau = 0.5 / \nu \approx 30$ ms.

In Figure 3.6, *J-E* loops used to extract the values included in Table 3.1 are shown. The four loops in the first row are of *b-t* measured at low frequency to extract E_{imp}, the second row shows *t-t* measured at low frequency to extract E_{c}, and the third row are *t-t* measured at a representative high frequency to extract experimental E_{c1}, E_{c2}.

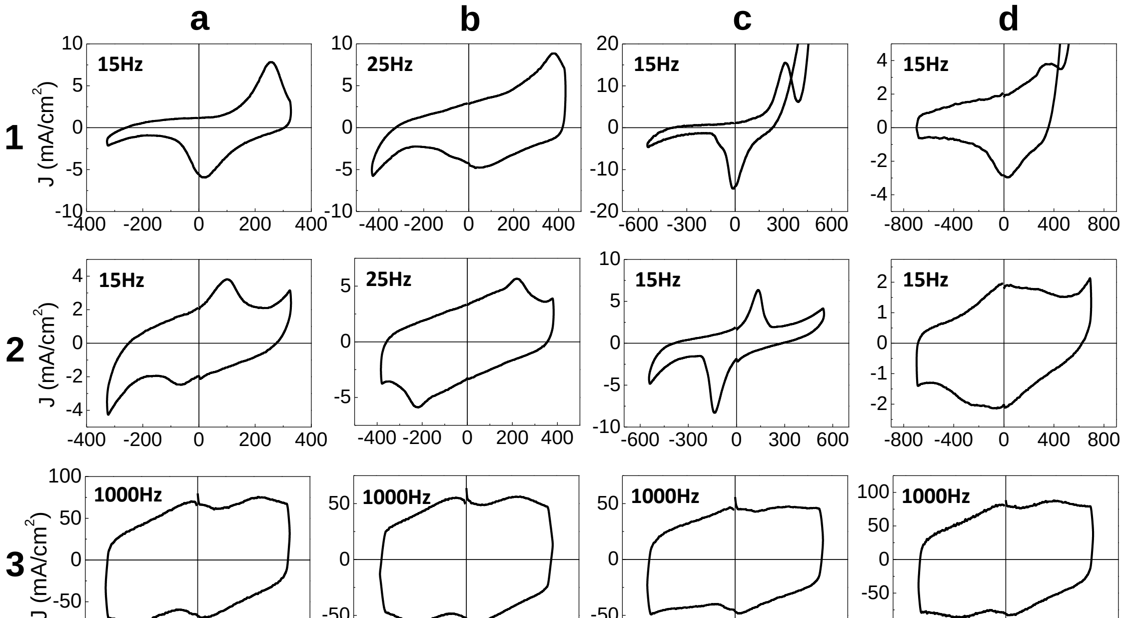

Figure 3.6. *J-E* loops of samples in Table 3.1 (except the sample BTO/LSMO//STO) recorded at representative frequencies. Column (a) BTO/SRO//STO, Column (b) BTO/LSMO//DSO, Column (c) BTO/SRO//DSO, Column (d) BTO/LSMO//LSAT. Row (1) *b-t* at low frequency to extract E_{imp}, Row (2) *t-t* at low frequency to extract E_{c}, Row (3) *t-t* at high frequency to extract experimental E_{c1}, E_{c2}.

It can be observed that estimated and experimental values of E_{c1} and E_{c2} are in good agreement in samples grown on LSAT and STO irrespectively on the bottom electrode (LSMO or SRO) used. Similar good agreement is obtained for BTO/SRO//DSO sample. It is remarkable that irrespective from their slightly different structural properties, see Figure 3.7 below, the estimated and measured E_{c1} and E_{c2} values for all samples nicely agree.

However, for the BTO/LSMO//DSO sample, the E_c value extracted from *b-t* and *t-t* configurations are unexpectedly different (161 and 225 kV·cm^{-1}, respectively). We assign this discrepancy to the fact that the properties of the bottom LSMO layer in this particular sample may be different as its anomalously shorter out-of-plane cell parameter anticipates, as shown in Figure 3.7.

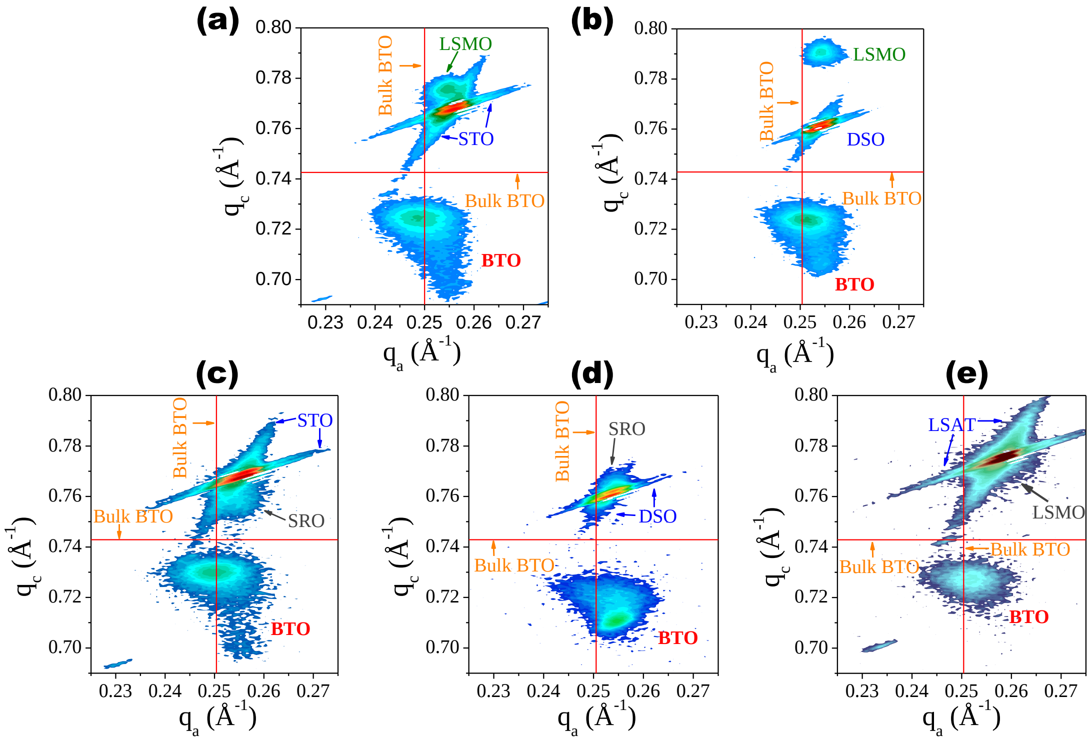

Figure 3.7. Reciprocal lattice maps around the (103) reflections of STO, DSO and LSAT. (a)Sample BTO/LSMO//STO, (b)sample BTO/LSMO//DSO, (c)sample BTO/SRO//STO, (d)sample BTO/SRO//DSO, (e)sample BTO/LSMO//LSAT. The red lines indicate the position of (103) reflection of BTO crystal values.

X-ray diffraction reciprocal space maps (q-plots) of the BTO(150)/LSMO(50)//STO, BTO(105)/LSMO(30)//DSO, BTO(90)/SrRuO$_3$(25)(SRO)//STO, BTO(90)/SRO (25)//DSO, and BTO(50)/LSMO(15)//LSAT samples around the (103) reflection are plotted in Figure 3.7. Comparing the five panels in Figure 3.7, it is clear that the BTO films have different in-plane and out-of-plane lattice parameters, thus implying that the films are in a different strain state and thus having partially relaxed differently, which will be detailed discussed in Chap. 6. Therefore, a different microstructure is anticipated. As all these films have a similar frequency dependent $P(E)$ loops, it indicates that the phenomenology described in this chapter is preserved irrespective from the BTO structural properties.

3.3.3 Photoresponsive double capacitors

The *J-E* response in ferroelectric capacitors is dictated by the ability of the system to efficiently screen the polarization charges, and illumination of semiconducting electrodes had been used to tailor screening and the amount of switchable polarization in ferroelectric thin films[53]. Similarly, in the experiments described above, one can envisage to modulate the polarization screening by inducing photoelectrons by photon absorption at the ferroelectric layer, which in turn will modify the required screening charge density at electrodes and subsequently the relative stability of tail-to-tail and tail-to head polarization configurations.

Aiming to test this proposal, we have illuminated the sample by using blue photons (3.06 eV), which it is known that can be absorbed by BaTiO$_3$ thin films[54], and we have recorded the *J-E* loops in *t-t* configuration at the same frequencies than in Figure 3.1. The results are presented in Figure 3.8a-c.

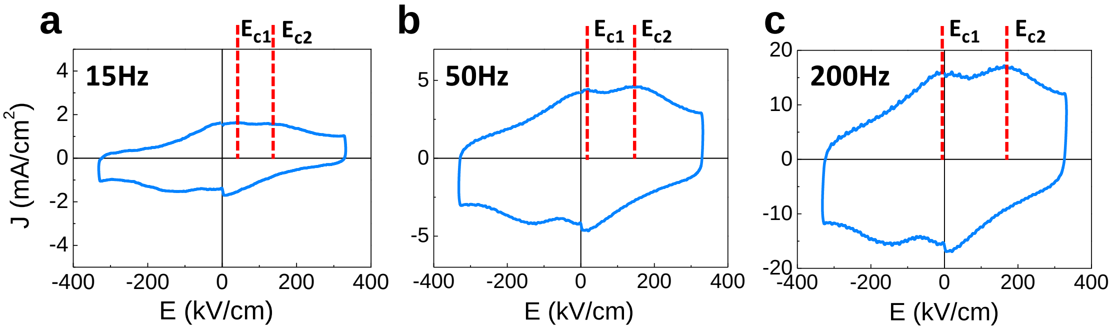

Figure 3.8. The *J-E* loops of sample BTO/LSMO//STO measured by *t-t* under blue laser (405 nm) illumination, at 15 Hz (a), 50 Hz (b), 200 Hz (c), respectively. The coercive fields E_{c1+}, E_{c2+} recorded on the increasing branch of the *J-E* are indicated (dashed lines).

In Figure 3.8a, we show the data collected at 15 Hz. It can be observed that the magnitude of the switching current peaks measured under blue laser (405 nm) illumination is definitely smaller than that recorded in dark (Figure 3.1). This is because photocarriers contribute to screen the polarization upon *P* reversal thus modifying the displacive current flowing in the external measuring circuit[20]. This is confirmed by the absence of any significant effect when similar experiments are performed using light of longer wavelength (532 nm), as shown in Figure 3.9.

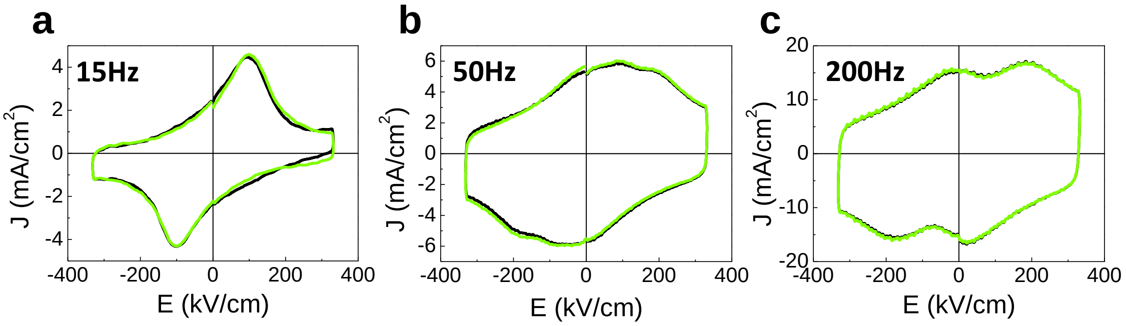

Figure 3.9. (a,b,c) The *J-E* loops of sample BTO/LSMO//DSO measured by *t-t* at 15, 50 and 200 Hz without illumination (black curves) and under the illumination of green (532 nm) laser (green curves).

In Figure 3.9, the *J-E* loops of the BTO/LSMO//STO sample, recorded at different frequencies in *t-t* configuration, under illumination with a green laser (532 nm) are compared with those recorded in dark. Measurement conditions are identical to those used in Figure 3.1d,f,h except for the different light wavelength. Negligible changes can be detected in the *J-E* loops, particularly at the switching peak, when comparing data under illumination (green) and in dark. This observation is consistent with the fact that the energy of the green laser (2.33 eV) is too low to activate electron-hole pairs in BTO neither across the intrinsic band gap (3.3 eV), nor at existing impurity levels. Furthermore, as the powers of the used green and blue laser are identical, the different response to different wavelengths eliminates any pyroelectric contribution affecting the observations reported here.

Analogous photoresponses under blue laser illumination are detected in other films, as the results of sample BTO/LSMO//DSO shown in Figure 3.10.

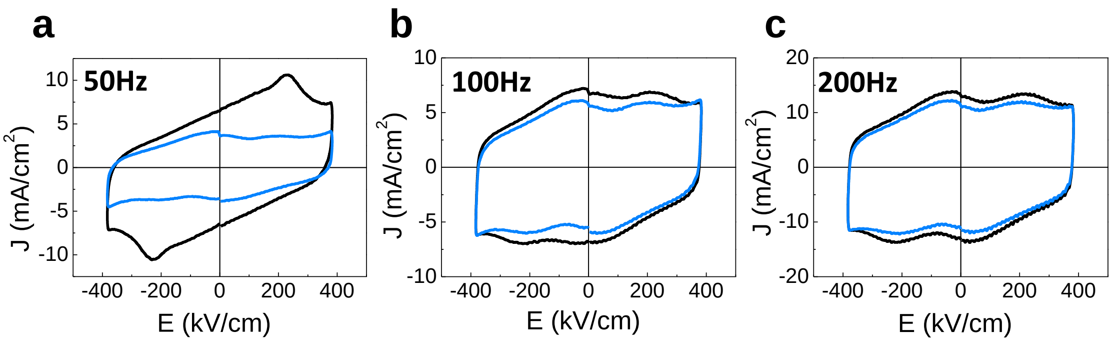

Figure 3.10. (a,b,c) The *J-E* loops of the sample BTO/LSMO//DSO measured in *t-t* configuration at 50, 100 and 200 Hz respectively, in dark (black curves) and under the illumination of a blue laser (blue curves).

Of higher relevance for the present work is the fact that in these low frequency measurements (Figure 3.8a), one can observe the emergence of two current switching peaks, which were not present in the measurements performed without illumination (Figure 3.1d). These two current switching peaks evolve when increasing the measuring frequency and become fully visible at 50 Hz and 200 Hz (Figure 3.8b and 3.8c, respectively) whereas they were only incipient under dark conditions (Figure 3.1f). Similar phenomenon can be also found in Figure 3.10. These measurements indicate that under illumination, polarization switching of the two in-series ferroelectric capacitors does not proceed as a single event (within the experimental time window) but as a double-step and thus it mimics the high frequency dark response (Figure 3.1d,f,h). This result is in full agreement with the picture of photocarriers modifying the electrostatic boundary conditions, namely the polarization screening, as sketch in Figure 3.11 shows, in such a way that tail-to-tail and head-to-head polar states become more stable.

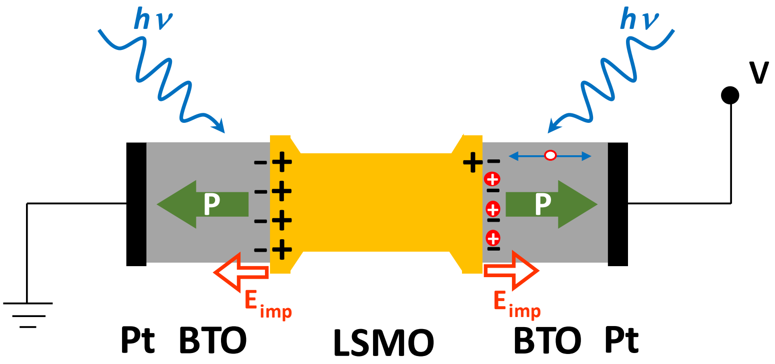

Figure 3.11. Sketch of stabilizing tail-to-tail polar states with the assistance of photocharges. On the right interface of LSMO and BTO, photocharges are drove by depolarization field and internally screen the polarization, compensating the shortage of positive screening charges in a certain period of time due to the electrostatic repulsion in LSMO at the tail-to-tail polar states.

J-*E* curves, similar to those show in Figure 3.1d,f,h and Figure 3.8a-c, recorded in dark and under illumination respectively, have been measured in a range of frequencies and used to determine the frequency dependence of the coercive fields in the ascending (E_{c1+} and E_{c2+}) and decreasing (E_{c1-} and E_{c2-}) branches of the voltage excursion. Data are summarized in Figure 3.12, where the frequency dependence of $E_{c1\pm}$ and $E_{c2\pm}$ is plotted. It can be appreciated that irrespectively if the sample is in dark (Figure 3.12a) or under illumination (Figure 3.12b), the splitting between E_{c1+} and E_{c2+} (and between

E_{c1-} and E_{c2-}) gradually increases when increasing frequency, indicating that faster measuring time allow to get access to the unstable head-to-head and tail-to-tail configurations, having distinguishable impact on the shape of the recorded *J-E*. The frequency at which the two-step switching starts to be visible should be in principle limited by the electronic reordering at top or bottom electrodes, which are primarily responsible for charge screening. However, it can be appreciated in Figure 3.12 that at a frequency as low as about 15 Hz, the two peaks begin to be visible. This leads to a response time $\tau \approx 30$ ms; this slow reaction time is at odds with the view that electronic transport within the electrodes determines the response time.

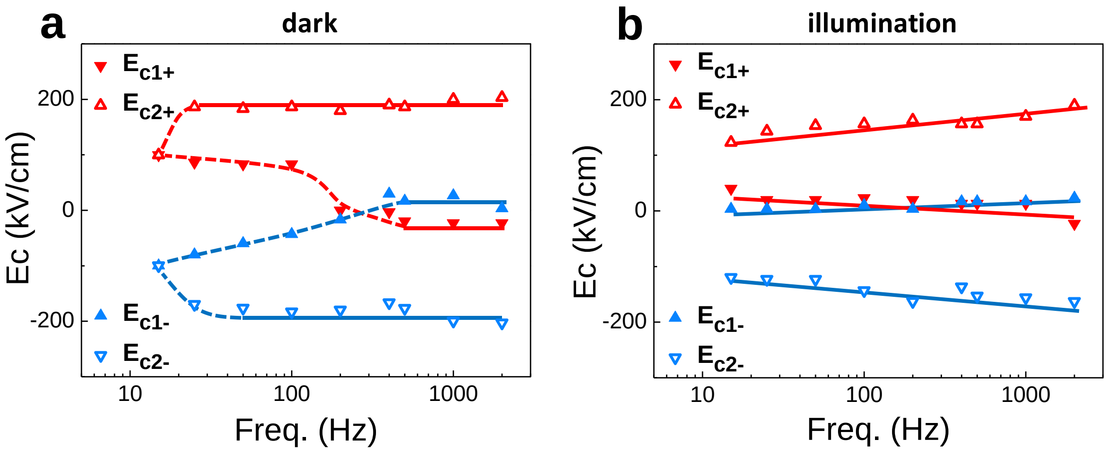

Figure 3.12. Dependence of the coercive fields on frequency, in dark (a) and under illumination (b). (E_{c1+}, E_{c2+}) and (E_{c1-}, E_{c2-}) indicate the position of the switching current peaks observed in the ascending and decreasing branches of the *J-E* loops, respectively.

Moreover, it is experimentally observed that the frequency dependence of the *J*(*E*) curves is independent on the distance between the *t-t* electrodes (either neighboring or further apart). In Figure 3.13(b,c,d) representative *P-E* loops recorded using electrodes placed at different distances are shown (see the sketch in Figure 3.13a). It can be appreciated that all of them are very similar irrespective of their separation (*L*), that is: different LSMO lengths. In Figure 3.13(e,f,g) we show the corresponding frequency dependence of the coercive field $E_c(\nu)$: their close coincidence indicates that the bulk properties of the LSMO bottom electrode do not play a role.

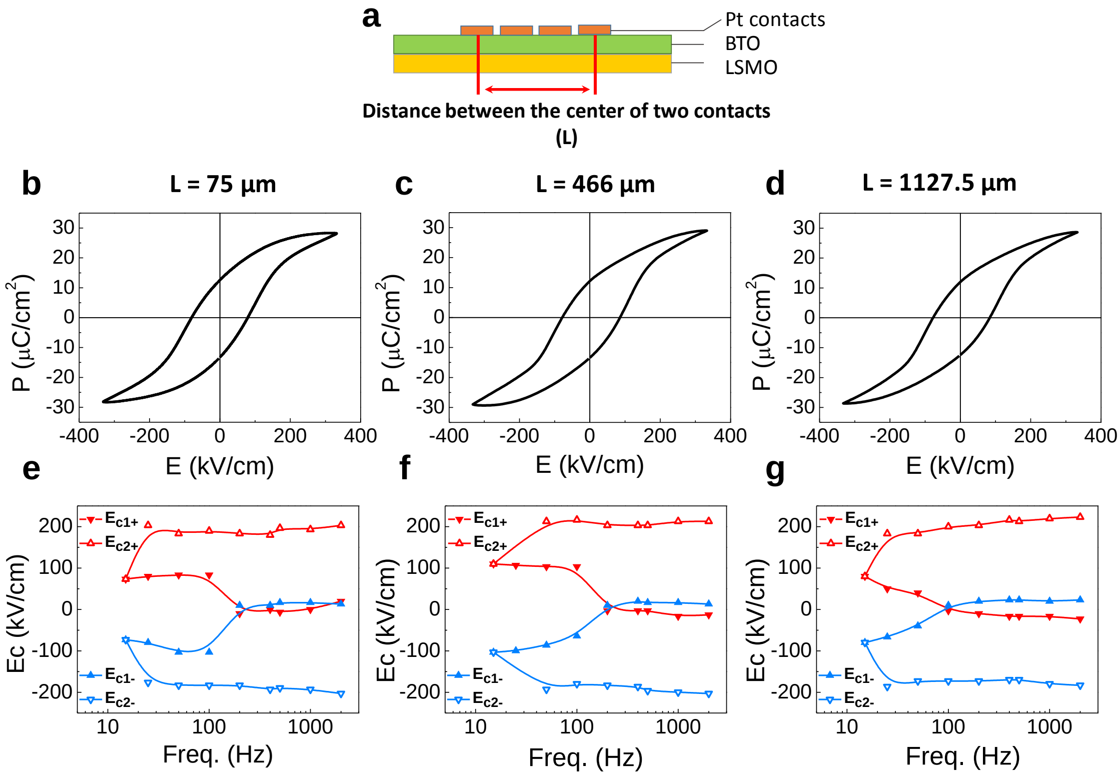

Figure 3.13. (a) Sketch of the *t-t* measurement configuration using pairs of electrodes separated different distances *L*, sample BTO/LSMO//STO (manuscript). (b,c,d) *P-E* loops recorded at 15 Hz for a pair of electrodes separated by different distances *L* as indicated. (e,f,g) Dependence on frequency of the coercive fields E_c extracted from $J(E)$measurements using pairs of electrodes separated by different distances *L*, as indicated in (b,c,d).

These observations confirm that the bulk properties of the LSMO bottom electrode do not play any role. On the other hand, as the majority carrier mobility in $BaTiO_3$ (typically BTO is a n-type semiconductor) is of about 1 $cm^2{\cdot}V^{-1}{\cdot}s^{-1}$ and the depolarizing filed is of about 10 $kV{\cdot}cm^{-1}$, the transit time for a layer of about 100 nm is expected to be much shorter (< 1 ns) than the time scale (τ) of relevance in the present experiments. Therefore, neither carriers in the electrodes nor the majority carriers in the ferroelectric seems to determine τ. This conclusion is further supported by the observation that the resistance of the device decreases upon illumination (blue laser) and rapidly recovers when illumination is switched off. In contrast, although the capacitance of the device is reduced under illumination, it does not revers back to the initial state, as shown in Figure 3.14, thus indicating that the change of impedance of the system is due to reordering of slow-moving charges rather than majority carriers.

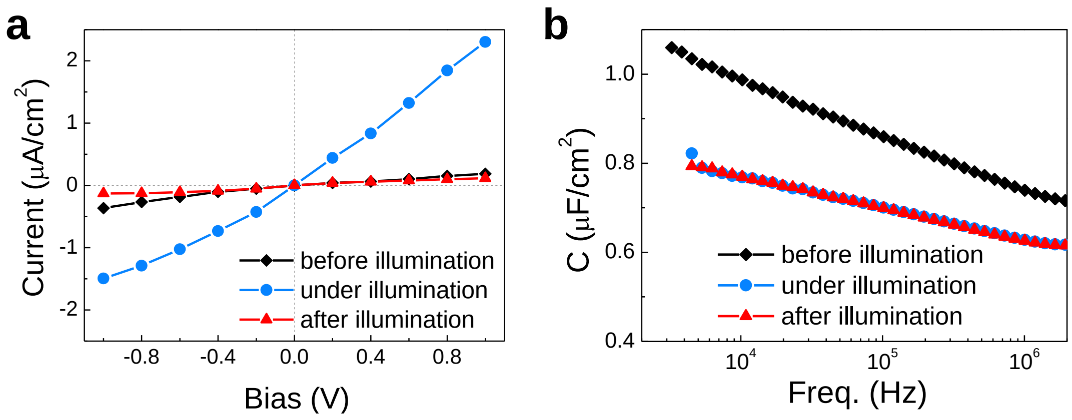

Figure 3.14. (a) *I*(*V*) characteristics of BTO/LSMO//STO sample measured in *t-t* configuration under different illumination conditions using a blue laser: before illumination (rhombi), during illumination (circle) and after illumination (triangle). (b) The device capacitance measured under the indicated illumination condition. Symbols are the same as in (a).

In Figure 3.14 we show the *I-V* curves of BTO/LSMO//STO sample, obtained in *t-t* configuration in dark, during illumination (blue laser) and back to the dark state again. It can be appreciated that the resistance changes reversibly upon sample illumination. In Figure 3.14b, we show the capacitance of the device measured in dark (before illumination), under illumination and back to dark condition again. It can be appreciated that the capacitance is reduced by suitable illumination, but it does not recover the initial state after illumination; this implies that photo-generated carriers have produced long time living charge redistribution and subsequent change in the impedance of the device. Therefore, minority carrier diffusion and / or ionic transport in $BaTiO_3$, which are both slower processes[55], appear to govern the observed transient response.

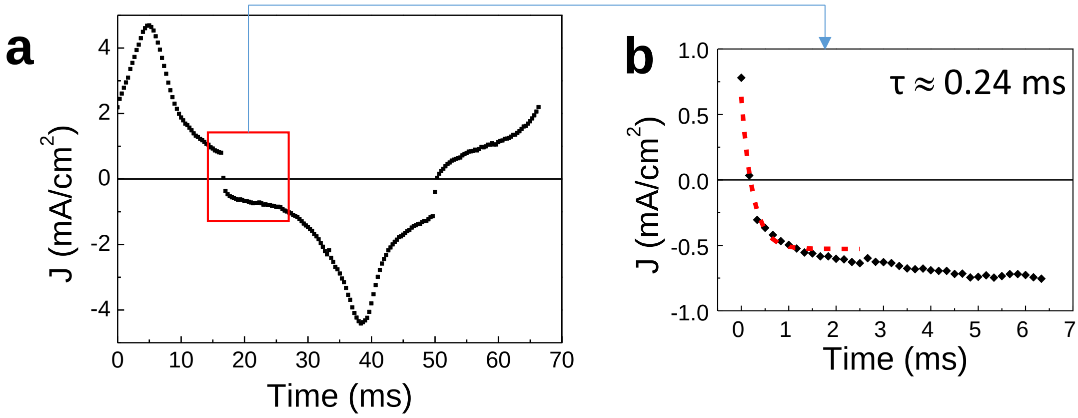

Figure 3.15. (a) Current dependence on time for a *P-E* loop recorded at 15 Hz. (b) Current vs time at the E_{max} in the $E(t)$ pulse.

In Figure 3.15, we shown the time dependence of the displacive current in *t-t* configuration, when a triangular voltage pulse is used. In (a) we depict the overall $J(t)$ during a complete measuring cycle. In (b) we display the current just after the $E(t)$ maxima. From the fitting of the $J(t) = J_0\,(1 - e^{t/\tau})$ in Figure 3.15(b) we extract the time constant of the circuit (τ_c). It turns out that it is of 0.24 ms ($\tau_c^{-1} \approx 4$ kHz). Thus, the time constant of our measuring circuit is also much shorter (≈ 240 μs, as shown in Figure 3.15), and thus it cannot be relevant in the observed time response.

Therefore, data suggest that charge screening and concomitantly the head-to-head /tail-to-tail time-life, might be, at least partially, satisfied by electronic charge (holes) and ions in n-type $BaTiO_3$.

3.3.4 Potential application of photoscreening

Retention is a big problem in the route of applying ferroelectric materials. The notion is used to describe the phenomenon that remanent polarization decays along with time after poling, mainly caused by the depolarization field originating from imperfect screening of polarization by electrodes[56]. It is more severe in ferroelectric thin films due to the small thickness. With the assistance of photocharges generated inside of

$BaTiO_3$ under proper illumination, better screening of polarization is achieved. Retention behavior of sample BTO/LSMO//DSO is measured after 15 second blue laser (3.06 eV) illumination and compared with the one without illumination. Results are plotted in Figure 3.16. Here the retention of the ferroelectric polarization remains near 100% (respect its value after 1s of poling) after we illuminate the system and wait at least 2 h, comparing to ~30% retention in dark. Therefore it provides a potential methodology to enhance the retention time in ferroelectric based memories.

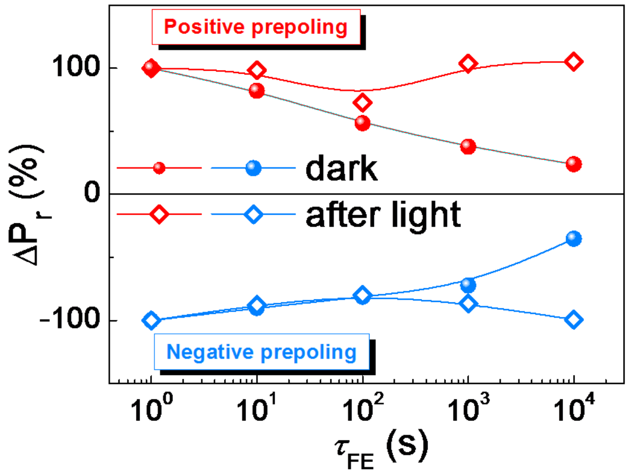

Figure 3.16. Retention behavior of sample BTO/LSMO//DSO in dark (solid circles) and after 15 second illumination (hollow diamonds). Values are normalized to *P*r after 1 second of poling.

3.4 Conclusion

Polarization of ferroelectric thin films is often explored using contact pads placed at the film's surface and a common metallic layer underneath is used as bottom electrode (top-top configuration). In this arrangement, the device under test is equivalent to two in-series ferroelectric capacitors connected via the common bottom electrode. Identical contacts may, *in-principle*, avoid asymmetric interface-related build-in electric fields, thus minimizing electric imprint E_{imp} fields. Here, we have shown that in presence of E_{imp}, in *t-t* configuration, *J-E* loops without any signature of E_{imp} are only obtained when measurements are performed at relatively low frequency, whereas distinctive double-step appear when *J-E* is recorded at high frequency. We have shown here these effects result from the non-cancellation of imprint field, which however, only shows up at higher frequency. We have argued that the observation of double-step in *J-E* is a consequence of the short-living head-to-head and tail-to-tail ferroelectric domains. In other words, E_{imp} may not be apparent in *J-E* and *P-E* loops, but it is not cancelled in symmetric *t-t* configuration. We have also demonstrated that modifying the charge screening capability of the device by suitable photogenerated carrier injection, allows modulating the relative stability of head-to-head (tail-to-tail) respect to tail-to-head (head-to-tail) ferroelectric domain configuration. Finally, we have proposed that in symmetric top-top electrode measuring configuration, polarization screening is partially provided by internal charges in $BaTiO_3$ which permit the camouflage of imprint fields without cancelling it. These findings may be of particular relevance in the field of photoresponse of ferroelectric films, where polarization screening plays a fundamental role.

Chapter 4. Influence of electrodes configuration on photocurrent responses

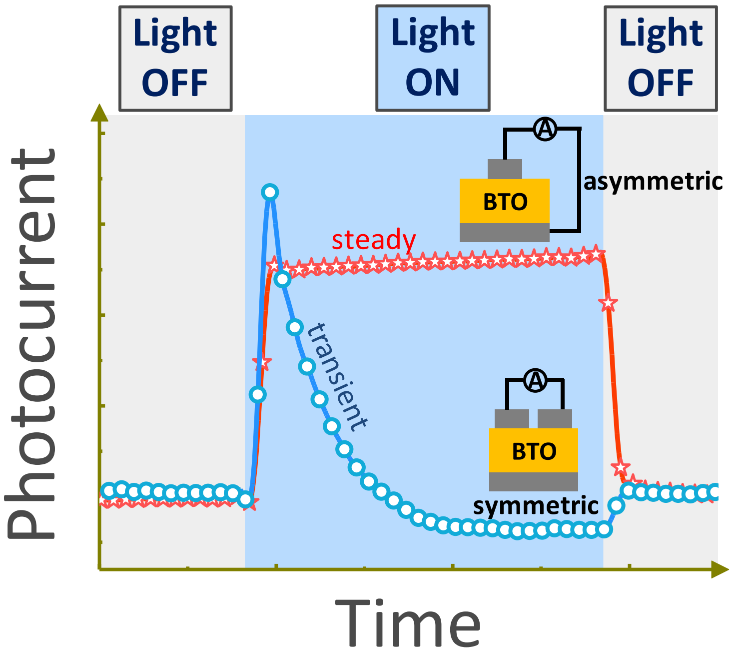

ABSTRACT

The ferroelectric polarization and short-circuit photocurrent in $BaTiO_3$ thin films have been studied for different contact configurations that allow to measure the photoresponse and polarization under the presence of large or negligible imprint field. It is found that in all cases, the direction of the photocurrent is dictated by the depolarizing field and ultimately by the film polarization, with a negligible contribution of the imprint electric field. However, dramatic differences are found in their time-dependent photoresponse. Whereas in presence of imprint, steady photocurrents are observed under suitable illumination, transient photocurrents are generated in absence of imprint. It is argued that this distinct behavior is determined by the different Schottky barrier height at electrodes which thus offer a simple way to tune the film photoresponse. These findings could be exploited for electro-optic read-out and writing of ferroelectric memories.

4.1 Introduction

In semiconductors, the absorption of a photon of suitable energy can generate an electron-hole (e-h) pair. To electrically detect the e-h pair it is necessary to split it and drain the electron and hole charges thus generating current (so-called photocurrent) that is proportional to the number of photogenerated carriers. Drain can occur due to the presence of an internal electric field. Ferroelectrics have recently attracted a renewed interest due to the observation above-bandgap open circuit photovoltage[35,57], or significant change on their transport properties driven by the ferroelectric polarization state or light[41,58-63]. The photoresponse of ferroelectric materials is primarily determined by its polarization state, the Schottky barriers at interfaces and the concomitant build-in electric fields, and the so-called bulk photovoltaic effect (BPE), which is related to the non-centrosymmetric character of the ferroelectric materials[64,65]. Assuming homogeneous light illumination, the charge-draining electric field can be either generated by a built-in potential steaming from: differences between the work functions of electrodes, polarization gradients, or asymmetric distribution of defects, all of them being also at the origin of the so-called imprint electric field (E_{dep}), or due to unscreened polarization and the concomitant depolarizing electric field (E_{dep})[41-45,66,67]. Alternatively, it is known[68] and recently reported in thin films[69], that ferroelectrics may display BPE because, even in absence of any built-in electric field E_{dep} or E_{dep}, photocarriers are asymmetrically scattered and generate a net charge flow[43,44,65].

Exhaustive studies have been done in order to infer the correlation between E_{dep} or E_{dep} electric field and the generated photocurrent[41-45,66]. However, the relation between them and the generated photocurrent remains unclear because separation of both contributions is challenging. Indeed conflicting results are found on the literature where E_{dep}[42,43], E_{dep}[60,70,71], or both[72,73] are claimed to be the driving force for observed photocurrent. On the other hand, the time response of photocurrents in photoferroelectrics is primarily dictated by the generation and recombination rates of photocarriers giving rise to transient responses, typically in the ms range, that we call here “steady” photoresponse because the equilibrium state is reached fast[74-76]. However, in some cases, transient photoresponses with intriguing orders of magnitude slower responses, ranging from few seconds to thousands of seconds, of undisclosed origin, have been reported[43,55,60,71,77-81]. In the present article, we disentangle the contributions of E_{dep} and E_{dep} to the short-circuit photocurrent measured in $BaTiO_3$ (BTO) thin films, and we show that transient or steady photocurrent can be selectively obtained. A simple contact configuration, which can be generalized to any ferroelectric thin film, allows us to distinguish between E_{dep} and E_{dep} contributions to the photocurrent. It turns out that the ultimate parameter determining the photocurrent (magnitude and sign) is the depolarizing field. This allows univocally inferring the polar state of the layer from the measured photocurrent. Beyond this finding, we also show that, by selecting the appropriate contact configuration: asymmetric or symmetric, on the very same film, steady or transient photoresponses are selectively obtained. We argue that this dramatic difference is determined by Schottky barriers. Possible implications for data writing and reading in ferroelectric memories are addressed.

4.2 Materials

$BaTiO_3$(150 nm)/$La_{2/3}Sr_{1/3}MnO_3$(50 nm) (LSMO) bilayers were grown in a single process by pulsed laser deposition on (001) $SrTiO_3$ (STO) substrates. After cooling down to room temperature, 20 nm thick platinum top electrodes of 60×60 μm^2 separated each by about 15 μm, were deposited ex-situ on the BTO surface by RF-sputtering, by using a mask allowing to deposit about 100 contacts simultaneously. Without specific claim, laser used in this chapter by default is a blue laser (405 nm) that provides homogeneous illumination on two adjacent electrodes with ~10 $W\cdot cm^{-2}$ power density.

4.3 Results and discussion

4.3.1 Influence of electrodes configuration on short-circuit photocurrent

In Figure 4.1a,b, we show the two different contact configurations used for electric measurements, that we named bottom-top (*b*-*t*) and top-top (*t*-*t*), respectively. In the *b*-*t* configuration (Figure 4.1a) the Pt top electrode is contacted and the bottom LSMO electrode is grounded. This contact configuration corresponds to a single capacitor with asymmetric electrodes (Pt and LSMO). We have defined the positive sign of the current (labeled "*J*" in Figure 4.1a,b) as that where positive carriers flow from Pt to LSMO (ground), as indicated by the arrow in Figure 4.1a. In the *t*-*t* configuration (Figure 4.1b), two top Pt electrodes are contacted, resulting in a nominally symmetric contact configuration. In this *t*-*t* configuration one of the Pt electrodes is grounded and the other is contacted. As before, positive current implies positive charges flowing towards the ground (arrow in Figure 4.1b).

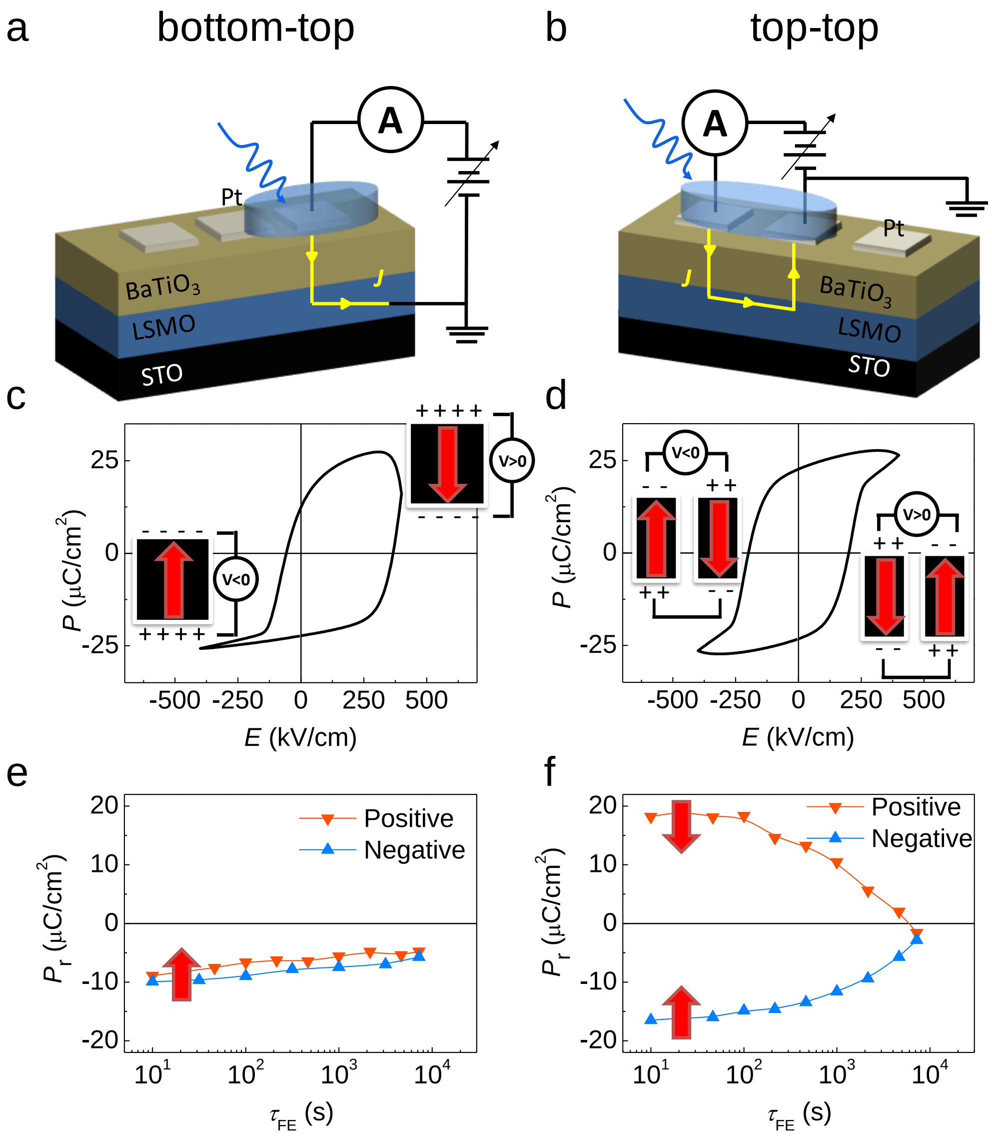

Figure 4.1. (a,b) Electric contacts configuration used for *b-t* (a) and *t-t* (b) measurements. Arrows indicate the positive sign of the current for positive applied voltage. (c,d) Dynamic ferroelectric hysteresis *P-E* loops recorded in dark at 200 Hz for *b-t* (c) and *t-t* (d) configurations. Sketched are the relations between applied voltage and ferroelectric polarization direction for both configuration and prepoling voltage sign. (e,f) Ferroelectric retention measurements obtained after pre-poling (with "positive" or "negative" voltage pulse, as labeled in the figure) the sample in a given direction and measuring the switchable charge, after a delay time τ_{FE}. Red arrows indicate the ferroelectric polarization direction.

The *P-E* loops recorded for both configurations are shown in Figure 4.1c,d. In *b-t* configuration (Figure 4.1c) a positive or negative voltage applied between top-Pt and bottom-LSMO results in saturated polarization pointing towards LSMO or Pt respectively, as sketched in the insets of the Figure 4.1c. In *t-t* configuration (Figure 4.1d) a positive voltage applied between two top adjacent Pt electrodes produces a pointing-down polarization ($P > 0$) in the capacitor where positive voltage is applied and pointing-up polarization ($P < 0$) in the grounded capacitor, and vice versa when the polarity of the poling field is reversed, as sketched in the insets of the Figure 4.1d. From now on, positive poling indicates a positive voltage applied to the non-grounded electrode.

Comparison of *P-E* data in Figure 4.1c and 4.1d reveals the profound impact of the contact configuration on the measured polarization loops. In Figure 4.1c, it is obvious that the *P-E* loop recorded in *b-t* configuration is shifted towards the right, revealing the presence of large imprint ($E_{dep} \approx -150$ kV·cm^{-1}). Notice that $E_{dep} < 0$ implies that E_{dep} points from LSMO towards Pt. The opening of the branches of the $P(E)$ at negative voltages (at about -300 kV·cm^{-1}) is a signature of leakage whereas the aperture of the loop at the largest positive voltages is consequence of the non-saturation of the film[82-84]. In the *t-t* configuration (Figure 4.1d), the almost symmetric *P-E* loop indicates that E_{dep} is virtually absent. This does not imply that E_{dep} has disappeared, but its strength is overruled by the series connection of unscreened ferroelectric capacitors. Indeed, if in *t-t* configuration E_{dep} would act, head-to-head and tail-to-tail ferroelectric capacitors, short-circuited via the common bottom electrode, would occur which would have a large electrostatic energy payload. Note also here the presence of the aperture of *P-E* loops near the highest applied voltage, consequence of the leakage current.

The presence of E_{dep} and E_{dep} is well visible in the retention measurements displayed in Figure 4.1e,f, where we show the remnant polarization P_{r} as a function of delay time between the prepoling pulse and the measurement pulse (τ_{FE}). For *b-t* configuration (Figure 4.1e), P_{r} is found to be very similar irrespective on the sign of the prepoling pulse (positive or negative). Indeed, right at the very first measurement (τ_{FE} = 10 s), the polarization is found to be already around −10 μC·cm^{-2}, irrespectively of the sign of the prepoling voltage. This is the consequence of the presence of E_{dep}, that produces a back-switch of the ferroelectric polarization after a short time (< 10 s) towards the most stable configuration (*P* pointing up). Moreover, one can observe in Figure 4.1e that there is a gradual decrease of the absolute P_{r} with τ_{FE}: more than 50% of the initial polarization ($\tau_{\mathrm{FE}} \approx 10$ s) is retained after $\tau_{\mathrm{FE}} \approx 10^4$ s. This observation signals the presence of the coexisting depolarizing field E_{dep}.

In the configuration *t-t*, it can be clearly appreciated (Figure 4.1f) that the sign of the remnant polarization is dictated by the sign of the poling field; this is fully consistent with the observed symmetric *P-E* loops (Figure 4.1d) and the corresponding virtual absence of E_{dep}. In contrast, the presence of E_{dep} is more visible, being responsible for the gradual loss of polarization with time. In this *t-t* configuration, the effect of a minor residual E_{dep} on P_{r} is evidenced by the slightly negative P_{r} observed at $\tau_{\mathrm{FE}} \approx 10^4$ s, irrespectively on the initial poling direction. One notices in Figure 4.1f that P_{r} is reduced by 50% at $\tau_{\mathrm{FE}} \approx 10^3$ s. compared to the initial value. Therefore, in *t-t* configuration the polarization decays faster than in *b-t*, where, as mentioned, P_{r} is reduced by less than 50% at 10^4 s.

4.3.2 Retention behavior and short-circuit photocurrent

In Figure 4.2, we show the dependence on time (t) and illumination delay time (τ_{light}) of the short-circuit photocurrent $J(t,\ \tau_{\mathrm{light}})$ for both contact configurations. Short-circuit photocurrent is measured for various τ_{light} (from 10 s up to 2 h) after a prepoling voltage pulse (a triangular pulse up to ±400 kV·cm^{-1} applied for 2.5 ms).

Figure 4.2a and 4.2c display the $J(t,\ \tau_{\mathrm{light}})$ data collected for configuration *b-t* after negative and positive poling pulses, respectively. It is observed that when light is switched on, indicated by the small red arrows in the figures, the current gradually increases until reaching a steady state that persists during illumination and only washes out after switching off the illumination. This photoresponse is similar to that observed in common pn-junctions. However, a striking observation is the fact that, irrespectively on the poling voltage sign, the photocurrent is always positive.

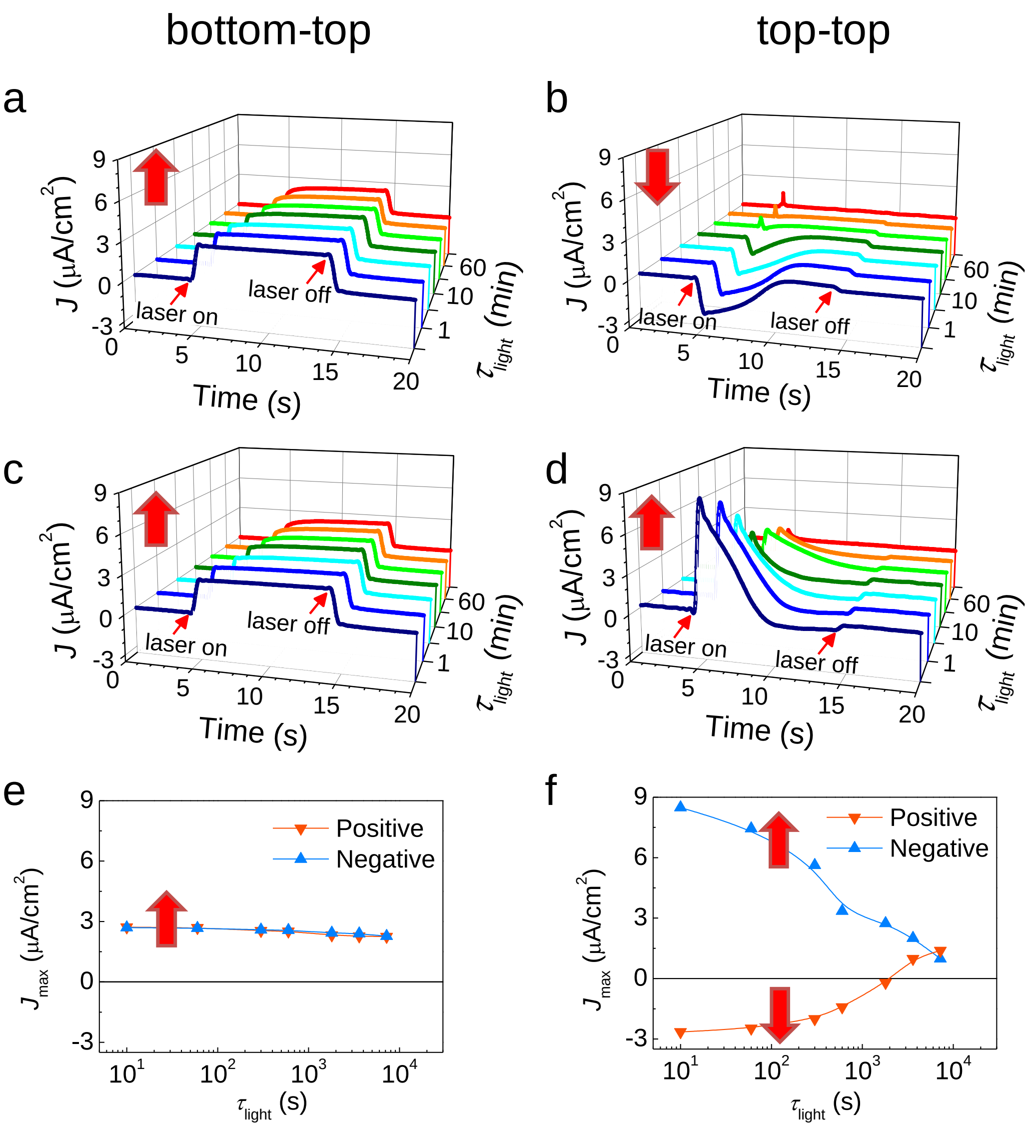

Figure 4.2. Time dependence of short-circuit photocurrent for different illumination delay times (τ_{light} = 10 s, 1 min, 5 min, 10 min, 30 min, 60 min and 120 min). (a,c) Data collected for *b-t* configuration after a positive and negative pre-poling, respectively. (b,d) Data collected for *t-t* configuration after a positive and negative pre-poling. The big red arrows indicate the majority polarization direction. (e,f) Dependencies of the maximum photocurrent (J_{max}) on τ_{light} for *b-t* and *t-t* configurations, respectively.

In Figure 4.2b and 4.2d, we show the corresponding data recorded in *t-t* configuration after positive and negative voltage poling, respectively. In a back-to-back configuration of two photodiodes, a negligible photoresponse should be expected, because both photodiode contributions would cancel out. Here, a radically different photocurrent response is observed, indicating that the switchable polarization rather than the contact asymmetry, is the driving force for the observed effects. Indeed, the sign of $J(t, \tau_{light})$ is always dictated by the poling direction and reverses when reversing the poling voltage. Here, J_{max} is also found to be dependent on τ_{light}, but in sharp contrast with the photoresponse of *b-t*, in *t-t* configuration the photocurrent rapidly decays with time during illumination and it displays a change of sign at longer times. On the other hand, BPE does not seem to play a major role on the measured photoresponse[65] because the measured open-circuit voltage is much smaller the BTO bandgap and that the photocurrent $J(t, \tau_{light})$ measured in similar but thicker films is reduced, as shown in Figure 4.3.

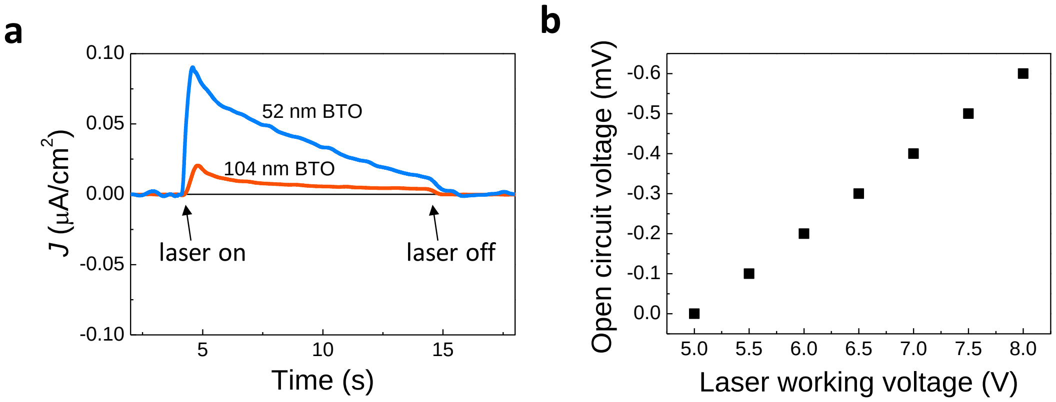

Figure 4.3. (a) Time dependence of short-circuit photocurrent for two BTO films of different thickness. (b) Dependence of open circuit voltage for a BTO film on laser working voltage (proportional to its power).

The first insight into the distinct photoresponse behavior of the same film under different contact configurations can be obtained from the comparison of the photocurrent data (Figure 4.2a-d) and the retention experiments (Figure 4.1e,f). It is obvious that the sign of $J(t, \tau_{\mathrm{light}})$ univocally depends on the sign of the polarization. To emphasize this observation we include in Figure 4.2a-d big red arrows indicating the direction of the observed polarization.

We turn now towards the observed time-dependencies of $J(t, \tau_{\mathrm{light}})$. In Figure 4.2e,f we plot J_{max} vs. τ_{light} for both contact configurations. First, we note that in *b-t* measurements (Figure 4.2e), the extrapolated time τ_{light} to reach about 50% of J_{max} is much longer than 10^4 s whereas in the *t-t* (Figure 4.2f), it is shorter than 10^3 s. A similarly different time-dependence was already observed in the retention measurements of Figure 4.1e,f. Indeed, if one compares Figure 4.1e,f and Figure 4.2e,f, their resemblance is rather impressive (except for the opposite sign). Therefore, one can conclude that there is an intimate relationship between the polarization retention and the measured short-circuit photocurrent.

On the other hand, it is well-visible that when using *t-t* configuration, the measured photocurrent has a time dependence that is strikingly different from that of photoactive structures based on semiconducting materials. Just after switching on the illumination, the current rapidly rises up to J_{max} and it gradually decreases (roughly by 50% in 1 – 3 s) until reaching a steady state. We also note that the current density at the maximum J_{max} lowers with increasing τ_{light}, roughly by 50% at 10 min ($\approx 10^3$). We stress that the time constant of the measuring circuit is much shorter ($\approx$ 10 μs), thus implying that the measured $J(t)$ in both configurations is a genuine time-dependent photoresponse. However, it does not result from the E_{dep} identified in polarization measurements, as shown by data in Figure 4.1e,f, because the depolarization time is several orders of magnitude longer. The dependence of $J_{\max}$ on τ_{light} and the physics of the transient peak [$J(t)$] will be discussed below. Before proceeding with this discussion, we strength here that the observed photocurrent is a photovoltaic effect rather than a spurious photoresponse, that could be originated by an inhomogeneous illumination or pyrocurrents. We performed similar experiments using laser of similar power but with photons of lower energy (green) and no photoresponse was observed, as Figure 4.4 shows.

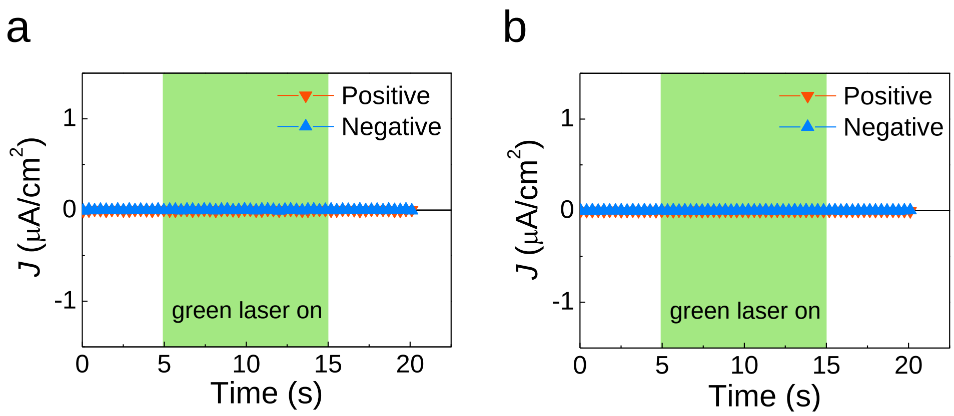

Figure 4.4. Short-circuit photocurrent dependence on time for *b-t* (a) and *t-t* (b) contact configurations under illumination with a green laser.

In Figure 4.4a and 4.4b the photoresponse measured, by using a green laser (532 nm wavelength) of similar power, in *b-t* and *t-t* configurations are shown. The absence of any measurable photocurrent indicates that heating or inhomogeneous illumination, are not at the origin of the effects observed using a blue laser.

4.3.3 Driving force of short-circuit photocurrent

Now we will discuss: i) the fact that the sign of P_r determines $J_{\max}$, ii) the correlation between the magnitude of both parameters, and iii) the distinct time dependence of the photocurrent $J(t)$ depending on the measurement configuration. Regarding point i), we first note that that the sign of the generated photocurrent is at odds with the sign of the ferroelectric E_{dep}. Indeed, as mentioned above, in *b-t* configuration the E_{dep} points from bottom LSMO towards top Pt, and thus, if E_{dep} was relevant, the photocurrent should have flow in the same direction in the measuring circuit (Figure 4.1a), that is: negative, according to the used sign convention. The possible sketches are plotted in Figure 4.5 and Figure 4.6.

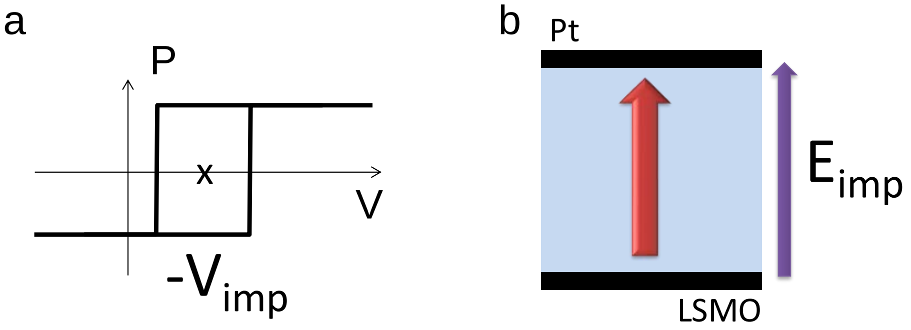

Figure 4.5. (a) Archetypical *P*-*V* loop for a ferroelectric material with strong imprint field. (b) Sketch of the direction of the polarization (red arrow) and the imprint field (purple arrow, E_{dep}) for an imprinted ferroelectric.

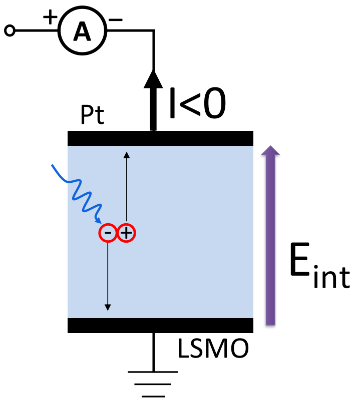

Figure 4.6. Sketch of the displacement of the carriers (electron-hole) photogenerated under the presence of an internal electric field (E_{int}). The directions of the carriers inside the material and the direction of the current in the circuit are indicated by the thin and thick black arrows, respectively. The sign of current meter defined in exeprimetnal setup is maked as “+” and “–”.

In Figure 4.5, we show the shift in the *P*-*V* (equivalent *P*-*E*) loop (Figure 4.5a) and the correspondence between the imprint electric field in the structure (Figure 4.5b) and.

Figure 4.6 shows the direction and the sign (in the current meter) of the generated photocurrent assuming an internal field pointing towards Pt as in Figure 4.5b.

Sketches and current direction in Figure 4.5 and 4.6 are **contrary** to the experimental observations (Figure 4.2a,c). Therefore we disregard a determinant role of the E_{dep} field in the measured photoresponse. Instead, the direction of J_{max} is highly correlated with P_{r} as inferred from the close similarity between the time dependence of the polarization retention $P_{\mathrm{r}}(\tau_{\mathrm{FE}})$ (Figure 4.1e,f) and the dependence of J_{max} on τ_{light} (Figure 4.2e,f). This correlation demandes a more detailed consideration. In Figure 4.7a,b we plot the dependence of $J_{\mathrm{max}}(\tau_{\mathrm{light}})$ on $P_{\mathrm{r}}(\tau_{\mathrm{FE}})$ extracted from Figure 4.1e,f and Figure 4.2e,f, for both configurations. From Figure 4.7a, where data for *b-t* are plotted, the narrow range of P_{r} variation experimentally accessible does not allow to extract any relevant conclusion on the impact of P_{r} on J_{max}. However, for *t-t*, as shown in Figure 4.7b, J_{max} vs. P_{r} data display a remarkably simple linear dependence over a wide range of P_{r} values including its change of sign. This linear relation can result from the presence of E_{dep}, i.e. $J = \sigma E_{\mathrm{dep}}$, where film conductivity σ contains the photoinduced carrier density, and the depolarizing field E_{dep} which itself is proportional to P_{r}. It is known that $E_{dep} = -\alpha \frac{P}{\varepsilon}$,[39,56] where ε is the dielectric permittivity of the ferroelectric and α accounts for the fraction of the unscreened polarization; therefore, $J = -\frac{\sigma\alpha}{\varepsilon}P$. On the other hand, it is known that in defective ferroelectric thin films, as it is the present case, a fraction of ferroelectric domains could be pinned and not switchable (or harder to switch) under the application of an electric field[85,86]. Therefore at remanence $P = P_r + P_{pin}$, where P_{r} accounts for the switchable polarization and P_{pin} for the pinned polarization. It results that J must show a linear dependence on P_{r} as follows:

$$J = -\frac{\sigma\alpha}{\varepsilon}P_r - \frac{\sigma\alpha}{\varepsilon}P_{pin} \tag{4.1}$$

For simplicity we have assumed in Equation (4.1) that the permittivity and conductivity of pinned and switchable ferroelectric domains are identical. Therefore, being $J_{\mathrm{max}} \propto J$, equation (4.1) predicts a linear $J_{\mathrm{max}}(P_{\mathrm{r}})$ dependence as observed (Figure 4.7b). Accordingly, data of Figure 4.7b have been fitted to the Equation (4.1). Using the conductance of our film $\sigma \approx 1.5\times10^{-4}$ μS·cm^{-1}, extracted from the slope of *J-E* characteristic under the used illumination (Figure 4.8) and $\varepsilon \approx 300\ \varepsilon_0$, extracted from the saturated *P-E* loops recorded (*t-t* configuration) under illumination (Figure 4.9), we obtain: $\alpha \approx 0.03$ (well within the common order of magnitude[56]), $E_{\mathrm{dep}} \approx 1.3$ kV·cm^{-1} (for 1 μC·cm^{-2}) and the polarization of the pinned domains is 4.8 μC·cm^{-2} (pointing towards the ground).

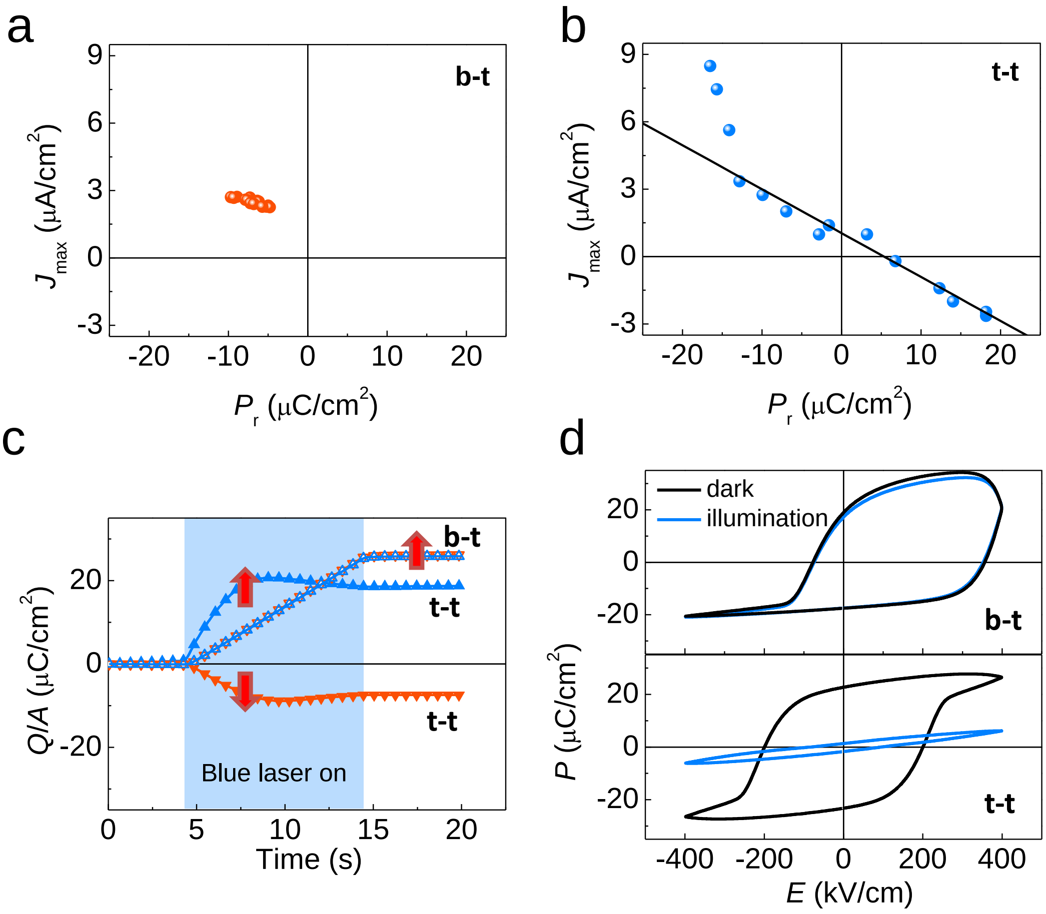

Figure 4.7. Dependence of the maximum of the photocurrent on remnant polarization determined from ferroelectric and photocurrent measurements shown in Figure 1 and 2 for (a) *b-t* and (b) *t-t* contact configuration. Line through data points

corresponds to the fitted line: $J_{\max} = 1.0(1)\mu A/cm^2 + 0.2(1)s^{-1} \cdot P_r$. (c) Time dependence of the integrated charge flow [$Q = \int I(t) \cdot dt$] normalized to the contact area from the short-circuit photocurrent measurements shown in Figure 2 with a delay time of 10 s for different polarization states and different contact configurations, as indicated. (d) *P-E* loops recorded in *b-t* (upper panel) and *t-t* (bottom panel) at 200 Hz in dark and under illumination.

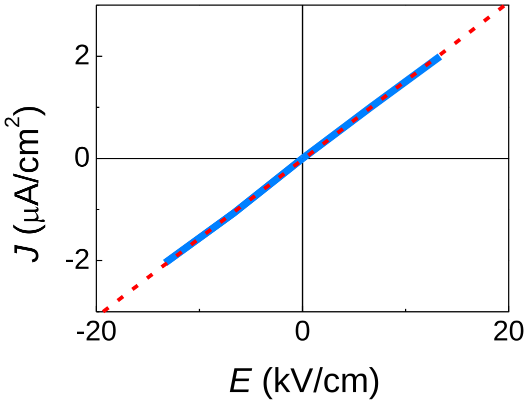

Figure 4.8. *J-E* characteristic in *t-t* configuration under light. From the slope of the fitted straight line (dashed) the conductivity 1.5×10^{-4} μS·cm^{-1} has been extracted.

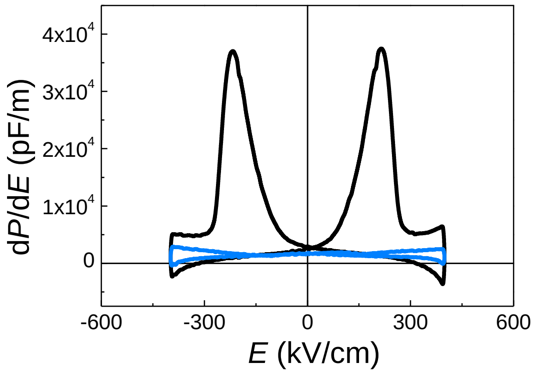

Figure 4.9. Derivative of the *P-E* loop in *t-t* configuration, recorded in dark (black line) and under light (blue line). Permittivity $\varepsilon = dP/dE$ are obtained.

Some $J_{\max}$ data points in Figure 4.7b, corresponding to the largest negative polarization, do not follow the predicted linear dependence. Within the scope of the model derived above, this implies that for this negative polarization the screening is less efficient. A possible reason could be that the available charges for screening are fewer and, accordingly, E_{dep} increases. We have observed a similar linear $J_{max}(P_r)$ dependence and obtained similar α values in another BTO/LSMO//STO structure, where all layers have nominally the same thickness as the one described in the previous part of this chapter. J_{max} vs. P_r for *t-t* configuration is plotted in Figure 4.10. From the fit of the data to Equation (4.1), we obtain a fraction of unscreened polarization of $\alpha \approx 0.001$.

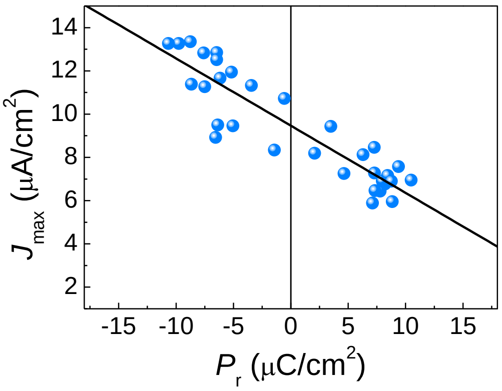

Figure 4.10. Dependence of the maximum of the photocurrent with remnant polarization extracted from separate ferroelectric and photocurrent measurements for *t-t* contact configuration for a different BTO/LSMO//STO sample.

Finally, we focus on the time dependence of the photocurrent observed in *t-t* and *b-t* configurations. In Figure 4.7c, we plot the time dependence of the charge that has flowed through the circuit normalized to the contact area (*Q*/*A*) obtained by integrating the photocurrent, at τ_{light} = 10 s, measured for *t-t* and t-b configurations (from Figure 4.2a-d). It is observed that for *b-t*, the charge that has circulated increases linearly during illumination and only stops increasing when light is switched off. This effect obviously results from the fact that the photocurrent is virtually constant during illumination (Figure 4.2a,c) and thus there is not upper bound for the total amount of flowing charge. In the *t-t* measurement, in contrast, the integrated charge does not grow anymore after a few seconds, in spite the sample is still being illuminated. The integrated charge is bounded by ≈ +20 μC·cm^{-2} and −10 μC·cm^{-2}. To understand this distinct response, *P-E* loops have been recorded in both configurations in dark and under illumination (Figure 4.7d). It can be observed that in *b-t* [Figure 4.7d (upper panel)] the *P-E* loop recorded under light overlaps the one recorded in dark. In contrast, in *t-t* [Figure 4.7d (bottom panel)] the loop recorded under illumination shows a reduction of the remnant polarization by ΔP = 20 μC·cm^{-2}. This value coincides with the upper limit of *Q*/*A* (time) shown in Figure 4.7c. This observation strongly indicates that in *t-t* configuration the photogenerated charges screen the polarization, similar to early observations of Dimos and Warren[87-91] and Land and Peercy[81,92-95] in BTO and in doped PZT, respectively. At this point it may be worth to recall that Wurfel and Batra[53], in their pioneering work on depolarizing fields, reported the opposite effect, that is an increase of polarization under illumination in metal/ferroelectric/semiconductor structures, which was attributed to photoinduced increase of carriers in the semiconductor electrode. The observed time scale for the transient photocurrent (few seconds), that is the time scale to build an space charge compensating the depolarizing field, is orders of magnitude longer than the carrier drift time τ_d. Indeed, for BTO, assuming a mobility $\mu_n \approx 1$ cm^2/(Vs), $E_{dep} \approx 2.3$ kV/cm^{-1} and an electrode-to-electrode distance of about 15 μm, it turns out that $\tau_d < 0.1$ μs. This characteristic time is obviously much shorter than the experimental one (few seconds). These observations, which are in agreement with the reported time-dependence of photoinduced changes of surface potential in BTO crystals[55,78], point that low-mobility charge species could be involved in the polarization screening process.

4.3.4 Mechanism of time dependence of short-cicuit photocurrent

In short, both in *b-t* and *t-t* configurations the photocurrent is dictated by the polarization and the accompanying depolarizing field. The radical difference being that, under suitable illumination, in *t-t* the photocurrent charges are limited by the ferroelectric polarization whereas in *b-t* photocarriers are continuously generated and leave the sample. A schematic view of the charge distribution and electron energy representing the situation of distinct electrodes (*b-t*) (Pt/BTO/LSMO) and identical (*t-t*) (Pt/BTO/Pt) electrodes is shown in Figure 4.11a and 4.11b, respectively. The sketch is made under the assumption that BTO is an n-type semiconductor[96], which can be related to the presence of oxygen vacancies, and a certain E_{dep} exists across the BTO film. The nature of the screening charges carriers at Pt/BTO interface cannot be safely inferred from the available data. The space charge regions at each interface are schematically indicated (shadowed regions).

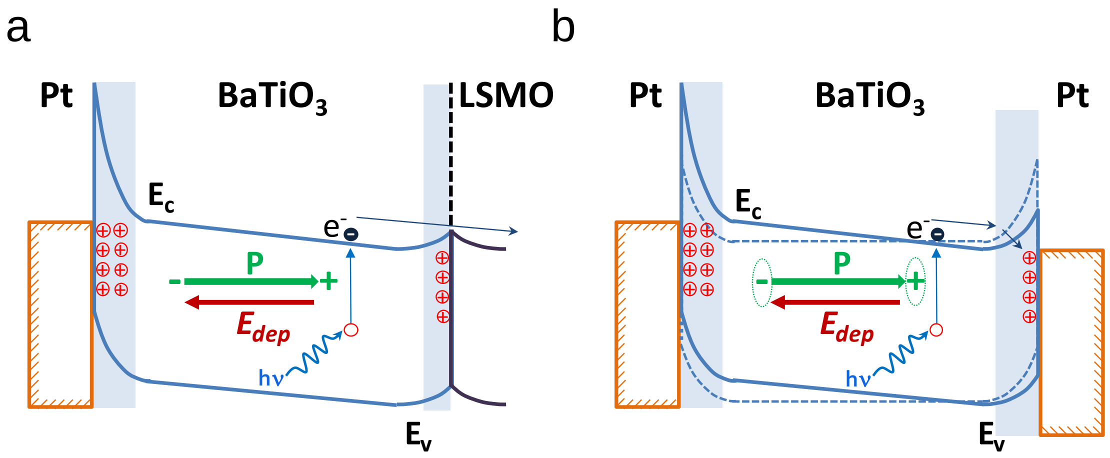

Figure 4.11. Sketch of the electronic energy band diagram in: (a) asymmetric *b-t* and (b) symmetric *t-t* configurations. Shadowed regions correspond to the space charge regions at each interface. The arrows indicate the trajectory of a photogenerated electron, flowing through the circuit in *b-t* (a) and being blocked at the interface in *t-t* (b). The blue dashed lines indicate the flattening of the electronic energy band because of the total screening of P_r. The LSMO electrode is not included in the sketch because, being more conductive than the Pt/BTO interface, it does not play a relevant role. For simplicity, only photogenerated electrons are depicted and holes are omitted.

The situation of asymmetric interfaces (*b-t*) is depicted in Figure 4.11a. We assume that the Schottky barrier at the LSMO interfaces to be smaller than at the Pt side. This situation is analogous to that found in Pt/BTO//Nb:STO[49] where Nb:STO plays a similar role than LSMO here. This is consistent with the measured *J-E* curves that show a rectifying diode-like behavior characteristic of a metal/n-type semiconductor junction and displaying a larger conductance for a positive biased Pt electrode as Figure 4.12 shows. In the symmetric electrode structure (*t*-*t* case sketched in Figure 4.11b, where the contribution of the LSMO bottom electrode has been neglected) we notice that, even when the system is poled, the Schottky barrier height and the space charge width at each interface differ and these asymmetries change when reversing the polarization direction. Here both Schottky barriers at the interfaces act as blocking layers. Upon illumination photogenerated electron-hole pairs will be driven towards the ferroelectric surface by E_{dep}. As a consequence, the screening-charge distribution in the electrodes will be modified and the corresponding excess charge will flow from one electrode to the other across the measuring circuit. After some transient time, the situation will end up with: the total screening of P_{r} and the concomitant suppression of E_{dep}, the flattening of the electron energy band (as indicated by the dashed band in the sketch of Figure 4.11b), and the suppression of the photocurrent. This total screening implies that the charge flow in the circuit will be limited by P_{r}, i.e. $Q/A \leq P_{\mathrm{r}}$. This limit is indeed observed when photocurrent is measured in the *t*-*t* configuration (Figure 3.7c).

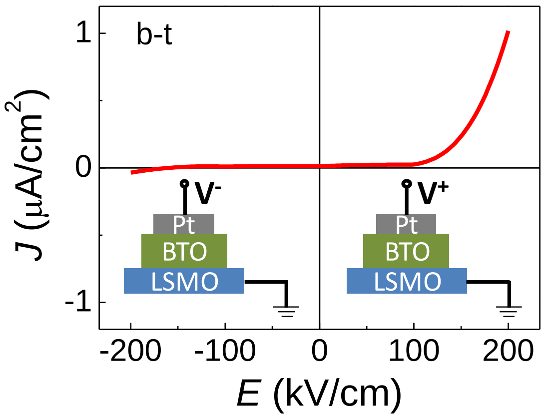

Figure 4.12. *J*-*E* characteristic recorded for the Pt/BTO/LSMO sample in *b*-*t* configuration in dark. In the inset, we indicate how sample is contacted, and the positive and negative voltage applied.

Before concluding we wish to comment on the assumption that the effective height of the Schottky barrier at the BTO/LSMO interface being relatively small and rather conducting. Carrier injection across Schottky barriers at high temperature, is commonly determined by thermionic injection, a process in which charges are thermally activated over an effective interface barrier of energy $W_B(V_A)$, where V_A is the voltage across the device and $W_B(V_A) = W_0 - \frac{\sqrt{q^3 E_A}}{4\pi\varepsilon}$, with E_A being the electric field at the interface and W_0 the zero field Schottky barrier. It follows that if E_A increases the barrier high decreases. It is well known[97-99] that at interfaces between dielectrics and electrodes, the electric field can be much enhanced, particularly for defective dielectrics, being this enhancement more pronounced for relatively thick films[97]. Therefore, it is easily conceivable that the BTO/LSMO interface, with BTO film *ex-professo* made defective, could have a depressed barrier height. The observation of an imprint field at the BTO/LSMO interface pointing away from LSMO could also contribute to reduce any build-in potential at this interface.

Photoexcitation across the bandgap should create electron-hole pairs. In the description made above, for simplicity focus has been put on the photogenerated electron carriers, thus neglecting the role of holes. Holes would contribute also to screen the polarization. Their inclusion would not modify the picture we build. However, being as minority carriers in BTO, holes are expected to have a smaller mobility and contribute less to the observed photocurrent.

4.4 Conclusion

Summarizing, we have used symmetric an asymmetric contact configurations in metal/ferroelectric/meal structures to disentangle the distinct role of imprint and depolarizing fields in the observed photoresponse. It is concluded that E_{dep} is the actual driving field for the generated photocurrent which, accordingly, reverses its direction if the polarization is reversed irrespectively on an eventual presence of E_{dep} which only imposes the direction of the polarization. Whereas the effect of the depolarizing field on the photocurrent magnitude and direction is found to be similar irrespectively on the contact configuration, dramatic differences are found in their time dependence photoresponses. Indeed, in presence of imprint, steady photocurrents are observed under suitable illumination, whereas transient photocurrents are generated in absence of an imprint. We have argued that this distinct behavior is controlled by the Schottky barriers at the electrodes, which thus offer a simple way to tune the film photoresponse. The observed univocal relation between photocurrent and polarization and its tuning by close-to-bandgap light exposure, in simple ferroelectric layers, may favor exploitation in optical writing and reading of ferroelectric memories. Indeed, pioneering attempts[88,100] to write polarization information used voltage biasing during illumination. The observed relevant role of the Schottky barrier demands further study of these effects with experiments involving electrodes with different conductors or controlled doping levels that can lead to enhanced responses. On the other hand, sensing polarization direction by photocurrents, demands that the electric field driving photogenerated carriers, shall be ruled by depolarizing field rather than other non-polarization dependent sources.[20] Here, we have shown that the contact configuration used allow to simultaneously alleviate theses requirement in a simple way.

Chapter 5. Influence of surface adsorbates on photo-induced polarization screening

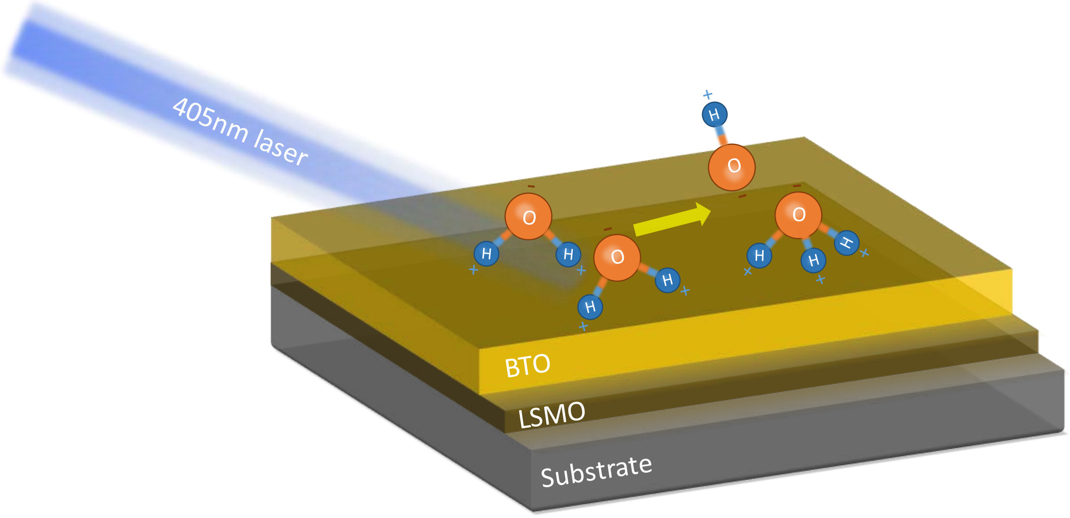

ABSTRACT

Internal electric fields present in ferroelectric perovskites are source of enhanced photoelectric response compared with their non-polar counterparts; thus, a flurry of research on ferroelectric materials for being integrated in photovoltaic devices has been risen during the last years. It is known that one of the interesting photoelectric phenomena appearing in ferroelectrics is the screening of switchable polarization by light. In the present work, we demonstrate that by manipulating the surface states in $BaTiO_3$ films, we can improve polarization photoscreening. In particular, we see that photoscreening effect significantly increases by promoting the presence of water (either by simple room temperature water *steam-treatment* or modifying growing conditions to tune the ferroelectric hydrophilic degree). Detailed XPS characterization allows disclosing that the ultimate mechanism at the origin of the photoscreening effect in our films is the splitting of surface water under light, which products promote surface reconstruction.

5.1 Introduction

Ferroelectric materials are appealing materials for charge-based non-volatile memory devices[101] and for being used in electromechanical actuators and sensors due to its piezoelectric response[28]. In recent years ferroelectric materials have also attracted the interest in photovoltaic research[57,102,103], due to the observation of large photovoltaic activity[35] and the intimate coupling between photocurrent and polarization[58]. From a different perspective, oxidic materials are being considered for their photocatalytic activity and efficiency for H_2O splitting and H_2 production[104]. Among oxides, it has been demonstrated that ferroelectric polarization[105] and internal electric fields[106] improve their surface reactivity.

Ferroelectric polarization, unless properly screened, destabilizes the ferroelectric ground state, due to the presence of uncompensated polarization charges and the accompanying depolarization electric field. In ferroelectric capacitors and related devices, charge screening is provided by metallic electrodes. However, at free surfaces of ferroelectric materials, screening can only be provided by internal charges, commonly arising from defects in the material, or by external screening due to adsorbates or surface reconstructions[107]. Understanding and controlling the balance among the different contributions is challenging but it is essential for many foreseen applications. For instance, switching of the direction of polarization has been achieved by simply changing the surrounding oxygen (or other gasses) partial pressure[108]. It has also been shown that adsorbates modify the ferroelectric switching dynamics and domain wall morphology and propagation speed[109-115]. May be not surprisingly, screening of polarization in presence of surface water, has been shown to be sensitive to UV radiation by the combined effect of photo-induced charges (internal screening) and photo-induced dissociated water-related adsorbates[55]. On of the consequences is that the image contrast between up and down domains in $BaTiO_3$ crystals has been shown the be modified as observed using low energy electron microscopy (LEEM)[55], by indirectly by temperature dependent X-ray diffraction experiments[116] or by proximity force microscopy techniques[78,117]. Experimental studies on photoinduced charge effects on parallel-plate capacitor configurations have also been done; it was reported for instance, that the remanent polarization in ferroelectrics is reduced by suitable light illumination[46,55,71,81,87-95,100,118]. This photoresponse was attributed to the additional contribution to the screening of polarization arising from photoexcited carriers. In brief, it is understood that the polarization charges in a ferroelectric material are screened by the complementary contribution of free carriers at the metallic electrodes, screening charges provided by surface adsorbates[119] and internal charges within the ferroelectric layer[120]. When the ferroelectric layer is lighted by photons with sufficient energy, photocarriers can be generated inside of the ferroelectric layer and the balance between internal and external screening is modified. Therefore, under suitable illumination, a fraction of ferroelectric polarization will be screened by internal photoinduced carriers[87] and by photo-induced polar adsorbates[121]. Indeed, photon irradiation can in principle also ionize adsorbates thus modifying their properties and subsequently changing both their screening properties and pinning strength. In the case of water adsorbates, water dissociation photo-catalytically induced might produce OH- and H+ products leading to the hydroxides or hydrides formation at the surface[122]. Consequently, the amount of switchable polarization may be reduced. In other words, the saturation and remnant (P_r) polarization will lower. It has also been suggested that irradiation can induce inhibition of self-poling, attributable to accumulation of photoinduced carriers at interfaces[71,118], which itself affect the switchable polarization. However, this response is not ubiquitous; for instance, recently an increase of P_r has been reported in PZT films irradiated by ultraviolet light[123], suggesting that more subtle mechanisms may be at work.

Overall, complete understanding polarization screening in ferroelectric and its photoresponse remains a challenge. Here we explore systematically the effect of light (405 nm) on the polarization of $BaTiO_3$ films of different thickness and strain state obtained by the growth on different substrates. Exhaustive X-ray characterization, topography studies and surface-sensitive chemical analysis by using X-ray Photoelectron Spectroscopy (XPS) allow disentangling the prominent role that H_2O-

related adsorbates have on the observed photo-induced suppression of the remnant polarization. In short, we conclude that photo-induce chemical decomposition of H_2O adsorbates at the interface between the metallic electrodes (Pt) and polar surface ($BaTiO_3$), somehow connected to early reports BTO/Pt photocatalytic activity[105] and BTO surface re-construction scenarios[121,122,124], modify the external screening and ferroelectric domain pinning, thus allowing to dictate the switchable polarization in the ferroelectric films. We will show that the remnant polarization can be photo-modulated as much as 75% by suitable $BaTiO_3$ film preparation.

5.2 Materials

A series of BTO (001) films of thicknesses 36.5, 73 and 109.5 nm where grown by pulsed laser deposition on $SrTiO_3$(001) (STO) and $DyScO_3$(110) (DSO) substrates buffered with a 30 nm $La_{2/3}Sr_{1/3}MnO_3$ (LSMO) film acting as bottom electrode. Growth details were reported elsewhere[46,125]. STO and DSO have a cubic structure and produce a nominal compressive mismatch on BTO of 2.20% and 1.23%, respectively. Pt top contacts (20 nm thick, and 60×60 μm^2 width) were grown *ex-situ* by room-temperature sputtering on as-grown BTO surface to perform electrical measurements. Polarization-Electric field (*P-E*) hysteresis loops were measured in top-top configuration[83,125], by applying an electric bias on one Pt electrode and grounding an adjacent one, spaced by 15 μm. *P-E* loops were measured either in dark or under illumination with blue laser (3.06 eV, 10 $W \cdot cm^{-2}$) with ~300 μm diameter spot, safely shinning two adjacent Pt electrodes homogeneously.

5.3 Results and discussion

5.3.1 Photo-induced polarization screening behavior and its structural dependence

The *P-E* loops collected in dark (black line) are shown in Figures 5.1(a-f). We first note that all samples show, in dark, a saturation polarization of near 30 μC·cm^{-2} and a remnant polarization of about 10 μC·cm^{-2}. The *P-E* loops collected under illumination, blue line in Figures 5.1(a-f), show that for all films the switchable ferroelectric polarization reduces, which is in agreement with earlier reports[46,88,89]. Moreover, data in Figures 5.1(a-f) indicates that when increasing film thickness, the change of remnant polarization upon illumination increases. To quantify the relative change of remnant polarization upon illumination we define $\Delta P_r = [P_r(\text{dark}) - P_r(\text{illumination})] / P_r(\text{dark})$, where P_r is the corresponding remnant polarization. In Figure 5.1(g) we collect the values of ΔP_r for samples of different thicknesses grown on STO and DSO. This plot clearly illustrates that ΔP_r tends to increase with thickness, irrespectively on the substrate. However, the effect is larger in samples grown DSO on STO. Therefore, the thickness is not the unique relevant parameter determining the polarization reduction by illumination.

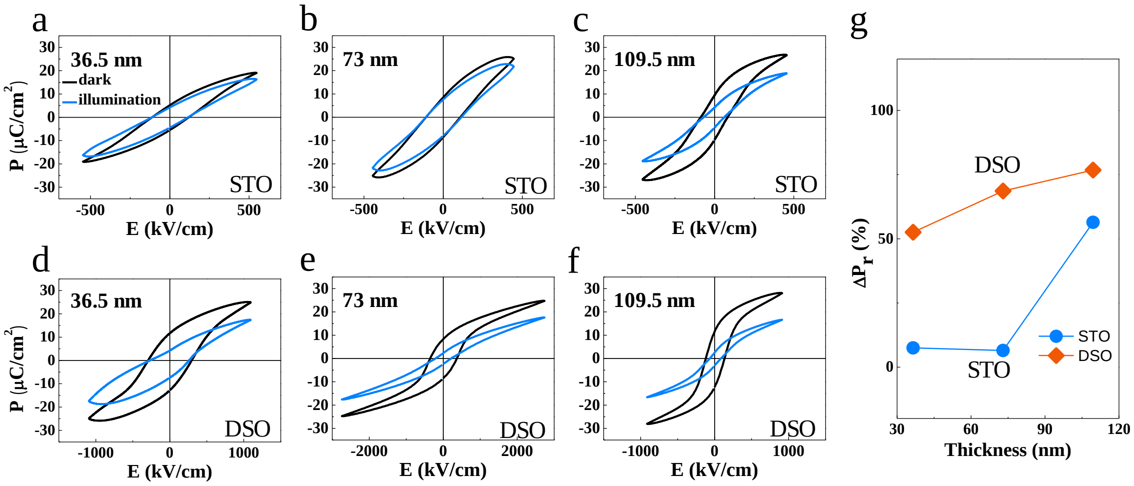

Figure 5.1. Illumination effect on polarization of BTO films of different thicknesses (36.5 nm, 73 nm, 109.5 nm) grown on different substrates. (a-c) loops recorded for BTO/LSMO//STO; (d-f) loops recorded for BTO/LSMO//DSO. Data are collected in dark (black line) and under illumination (blue line). (g) Dependence of ΔP_r [$\Delta P_r = [P_r(\text{dark}) - P_r(\text{illumination})] / P_r(\text{dark})$, where P_r is the remnant polarization] on thickness for samples grown on STO and DSO as labelled.

Being the strain imposed by the STO and DSO substrates different and consequently the corresponding strain relaxation also different for samples with different thickness, one may wonder if strain plays a significant role on the observed ΔP_r variations. Therefore, we first focus our attention on structural aspects. Structural variations of the BTO film have been inspected by using X-ray diffraction (XRD). In Figure 5.2(a) we show a representative zoom of a XRD *θ-2θ* scan [BTO (109.5 nm)/LSMO//DSO]. The corresponding XRD data for all the samples are displayed in Figure 5.3. The (*002*) reflection of LSMO is well visible at large angles than the (*002*) DSO substrate and the relatively broad peak appearing at lower angles corresponds to the BTO film. It is clear that this peak is a superposition of two (*002*) BTO peaks both appearing at Bragg angles lower than that of BTO bulk (vertical dotted line). This is a signature of the coexistence of two differently strained regions in the BTO film, having different out-of-plane parameters. The corresponding peak positions and relative areas have been determined by simply considering two Gaussian contributions representing each family of (*002*) BTO crystallites with different out-of-plane cell parameters and performing the corresponding fit. The dark and light grey regions under the BTO peak are the results from the fit. The more strained one [in the following refereed as strained phase (**S**)] has a c-axis of 4.211(2) Å. The more relaxed one [in the following refereed as (partially) relaxed phase (**R**)] has a c-axis of 4.136(2) Å.

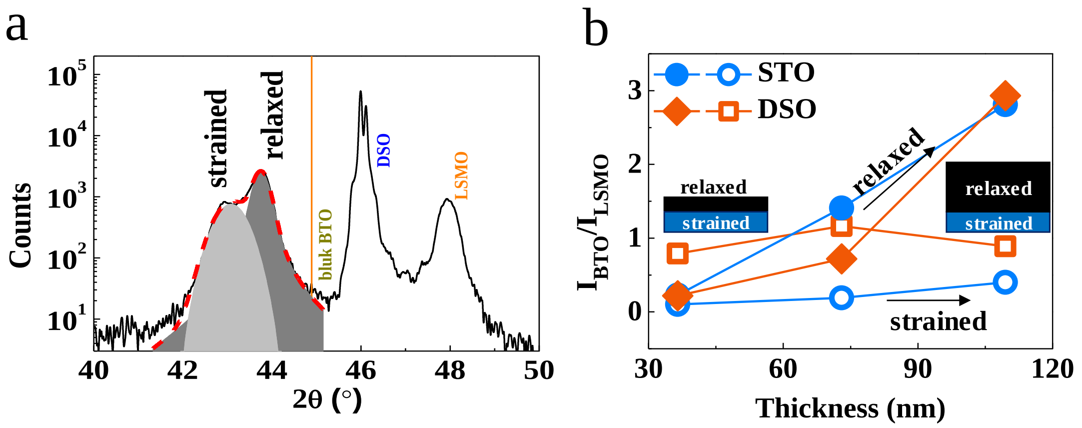

Figure 5.2. (a) XRD scan spectra of 109.5 nm sample grown on LSMO//DSO. The dark and light grey regions under the peak of BTO correspond to the fitting by two

Gaussian curves of the data. The peak corresponding to the strained and relaxed BTO phases are labelled in the spectra. Substrate (DSO) and LSMO peaks are also labelled. Bulk-BTO position is indicated. (b) Thickness dependence of intensity of strained and relaxed BTO phases obtained by Gaussian fitting. I_{BTO} is normalized to the intensity of LSMO peak (I_{BTO}/I_{LSMO}). Insets show the distribution and relative quantity of two BTO phases in both thin and thick films.

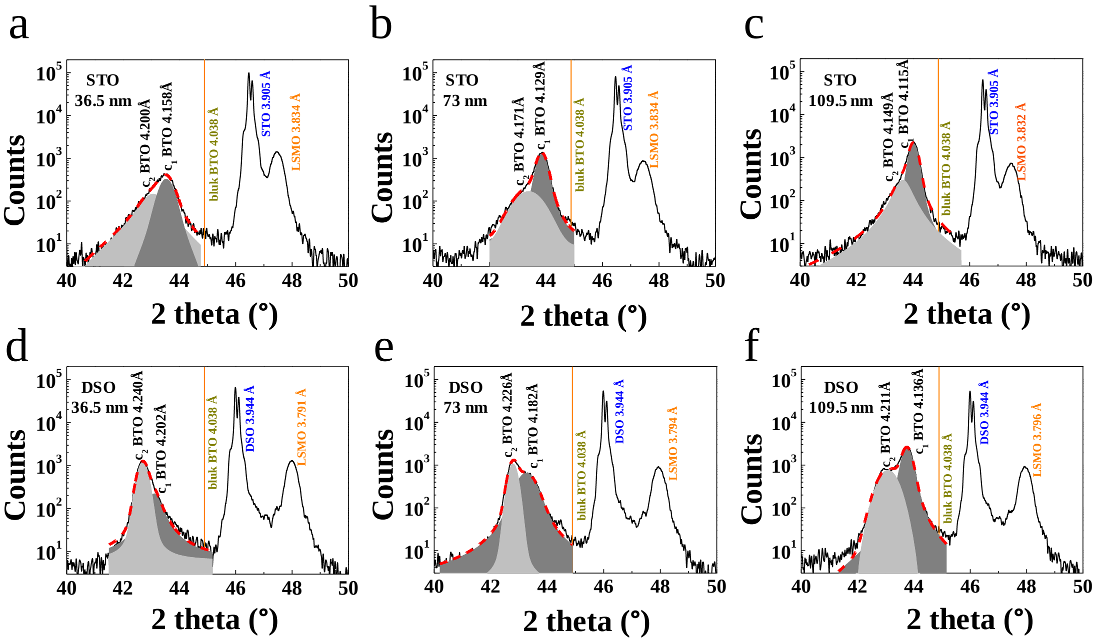

Figure 5.3. XRD 2-theta scan spectrum of (a,b,c) 36.5, 73 and 109.5 nm samples grown on LSMO//STO substrate (d,e,f) 36.5, 73 and 109.5 nm samples grown on LSMO//DSO substrate, respectively. The dark and light grey region under the peak of BTO correspond to the fitting by two Gaussian curves of the data.

Note in passing that both peaks, which are present in all samples (Figure 5.3), have c-axis values larger than the corresponding bulk one (4.038 Å). This cell expansion is commonly found in BTO films, and attributed to some non-stoichiometry effects[126]. In order to quantify the relative concentrations of **S** and **R** phases we use the ratio $I_{R,S}/I_{LSMO}$. Here I_S, I_R and I_{LSMO} stand for the relative intensities of the (*002*) Bragg peaks of the **S** and **R** fractions of BTO (*002*) Bragg peaks and that of (*002*) LSMO, respectively. In Figure 5.2(b) we summarize the calculated ($I_{\mathbf{R},\mathbf{S}}/I_{LSMO}$) vs BTO film thickness. Data in Figure 5.2(b) indicates that the concentration of the **S** phase (empty symbols) is rather constant whereas that of the **R** phase increases with thickness irrespective of the substrate (solid symbols). This finding would signal the presence of the more strained BTO phase residing close to the bottom (LSMO//DSO) interface with constant thickness, whereas the (partially) relaxed **R**-phase will have a thickness that increases with sample thickness, and most likely would be located at the upper part of the BTO film, as sketched in the Figure 5.2b (inset). The c-axis of both phases monotonously decreases towards the bulk value as the sample thickness increases as shown in Figure 5.4a,b, implying that both phases relax when increasing thickness. We have explored any possible connection between the amount of **R**/**S** phases and their cell parameters with the observed variation under illumination ΔP_r. However, it turns out that ΔP_r does not appear to be correlated neither with ($I_{\mathbf{R},S}/I_{LSMO}$) nor by the strain state (c-axis value) of each phase, see Figure 5.4c-f. Therefore, it should be concluded that structural properties are not directly driving the ΔP_r response. In Chap. 6, the **R** and **S** phases of BTO films are discussed in detail.

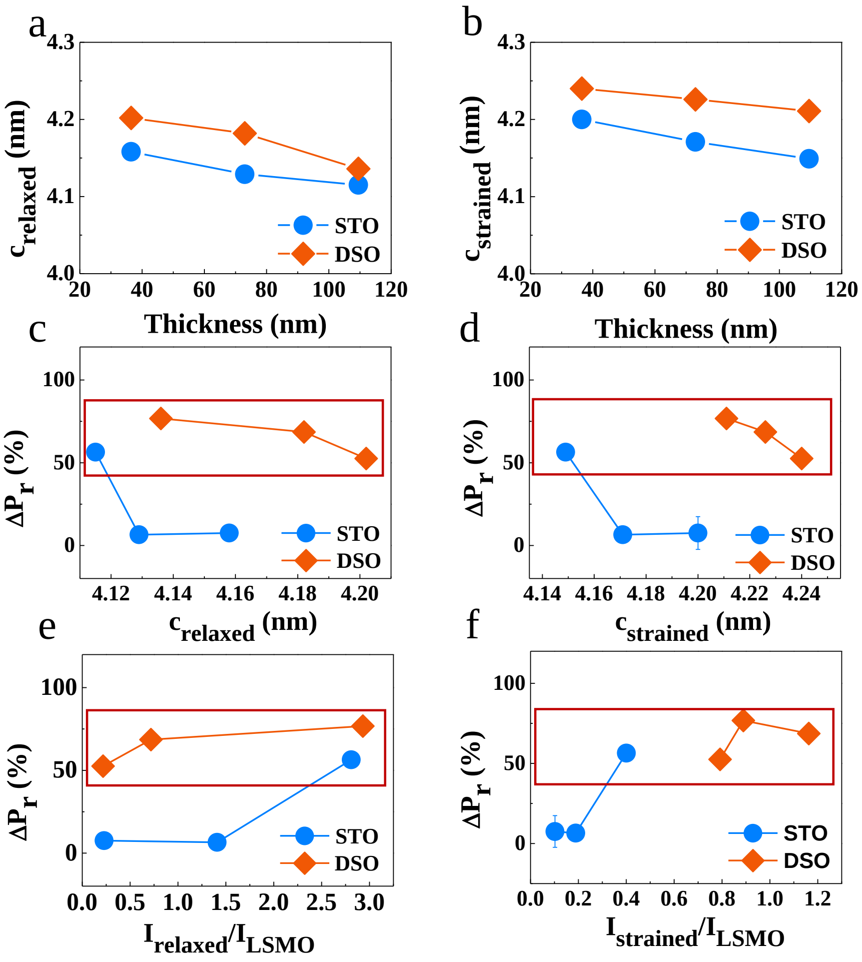

Figure 5.4. Out of plane parameters for both phases: (a) c_{relaxed} and (b) c_{strained} extracted by Gaussian fitting from the XRD 2-theta scan spectrum of Figure 5.3. Dependence of ΔP_r on relaxed and strained phase: (c,d) ΔP_r versus c_{relaxed} and c_{strained} values, respectively. (e,f) ΔP_r versus the intensity of the relaxed (I_{relaxed}) and strained (I_{strained}) peaks, respectively, extracted from the Gaussian fitting, normalized to the LSMO peak intensity (I/I_{LSMO}).

5.3.2 Correlation of photoscreening behavior and surface states

We turn now our attention to the surface chemistry of the films. In Figure 5.5(a), we show the O1s XPS spectra for 36.5 nm sample grown on STO. It is dominated by a main O1s peak (I_0) located at about 528 eV, characteristic of O^{2-} ions in BTO[127]. Extending towards larger binding energies a shoulder is well visible. On the basis of previous XPS analysis of BTO[55,121,127-129] and other perovskites[130], we interpret this feature as resulting from the contribution of differently bonded O1s species at the BTO surface. In earlier reports[55,121,127-130], three components in the O1s XPS spectra have been identified, occurring at about: (I) 530 eV, (II) 531.5 eV and (III) 533 eV. Peak I (530 eV) has been attributed to protonated lattice oxygen ($O_{lattice}H$)[55,121] or/and $BaCO_3$[128], we will return latter to this identification. Peak II (531.5 eV) has been attributed to hydroxyl OH^- groups bounded at surface cations[55,121], more likely Ti^{4+} ions[121,122] and peak III (533 eV) is commonly assigned to oxygen in physisorbed water H_2O molecules[130]. On the other hand, the position of the main I_0 peak (O^{2-} bonded in BTO) is virtually identical for all films. Similarly, no relevant changes are visible in the position of the $Ba3d_{5/2}$ and $Ti2p_{5/2}$ binding energies, although a shoulder is visible (corresponding line I) at the high energy side of the main Ba3d5/2 line (corresponding I_0) (see Figure 5.6). According to current literature the main Ba3d5/2 line (I_0) correspond to Ba^{2+} in $BaTiO_3$ and the shoulder (line I) to $BaCO_3$[128]. Focusing now the attention on the evolution of the O1s spectra for different films, it is clear that substantial differences are visible at the high-energy shoulder of O1s. Using suitable deconvolution procedures (see Chap. 2 for details), the relative contribution of each component (I, II, and III and I_0) to the whole O1s spectrum was determined and used as proxy for their relative abundance. In Figures 5.5(a-c) and Figures 5.5(d-f) we show the decomposition of the fitted sub-peaks for BTO films of various thickness on LSMO//STO and LSMO//DSO, respectively. A similar procedure has been used to decompose and extract the corresponding I and I_0 intensities of the Ba3d5/2 line for all films, see Figure 5.6. In Table 5.1, we summarize the relative fractions of BTO I_0, I, II, III contributions to the O1s peak as well as the corresponding values for I_0 and I of Ba3d5/2.

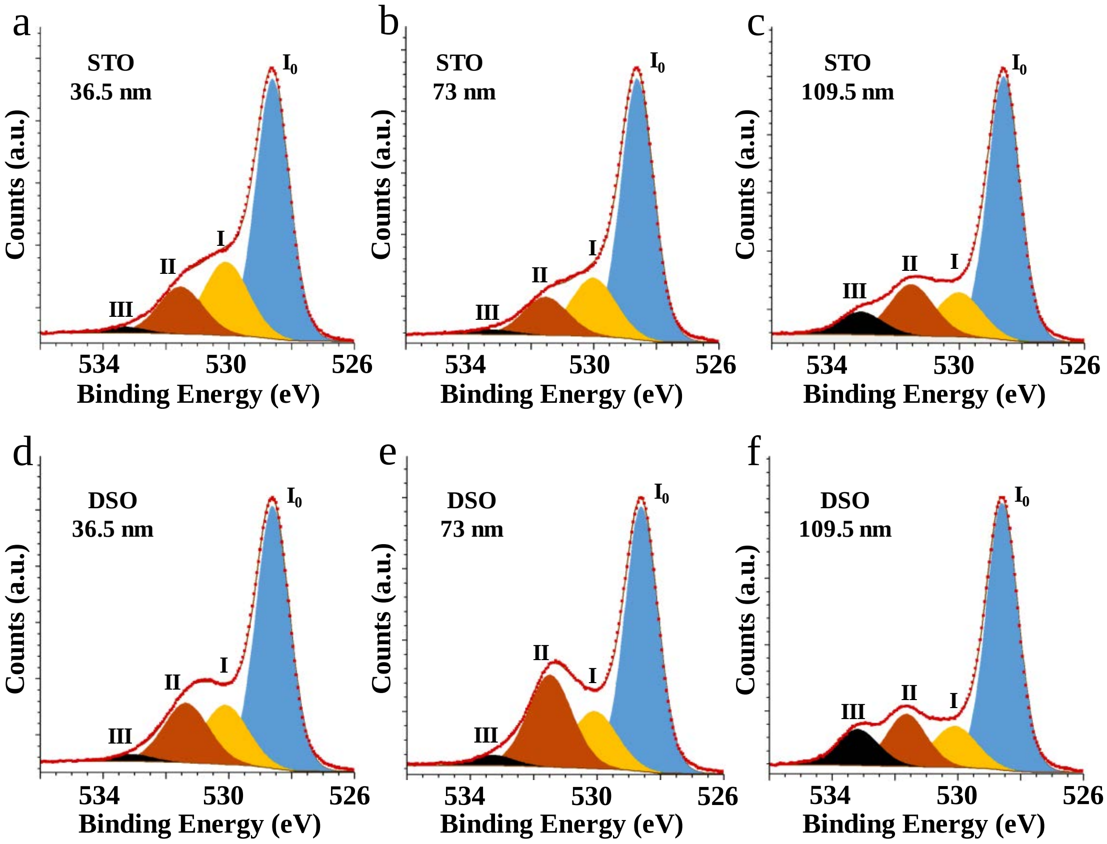

Figure 5.5. XPS spectra of O 1s core level. (a,b,c) 36.5, 73 and 109.5 nm thick BTO films on LSMO//STO substrate, respectively. (d,e,f) 36.5, 73 and 109.5 nm samples grown on LSMO//DSO substrate, respectively. The fitting was performed as described in the Method section 2.3.1 by decomposing the spectra by 4 different contributions, the structural main oxygen peak (labelled I_0), plus three other components (labelled I, II, and III) as indicated. The percentage of each specie (I_0, I, II, III) is defined as: A(j) (%) = A(j) / A(Tot) (j = I_0, I, II, III), where A(j) and A(Tot) indicate the area of j component and the total area of whole O1s spectrum above the background. The sum of the four components corresponds to the fit (brown line) to data points.

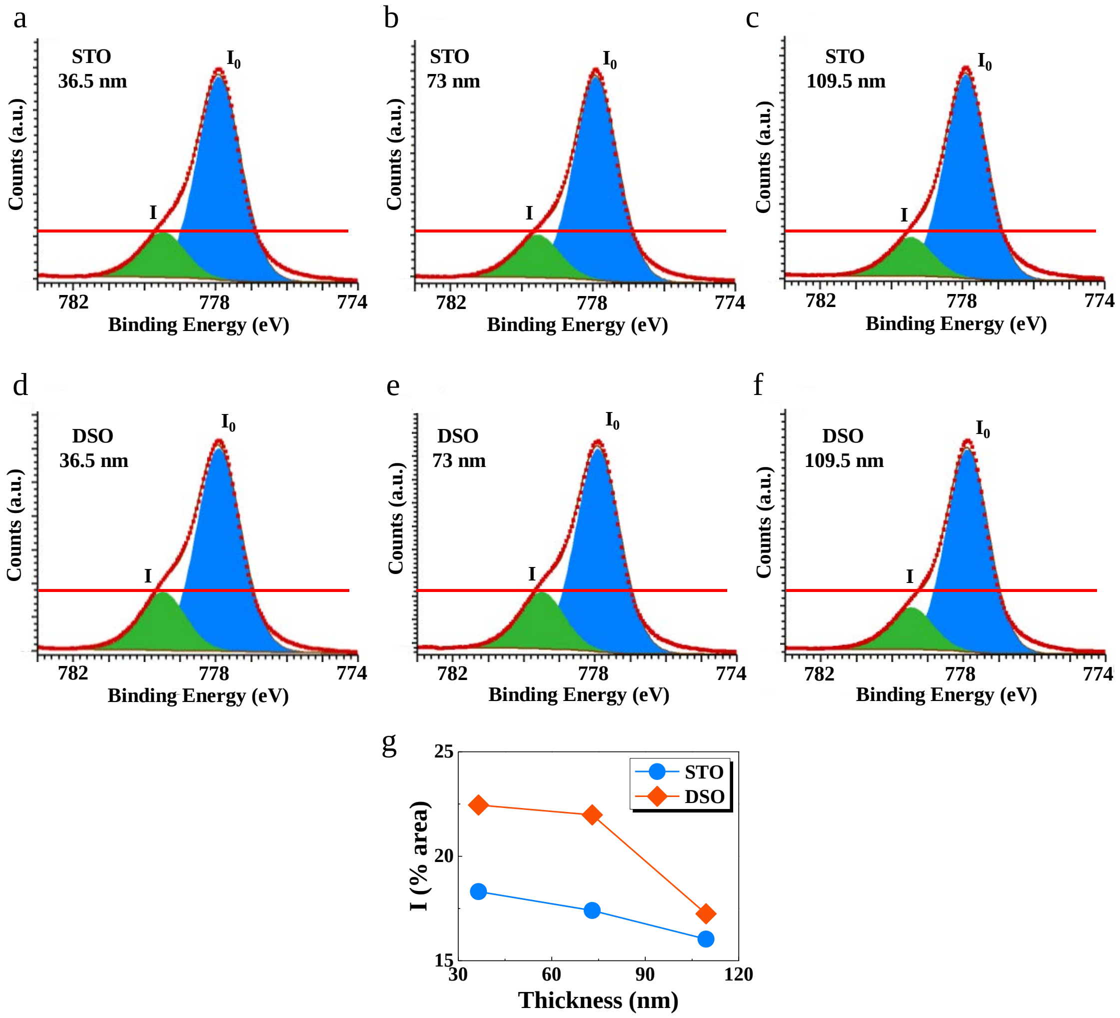

Figure 5.6. XPS normalized spectra of the six samples: XPS spectra of Ba 3d5/2 core level. (a,b,c) 36.5, 73 and 109.5 nm thick BTO films grown on LSMO//STO substrate, respectively. (d,e,f) 36.5, 73 and 109.5 nm thick BTO grown on LSMO//DSO substrate, respectively. The fitting was performed as described in the Methods section by decomposing the area above the background into 2 contributions: the main BTO peak (labeled I_0) and the $BaCO_3$ contribution[128] (labelled I) as indicated in panel (a). Red line indicates the maximum of the high energy contribution for the thinnest film of each set of samples to serve as eye-guide to compare its decreasing contribution for increasing thickness (c) Dependence of $BaCO_3$ intensity fraction on sample thickness.

Substrate	***t*** (nm)	**O 1s**				**Ba 3d5/2**
		I_0 (BTO)	I ($BaCO_3$)	II (OH^-)	III (H_2O)	$BaCO_3$
$SrTiO_3$	36.5	60.6(0.2)%	23.1(0.1)%	14.6(0.1)%	1.7(0.1)%	18.3(0.1)%
	73	65.1(0.2)%	20.1(0.2)%	13.0(0.1)%	1.8(0.1)%	17.4(0.1)%
	109.5	61.4(0.1)%	14.5(0.2)%	16.8(0.2)%	7.3(0.1)%	16.0(0.1)%
$DyScO_3$	36.5	60.6(0.4)%	18.6(0.2)%	18.7(0.1)%	2.1(0.2)%	22.4(0.1)%
	73	56.7(0.1)%	18.0(0.1)%	22.7(0.2)%	2.6(0.1)%	22.0(0.1)%
	109.5	60.9(0.3)%	13.1(0.1)%	15.0(0.2)%	11.0(0.1)%	17.2(0.1)%

Table 5.1. Relative fractions of the I_0, I, II and III contributions to O1s peaks shown in Figure 5.5, and contributions of $BaCO_3$ phase to Ba 3d5/2 peaks shown in Figure 5.6, of all six samples. The percentage of each contribution is defined as: A(j) (%) = A(j) / A(Tot) (j = I_0, I, II, III and $BaCO_3$ in Ba 3d5/2), where A(j) and A(Tot) indicate the area of j contribution and the total area of whole spectrum above the background. Numbers in the bracket are the errors from fitting.

In Figures 5.7(a) and 5.7(b), we plot the relative contributions of (II + III) [OH^- and H_2O molecules] of O1s XPS, determined from BTO films of different thickness, on STO and DSO respectively. In Figure 5.7(c,d) we show the corresponding I ($O_{lattice}H$ and/or $BaCO_3$) contribution. In Figures 5.7(c,d) we also include relative I fraction of the Ba 3d5/2 XPS spectra. It can be appreciated in Figures 5.7(c,d) that, irrespectively of the substrate, the relative fraction of I sub-spectrum decreases when the BTO thickness increases. We strength that a reduction of I line in the O1s spectrum with BTO thickness is consistent with the observed similar reduction of the $BaCO_3$ contribution in the $Ba3d_{5/2}$ XPS spectra [data in Figures 5.7(c,d) and Figure 5.6). Moreover, data in Figures 5.7(a,b) reflects a concomitant increase of the relative fraction of (II + III) components (related to OH^- and H_2O, respectively), with BTO thickness, irrespectively on the substrate used (STO or DSO). Figure 5.7(e) sketches the observed reduction of I ($BaCO_3$) contribution to the O1s and Ba3$d_{5/2}$ XPS spectra and the accompanying II+III (OH^- + H_2O) increase when increasing BTO thickness without disregarding the presence of $O_{lattice}H$.

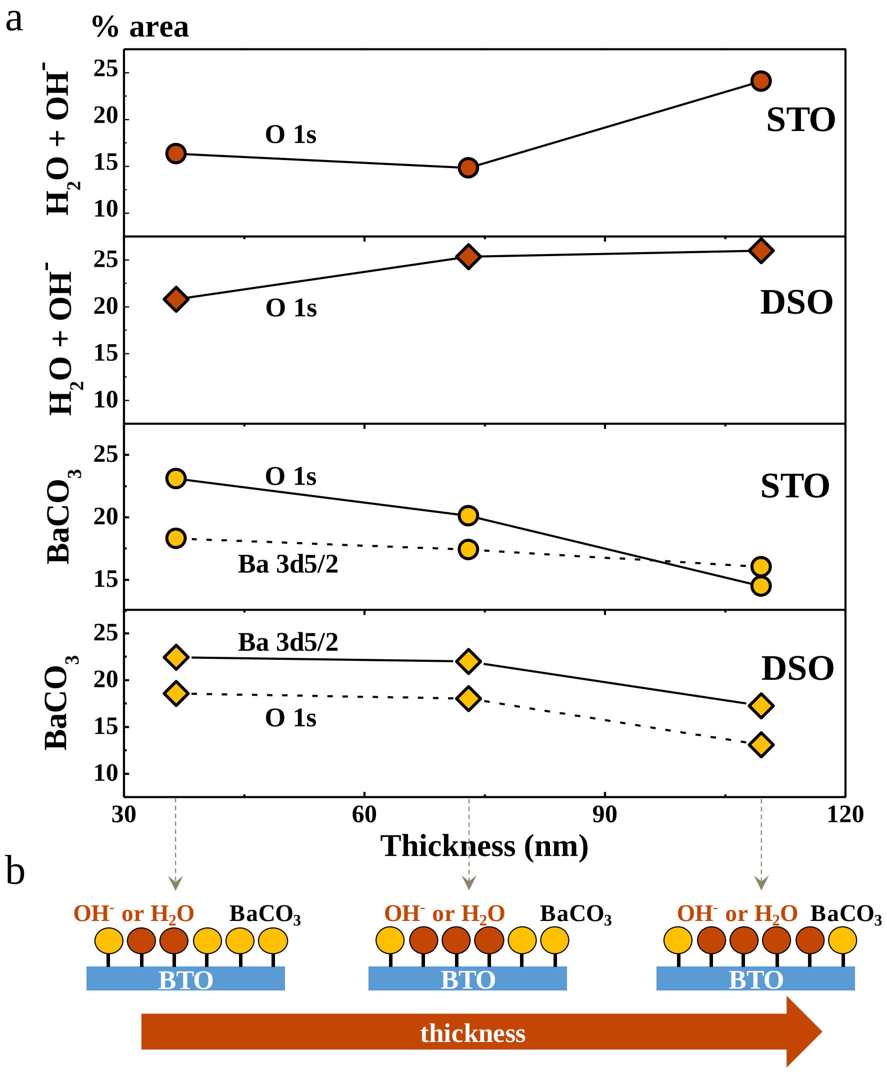

Figure 5.7. (a) Relative weight of component I ($BaCO_3$) in the O 1s, and II+III (H_2O + OH^-) in the O 1s and Ba 3d5/2 XPS spectra of BTO films of different thickness grown on STO or DSO substrates. (b) Sketch of the increasing H_2O/OH^- and decreasing CO_3^{2-} contribution with thickness, as revealed by data shown in panel (a).

A possible way to rationalize this trend is to consider the influence of the BTO surface morphology. Indeed, the BTO surface roughness could be a relevant surface parameter for chemical or physical adsorption and it may vary systematically when increasing

BTO thickness or changing the substrate. To address this issue, we have measured the roughness of all films and shown in Figure 5.8, and found that it increases very modestly from 0.2 to 0.5 nm for BTO/LSMO//STO films and a similar trend is found for BTO/LSMO//DSO films, although with marginally larger RMS values (0.3 – 0.7 nm). Therefore, although there is some enhancement of specific surface with thickness, which is even more pronounced in BTO films on DSO substrates, the observation of an opposite trend for the evolution of I and (II + III) species with thickness denies that changes of specific surface are at the root of this observation.

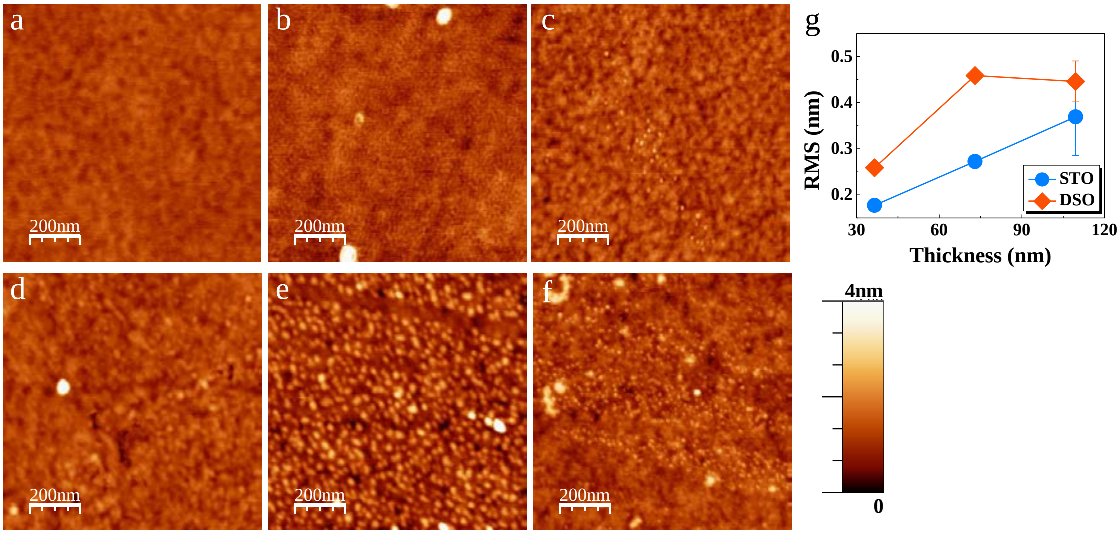

Figure 5.8. (a-f) AFM topography images (2 μm × 2 μm) of BTO films of thicknesses 36.5 nm, 73 nm, 109.5 nm grown on STO (a,b,c) and DSO (d,e,f) respectively. White dots seem to be more present in thicker samples denote the increasing presence of adsorbates as thickness increases. (g) Surface roughness (RMS) vs. film thickness.

Alternatively, one can consider that the observed changes of surface composition result from mechanisms of polarization screening of BTO films when exposing the film to the atmosphere. As mentioned above, screening can be provided by internal charges (likely point defects) or external charges at electrodes and adsorbates. Our as-grown films are self-poled and the polarization points towards the surface, as shown in Figure 5.9, and therefore negative charged species are required at the free surface. This can be achieved either by polar H_2O molecules and OH^- adsorbates or by internal charges.

Indeed, BTO is typically an n-type semiconductor and electrons released from oxygen vacancy donors can be driven to the upper surface to screen polarization[96]. The observed relative increase of (II+III) and the accompanying decrease of (I) species when increasing thickness [sketched in Figure 5.7(e)] indicates that screening by H_2O and OH^- gets a more prominent role than internal charges screening when increasing film thickness. In other words, the efficiency of internal screening decreases with film thickness. The conclusion, derived from XRD data, that the **R** phase becomes more prominent as BTO thickness increases and it is located mainly at the free surface provides the simplest and soundest explanation to this observation. Indeed, the strained **R** fraction, having a (relatively) shorter out-of-plane cell parameter would have a smaller density of point defects and thus the amount of available charges (electrons) for internal screening more limited. Consequently, most of screening charges will be provided by externally, that is by negatively charged (II+III) adsorbates. This simple picture is also compatible with the experimental observation (Figure 5.10) that leakage current decreases when increasing film thickness[131].

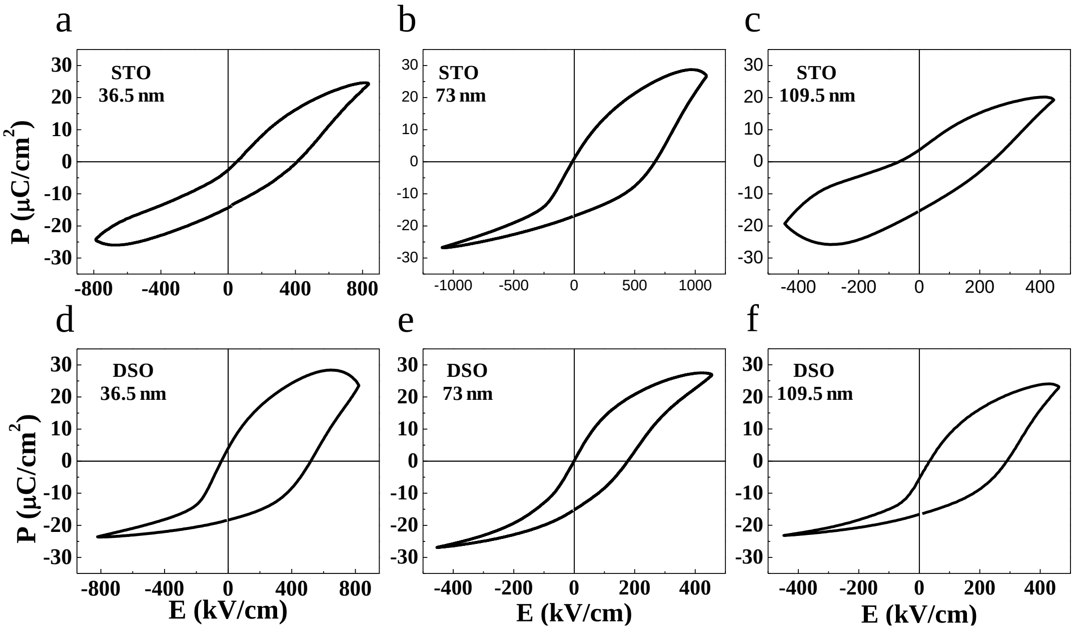

Figure 5.9. *P-E* loops measured using bottom-top contact configuration, where LSMO bottom electrode is grounded and one top Pt-electrode is biased, for (a,b,c) 36.5, 73, 109.5 nm BTO/LSMO//STO films, respectively; and (d,e,f) 36.5, 73, 109.5 nm BTO/LSMO//DSO films, respectively. In all cases, a right a positive shift of the loop is

observed. It denotes the presence of an internal electric field that promotes polarization pointing away from the bottom electrode[83,125].

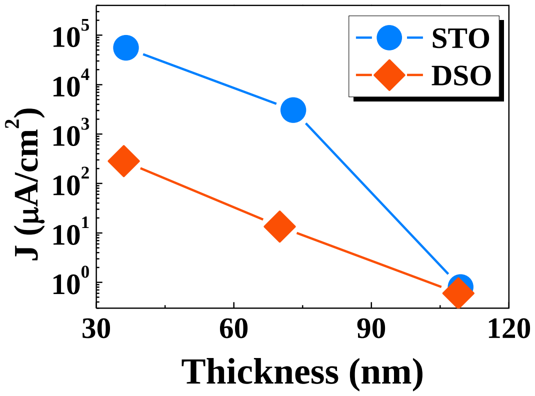

Figure 5.10. Current density versus sample thickness for samples grown on different substrates measured at 0.5 V.

We turn now to the observed ΔP_r photoresponse and its connection with material's properties and screening mechanisms. A deep insight is provided by data in Figures 5.11(a,b) where we plot the relative intensity of the I (O_I) and II+III (OH^- and H_2O) components, extracted from the XPS spectra of Figure 5.5, versus the corresponding ΔP_r of Figure 5.1. Data in Figure 5.11(b) suggest that ΔP_r increases when the relative fraction of (II + III) (OH^- and H_2O) increases. This trend holds true for BTO films grown on both STO and DSO substrates. In contrast, ΔP_r decreases as the relative fraction of phase I increases [Figure 5.11(a)].

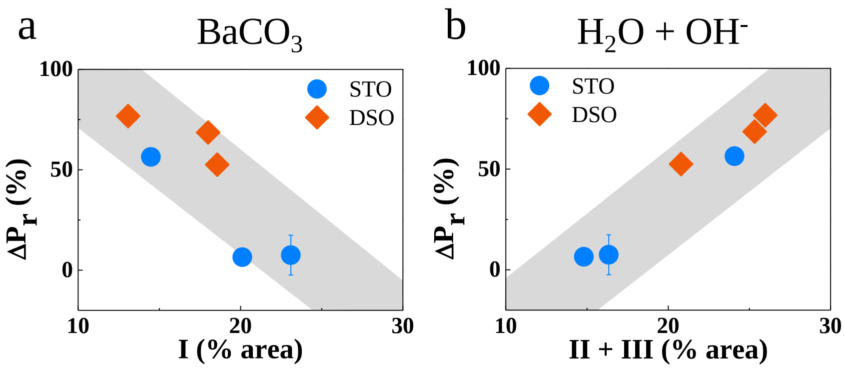

Figure 5.11. Dependence of the change of remnant polarization with light (ΔP_r) on the relative weights (%) of I and II+III components extracted from O 1s XPS spectra

shown in Figure 5.5. (a) Component I corresponding to oxygen in $BaCO_3$); (b) Components II+III corresponding to hydroxyl OH^- groups bounded at the surface cations and to the physisorbed water H_2O). The grey backgrounds on data points are eye-guides.

5.3.3 Surface H_2O/OH^- adsorbates enhancing by *Steam-treatment*

Observations from Figure 5.11 suggest a direct correlation between the presence of adsorbed surface water-related species and ΔP_r. In order to confirm this hypothesis, *ad-hoc* experiments were designed to modify the concentration by H_2O and OH^- adsorbed species. With that purpose, fresh grown BTO films were exposed to a water steam and the photoresponse of the remnant polarization was compared to that of virgin (un-treated) samples. The *steam-treatment* consists on placing the film, at 100 ºC, to a jet of water vapor (800 $cm^3 \cdot min^{-1}$) at atmospheric pressure for 10 hours. Water liquid residues were eliminated from the BTO surface by a jet of N_2 for 1 min immediately after the *steam-treatment*.

In Figure 5.12(a), we show the *P-E* loops of a 109.5 nm BTO/LSMO//STO film with Pt contacts deposited immediately after film growth, to minimize the presence of adsorbates at the surface. The loop recorded under illumination shows only minor variations when compared with the loop recorded in dark. The seemingly small increase of polarization is due to the somewhat larger leakage current under illumination. After this control experiment, we performed the aforementioned *steam-treatment*, and subsequently deposited new Pt top electrodes. In Figure 5.12(b) we show the corresponding *P-E* loops recorded in dark and under illumination. It can be observed that the remnant polarization recorded under illumination is dramatically reduced compared to the one recorded in dark. This observation is in agreement with all results in Figure 5.1. Interestingly, the *P-E* loops recorded in dark and under illumination using the original electrodes, shown in Figure 5.12(c), although the sample has been stream-treated, do not show any variation under illumination. Therefore, the Pt electrode protects the underneath $BaTiO_3$ surface from H_2O adsorption and confirms that water exposure is a key ingredient for the observed photoresponse. Consequently, we attribute the enhanced photoresponse after the *steam-treatment* to the presence of H_2O and OH^- groups at the $BaTiO_3$ surface, underneath the newly grown Pt electrodes after treatment [sketched in the insets of Figure 5.12(a-c)]. Consistently, the AFM images collected before and after the *steam-treatment* show an increased presence of adsorbate-related products, without any relevant change on the structural (XRD) properties, see Figure 5.13. To get further insight, XPS spectra of this BTO/LSMO//STO film were recorded before [Figure 5.12(d)], and after [Figure 5.12(e)], the *steam-treatment*. The comparison of data in Figure 5.12(d) and Figure 5.12(e), evidences an important increase of the high energy shoulder of the main O1s peak after *steam-treatment*. Using the same protocol as above, these spectra were analyzed to determine the different contributions to the spectra and their evolution by *steam-treatment*. Table 5.2 summarizes the relative fractions of the I_0, I, II, and III lines before and after *steam-treatment*. Data in Table 5.2 shows that the major differences in the spectra of Figures 5.12(d,e) are related to the II+III components, which significantly increase after *steam-treatment*. As II and III O1s peaks are ascribed to the presence of H_2O related adsorbates, these results conclusively demonstrate that the *steam-treatment* promotes its presence and are responsible for the enhanced ΔP_r photoresponse.

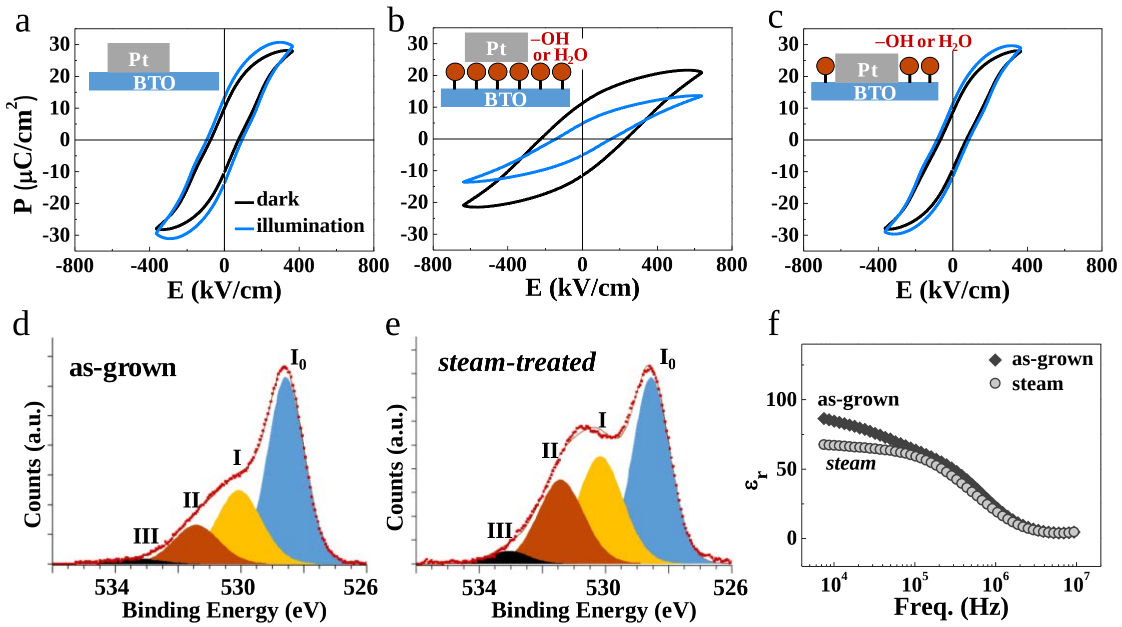

Figure 5.12. (a) *P-E* loops of 109.5 nm BTO/LSMO//STO sample, obtained before *steam-treatment* in dark and under illumination (b) *P-E* loops in dark and under illumination in electrodes deposited after 10 h *steam-treatment*. (c) *P-E* loops in dark and under illumination after 10 h *steam-treatment* in electrodes deposited before the treatment. In the insets, it is sketched the BTP/Pt interface, where brown circles are H_2O or OH^- groups attached to the surface. (d, e) O1s XPS spectrum of a nominally equivalent sample before and after *steam-treatment*. (f) Dependence of the relative dielectric permittivity (ε_r) of the film in dark on frequency in Pt electrodes deposited before and after the *steam-treatment*.

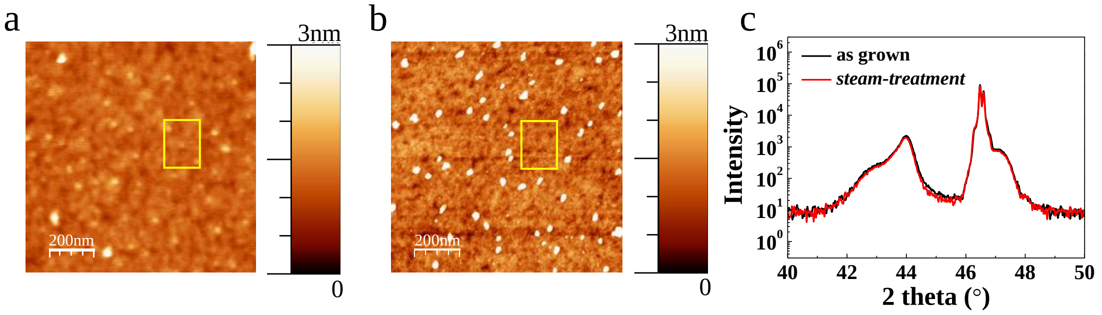

Figure 5.13. (a,b) AFM surface topography image collected for the 109.5 nm BTO film grown on LSMO//STO substrate of Figure 6 of the main text before and after the *steam-treatment*, respectively. The RMS values extracted from the area enclosed by the yellow rectangle in (a,b) are 0.22 and 0.25 nm, respectively (c) XRD 2theta scan spectra, before and after *steam-treatment*.

	O 1s			
	I_0 (BTO)	I ($BaCO_3$)	II (OH^-)	III (H_2O)
as-grown	56.2(0.1)%	27.3(0.2)%	14.5(0.1)%	2.0(0.1)%
steam-treatment	42.2(0.1)%	27.4(0.4)%	26.8(0.1)%	3.6(0.1)%

Table 5.2. Data extracted from O 1s XPS spectra fitting before and after *steam-treatment*. The percentage is shown for each of the 4 contributions to the O 1s XPS spectra of Figures 5.12(d,e), before and after the *steam-treatment*, respectively. The

percentage of each contribution is calculated as described in Table 5.1. Numbers in the bracket are the errors from fitting.

Further evidence of the important role of adsorbates is obtained from frequency-dependent impedance measurements. Indeed, it is well known that the low-frequency capacitance in metal/dielectric/metal structures can be severely affected by parasitic interface capacitance and thus it can be used as a fingerprint of their presence[12,14-17,132]. In Figure 5.12(f) we show the permittivity of the Pt/BTO/LSMO film where the Pt contacts have been deposited either on the fresh BTO surface (solid symbols) or after (empty symbols) *steam-treatment*. It is clear that at low frequency, the capacitance of the *steam-treated* structure is smaller than in the pristine sample, which as analysed in detail in previous literature[12,14-17,132], indicates than in the former there is a series interface capacitance. Overall, this new set of results clearly confirms a relative increase of H_2O and their related dissociation products (OH^- hydroxyls and protonated oxygen species) at the BTO surface, after *steam-treatment,* and an accompanying larger photoelectric effect.

Additional works on studying the influence of the condition of Pt electrodes on *steam-treatment* and corresponding ferroelectric properties and photoresponses are depicted in Appendix Figure A-2 to A-5.

5.3.4 Phenomenological explanation of photo-induced polarization screening in $BaTiO_3$ thin film

To sum up, the presence of water and associated OH^- and/or $O_{lattice}H$ adsorbates at the surface of ferroelectric BTO film, modulate the magnitude of the switchable polarization and the polarization variation under illumination. A plausible scenario is described in the following.

Fresh surfaces of BTO films (minimal exposure of BTO surface to air conditions) display a minor photo-induced change of remnant polarization ΔP_r, indicating that neither external nor internal screening are significantly modified by blue-laser illumination. This latter observation results from the fact that the bang gap of BTO is significantly larger than the photon energy used in these experiments and photoinduced carriers play a minor role on the amount of measured switchable polarization. Screening charges are mainly provided by electrodes. In contrast the presence of H_2O, or hydroxyl groups (OH^-), probably bonded to Ti ions, or also $O_{lattice}H$[122], has an important dual effect. First, they provide screening charges and promote pinning of some of the ferroelectric domains [Figure 5.14(a)], thus producing a reduction of the switchable polarization as measured by $P(E)$ loops. Second, the photocatalytic decomposition of H_2O at BTO polar surfaces produces a larger concentration of OH^- and H^+ species that screen the polarization charges, reduces further the switchable polarization and ultimately are the responsible of the photosensitivity of the remnant polarization ΔP_r [Figure 5.14(b)].

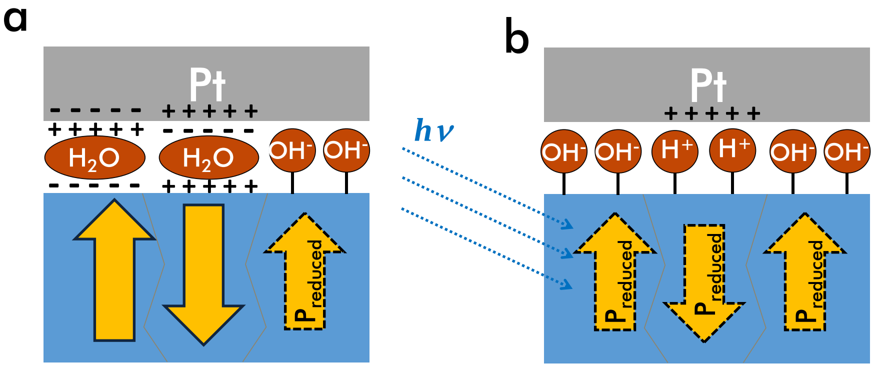

Figure 5.14. (a) Sketch of the polarization screening in a $BaTiO_3$/Pt where the metallic electrode has been grown ex-situ after ambient exposure. Physisorbed H_2O molecules and OH^- radicals, bonded to the surface, screen and pin some ferroelectric domains. (b) When sample is lightening through a partially transparent Pt electrode, photodissociation of H_2O molecules occurs and chemisorbed photoreaction products (OH^- and H^+) modify screening and pinning of ferroelectric domains.

5.4 Conclusions

We have characterized the response of the ferroelectric polarization of BTO films upon blue-laser illumination and observed that, in some cases, a substantial reduction of remnant polarization occurs under illumination. By exploring the structural, morphologic and surface chemistry by XPS, we have shown that the observed photoresponse is governed by the presence of H_2O-derived adsorbates, whose photoinduced decomposition provide external screening charges and possibly enhanced ferroelectric domain pinning both reducing the amount of switchable polarization as measured by I-V curves. The results presented show how the synergy between photocatalytic and photoelectric activity at the surface of a ferroelectric material can be exploited to tune ferroelectric properties, providing a simple receipt to manipulate it.

Chapter 6. Coexistence of strained and relaxed phases in $BaTiO_3$ thin films

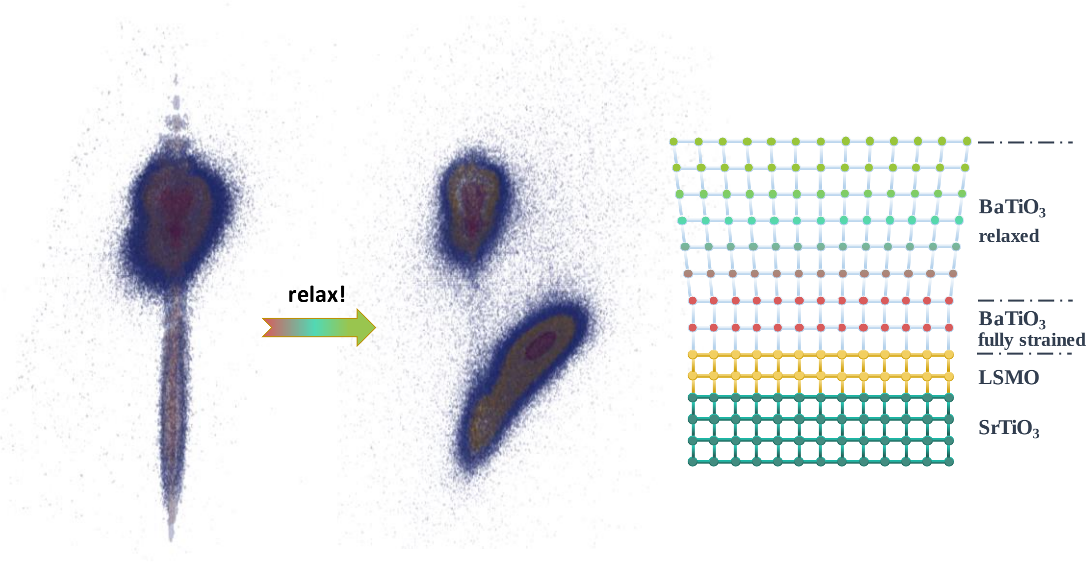

Abstract

In this chapter, efforts are made to study fine crystal structure and strain states in $BaTiO_3$, trying to understand the asymmetric or double BTO peaks in XRD spectra that are commonly observed in thin films studied in this thesis. $BaTiO_3$ (BTO) (001) epitaxial films were prepared by pulsed laser deposition (PLD) on $SrTiO_3$ (STO) and $DyScO_3$ (DSO) substrates, which impose a compressive strain of 2.6% and 1.6% respectively. Structural characterization was performed by high resolution reciprocal space maps using synchrotron X-ray radiation (KMC-2 beamline, HZB BESSY II synchrotron, Berlin) on films ranging from about 4 to 110 nm. Data show that films are composed by two coexisting crystalline phases and their cell parameters were determined. In BTO films on STO thicker than critical thickness, one phase (denoted **S**) is fully strained (with the same in-plane lattice parameters than the substrate underneath) and another (denoted **R**) is partially relaxed. Grazing incidence experiments indicate that the **S** phase is located closer to the substrate whereas the **R** phase is closer to the free surface. It turns out that when increasing the BTO thickness, the cell parameters (*a*,*c*) of the **R** fraction approach gradually to those of bulk BTO, whereas those of the **S** phase are insensitive to film thickness. Remarkably, the *c*-axis of the **S** phase is larger than that of bulk BTO and that expected for fully strained (volume preserving) film. In contrast, the (*a*,*c*) parameters of the **R** phase evolve with thickness towards the bulk value; however although the in-plane reaches the bulk value for the thickest film (~110 nm), the *c*-axis remains also larger than expected. These results indicate the existence of an anomalous expansion of *c*-axis both in **S** and **R** phases.

When comparing structural data of BTO films grown on STO and DSO, it is found that films up to 110 nm grown on DSO are fully strained with minor fraction of the relaxed phase, which results from its smaller lattice mismatch compared with STO.

The ferroelectric Curie temperatures (T_c) of **R** and **S** phases were identified by X-Ray from the temperature dependence of *c*-axis indicates the corresponding T_c. In contrast,

in-plane lattice parameters show no evidence of the phase transition probably because of the substrate clamping. Overall, it is found that, for a given film thickness and substrate, the **S** and **R** phases have Curie temperatures much higher than bulk $BaTiO_3$, thus suggesting that pure elastic strain is not enough to describe the observed results.

6.1 Introduction

The ferroelectricity endows ferroelectric materials with spontaneous polarization and subsequent properties such as large electroresistance[31] and photovoltaics[133], which promise great applications in non-volatile memories[70], optoelectronics[134], energy harvesting[135] and photocatalysis[105]. Ferroelectricity occurs in non-centrosymmetric crystallographic structures that allow existence of spontaneous self-ordered dipoles. As the strain states can greatly influence the crystallographic structure, external strain is most widely applied to tune the magnitude of spontaneous polarization[136], especially on ferroelectric materials thin films. In $BaTiO_3$ thin films, a widely studied ferroelectric system, compressive or tensile strain is introduced by growing the films on different substrates that possess different lattice mismatch with BTO, such as $SrTiO_3$ (STO), $DyScO_3$ (DSO), $GdScO_3$ (GSO), etc. Typically, when increasing the film thickness, the strain relaxes beyond a critical thickness that can vary from several nanometers[137] to more than 100 nm[126]. Therefore, more than one strain state can exist in BTO thin films exceeding the critical thickness (t_c), which was presented as several phases as reported in previous research[126,138].

Asymmetric or double BTO peaks in XRD spectra that are commonly observed in thin films studied in this thesis, e.g. XRD spectra shown in Figure 5.3. Therefore, in this chapter, we attempt to characterize the fine crystal structure of BTO and study its strain state, trying to understand the evolution of strain relaxing and its influencing factors. We study the strain relaxing process of $BaTiO_3$ thin films by using diffraction technique with synchrotron X-ray light source. (001) oriented BTO films were grown on STO and DSO substrates which impose compressive strains on the films. Increasing of in-plane lattice parameters (a) and decreasing of out-of-plane lattice parameters (c) are the iconic microstructural features in the relaxation of compress-strain epitaxial films, which can be directly characterized by X-ray diffraction due to Bragg’s law. Two influencing factors were introduced in the strain relaxing process: the thickness of BTO and the lattice mismatch between BTO and substrates. Choosing these two variables is because they are easier to repeat and control than other PLD parameters, such as oxygen pressure and energy density of the laser as reported in other research[126,138,139]. Temperature dependence of lattice parameters are also studied.

6.2 Materials and methods

8 $BaTiO_3$ films with thickness (t) from ~4 nm to ~110 nm were grown on (001) $SrTiO_3$ and (110) $DyScO_3$ substrates (5 × 5 × 0.5 mm single crystal from CrysTec) by pulsed laser deposition. STO is cubic structure that provides a strict 3.905 × 3.905 Å square base while DSO is orthorhombic which provides a near-square 3.944 × 3.944 Å lattice base[140]. A ~30 nm think layer of $La_{2/3}Sr_{1/3}MnO_3$ (LSMO) was first grown by PLD on the substrate as the buffer layer. One pair of BTO/LSMO films were grown simultaneously on a STO substrate and on a DSO substrate in a single PLD process, hence 4 pairs of BTO films obtained where t are the same in every pair. The 4 pairs BTO films were deposited by 100, 1000, 2000 and 3000 pulsed respectively. A BTO single layer (without LSMO) was deposited on by 2000 pluses on STO in the same branch, where its thickness is 73 nm determined by X-ray reflectivity (see methodology in chapter 2, section 2.4.1). Then we extrapolate thicknesses of these 4 pairs BTO are approximately equal to 3.65 nm, 36.5 nm, 73 nm and 109.5 nm.

Lattice mismatch $f = (a_{sub} - a_{BTO})/a_{BTO}$, where a_{sub} is the in-plane parameter of the substrate and a_{BTO} is the in-plane parameter of strain-free $BaTiO_3$ that is equivalent to a of bulk BTO at room temperature. As $a_{STO} = 3.905$ Å, $a_{BTO} = 3.993$ Å and equivalent in-plane parameter $a_{DSO} = 3.944$ Å, it can be calculated that $f_{STO} = -2.2\%$ and $f_{DSO} = -1.2\%$, where negative sign stands for compressive strain.

Reciprocal space maps (RSMs) of $BaTiO_3$ films on STO substrate (BTO//STO) with t = 3.65 nm, 36.5 nm, 73 nm, 109.5 nm were built around $(\overline{1}11)$, $(\overline{2}22)$ and $(\overline{1}03)$ planes. And RSMs of $(\overline{2}11)$, $(\overline{1}12)$, $(\overline{2}02)$ and $(\overline{3}01)$ planes were only collected for 36.5 nm, 73 nm, 109.5 nm films. Grazing incidence X-ray diffraction (GIXD) were performed at $(\overline{2}22)$ plane on 109.5 nm BTO//STO subsequently. RSMs of 109.5 nm BTO film on

DSO substrate (BTO//DSO) were obtained on $(\bar{1}11)$, $(\bar{2}22)$, $(\bar{1}03)$ and $(\bar{3}01)$ planes to compare with BTO//STO films of the same thickness. All data above were collected at room temperature and under ambient atmosphere. Afterwards, RSMs from room temperature to 750°C were collected around $(\bar{2}22)$ diffraction plane on 109.5 nm BTO//STO and BTO//DSO films. And the correspondences between coordinates of RSMs (q_x, q_y and q_z) and real space interplanar spacing (d) are obtained by the relations: $q_y = h/d_h$, $q_x = k/d_k$ and $q_z = l/d_l$. h, k, l are the Miller indexes of (hkl) crystallographic plane.

For comparing with results of RSMs, XRD θ-2θ scan of all 8 samples were performed by a *Bruker* D8 Discover A25 high resolution diffractometer at ICMAB.

6.3 Results and Discussion

6.3.1 Thickness dependence of lattice parameters of BTO//STO films

XRD θ-2θ scans around (002) plane of BTO//STO films with four different t were firstly checked. Double peaks of BTO are clearly shown in Figure 6.1b-d, representing two BTO phases with different c. The wide peak in Figure 6.1a is due to the broaden effect of ultra-thin BTO. Notice the left BTO peaks in Figure 6.1c,d are with even larger c than fully strained BTO on STO, which considers BTO cells as incompressible (volume preserving). Similar phenomenon is found in XRD θ-2θ scans of 4 BTO//DSO films, where asymmetric peak instead of double BTO peaks are observed, see Figure A-6 in Appendix.

These “anomalous” expanded c causes great interests and guide us to seek for solutions through synchrotron X-ray light source, which is able to define both in-plane and out-of-plane lattice parameter precisely via RSMs in higher resolution and intensity than those obtained by conventional X-ray diffractometers (e.g. Figure 3.7).

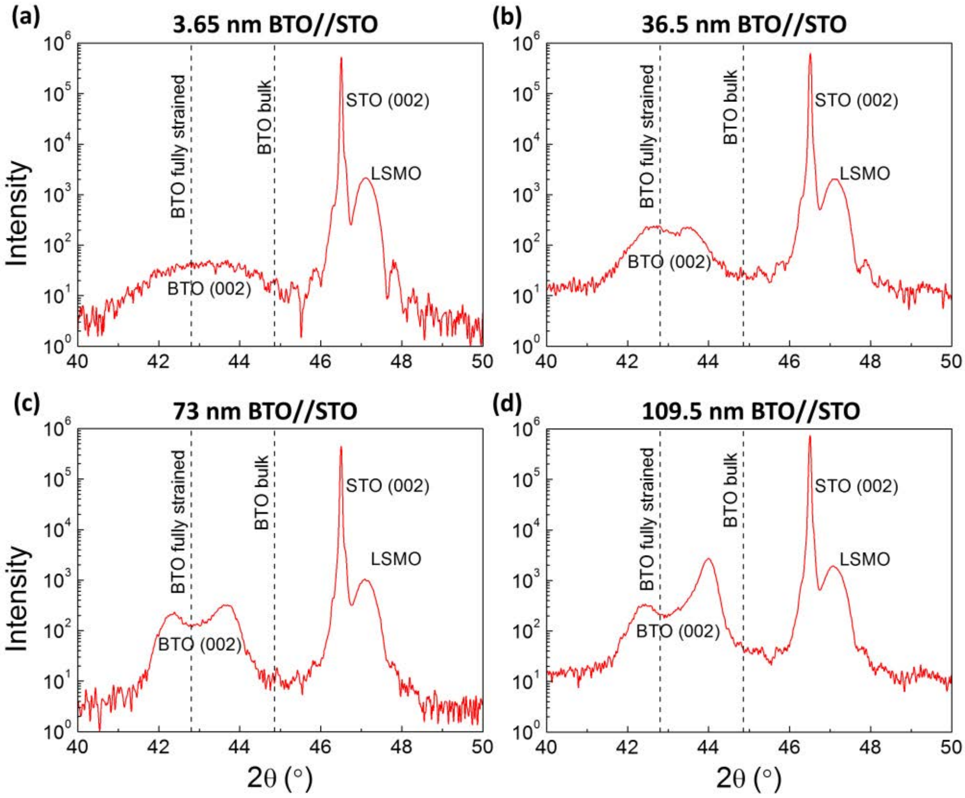

Figure 6.1. XRD θ-2θ scans around (002) plane of BTO//STO films. (a) 3.65 nm, (b) 36.5 nm, (c) 73 nm and (d) 109.5 nm BTO film on STO. Annotations mark the position of the STO substrate, the LSMO buffer layer and the BTO film. Two dashed lines indicate the *c* of bulk BTO and fully stained BTO epitaxially grown on STO which considering BTO cells as incompressible.

Figure 6.2 shows the 3-dimensional (3D) RSMs at $(\bar{2}22)$ of BTO//STO films of four different thickness. In each RSM, the yellow and red “cores” are regions with relative higher intensity than blue “shells” that represent the region with lower intensity. The color bar is representing the intensity from minimum (1) to the maximum in logarithmic scale. And for better visibility, the first 1/3 range of color bar is set scaling from blue to yellow to red, and the rest 2/3 range is set all red.

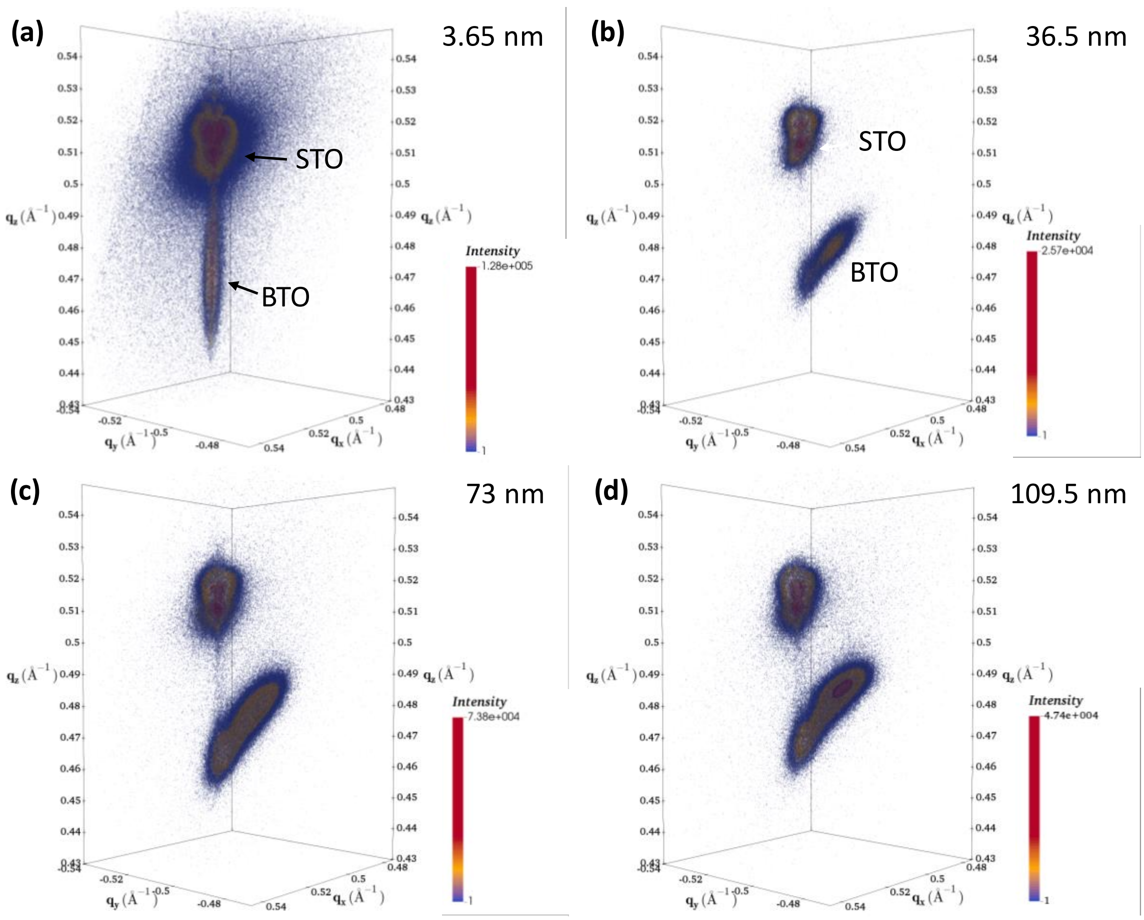

Figure 6.2. 3-dimensional reciprocal space maps at $(\bar{2}22)$ plane of 4 BTO films with thickness of (a) 3.65 nm, (b) 36.5 nm, (c) 73 nm and (d) 109.5 nm on STO substrates. Regions of BTO and STO in RSMs are marked in (a) and (b), and the pattern of LSMO is not marked as its position is very close to STO and with lower intensity. Color scales are set from blue to red corresponding to the intensity from the minimum intensity (1) to the maximum in logarithmic scale.

A clear way to manifest the relaxation is projecting 3D RSMs on a 2-dimentional plane. We call this projection a 2D RSM. Figure 6.3 shows 2D RSMs at $(\bar{2}22)$ by projecting 3D RSMs shown in Figure 6.2 on the q_z-q_y plane: $I(q_y, q_z) = \int_{q_x} I(q_x, q_y, q_z) dq_x$. In this q_z-q_y projection both in-plane and out-of-plane lattice parameters are visible. Figure 6.3a shows a fully strained BTO with $t \approx 4$ nm. In Figure 6.3 b-d, observed expansion of pattern BTO both in q_z and q_y direction as t increasing points the relaxing tendency, and forms two phases in BTO – a strained phase (**S**) preserving similar *a* as the substrate and a relaxed phase (**R**) with larger *a*, smaller *c* than **S**. Definitely, it can be learnt that t_c of BTO//STO films in this work is between 4 and 36.5 nm. It can be observed in Figure 6.3d that the center position of relaxed BTO is close to bulk BTO, which implies that relaxed phase is almost fully relaxed at t = 109.5 nm. Similar results are obtained in q_z-q_y 2D RSMs at $(\bar{2}22)$ and $(\bar{1}03)$ planes, see Figure A-7 and Figure A-8 in Appendix. Good consistency of in-plane parameters between STO and LSMO can be observed in all 4 films, indicating fully strained state of LSMO that perfectly transfers the strain from STO to BTO. This is in agreement with earlier results[141]. Actually, all LSMO in this work show no signs of relaxation thus they are considered to be fully strained by in the following discussion.

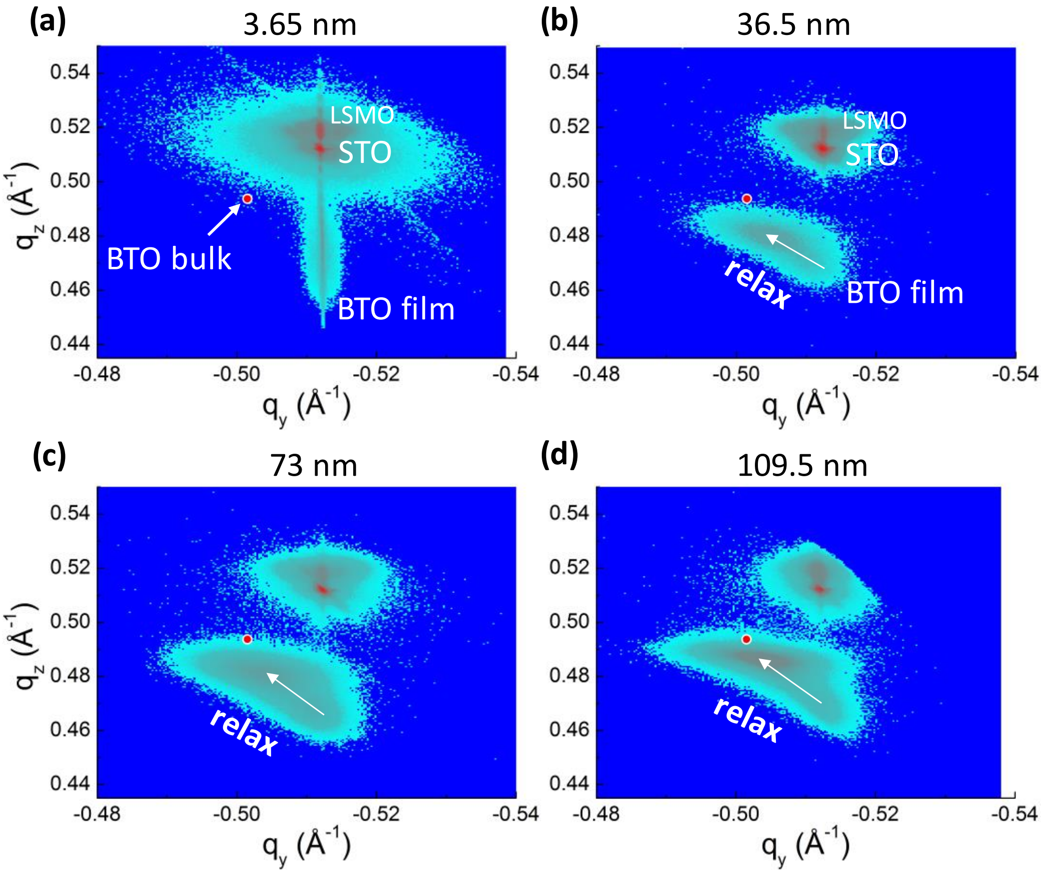

Figure 6.3. Projections of 3D RSMs of $(\bar{2}22)$ plane on q_z-q_y reciprocal plane. RSMs are from BTO//STO films with t = (a) 3.65 nm, (b) 36.5 nm, (c) 73 nm and (d) 109.5 nm. Color transition from blue to cyan to purple and to red indicates the increasing of

intensity in logarithmic scale. Regions of BTO, STO and LSMO are marked in (a) and (b), also the directions of relaxation are marked by the white arrows in (b), (c) and (d). A red circle in each sub-figure points the lattice parameters of bulk $BaTiO_3$.

Quantitative study is performed by projecting 2D RSMs on a one-dimension vector: q_x, q_y or q_z, to obtain more precise evaluation of lattice parameters. Figure 6.4 shows the q_y and q_z projection of $(\bar{2}22)$ diffraction of the 4 BTO//STO samples. In q_z projection, spectra include BTO, STO and LSMO peaks, while in q_y projection only BTO peak is shown by choosing a range of integration that excludes STO (and LSMO) contribution. This is because patterns of BTO, STO and LSMO can be separated in q_x-q_y 2D RSM but not in q_z-q_x nor q_z-q_y. In Figure 6.4a, clear double peaks of BTO in q_z projection of 73 nm and 109.5 nm film can be seen. However, in the thinner 36.5 nm film, a “shoulder” rather than two peaks are observed due to its low intensity. For the ultra-thin 3.65 nm BTO film, a very wide peak is manifested due to the film-size effect. Relaxed phase in Figure 6.4a shows an obvious tendency to higher q_z-values – smaller c – as t increasing, indicated by black arrow in the plots. In Figure 6.4b, the two peaks of BTO are not discernible. It indicates the relaxing magnitude of in-plane lattice parameter is smaller than that of out-of-plane. But it is not difficult to determine the lattice parameters in Figure 6.4b because the sharp peaks of 3.65 nm BTO film specify the precise position of strained phase. Additional q_z and q_y projections of RSMs at $(\bar{1}11)$, $(\bar{1}03)$ $(\bar{1}12)$, $(\bar{2}11)$, $(\bar{2}02)$ and $(\bar{3}01)$ planes are obtained, see Appendix Figure A-9, Figure A-10.

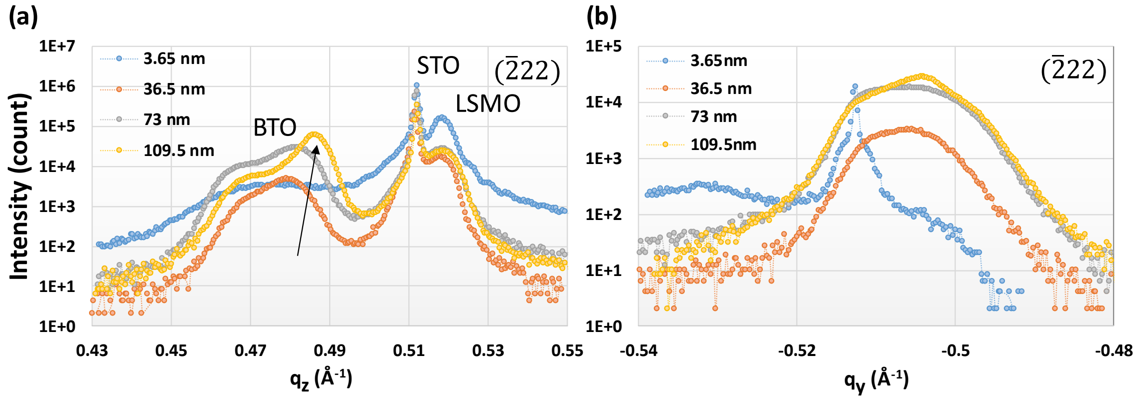

Figure 6.4. The projections of $(\bar{2}22)$ 2D RSMs on one-dimension vectors of 4 BTO//STO films. (a) Projections on q_z. The black arrows guide the view of increasing of q_z value, namely the out-of-plane relaxation, along with the increasing of thickness. (b) Projections on q_y with BTO peaks only.

Values of lattice parameters are obtained by fitting the BTO peaks in one-dimensional projected spectra via pseudo-Voigt function with goodness of fit $R^2 > 0.99$. An example of fitting is shown in Figure 6.5. The t dependence of a and c are plotted in Figure 6.6, and c extracted from XRD θ-2θ scan (Figure 6.1) are plotted together for comparison. The absence of points in relaxed BTO branches is due to the fully strained state of 3.65 nm BTO film. Points are averages of lattice parameters obtained in different diffraction planes. In both in-plane and out-of-plane parameters, strained BTO phase maintains relatively constant when $t > t_c$. In contrast, relaxed BTO phase evolves decreasing c and increasing a as t increasing, which means the relaxed phase continues relaxing, complying the general understanding of relaxation process[138,142,143]. Notice the dashed lines that mark the lattice parameters of fully stained and fully relaxed BTO (c = 4.038 Å and a = 3.993 Å[2]). a cell parameter of fully strained BTO is identical to a of STO substrate which is 3.905 Å, and fully strained c value is calculated considering the BTO cell volume preserves constant after deformation, i.e. incompressible cells with Poisson's ratio $v = 0.5$. c calculated in this way is 4.222 Å, being coherent with the c value of 3.65 nm BTO shown in Figure 6.6a.

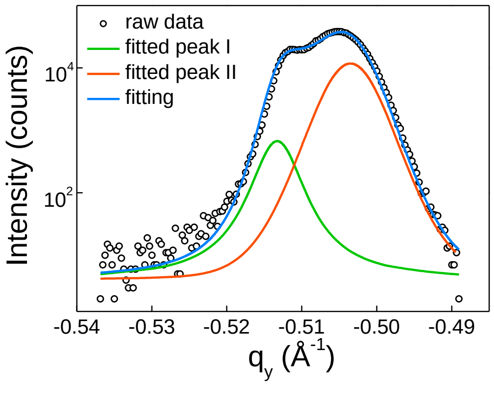

Figure 6.5. Example of pseudo-Voigt fitting for determining lattice parameters. The raw data is from the q_y projection of $(\bar{2}22)$ 2D RSM of 73 nm BTO//STO film.

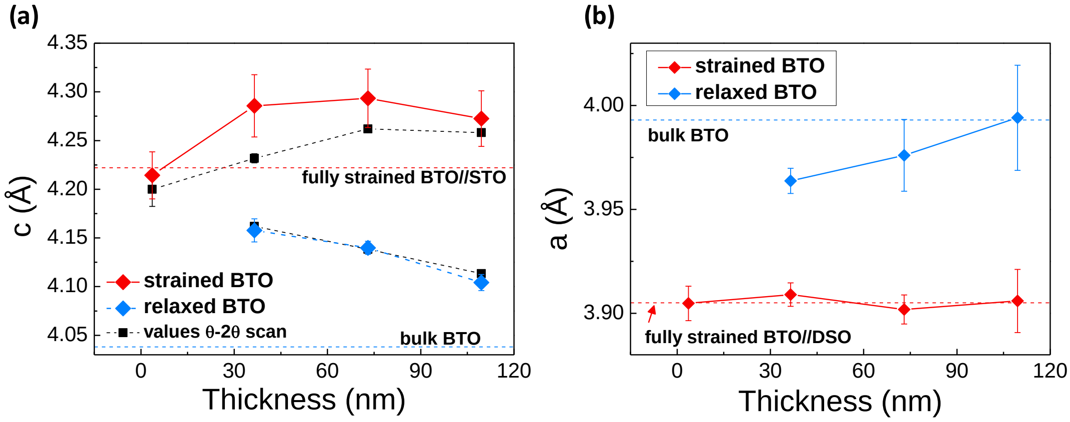

Figure 6.6. Thickness dependence of (a) out-of-plane and (b) in-plane lattice parameters of BTO//STO films fitted from q_z and q_y projections of RSMs, respectively. Points stand for average values of lattice parameters obtained from RSMs of different diffraction planes, and error bars are standard deviations. The red and blue dashed lines mark the lattice parameters of fully strained BTO on STO and bulk BTO, respectively. Lattice parameters extracted from θ-2θ scan in Figure 6.1 are plotted in (a) for comparison.

Interestingly, *c* values of **S** phase are actually larger than the estimated fully strained BTO//STO when $t > t_c$. Similar results were previously found in BTO films especially grown by highly-energetic growth processes such as sputtering[144] and PLD[145]. The mechanism of this anomalous expansion of *c* is still not well understood, but it is generally considered to be correlated with point defects (interstitial atoms and vacancies) in BTO films. These defects are likely introduced by energetic bombardment during deposition[139] due to lattice strain[146]. Regardless details in the mechanism how defects result in the anomalous *c* expansion, it can be conducted that they mainly influence out-of-plane rather than in-plane parameters via comparing Figure 6.6a and 6.8b, which *a* of **S** phase keeps similar value as STO despite of increasing *t*. Additionally, as **R** phase is dominating in the relaxed BTO films (higher intensity of **R** than **S**), *c* of **R** phase should also be partially influenced by the anomalous expansion, which it is definitely the case in 109.5 nm BTO//STO where $a \approx a_{\mathrm{bulk}}$ while $c > c_{\mathrm{bulk}}$.

6.3.2 Lattice parameters comparison between BTO on STO and DSO

Growing epitaxial films on different substrates with various lattice mismatches is a main way to tune the strain states of oxides thin film. In the previous section, we found that the 109.5 nm BTO//STO film is dominated by **R** phase which *a* is fully relaxed. In this section, RSMs obtained from a 109.5 nm BTO//DSO film are studied and compared to the 109.5 nm BTO//STO film grown in the same PLD process. Lattice mismatch between BTO and these two substrates are $f_{\mathrm{STO}} = -2.2\%$ and $f_{\mathrm{DSO}} = -1.2\%$, where negative sign stands for compressive strain.

Figure 6.7 compares q_z-q_y 2D RSM obtained from $(\bar{2}22)$ diffraction of 109.5 nm BTO//STO with the one of 109.5 nm BTO//DSO. Due to the relative high *l* and *h* index, RSM of this reflection is sensitive to difference in both in-plane and out-of-plane strain states. Comparing Figure 6.7a and 6.7b, one can easily notice that the relaxing in BTO//DSO is fainter than in BTO//STO. The **R** phase shows as a small "tail" at the corner of the BTO pattern, indicating the intensity of relaxed phase is not compatible with main part. In-plane parameter of main part of BTO pattern is coherent with DSO, where is the opposite case in BTO//STO. In general, it is found that stained state is better preserved in films epitaxially grown on substrate with smaller lattice mismatch, which was well explained both theoretically and experimentally, as t_c varies approximately inversely with lattice mismatch[136,147-149]. Indeed t_c of BTO//DSO was reported between 50 and 100 nm[149], and ~10 nm in BTO//STO[138].

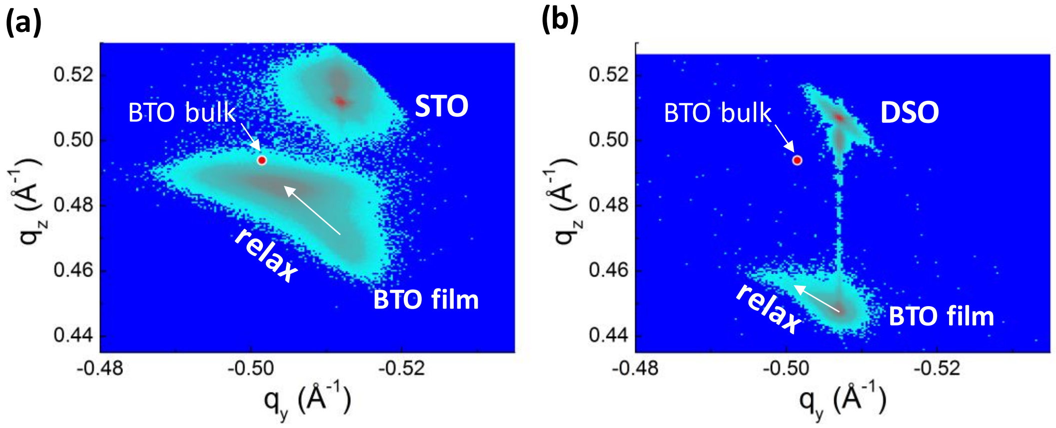

Figure 6.7. (a,b) q_z-q_y projection of RSMs at $(\bar{2}22)$ plane of 109.5 nm-thick BTO//STO and BTO//DSO film, respectively. White arrows guide the view of relaxing direction. Logarithmically intensity increasing is expressed by color transition from blue to cyan to purple and to red.

Quantitative study is carried out and shown in Figure 6.8. The q_y projection of BTO peaks of $(\bar{2}22)$ diffraction of the two BTO films are compared in Figure 6.8a, and averaged a value of $(\bar{2}22)$, $(\bar{1}03)$, $(\bar{3}01)$ and $(\bar{1}11)$ diffractions are plotted in Figure 6.8b. Due to different lattice mismatch, magnitude of anomalous c expansion can be different in BTO//STO and BTO//DSO films, thus out-of-plane parameters are not compared here. In Figure 6.8a, BTO//STO shows very clear one fully strained and one relaxed phase, while in BTO//DSO fully strained phase shapes the peak and relaxed phase only make it asymmetric. Fully relaxed states of **R** phase both in BTO//STO and BTO//DSO film is revealed in Figure 6.8b. However, the proportion of both phases are much difference, as shown in Figure 6.8c. In this figure, we plot the intensity ratio of **S** and **R** to semi-quantitatively express their relative amount in the film. Evidently, **R** phase dominates in BTO//STO while **S** phase overwhelms in BTO//DSO. These studies confirm and enrich the conclusion from qualitative observation in the previous paragraph.

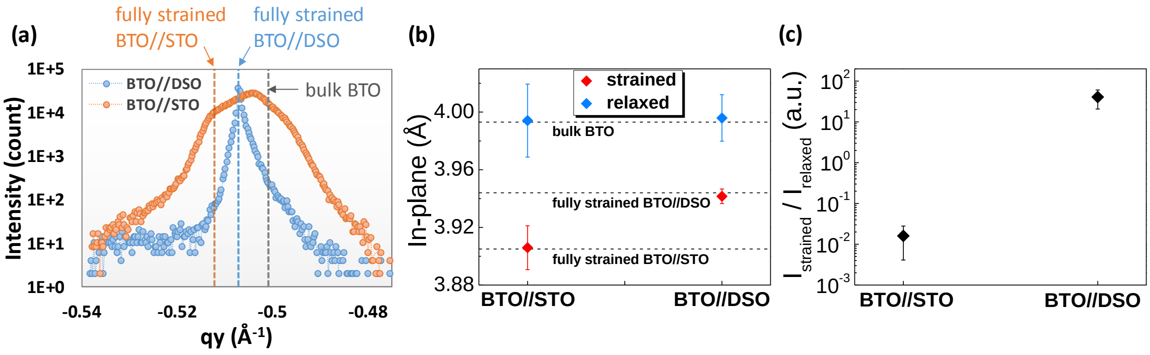

Figure 6.8. Comparison of in-plane lattice parameters between BTO//STO and BTO//DSO with the same 109.5 nm thickness. (a) q_y projection of RSMs at $(\bar{2}22)$ plane with BTO peaks only. Orange and blue dashed lines indicate a values of fully strained

BTO on STO and DSO, respectively. Black dashed line shows the value of bulk BTO. (b) Averaged a value obtained from $(\bar{2}22)$, $(\bar{3}01)$, $(\bar{1}03)$ and $(\bar{1}11)$ diffractions. Three black dashed line marked the fully strained and bulk BTO lattice parameters. (c) Intensity ratio of **S** to **R**. Points are averaged values obtained from diffractions of the four planes.

6.3.3 Thickness distribution of S and R phases in BTO//STO film

It is known from sections above that two strain phases, one fully strained and another partially relaxed, coexist in BTO films under epitaxially compressive strain. Grazing incidence X-ray diffraction (GIXD) is used to study the thickness distribution of the two phases due to it is a surface sensitive structural analysis method. Depth profile of RSM can be built by changing the incident angle in a small range. Experimental setup of GIXD is described in chapter 2, section 2.4.2.

GIXD was performed on $(\bar{2}22)$ plane of 109.5 nm BTO//STO. $(\bar{2}22)$ reflection is selected because it contents the requirement of grazing incidence diffraction geometry and the diffraction intensity is acceptable in limited signal collecting time. Angle η of the goniometer (see Figure 2.20) is set as 0.1°, 0.2°, 0.3°, 0.4°, 0.5° and 0.66° to execute the experiment, proportionally corresponding to real incident angle γ = 0.0762°, 0.152°, 0.228°, 0.305°, 0.381° and 0.503°. See the calculation in chapter 2, section 2.4.2. The following discussion will use η to represent incident angle γ to for simpler digits.

q_y-q_z projections of RSMs with η = 0.1° to 0.66° are shown in Figure 6.9, manifesting both in-plane and out-of-plane parameters. It is worth noting that measurements were done excluding the region of reciprocal space where STO peak appears. In Figure 6.9 f (that with the highest incident angle) clearly shows the intensity coming from **R** (the most intense) and **S** phases of BTO film. As incident angle decreases (and also the penetration length), Figures 6.14a-e, the part of the intensity coming from **S** phase becomes weaker, and is nearly undetectable for η = 0.2° and below (Figures 6.14a,b). It indicates the **S** phase is located deeper in the film and thus closer to the substrate. A similar conclusion can be drawn from q_x-q_y projections included in Appendix, see Figure A-11.

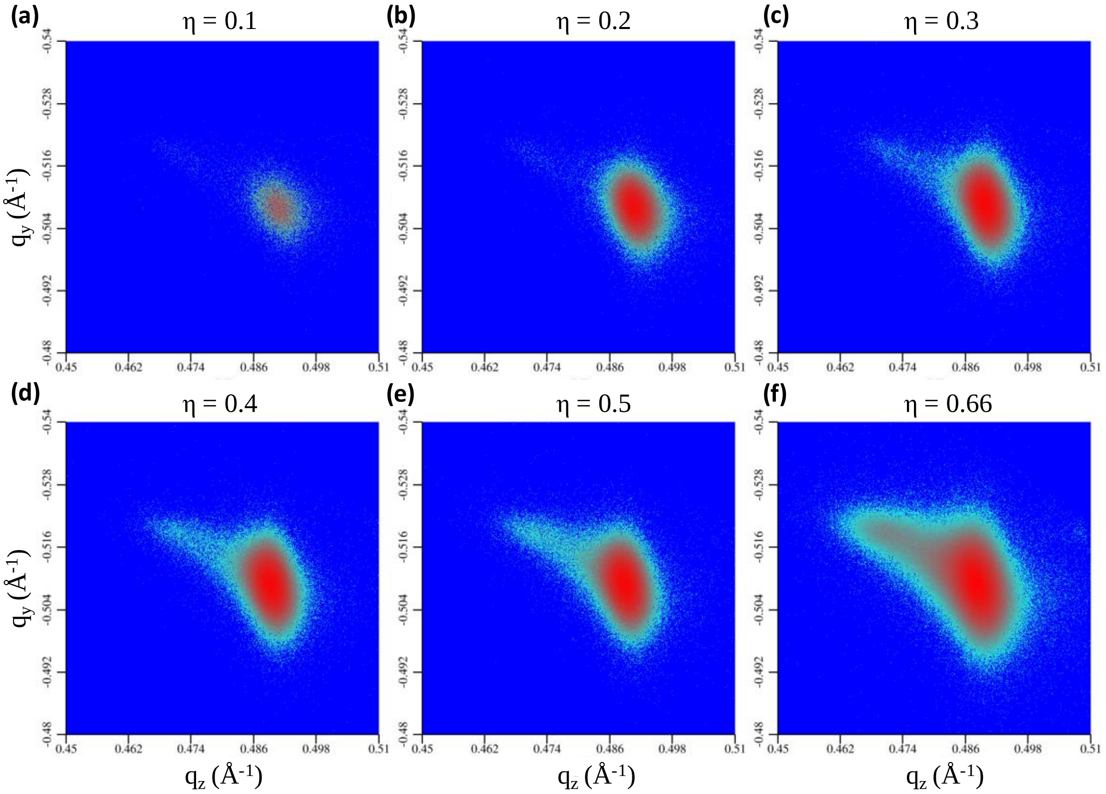

Figure 6.9. q_y-q_z projections of RSMs obtained by GIXD at $(\bar{2}22)$ plane of 109.5 nm-thick BTO//STO film. (a-f) q_z-q_y projected RSMs at different incident angles, with η = 0.1°, 0.2°, 0.3°, 0.4°, 0.5°, 0.66°, respectively. Logarithmically intensity increasing is expressed by color transition from blue to cyan to purple and to red.

This qualitative analysis is somehow insufficient because when lowering the incident angle the part of the incident beam that is fully reflected by sample surface enlarges and the overall intensity diminishes. Quantitative analysis is shown in Figure 6.10. 2D RSM of η = 0.2° to 0.66° are projected to q_z and normalized by the maximum intensity to correct the part of the beam lost due to reflection. We choose q_z rather than q_y because it allows easier identification of the two BTO phases and the corresponding cell parameters as a function of depth. Therefore q_z projection is used to present tendency of depth dependence of lattice parameters, as Figure 6.10a shows. The η = 0.1°

projection is excluded due to its very low intensity resulting in a noisy q_z projection. Pseudo-Voigt fitting similar as Figure 6.5 were performed on q_z projection and depth dependence (η dependence) of intensity ratio of **S** to **R** is plotted in Figure 6.10b. The increasing tendency of the ratio corroborates the thickness distribution of two phases observed. Additionally, c values plotted in Figure 6.10c shows a depth dependence strain gradient. In summary, strained BTO phase is distributed closer to the substrate while relaxed phase locates closer to the surface with a strain gradient, as the sketch shown in Figure 6.10d.

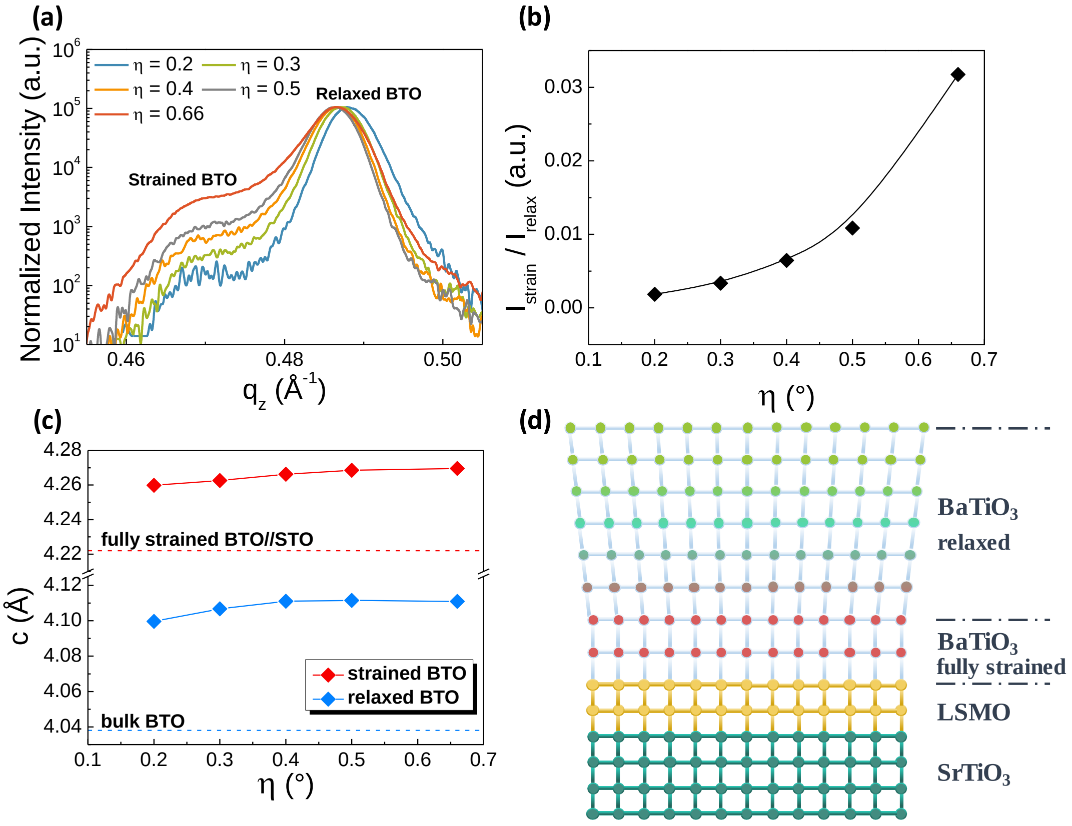

Figure 6.10. Variation of stain states along with the increasing of incident angle in grazing incidence diffraction on $(\bar{2}22)$ of 109.5 nm BTO//STO film. (a) q_z projection of RSMs obtained with incident geometry η = 0.2°, 0.3°, 0.4°, 0.5°, 0.66°, respectively. Intensity in logarithmic scale is normalized at the maximum value. The curve of η = 0.1° is absence due to its low intensity. (b) Intensity ratio of the strained to relaxed BTO phase at various η values. A spline curve is drawn to guide the view. (c) Variation of c along with η increasing. Lattice parameters of fully strained and bulk BTO are shown

as a red and blue dashed line respectively. (d) Sketch of thickness distribution of **S** and **R** phases in BTO film.

6.3.4 Temperature dependence of lattice parameters of BTO//STO and BTO//DSO

Curie temperature (T_c) of ferroelectric epitaxial films are strongly correlated with strain state[150]. Researchers have built models to predict the T_c enhancement of $BaTiO_3$ thin films under large biaxial strains ($|\varepsilon| > 0.4\%$) in both compressive and tensile condition using Landau thermodynamic theories[136,151]. As two different strain states coexist in BTO films, it is expected that different T_c should exist. Thus distinctive signature of T_c should be visible in the temperature (T) dependence of lattice parameters of these two phases. RSMs of 109.5 nm BTO//STO and 109.5 nm BTO//DSO were built on $(\bar{2}22)$ diffraction from room temperature (RT) up to 750°C. a and c were determined by fitting BTO peaks in projections of RSMs on q_y and q_z, and their T dependences were plotted in Figure 6.11. In Figure 6.11a,c, in-plane parameters as a function of T of both **S** or **R** phase shows similar slope as the substrate and no clear sign of phase transition is observed. The slopes of **S** and **R** are 4.5×10^{-3} pm·K^{-1}, 4.4×10^{-3} pm·K^{-1} for BTO//STO and 3.0×10^{-3} pm·K^{-1}, 3.1×10^{-3} pm·K^{-1} for BTO//DSO, which is close to measured slope of STO (4.1×10^{-3} pm·K^{-1}) and DSO (2.7×10^{-3} pm·K^{-1}). Meanwhile, measured a slope of STO and DSO are coherent to their reported thermal expansion properties at this T range[152,153], demonstrating good temperature control in our experimental setup. This phenomenon indicates the in-plane BTO lattice is confined by biaxial strain up to high T, i.e. clamped by the substrate, being coherent with previous research[136,139]. In contrast, the phase transition is well visible in out-of-plane direction, as shown in Figure 6.11b,d. Additionally, slopes of c extracted from low T linear region are quite different from those of substrates (2.6×10^{-3} pm·K^{-1}, 2.8×10^{-3} pm·K^{-1} for **S** and **R** of BTO//STO compare to 3.5×10^{-3} pm·K^{-1} for STO; 8.4×10^{-3} pm·K^{-1}, 8.1×10^{-3} pm·K^{-1} for **S** and **R** of BTO//DSO compare to 6.0×10^{-3} pm·K^{-1} for DSO), implying the independence of out-of-plane parameters of BTO.

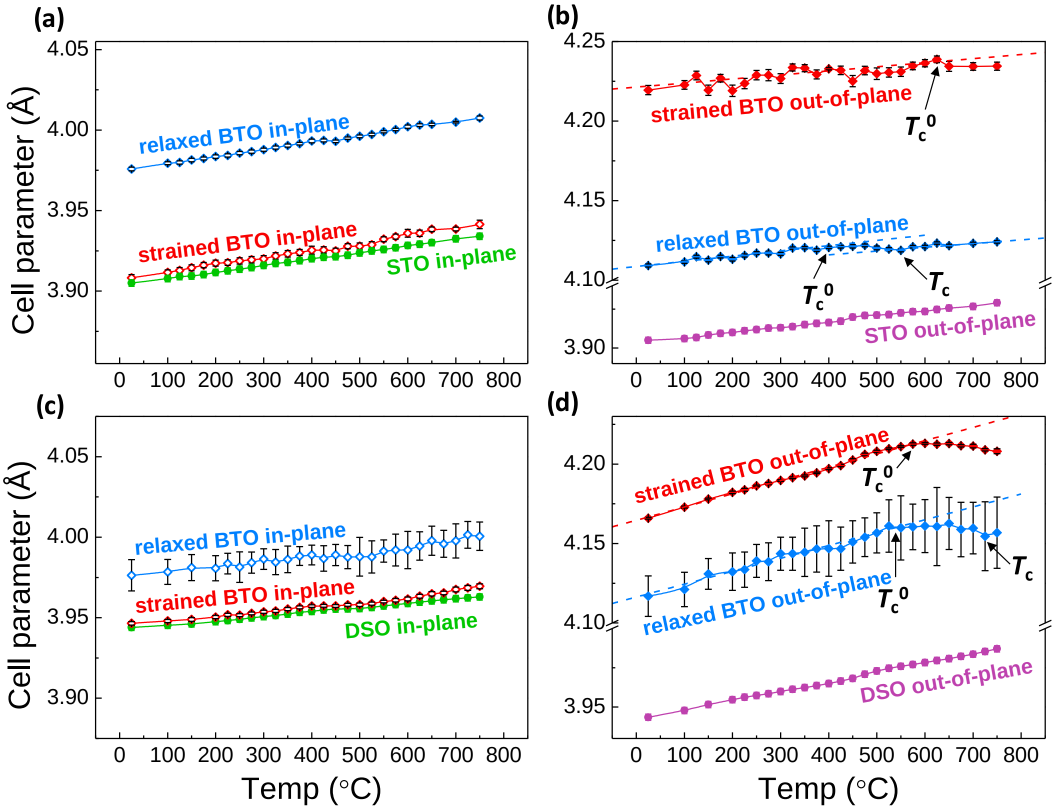

Figure 6.11. Temperature dependence of lattice parameters of 109.5 nm BTO//STO and BTO//DSO. (a,b) *a* and *c* values of BTO//STO. (c,d) *a* and *c* values of BTO//DSO. Error bars are fitting deviations of lattice parameters. Axes of “Cell parameters” between (a) and (b), (c) and (d) are tuned to the same scale for a better perspective to compare (exclude the range of break scales). Dashed lines in (b) and (d) are fitting of the curves in linear ranges for better determining the slope changing. T_c^0 and T_c are starting and finishing temperature of phase transition.

Inspection of data in Figure 6.11b shows that T_c of BTO//STO is 550°C for **R** but the phase transition of **S** just starts at 650°C and not finished up to 750°C, thus T_c of it is even higher. Similar behavior is observed in T_c of BTO//DSO (Figure 6.11d), where T_c of **R** is ~725°C but not finished until 750°C for **S**. Considering the in-plane parameters shown in Figure 6.8b, **S** phases are fully strained and **R** phases are fully relaxed in these two films. As biaxial in-plane strain is defined by $\varepsilon = (a_{\parallel} - a_0)/a_0$, where $a_{\parallel}$ is in-plane lattice parameter under biaxial strained – equivalent to *a* of the substrate in fully strained phase, and a_0 is the lattice parameter of the ferroelectric material in its cubic state under stress-free conditions (free-standing)[154]. Here we use a_0 = 4.008 Å considering the volume of tetragonal (a = 3.993 Å, c = 4.038 Å) and cubic BTO are the same, which is very similar as reported experimental and theoretical values[155,156]. Thus $\varepsilon_{STO}^{strained} \approx -2.6\%$, $\varepsilon_{DSO}^{strained} \approx -1.6\%$ and $\varepsilon_{STO}^{relaxed} = \varepsilon_{DSO}^{relaxed} \approx -0.4\%$. Comparing with theoretically expected T_c considering biaxial in-plane strain only[136,151], T_c of **S** can be reasonable but that of **R** is much higher than expected. As reported experimental T_c > 800°C in BTO due to coupling of epitaxial strain and defect dipoles[139], we use $c_{exp} - c_{bulk}$ to express the whole c expansion including contributions from biaxial strain and defects, where c_{exp} and c_{bulk} are measured value and bulk BTO value at RT. c_{exp}, $c_{exp} - c_{bulk}$ and T_c^0 are listed in Table 6.1.

	c_{exp} (Å)	$c_{exp} - c_{bulk}$ (Å)	T_c^0 (°C)
BTO//STO (S)	4.273	0.235	600
BTO//STO (*R*)	4.104	0.066	400
BTO//DSO (S)*	4.221	0.183	575
BTO//DSO (*R*)*	4.131	0.t093	525

Table 6.1. Out-of-plane lattice parameters of strained and relaxed phases of 109.5 nm BTO//STO and BTO//DSO at room temperature. Starting temperatures of phase transition are also listed.

*Data extracted from q_z projection of RSM displayed in Figure 6.7b.

We plot T_c^0 vs. $c_{exp} - c_{bulk}$ in Figure 6.12 from data in Table 6.1. This figure suggests that T_c increases along with the whole c expanding. In summary, different T_c of BTO with two strain states are observed and tuned by biaxial strain and anomalous c expansion together.

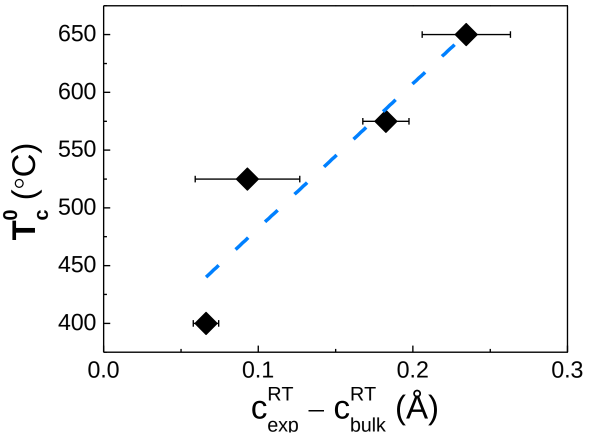

Figure 6.12. Starting temperature of phase transition T_c^0 vs. the c expansion $c_{exp} - c_{bulk}$ at room temperature. Blue dashed line is the linear fitting of data points.

6.4 Conclusion

In this work, a series of $BaTiO_3$ thin films on different substrates and with different thickness are studied by synchrotron radiation X-ray diffraction. Regions of the films with two different strain states are identified, that one fully strained and another partially relaxed coexisting in BTO films thicker than t_c. The relaxed BTO phase gradually evolve with thickness and reaches the fully relaxed state at ~110 nm, while fully strained phase keeps constant. Comparing BTO//STO and BTO//DSO with same thickness (~110 nm) reveals relaxed BTO is dominating in film with larger lattice mismatch (BTO//STO), while the overwhelming phase is fully strained BTO in the film with smaller lattice mismatch (BTO//DSO), in agreement with earlier reports. Anomalous expansion of out-of-plane parameters not caused by biaxial strain are observed in all relaxed BTO films. A depth profile of reciprocal space maps of the ~110 nm BTO//STO are obtained by grazing incidence diffraction. Relaxed phase is found distributed closer to upper surface of BTO and strained phase locates closer to the substrate (and buffer layer). Temperature dependence of lattice parameters are measured to determine T_c of strained and relaxed phases in BTO//STO and BTO//DSO. Results show that in-plane lattice is clamped by the substrate from room temperature to 750°C, and phase transition shows up only in out-of-plane parameters. T_c of both fully strained and fully relaxed phases are much higher than bulk BTO, which is enhanced by both biaxial strain and anomalous *c* expansion possibly caused by defects. These microstructural details of $BaTiO_3$ thin films found by high resolution X-ray diffraction thanks to synchrotron radiation enriched the cognition of stain states and relaxing process in $BaTiO_3$ thin films, and can be helpful to understand novel physical properties in multilayer oxides system.

Chapter 7. Influence of ammonia treatment on ferroelectric, photoresponse and optic properties of $BaTiO_3$ thin films

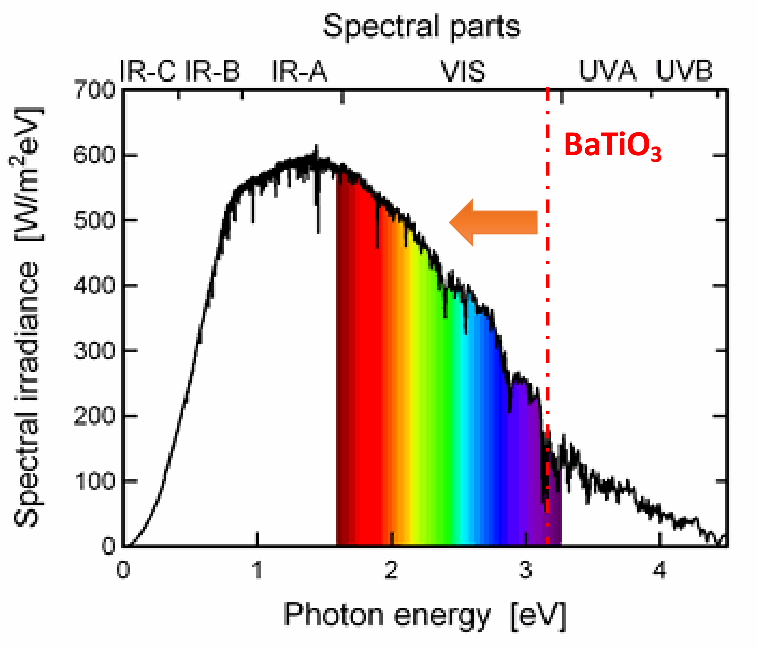

*This chapter contains a description of a work in progess. Motivation, materials used and results are presented, detailed discussions and analysis are not performed.

7.1 Motivation and introduction

Photoelectric effects on $BaTiO_3$ thin films and various controlling/influencing factors are detailed studied in the previous chapters. The use of blue laser with 3.06 eV photon energy, which is slightly smaller the band-gap (E_{bg}) of BTO (3.3 eV[54]), as it has been described in previous chapters, can results in sizable photocurrent. It is agreed that in this case photocharges are originated from excitation of impurity levels in BTO[6-8] near conduction band. However, no effect is observed with light source of 2.3 eV or smaller photo energy. As far as cirque 50% sun spectrum falls under 2.3 eV, it is required to lower the band-gap to make the photoresponses more efficient. Simultaneously, ferroelectric nature of BTO should be preserved because the bipolar states provide distinguishable properties than dielectric materials, such as controlling photocurrents by polarization as discussed in Chapter 4, and enhancing photoelectric effects.

Nitrogen doping has been proved to be an effective method to narrow the band-gap of wide band-gap oxides like ZnO[157] (E_{bg} = 3.3 eV), TiO[158,159] (E_{bg} = 3.2 eV) and BTO[160] (E_{bg} = 3.3 eV) due to the lower N electronegativity compared with O. Two different procedures are used for N doping. One is to directly control raw materials in the process of preparation, such as tuning precursors in sol-solvothermal process[159], sputtering in a N_2 atmosphere[161]. The second is to perform post-preparation treatment, e.g. annealing together with urea[160], annealing in the flow of ammonia[157,158,160,162,163], annealing precursors ($BaTiO_{2.5}H_{0.5}$) in N_2 gas flow[164]. In this chapter, ammonia (NH_3) annealing is employed to attempt BTO N doping.

7.2 Materials

Two sets of of BTO films are prepared by PLD. In the first set, BTO/LSMO bilayers are deposited on two 5 × 10 mm^2 STO(001) substrate simultaneously in a single PLD process. After depositing, the two pieces of BTO/LSMO//STO films are cut into 8 pieces of 2.5 × 5 mm^2 samples. One of them is set as the reference sample (Ref), the other 7 samples are annealed in NH_3 gas flow subsequently (N2 – N8) and Pt electrodes on them are sputtered afterwards. In the second branch, to avoid the influence of variation in properties of LSMO layer during NH_3 annealing, conductive Nb doped STO(001) crystal (Nb:STO) is selected as the substrate, and single BTO layers are deposited on two 5 × 5 mm^2 substrates simultaneously in a single PLD process. Then they are cut into 4 pieces of 2.5 × 5 mm^2 films. 3 of them are subjected to NH_3 annealing (N9 – N11) and compared with the remaining reference piece (Ref_2). Also Pt electrodes on N9 – N11 for measurement are grown after NH_3 annealing. All BTO films have uniform nominal thickness of ~109.5 nm and LSMO layer of ~30 nm in the case of BTO/LSMO//STO samples. During NH_3 annealing 3 parameters are modified: annealing temperature T_a, annealing time t_a and volume flow rate of NH_3 Q. Experimental details of NH_3 annealing is described in Chapter 2. Summary of the characterized samples are shown in Figure 7.1. Additionally, a single layer of BTO (109.5nm) on STO and a single layer of LSMO (30 nm) on STO are also deposited for comparison with BTO/LSMO//STO multi-layers. Moreover, two control experiments are performed, one is annealing a piece of STO single crystal in NH_3 flow to check its change in transmittance and another is annealing a ~109.5 BTO/LSMO//STO film in N_2 flow for testing the possible influence from oxygen vacancies generation.

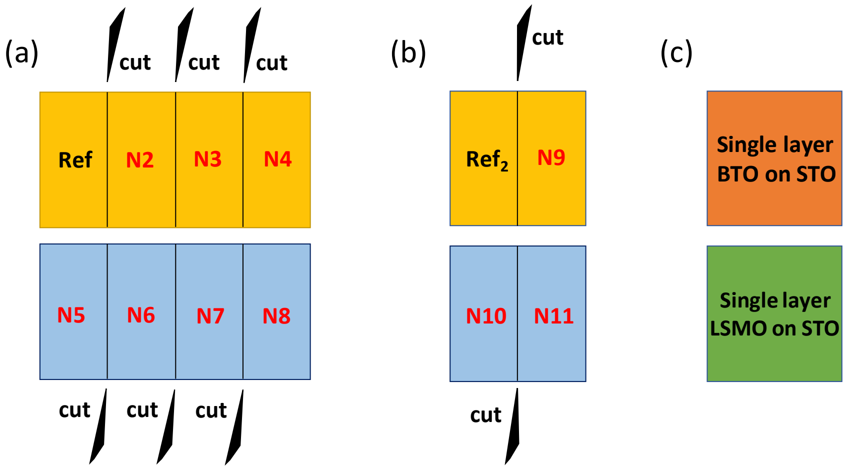

Figure 7.1. Drawing of samples grown by PLD and how they are cut and numbered. (a) BTO/LSMO//STO samples. (b) BTO//Nb:STO samples. (c) Single layer of BTO on STO and single layer of LSMO on STO.

7.3 Results and discussion

7.3.1 Influence of NH_3 annealing on the polarization of BTO

NH_3 annealing conditions of sample N2 – N8 are listed in Table 7.1 XPS and XRD 2θ scan analysis were firstly performed after annealing and results are shown in Figure 7.2 and Figure 7.3.

Sample	T_a (°C)	t_a (hour)	Q ($cm^3 \cdot min^{-1}$)	J_{sw} ($A \cdot cm^{-2}$)
Ref	No annealing			6.03
N2	500	4	600	0
N3	400	4	600	5.03
N4	450	4	600	2.93
N5	450	8	1000	0
N6	450	8	600	1.48
N7	450	2	1000	0.85
N8	450	4	1000	0
single layer BTO	450	8	1000	N/A
single layer LSMO	450	8	1000	N/A

Table 7.1. Column 2-4: NH_3 annealing parameters of all treated samples. Column 5: magnitude of ferroelectric switching current extracted from *J-E* loops, where "0" means it is not able to pick up a J_{sw} from *J-E* loop since ferroelectric switching is weak. N/A means not applicable.

In Figure 7.2, one can find that N peaks show very weak intensity. That indicates the amount of N in all samples is low. Peak at about E_b = 400 eV is clearly observed in spectra of all annealed samples and even visible in the as grown sample, which is related to chemisorbed nitrogen on the surface (γ-N_2)[161,165,166]. Another peak located at E_b = 396 – 397 eV that is only detected in samples N4 and N5. This lower energy peak is the feature of N atoms doping BTO and substituting O atoms in the lattice (β-N)[161,165-167].

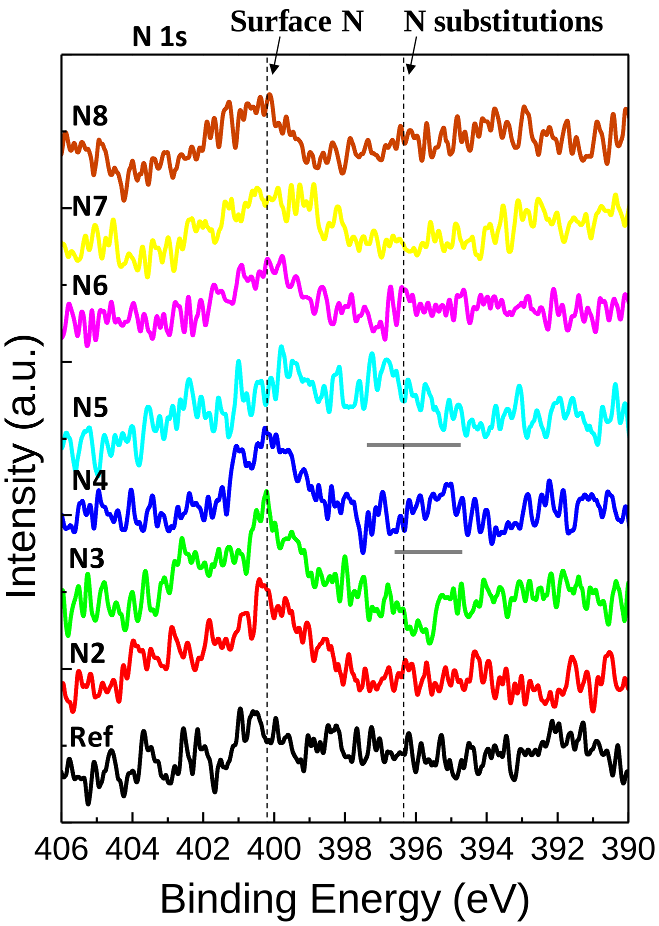

Figure 7.2. XPS N1s spectra of all BTO/LSMO//STO samples. Position of peaks for N in surface adsorbents and in BTO that substitutes O are marked.

XRD 2θ scan were performed on each sample before and after NH_3 annealing and are shown in Figure 7.3. In each spectrum of Figure 7.3 we can observe two BTO peaks representing the strained and relaxed phases in BTO that are discussed in Chapter 6, peak of STO and LSMO. Very small variations in both intensity and 2θ position of BTO peaks, and in dramatic decreasing in intensity of LSMO peaks is found except sample N3 and N4. Variation of BTO and LSMO peaks can be further verified by similar XRD spectra recorded before and after NH_3 annealing of single layer BTO/LSMO on STO, as Figure 7.4 shows. These results indicate that the microstructure (lattice parameters) of BTO does not change at all, while LSMO encounters striking modification thought the process of NH_3 annealing.

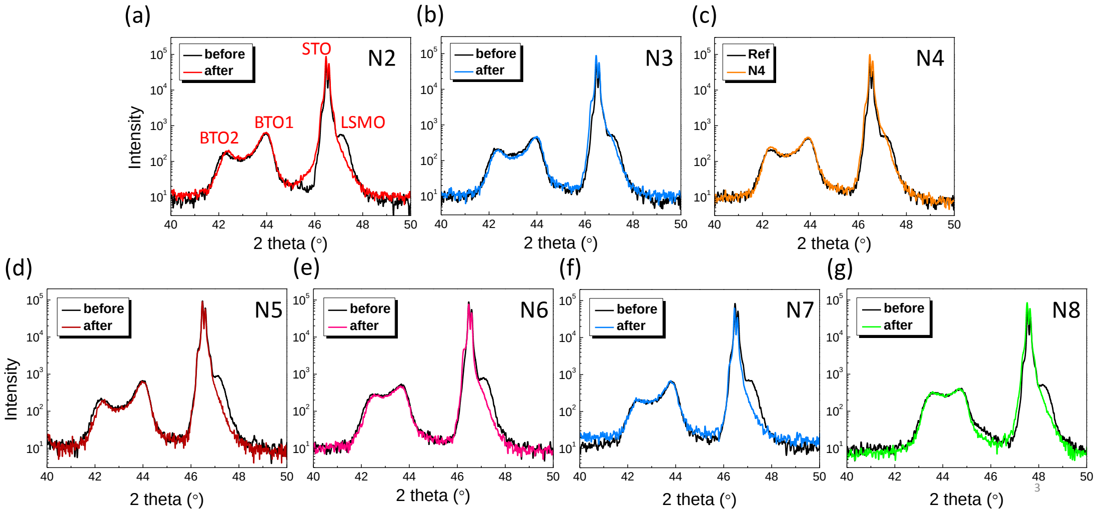

Figure 7.3. (a-g) XRD 2θ scan spectra comparison before and after NH_3 annealing of sample N2 – N8. Peaks of strained and relaxed BTO, STO substrate and LSMO layer are annotated in (a).

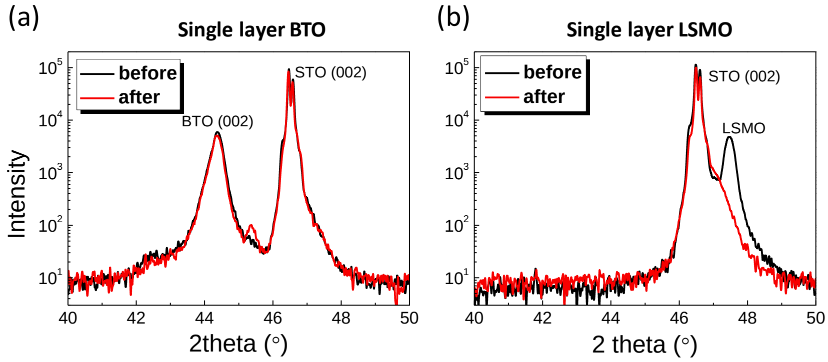

Figure 7.4. XRD 2θ scan spectrum of (a) single layer BTO on STO and (b) single layer LSMO on STO recorded before and after NH_3 annealing.

J-E Ferroelectric hysteresis loops in *t-t* configuration before and after NH_3 treatment are measured and results are shown in Figure 7.5. *J-E* loops are shown instead of *P-E* loops because large leakage current appears after NH_3 annealing, which produce misleading *P-E* loop. Important differences are shown while comparing different samples, reflecting high sensitivity of measurable ferroelectrics to the NH_3 annealing condition. In table 7.1 we list the average (positive and negative branch) peak magnitude of ferroelectric switching current J_{sw} for quantitative analysis.

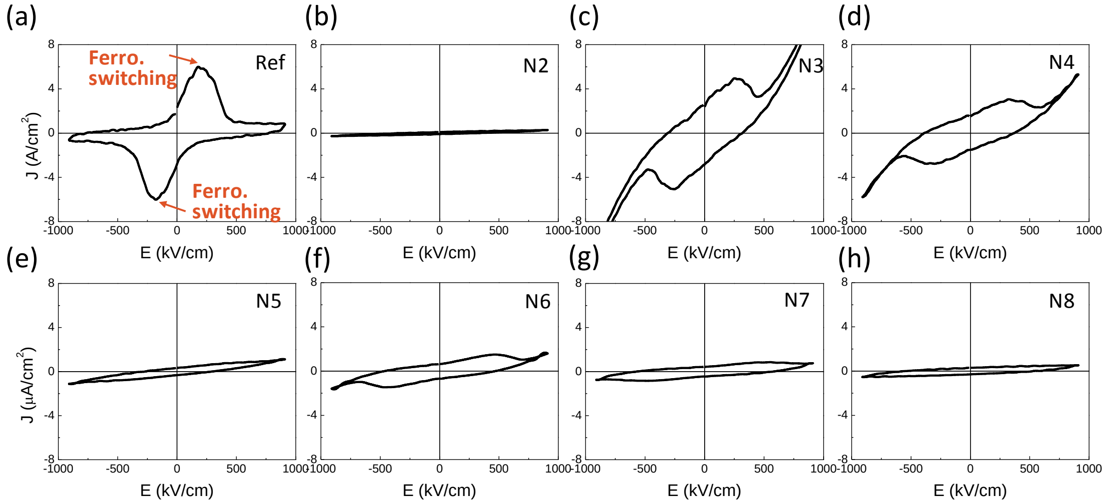

Figure 7.5. (a-h) *J-E* loops of sample Ref and N2 – N8 after NH_3 annealing. Loops are recorded at the frequency of 10 kHz, *t-t* configuration. The positions where J_{sw} is picked are marked in (a), and values of J_{sw} listed in Table 7.1 are the average of absolute values of J_{sw} at positive and negative branches.

From careful inspection of data obtained in Table 7.1 we can conclude that:

a) Increasing T_a, J_{sw} decreases. Comparing N2, N3 and N4 those annealed at the same t_a and Q. Actually, N2, N3 and N4 are the first three treated samples, and the results of ferroelectric measurement and XPS analysis shows that 450°C is the optimal T_a, as ferroelectrics remains and substitute N shows up. Then N5-N8 are all annealed at 450°C.

b) Increasing t_a, J_{sw} decreases. Comparing N5, N7 and N8 those annealed at the same T_a and Q.

c) Increasing Q, J_{sw} decreases. Comparing N4 and N8 those annealed at the same T_a and t_a.

Thus, after NH_3 treatment, in all cases ferroelectrics is partially vanished.

In Figure 7.6 we show the short-circuit photocurrent J_p in *t*-*t* configuration after positive or negative prepolarization, using the methodology described in Chapter 4. Here we collect J_p under blue laser (3.06 eV) illumination and with τ_{light} = 10 s (delay between prepolarization and J_p measuring) of all 8 BTO/LSMO//STO samples.

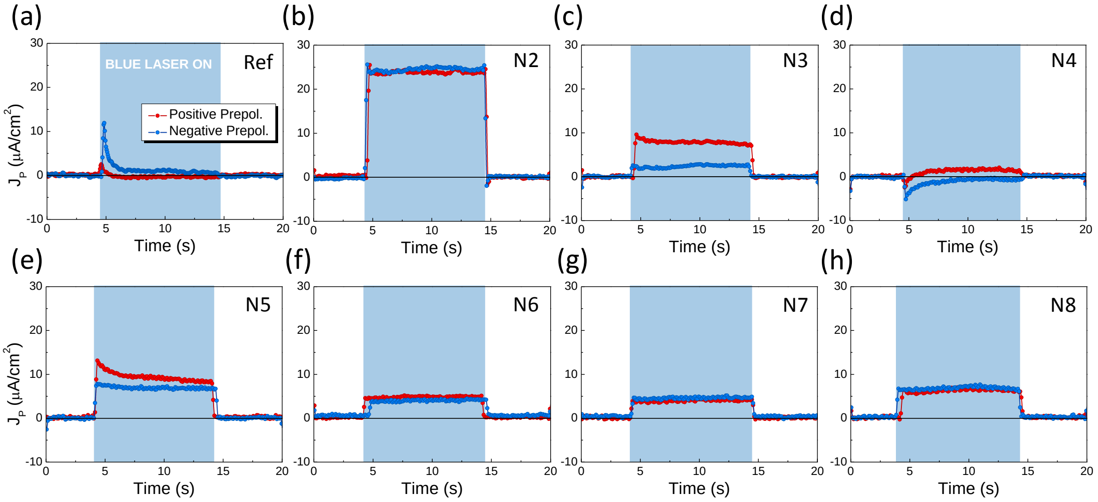

Figure 7.6. (a-h) Short-circuit photocurrent recorded after τ_{light} = 10 s delay of prepolarization. The period of laser on is colored in light blue background. Red and navy curves represent J_p after positive and negative prepolarization, respectively.

$\Delta J_p = J_p^{max+} - J_p^{max-}$ reflects the effect of switchable polarization (Chapter 4), which is the divergence of maximum of J_p after positive and negative prepolarization, therefore it is an indirect measurement of the P.

In Figure 7.7, we summarize the J_{sw} and ΔJ_p values obtained for samples annealed (N2 – N4) with the same t_a and Q but different T_a. Both J_{sw} and ΔJ_p decrease along with T_a increasing. N6 is also included, and it was annealed at the same T_a and Q as N4 but double the t_a, resulting in smaller J_{sw} and ΔJ_p than those of N4. ΔJ_p vs. J_{sw} is also plotted in Figure 7.7b, showing a positive correlation. These results show that the presence of switchable polarization is essential to obtain switchable J_{sw}. N5, N7 and N8 are not discussed due to different Q of annealing and very small J_{sw}.

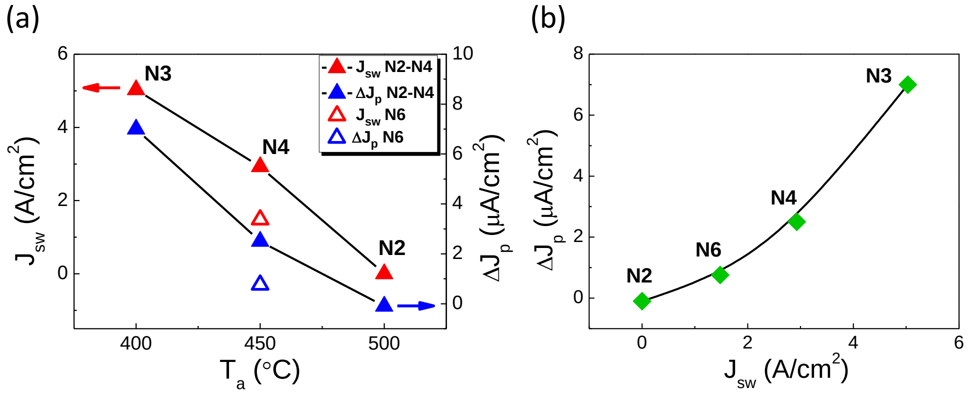

Figure 7.7. (a) Annealing temperature T_a dependence of J_{sw} and ΔJ_p. Values of sample N2-N4 are plotted as solid triangles and connected to show the tendency, while N6 is shown as hollow triangle to compare with N4. (b) Relationship between ΔJ_p and J_{sw} of sample N2-N4 and N6. Black curve is plotted to guide the view.

7.3.2 Influence of NH_3 annealing on band-gap of BTO

Figure 7.8a shows transmittance spectra for all BTO/LSMO//STO samples. It can be observed that transmittance of all sample gradually decrease from 800 to 400 nm, and abruptly decay to zero transmittance from 400 to 380 nm. All annealed samples have smaller transmittance (T%) than Ref sample at the range $\lambda = 800 - 400$ nm. However, considering the huge difference in thickness between BTO film (~100 nm) and STO (0.5 mm), any small variation from STO would make importantly contribute to the total measured T%. To distinguish the contribution of BTO film and STO substrate to transmittance spectra, a piece of STO single crystal was annealed in a more severe condition than any BTO samples: $T_a = 450°C$, $t_a = 12$ h and $Q = 1000\ cm^{-3}\cdot min^{-1}$ and its transmittance spectrum was measured before and after annealing. Results plotted in Figure 7.8b shows no variation after annealing and a similar abruptly decay at 400 – 380 nm. This fact reveals the reduced transmittance at $\lambda = 400 - 800$ of BTO/LSMO//STO samples after annealing is due to the change of BTO, and the decay at $\lambda = 400 - 380$ nm is mainly contributed by STO substrate. Additionally, transmittance spectrum obtained by placing BTO side or STO side towards the measuring light beam shows no difference, which the surface roughness of these two sides are different, indicating the influence of reflection on T% is negligible. Therefore, T% reduction of annealed samples should be attributed to enhancement of adsorption.

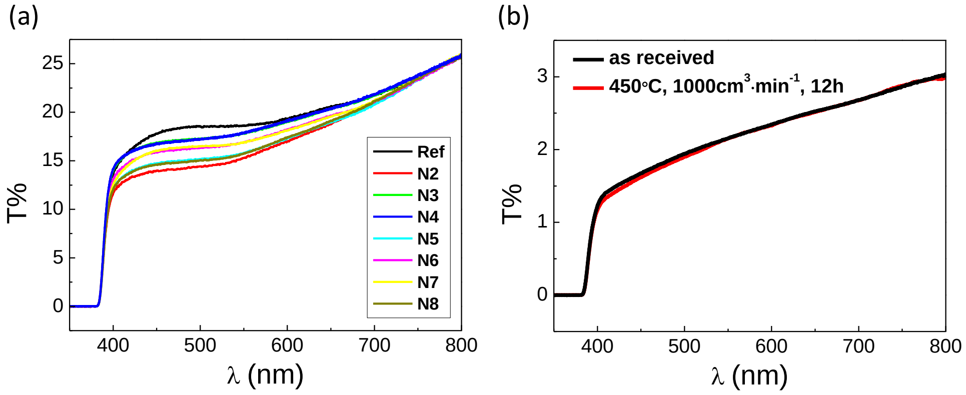

Figure 7.8. (a) Transmittance spectra of all BTO/LSMO//STO samples at the range of visible light. (b) Transmittance spectrum of STO single crystal measured before (black) and after (red) NH_3 annealing.

I-V curves under laser light with identical power density arranging from blue to red, λ = 405, 450, 520 and 638 nm, are measured in *b*-*t*, and shown in Figure 7.9. Both conductivity under illumination and magnitude of short-circuit photocurrent (intercept on y axis) are dramatically enhanced in annealed samples. Interestingly all annealed samples show response at 638 nm (1.94 eV), demonstrating critical exciting photon energy is reduced by NH_3 annealing. Short-circuit photocurrent (J_{sc}) are extracted and listed in Figure 7.10a. One can also observe that the sign of J_{sc} also changed in the annealed sample.

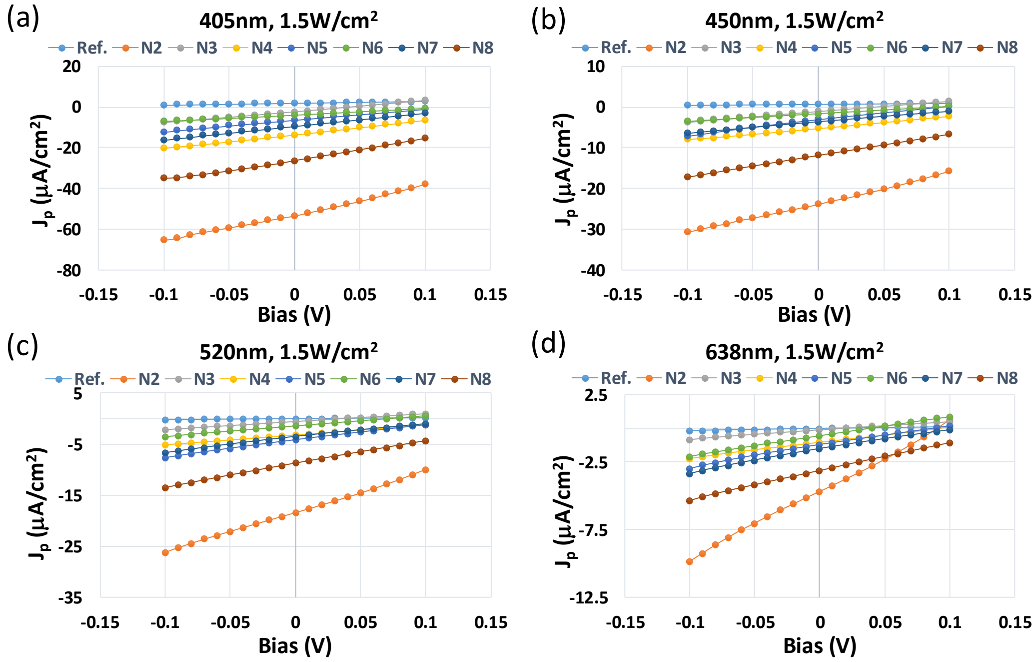

Figure 7.9. I-V curves of all BTO/LSMO//STO samples measured in *b-t* under laser illumination with 1.5 W·cm-2 power density, at $\lambda = 405$ nm (a), 450 nm (b), 520 nm (c) and 638 nm (d) respectively.

From the discussion in Chapter 4, we learnt internal electric field E_{int} in BTO drives J_{sc} and consists of imprint E_{imp} which is intrinsic and depolarization field E_{dep} which is proportional to P:

$$E_{\text{int}} = E_{\text{imp}} + E_{\text{dep}} = E_{\text{imp}} + \alpha P \tag{7.1}$$

where α is the ratio of unscreened polarization. As E_{imp} is always pointing from LSMO towards Pt in our BTO films, in *b-t* configuration P remains the same direction as E_{imp} in the case without external electric field applied. Thus E_{dep} always points the opposite direction to E_{imp}. Then the sign of E_{int} is decided by the larger one between E_{imp} and E_{dep}. In as-grown BTO film, E_{dep} is larger than E_{imp} in most cases as Chapter 4 shows, leading to “positive” J_{sc} in the definition of our experimental setup, as Figure 7.10b manifests. However, P is dramatically suppressed by NH_3 annealing process, resulting in the decrease of E_{dep} and dominating role of E_{imp} in E_{int}. Accordingly, J_{sc} changes the sign in NH_3 annealed samples as Figure 7.10c sketches. Evidently, if E_{imp} is assumed to be constant during NH_3 annealing, E_{int} will be larger as P decreases, leading to larger J_{sc}.

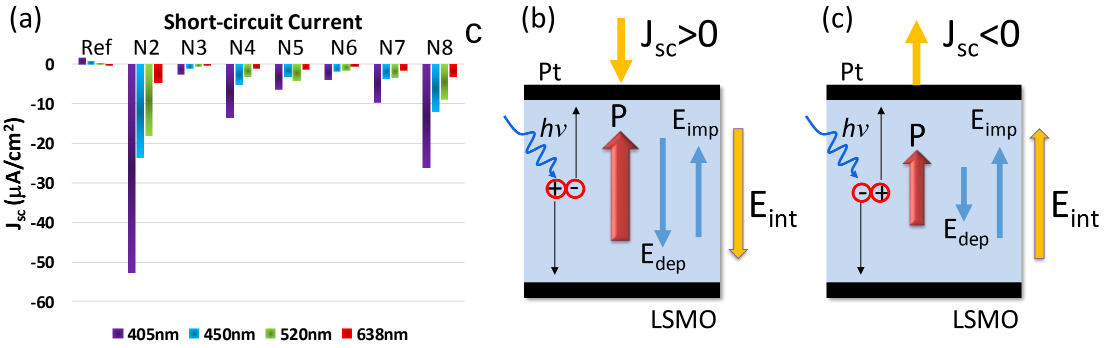

Figure 7.10. (a) J_{sc} extracted from Figure 7.9. (b,c) Sketch of distribution on internal electric field and sign of J_{sc} in Ref sample and NH_3 annealed samples, respectively.

7.3.3 Influence of N_2 annealing on BTO

Annealing in the atmosphere lack of oxygen can cause the creation of oxygen vacancies in ferroelectric perovskite[168,169], and they could induce doping levels in the band gap of BTO, leading to evident variations in the electrical and optical properties of BTO[10,170]. To verify the influence of possible created oxygen vacancies on N doping, polarization and band-gap modification in NH_3 annealing process, a BTO/LSMO//STO sample is deposited in the same condition and thickness as sample Ref and N2 – N8. It is annealed in N_2 flow with $T_a = 450°C$, $t_a = 8$ h and $Q = 1000$ cm^3·min^{-1}, the same as N5. XRD 2θ scan, XPS analysis, transmittance spectroscopy and ferroelectric characterization are performed before and after annealing or compared with sample Ref, plotted in Figure 7.11. Firstly, XRD 2θ scan shows a slightly decrease in intensity of relaxed BTO phase after N_2 annealing, but peak positions of both strained and relaxed phases do not vary at all. Then, in XPS N1s spectrum of N_2 annealed BTO, only a weak peak representing N in surface adsorbent appears, similar as sample Ref. Additionally, two completely overlapped transmittance spectra are recorded before and after N_2 annealing. Furthermore, constant P_{max} detected in P-E loops in Figure 7.11d means same amount of switchable polarization, only coercive field varies after N_2 annealing. In summary,

N_2 annealing and possible created oxygen vacancies does not exert critical influence on key properties of BTO. It infers properties' variation caused by NH_3 annealing is mainly due to factors other than oxygen vacancies.

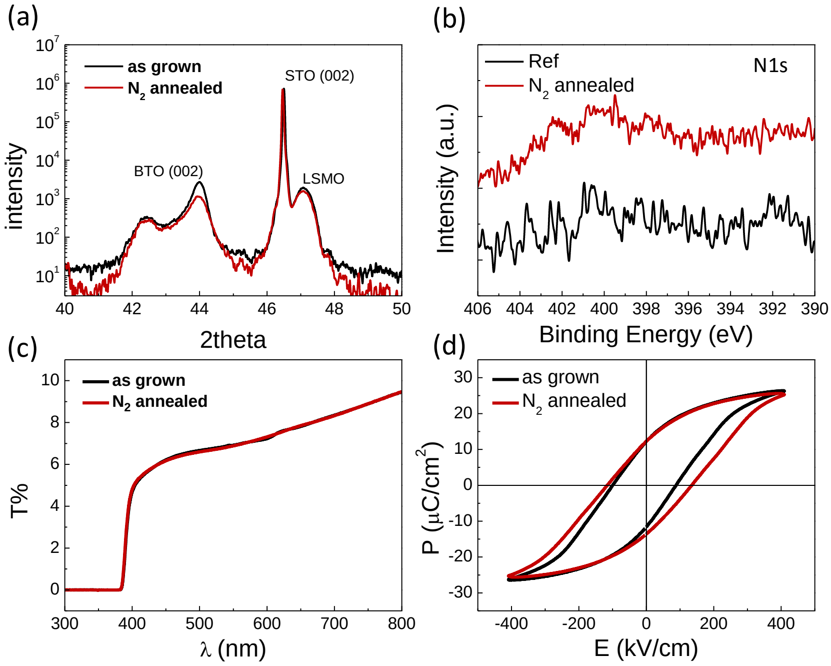

Figure 7.11. Properties' variations of BTO caused by N_2 annealing. (a) Structure. XRD 2θ scan spectrum. (b) Surface chemical state. XPS N1s spectrum measured after N_2 annealing and compare with that of sample Ref. (c) Band-gap. Transmittance spectrum. (d) Ferroelectrics. *P*-*E* loop recorded in *t*-*t* at frequency of 2 kHz.

7.3.4 NH_3 annealing on BTO//Nb:STO samples

In NH_3 annealing experiments on BTO/LSMO//STO samples, LSMO is found encountering dramatic structural variation. Further analysis reveals the fact that the resistivity of LSMO increases up to 4 order of magnitude (see Figure 7.12a). Although it is still much smaller than that of BTO (see Figure 7.12b) and may not influence the measurement of ferroelectric loops, it is possible to introduce unexpected contribution to other characterization.

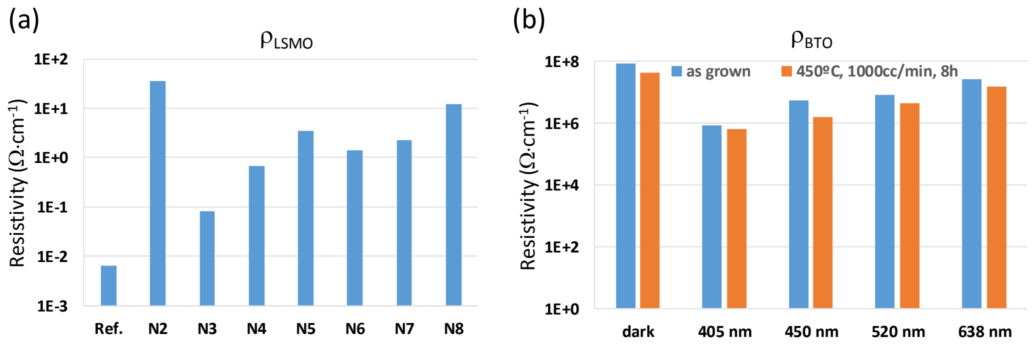

Figure 7.12. Resistivity measured by van der Pauw method. (a) ρ of sample Ref and N2 – N8. (b) ρ of BTO thin film in dark and under 4 λ laser illumination. Measured before and after NH_3 annealing for $T_a = 450°C$, $t_a = 8$ h and $Q = 1000$ cm^3·min^{-1}

To avoid these interference, study on NH_3 annealing of BTO on Nb:STO are executed. Annealing parameters are listed in Table 7.2.

Sample	T_a (°C)	t_a (hour)	Q (cm^3·min^{-1})
N9	450	8	1000
N10	450	4	1000
N11	450	12	1000

Table 7.2. NH_3 annealing parameters of BTO//Nb:STO samples.

XRD 2θ scan and XPS analysis are performed firstly. As sample N2 – N9, very few structural variations after NH_3 annealing can observed from XRD spectra in Figure 7.13. From XPS N1s spectra displayed in Figure 7.14, the peak of N in surface adsorbents is clearly seen and keeps almost constant after NH_3 annealing. Nothing appears at range E_B = 396 – 398 eV where the peak of substitute N located, however a weak peak at ~394 eV appears in N11, which further investigation is needed to disclose its chemical state.

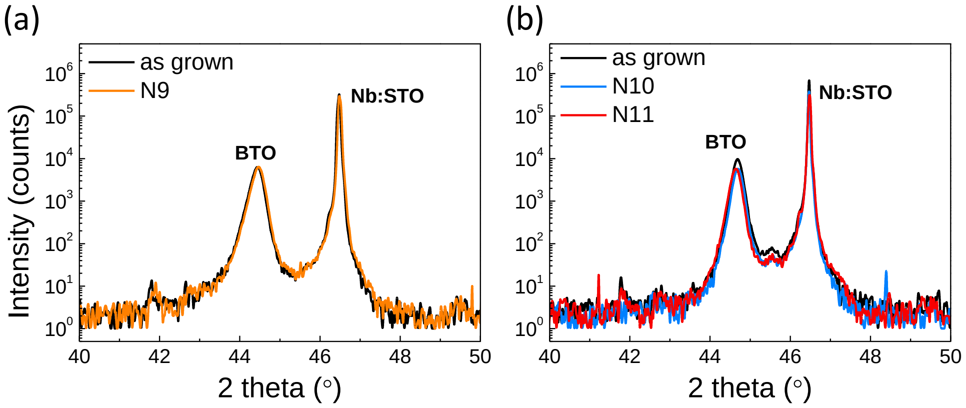

Figure 7.13. (a,b)XRD 2θ scan of sample N9 – N11 before and after NH_3 annealing.

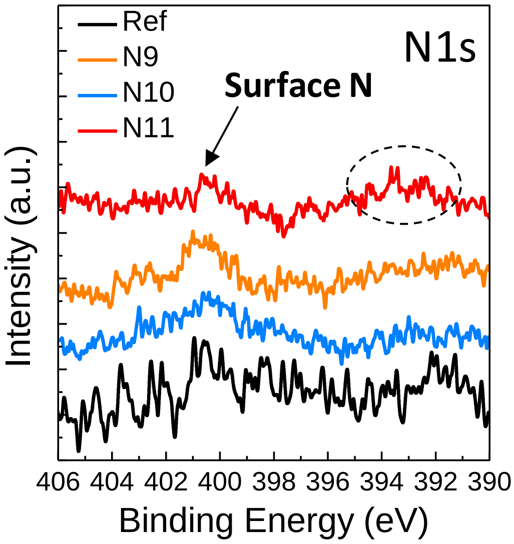

Figure 7.14. XPS N1s spectra of sample N9 – N11 after NH_3 annealing, and comparing with sample Ref. Position of N in surface adsorbent is marked and an emerging peak on the spectrum of N11 is annotated by the dashed oval.

J-E loops are measured to characterize the ferroelectric properties. However, Nb:STO seems to be a bottom electrode cannot provide enough charges to screen ferroelectric polarization of BTO, and non visible switching peaks in *J-E* loops are shown in Figure 7.15. Thus it is difficult to characterize the variation of switchable polarization after NH_3 annealing. The only visible change in *J-E* loops is the leakage current, which increases after annealing.

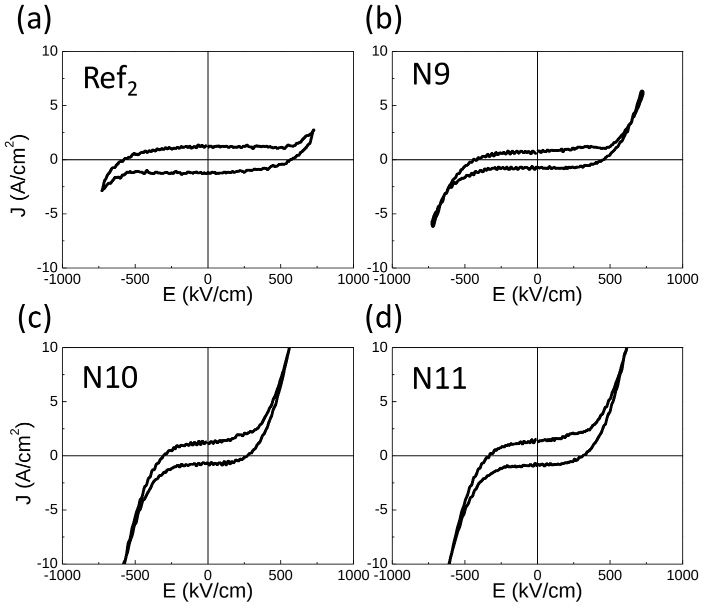

Figure 7.15. *J-E* loops of sample Ref$_2$ (a) and N9 – N11 after NH$_3$ annealing (b-d), recorded in *t-t* at frequency of 10 kHz.

Transportation property analysis is applied under illumination to obtain the information of exciting photon energy of BTO. *I-V* curves in Figure 7.16 shows only sample N11 that is annealed for the longest time presents evidently increased photoconductivity, others keep almost constant comparing with Ref$_2$. And enhancement of J_{sc} is only detected in the case of under 405 nm laser illumination. These behaviors are quite different from BTO/LSMO//STO samples annealed in same conditions. Further investigation is strongly required to clarify the difference of BTO grown on STO or Nb:STO and the role of LSMO in this solid-gas reacted NH$_3$ annealing process.

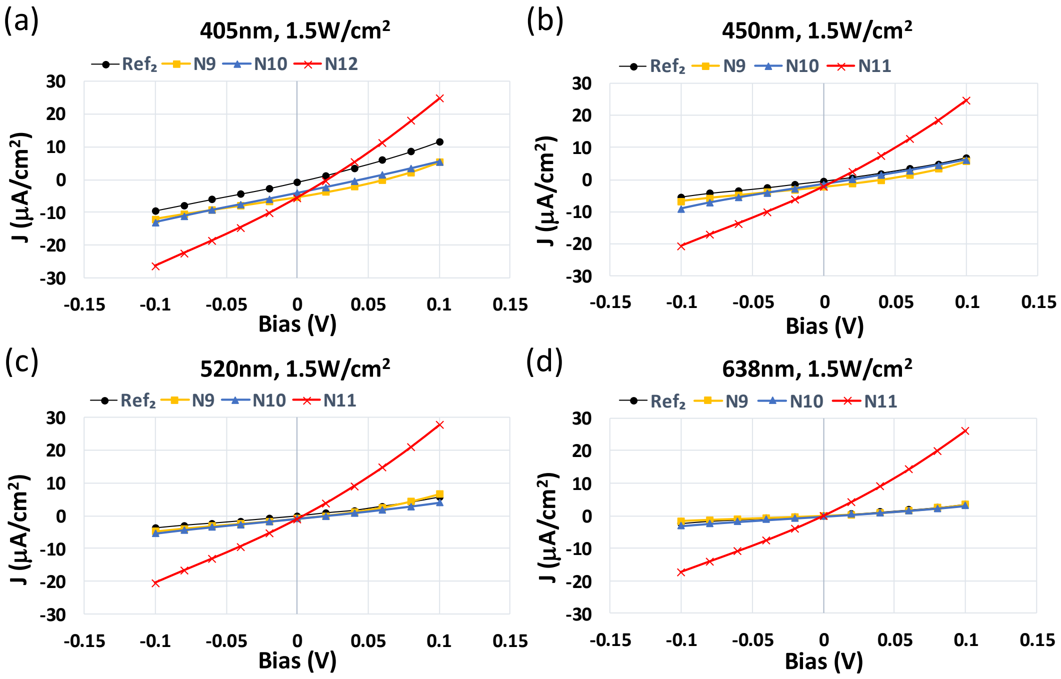

Figure 7.16. (a-d) *I-V* curves measured in b-t and under illumination of laser light with λ = 405, 450, 520 and 638 nm respectively. Power density of lasers are tuned to identical.

7.4 Conclusion

BTO/LSMO//STO thin films have been annealed in NH_3 gas flow at relative low temperature to dope N into the lattice of BTO and preserve ferroelectricity simultaneously. These goals are achieved at optimized annealing conditions: $T_a = 450$°C, $t_a = 4$ h and $Q = 600$ cm^3·min^{-1}, with reduced P but tunable short-circuit photocurrents, peak of substitute N appearing in XPS spectrum, enhanced capability to absorb visible light and drastically increased photoconductivity. All other NH_3 annealed samples encounter the decrease of P, increase of visible light absorption and photoconductivity. Control experiment with similar BTO film annealed in N_2 gas flow shows no evident variation took place in P, XPS spectrum and visible light absorption, indicating no important contribution from oxygen vacancies in the results of NH_3 annealing. BTO grown on Nb:STO substrate does not show measurable ferroelectrics so no conclusion can be drawn.

Chapter 8. General Conclusion

This thesis aims to reveal factors influencing the photoelectric effects in $BaTiO_3$ thin films and attempts to control them. Short-circuit photocurrents J_{sc} and polarization photoscreening ΔP_r (reduced remanent polarization under illumination) are the main photoelectric effects studied in this thesis.

The main purpose of the first work is to understand how E_{imp} behaves in top-top electrode configuration. By careful comparison of loops recorded at different frequencies, the existence of E_{imp} is verified. In top-top configuration, it shows up as double switching peaks only at high frequency due to short life time of head-to-head/tail-to-tail polarization configuration. With the aid of internal screening by photocarriers excited by proper illumination, this life time is prolonged and make it possible to access the double switching at lower frequency.

With the knowledge of how E_{imp} behaves in *t-t* and conventional *b-t* configuration, we tested J_{sc} and ΔP_r in both cases. Steady J_{sc}, $\Delta P_r = 0$ in *b-t* and transient J_{sc}, $\Delta P_r > 0$ in *t-t* under are observed under blue laser illumination. Through characterizing retention behavior and corresponding J_{sc}, it is found that depolarization field E_{dep} is always the driving force of J_{sc} while the direction of P_r is related with E_{imp}, where E_{imp} constrained the direction of P_r in *b-t* but cancelled out in t-t hence allowing switchable P_r. Photoscreening behavior in *t-t* is explained by two Pt/BTO Schottky barriers rather than one Schottky Pt/BTO and one ohmic BTO/LSMO interface of *b-t*. Thus transient J_{sc} due to photoscreening and steady J_{sc} representing the flow of photocharges in the circuit are obtained in *t-t* and *b-t* respectively.

The next challenge we encountered is that ΔP_r of *t-t* varies strikingly among BTO films with different thickness or grown on different substrates, with magnitude from ≈ 0% to more than 70%. Structural study by XRD and surface chemical analysis by XPS point that H_2O/OH^- absorbed on the surface of $BaTiO_3$ is the direct factor influencing the photoscreening. Actively introducing H_2O/OH^- by *steam-treatment* is proved to an effective method to enhance the adsorption of H_2O/OH^- so do ΔP_r. However, the thickness dependence of intrinsic H_2O/OH^- adsorbing capability suggests possible correlation with strain state of $BaTiO_3$.

Consequently, an independent study of strain state and relaxation of $BaTiO_3$ thin film was performed synchrotron X-ray diffraction. Reciprocal space maps of $BaTiO_3$ thin films with various thickness and deposited on $SrTiO_3$ or $DyScO_3$ substrate were built. GIXD was also employed to create the depth profile of lattice parameters. Results reveals two strain states coexist in $BaTiO_3$ and the relaxed phase locates closer to the surface while the strained phase is closer to the substrate. Temperature dependence of lattice parameters obtained by heating samples from RT to 750°C detected different T_c of the two phases, and both are larger than T_c of bulk $BaTiO_3$ with the contribution from biaxial strain and anomalous c expansion together.

Post-deposition NH_3 annealing was performed on $BaTiO_3$ films. Surface chemicals, transmittance spectroscopies and transportation properties under illumination were measured to test the effect. After annealing, P is suppressed but light absorption and J_{sc} are enhanced, and exciting wavelength of BTO is extend from 405 nm to 638 nm. By optimizing annealing parameters, both evidently narrowed band-gap and tunable J_{sc} owing to preserved bipolar states are obtained in $BaTiO_3$ thin film.

Summarily, E_{imp}, E_{dep}, electrode/BTO interface, surface states as influencing factors, electrode configuration, steam-treatment and NH_3 annealing as tuning or controlling methods are researched for understanding the photoresponses of $BaTiO_3$ thin films, which mainly refer to short-circuit photocurrents and photoscreening. Stain state of BTO can be considered as an independent study in this thesis, however, it helps building a comprehensive understanding of $BaTiO_3$ thin film and provides fundamentals for untangling the profound correlation between microstructure and photoresponses in the future. At the end, a mind map is created to help understanding the logic among contents in the whole thesis.

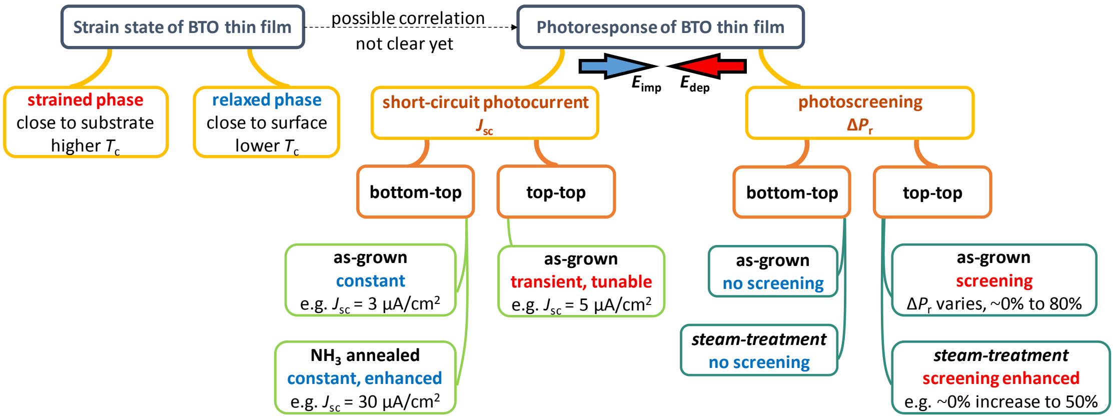

Figure 8.1. Mind map showing logic among research contents in the thesis.

Reference

1 Pintilie, L., Vrejoiu, I., Hesse, D. & Alexe, M. The influence of the top-contact metal on the ferroelectric properties of epitaxial ferroelectric $Pb(Zr_{0.2}Ti_{0.8})O_3$ thin films. *Journal of Applied Physics* **104**, 114101 (2008).

2 Gutierrez Yatacue, D. F. Electrical properties of $BaTiO_3$, $CoFe_2O_4$ and $La_{1/2}(Ca,Sr)_{1/2}MnO_3$ thin films and their importance for active barriers in tunnel transport. *PhD thesis*, Universitat Autònoma de Barcelona (2014).

3 GmbH, a. S. User Manual of TF Analyzer 2000.

4 Meyer, R., Waser, R., Prume, K., Schmitz, T. & Tiedke, S. Dynamic leakage current compensation in ferroelectric thin-film capacitor structures. *Applied Physics Letters* **86**, 142907 (2005).

5 Wemple, S. Polarization Fluctuations and the Optical-Absorption Edge in $BaTiO_3$. *Phys. Rev. B* **2**, 2679 (1970).

6 Laguta, V. V. *et al.* Electron spin resonance investigation of oxygen-vacancy-related defects in $BaTiO_3$ thin films. *Applied Physics Letters* **87**, 022903 (2005).

7 Moreira, M. L. *et al.* Photoluminescence of Barium Titanate and Barium Zirconate in Multilayer Disordered. *The Journal of Physical Chemistry A* **112** (2008).

8 Choi, M., Oba, F. & Tanaka, I. Electronic and structural properties of the oxygen vacancy in $BaTiO_3$. *Applied Physics Letters* **98**, 172901 (2011).

9 Chang, J. Y., Garrett, M. H., Jenssen, H. P. & Warde, C. Intensity dependent absorption/transparency of a reducing $BaTiO_3$. *Applied Physics Letters* **63**, 3598-3600 (1993).

10 Zhao, T. *et al.* Electrical and optical properties of strongly reduced epitaxial $BaTiO_{3-x}$ thin films. *Applied Physics Letters* **77**, 4338 (2000).

11 Pauw, L. J. V. d. A Method of Measuring Specific Resistivity and HALL Effect of Discs of Arbitrary Shape. *Philips Research Reports* **13**, 9 (1958).

12 O'Neill, D., Bowman, R. M. & Gregg, J. M. Dielectric enhancement and Maxwell–Wagner effects in ferroelectric superlattice structures. *Applied Physics Letters* **77**, 1520-1522 (2000).

13 Lunkenheimer, P. *et al.* Origin of apparent colossal dielectric constants. *Physical Review B* **66** (2002).

14 Pintilie, L., Vrejoiu, I., Hesse, D., LeRhun, G. & Alexe, M. Extrinsic contributions to the apparent thickness dependence of the dielectric constant in epitaxial $Pb(Zr,Ti)O_3$ thin films. *Physical Review B* **75**, 224113 (2007).

15 Langenberg, E. *et al.* Dielectric properties of $(Bi_{0.9}La_{0.1})_2NiMnO_6$ thin films:

Determining the intrinsic electric and magnetoelectric response. *Physical Review B* **86**, 085108 (2012).

16 Schmidt, R. *et al.* Magnetoimpedance spectroscopy of epitaxial multiferroic thin films. *Physical Review B* **86**, 035113 (2012).

17 Gutierrez, D., Foerster, M., Fina, I. & Fontcuberta, J. Dielectric response of epitaxially strained CoFe2O4 spinel thin films. *Physical Review B* **86**,125309 (2012).

18 Li, W., Auciello, O., Premnath, R. N. & Kabius, B. Giant dielectric constant dominated by Maxwell-Wagner relaxation in Al_2O_3/TiO_2 nanolaminates synthesized by atomic layer deposition. *Applied Physics Letters* **96**, 162907 (2010).

19 Hüfner, S. Photoelectron Spectroscopy. *Springer-Verlag*, Berlin, Germany (2003).

20 Wang, J. Modifications of the chemical and electronic ferroelectric surface structure under water adsorption. *PhD thesis*, Universit´e Pierre et Marie Curie - Paris VI (2013).

21 Physical Electronics. https://www.phi.com/surface-analysis-techniques/xps-esca.html.

22 CasaXPS. www.casaxps.com.

23 Wu, Q. A nanoscale study of MOSFETs reliability and Resistive Switching in RRAM devices. *PhD thesis*, Universitat Autònoma de Barcelona (2017).

24 Többens, D. M. & Zander, S. KMC-2: an X-ray beamline with dedicated diffraction and XAS endstations at BESSY II. *Journal of large-scale research facilities JLSRF* **2**, 65 (2016).

25 KMC-2 Manual. https://www.helmholtz-berlin.de/pubbin/igama_output?modus=datei&did=284. (2006).

26 Scott, J. F. Applications of modern ferroelectrics. *Science* **315**, 954-959, 1129564 (2007).

27 Scott, J. F. & Paz de Araujo, C. A. Ferroelectric Memories. *Science* **246**, 1400-1405 (1989).

28 Trolier-McKinstry, S. & Muralt, P. Thin Film Piezoelectrics for MEMS. *Journal of Electroceramics* **12**, 11 (2004).

29 Tsymbal, E. Y. & Kohlstedt, H. Tunneling Across a Ferroelectric. *Science* **313**, 181-183 (2006).

30 Maksymovych, P. *et al.* Polarization Control of Electron Tunneling into Ferroelectric Surfaces. *Science* **324**, 1421-1425 (2009).

31 Garcia, V. *et al.* Giant tunnel electroresistance for non-destructive readout of

ferroelectric states. *Nature* **460**, 81-84 (2009).

32 Chanthbouala, A. *et al.* Solid-state memories based on ferroelectric tunnel junctions. *Nat Nano* **7**, 101-104 (2012).

33 Garcia, V. & Bibes, M. Ferroelectric tunnel junctions for information storage and processing. *Nature communications* **5**, 4289 (2014).

34 Barrionuevo, D. *et al.* Tunneling electroresistance in multiferroic hetero-structures. *Nanotechnology* **25**, 495203 (2014).

35 Yang, S. Y. *et al.* Above-bandgap voltages from ferroelectric photovoltaic devices. *Nat Nano* **5**, 143-147 (2010).

36 Kundys, B., Viret, M., Colson, D. & Kundys, D. O. Light-induced size changes in $BiFeO_3$ crystals. *Nature materials* **9**, 803-805 (2010).

37 Alexe, M. & Hesse, D. Tip-enhanced photovoltaic effects in bismuth ferrite. *Nature communications* **2**, 256 (2011).

38 Bhatnagar, A., Roy Chaudhuri, A., Heon Kim, Y., Hesse, D. & Alexe, M. Role of domain walls in the abnormal photovoltaic effect in $BiFeO_3$. *Nature communications* **4**, 2835 (2013).

39 Tagantsev, A. K. & Gerra, G. Interface-induced phenomena in polarization response of ferroelectric thin films. *Journal of Applied Physics* **100**, 051607 (2006).

40 Brody, P. S. & Rod, B. J. Decay of remanent polarization in ferroelectric films using polarization-dependent photovoltages. *Integrated Ferroelectrics* **3**, 245-257 (1993).

41 Ji, W., Yao, K. & Liang, Y. C. Bulk photovoltaic effect at visible wavelength in epitaxial ferroelectric $BiFeO_3$ thin films. *Advanced materials* **22**, 1763-1766 (2010).

42 Pintilie, L., Stancu, V., Vasile, E. & Pintilie, I. About the complex relation between short-circuit photocurrent, imprint and polarization in ferroelectric thin films. *Journal of Applied Physics* **107**, 114111 (2010).

43 Zhang, J. *et al.* Enlarging photovoltaic effect: combination of classic photoelectric and ferroelectric photovoltaic effects. *Scientific reports* **3**, 2109 (2013).

44 Yang, Y. S. *et al.* Schottky barrier effects in the photocurrent of sol-gel derived lead zirconate titanate thin film capacitors. *Applied Physics Letters* **76**, 774 (2000).

45 Qin, M., Yao, K. & Liang, Y. C. Photovoltaic mechanisms in ferroelectric thin films with the effects of the electrodes and interfaces. *Applied Physics Letters* **95**, 022912 (2009).

46 Liu, F. *et al.* Selecting Steady and Transient Photocurrent Response in $BaTiO_3$ Films. *Advanced Electronic Materials* **1**, 201500171 (2015).

47 Zhou, Y., Chan, H. K., Lam, C. H. & Shin, F. G. Mechanisms of imprint effect on ferroelectric thin films. *Journal of Applied Physics* **98**, 024111 (2005).

48 Koval, V., Viola, G. & Tan, Y. in Ferroelectric Materials - Synthesis and Characterization, Ch. 09. *InTech*, (2015).

49 Rault, J. E. *et al.* Interface electronic structure in a metal/ferroelectric heterostructure under applied bias. *Physical Review B* **87**, 155146 (2013).

50 Evans, J. T. & Cardoza, H. E. The imprint mechanism in ferroelectric capacitors. *Integrated Ferroelectrics* **10**, 267-277, (1995).

51 Cui, B. *et al.* Magnetoelectric Coupling Induced by Interfacial Orbital Reconstruction. *Advanced materials* **27**, 6651-6656 (2015).

52 Radaelli, G. *et al.* Large Room-Temperature Electroresistance in Dual-Modulated Ferroelectric Tunnel Barriers. *Advanced materials* **27**, 2602-2607 (2015).

53 Wurfel, P. & Batra, I. P. Depolarization-Field-Induced Instability in Thin Ferroelectric Films—Experiment and Theory. *Physical Review B* **8**, 5126-5133 (1973).

54 Wemple, S. Polarization Fluctuations and the Optical-Absorption Edge in $BaTiO_3$. *Physical Review B* **2**, 2679-2689 (1970).

55 Wang, J. L., Vilquin, B. & Barrett, N. Screening of ferroelectric domains on $BaTiO_3$(001) surface by ultraviolet photo-induced charge and dissociative water adsorption. *Applied Physics Letters* **101**, 092902 (2012).

56 Mehta, R. R. Depolarization fields in thin ferroelectric films. *Journal of Applied Physics* **44**, 3379 (1973).

57 Kreisel, J., Alexe, M. & Thomas, P. A. A photoferroelectric material is more than the sum of its parts. *Nature materials* **11**, 260 (2012).

58 Choi, T., Lee, S., Choi, Y. J., Kiryukhin, V. & Cheong, S.-W. Switchable Ferroelectric Diode and Photovoltaic Effect in $BiFeO_3$. *Science* **324**, 63-66 (2009).

59 Yang, S. Y. *et al.* Photovoltaic effects in $BiFeO_3$. *Applied Physics Letters* **95**, 062909 (2009).

60 Yi, H. T., Choi, T., Choi, S. G., Oh, Y. S. & Cheong, S. W. Mechanism of the switchable photovoltaic effect in ferroelectric $BiFeO_3$. *Advanced materials* **23**, 3403-3407 (2011).

61 Lee, D. *et al.* Polarity control of carrier injection at ferroelectric/metal interfaces for electrically switchable diode and photovoltaic effects. *Physical Review B* **84**,

125305 (2011).

62 Won, C. J., Park, Y. A., Lee, K. D., Ryu, H. Y. & Hur, N. Diode and photocurrent effect in ferroelectric $BaTiO_{3-\delta}$. *Journal of Applied Physics* **109**, 084108 (2011).

63 Park, Y. A., Sung, K. D., Won, C. J., Jung, J. H. & Hur, N. Bipolar resistance switching and photocurrent in a $BaTiO_{3-\delta}$ thin film. *Journal of Applied Physics* **114**, 094101 (2013).

64 Boerasu, I., Pintilie, L., Pereira, M., Vasilevskiy, M. I. & Gomes, M. J. M. Competition between ferroelectric and semiconductor properties in $Pb(Zr_{0.65}Ti_{0.35})O_3$ thin films deposited by sol-gel. *Journal of Applied Physics* **93**, 4776-4783 (2003).

65 Fridkin, V. M. Photoferroelectrics. *Springer-Verlag*, Berlin Heidelberg (1979).

66 Qin, M., Yao, K. & Liang, Y. C. High efficient photovoltaics in nanoscaled ferroelectric thin films. *Applied Physics Letters* **93**, 122904 (2008).

67 Qin, M., Yao, K., Liang, Y. C. & Shannigrahi, S. Thickness effects on photoinduced current in ferroelectric $(Pb_{0.97}La_{0.03})(Zr_{0.52}Ti_{0.48})O_3$ thin films. *Journal of Applied Physics* **101**, 014104 (2007).

68 Buse, K. Light-induced charge transport processes in photorefractive crystals I: Models and experimental methods. *Applied Physics B* **64**, 273-291 (1997).

69 Zenkevich, A. *et al.* Giant bulk photovoltaic effect in thin ferroelectric $BaTiO_3$ films. *Physical Review B* **90**, 161409 (2014).

70 Guo, R. *et al.* Non-volatile memory based on the ferroelectric photovoltaic effect. *Nature communications* **4**, 1990 (2013).

71 Kholkin, A., Boiarkine, O. & Setter, N. Transient photocurrents in lead zirconate titanate thin films. *Applied Physics Letters* **72**, 130-132 (1998).

72 Thakoor, S. Photoresponse probe of the space charge distribution in ferroelectric lead zirconate titanate thin film memory capacitors. *Journal of Vacuum Science & Technology A: Vacuum, Surfaces, and Films* **12**, 295 (1994).

73 Cao, D. *et al.* Polarization effect on the photocurrent of Pt sandwiched multi-crystalline ferroelectric films. *Materials Chemistry and Physics* **129**, 783-786, (2011).

74 Chen, B. *et al.* Effect of top electrodes on photovoltaic properties of polycrystalline $BiFeO_3$ based thin film capacitors. *Nanotechnology* **22**, 195201 (2011).

75 Zhang, P. *et al.* Enhanced photocurrent in $Pb(Zr_{0.2}Ti_{0.8})O_3$ ferroelectric film by artificially introducing asymmetrical interface Schottky barriers. *Materials Chemistry and Physics* **135**, 304-308 (2012).

76 Alexe, M. Local Mapping of Generation and Recombination Lifetime in $BiFeO_3$

Single Crystals by Scanning Probe Photoinduced Transient Spectroscopy. *Nano letters* **12**, 2193-2198 (2012).

77 Moubah, R. *et al.* Photoelectric Effects in Single Domain $BiFeO_3$ Crystals. *Advanced Functional Materials* **22**, 4814-4818 (2012).

78 Shao, R., Nikiforov, M. P. & Bonnell, D. A. Photoinduced charge dynamics on $BaTiO_3$ (001) surface characterized by scanning probe microscopy. *Applied Physics Letters* **89**, 112904 (2006).

79 Yan, F., Chen, G., Lu, L. & Spanier, J. E. Dynamics of Photogenerated Surface Charge on $BiFeO_3$ Films. *ACS Nano* **6**, 2353-2360 (2012).

80 Yarmarkin, V. K., Gol'tsman, B. M., Kazanin, M. M. & Lemanov, V. V. Barrier photovoltaic effects in PZT ferroelectric thin films. *Physics of the Solid State* **42**, 522-527 (2000).

81 Land, C. E. & Peercy, P. S. Photoferroelectric effects in PLZT ceramics. *Ferroelectrics* **22**, 677-679 (1978).

82 Scott, J. F. Ferroelectrics go bananas. *Journal of Physics: Condensed Matter* **20**, 021001 (2008).

83 Fina, I. *et al.* Nonferroelectric contributions to the hysteresis cycles in manganite thin films: A comparative study of measurement techniques. *Journal of Applied Physics* **109**, 074105 (2011).

84 Fina, I. Ferroelectricity and Magnetoelectric Coupling in Magnetic Ferroelectrics and Artificial Multiferroic Heterostructures. *PhD thesis*, Universitat de Barcelona (2012).

85 Yang, T. J., Gopalan, V., Swart, P. J. & Mohideen, U. Direct Observation of Pinning and Bowing of a Single Ferroelectric Domain Wall. *Physical Review Letters* **82**, 4106-4109 (1999).

86 Han, M.-G. *et al.* Interface-induced nonswitchable domains in ferroelectric thin films. *Nature communications* **5**, 4693 (2014).

87 Dimos, D., Potter, B. G., Sinclair, M. B., Tuttle, B. A. & Warren, W. L. Photo-induced and electrooptic properties of $(Pb,La)(Zr,Ti)O_3$ films for optical memories. *Integrated Ferroelectrics* **5**, 47-58 (1994).

88 Warren, W. L. & Dimos, D. Photoinduced hysteresis changes and charge trapping in $BaTiO_3$ dielectrics. *Applied Physics Letters* **64**, 866 (1994).

89 Warren, W. L. & Dimos, D. Photo-assisted switching and trapping in $BaTiO_3$ and $Pb(Zr, Ti)O_3$ ferroelectrics. *Journal of Non-Crystalline Solids* **187**, 448-452 (1995).

90 Warren, W. L. *et al.* Polarization suppression in $Pb(Zr,Ti)O_3$ thin films. *Journal of Applied Physics* **77**, 6695-6702 (1995).

91 Warren, W. L., Seager, C. H., Dimos, D. & Friebele, E. J. Optically induced absorption and paramagnetism in lead lanthanum zirconate titanate ceramics. *Applied Physics Letters* **61**, 2530-2532 (1992).

92 Land, C. E. & Peercy, P. S. A review of the effects of ion implantation on the photoferroelectric properties of PLZT ceramics. *Ferroelectrics* **45**, 25-43 (1982).

93 Peercy, P. S. & Land, C. E. Optical image storage in ion implanted PLZT ceramics. *Nuclear Instruments and Methods* **182**, 787-796 (1981).

94 Peercy, P. S. & Land, C. E. Photographic image storage in ion implanted PLZT ceramics. *Nuclear Instruments and Methods in Physics Research* **209**, 1167-1178 (1983).

95 Peercy, P. S. & Land, C. E. Ion-implanted PLZT ceramics: A new high-sensitivity image storage medium. *IEEE Transactions on Electron Devices* **28**, 756-762 (1981).

96 Chan, N. H., Sharma, R. K. & Smyth, D. M. Nonstoichiometry in Undoped $BaTiO_3$. *Journal of the American Ceramic Society* **64**, 556-562 (1981).

97 Shin, J. C., Park, J., Hwang, C. S. & Kim, H. J. Dielectric and electrical properties of sputter grown $(Ba,Sr)TiO_3$ thin films. *Journal of Applied Physics* **86**, 506-513 (1999).

98 Baniecki, J. D. *et al.* Hydrogen induced tunnel emission in $Pt/(Ba_xSr_{1-x})Ti_{1+y}O_{3+z}/Pt$ thin film capacitors. *Journal of Applied Physics* **89**, 2873-2885 (2001).

99 Schroeder, H., Schmitz, S. & Meuffels, P. Leakage currents in high-permittivity thin films. *Applied Physics Letters* **82**, 781-783 (2003).

100 Dimos, D., Warren, W. L., Sinclair, M. B., Tuttle, B. A. & Schwartz, R. W. Photoinduced hysteresis changes and optical storage in $(Pb,La)(Zr,Ti)O_3$ thin films and ceramics. *Journal of Applied Physics* **76**, 4305 (1994).

101 Auciello, O., Scott, J. F. & Ramesh, R. The Physics of Ferroelectric Memories. *Physics Today*, 6 (1998).

102 Paillard, C. *et al.* Photovoltaics with Ferroelectrics: Current Status and Beyond. *Advanced materials* **28**, 5153-5168 (2016).

103 Huang, H. Solar energy: Ferroelectric photovoltaics. *Nat Photon* **4**, 134-135 (2010).

104 Qu, Y. & Duan, X. Progress, challenge and perspective of heterogeneous photocatalysts. *Chem Soc Rev* **42**, 2568-2580 (2013).

105 Cui, Y., Briscoe, J. & Dunn, S. Effect of Ferroelectricity on Solar-Light-Driven Photocatalytic Activity of $BaTiO_3$—Influence on the Carrier Separation and Stern Layer Formation. *Chemistry of Materials* **25**, 4215-4223 (2013).

106 Li, L., Salvador, P. A. & Rohrer, G. S. Photocatalysts with internal electric fields. *Nanoscale* **6**, 24-42 (2014).

107 Kalinin, S. V., Kim, Y., Fong, D. & Morozovska, A. Surface Screening Mechanisms in Ferroelectric Thin Films and its Effect on Polarization Dynamics and Domain Structures. *arXiv*, 135 (2016).

108 Wang, R. V. *et al.* Reversible Chemical Switching of a Ferroelectric Film. *Physical Review Letters* **102**, 047601 (2009).

109 Shur, V. Y., Ievlev, A. V., Nikolaeva, E. V., Shishkin, E. I. & Neradovskiy, M. M. Influence of adsorbed surface layer on domain growth in the field produced by conductive tip of scanning probe microscope in lithium niobate. *Journal of Applied Physics* **110**, 052017 (2011).

110 Ievlev, A. V., Morozovska, A. N., Shur, V. Y. & Kalinin, S. V. Humidity effects on tip-induced polarization switching in lithium niobate. *Applied Physics Letters* **104**, 092908 (2014).

111 Blaser, C. & Paruch, P. Subcritical switching dynamics and humidity effects in nanoscale studies of domain growth in ferroelectric thin films. *New Journal of Physics* **17**, 013002 (2015).

112 Dahan, D., Molotskii, M., Rosenman, G. & Rosenwaks, Y. Ferroelectric domain inversion: The role of humidity. *Applied Physics Letters* **89**, 152902 (2006).

113 Rodriguez, B. J., Jesse, S., Baddorf, A. P., Kim, S. H. & Kalinin, S. V. Controlling Polarization Dynamics in a Liquid Environment: From Localized to Macroscopic Switching in Ferroelectrics. *Physical Review Letters* **98**, 247603 (2007).

114 Kalinin, S. V. & Bonnell, D. A. Screening Phenomena on Oxide Surfaces and Its Implications for Local Electrostatic and Transport Measurements. *Nano letters* **4**, 555-560 (2004).

115 Ievlev, A. V. *et al.* Intermittency, quasiperiodicity and chaos in probe-induced ferroelectric domain switching. *Nat Phys* **10**, 59-66 (2014).

116 Fong, D. D. *et al.* Stabilization of Monodomain Polarization in Ultrathin $PbTiO_3$ Films. *Physical Review Letters* **96**, 127601 (2006).

117 Gruverman, A., Rodriguez, B. J., Nemanich, R. J. & Kingon, A. I. Nanoscale observation of photoinduced domain pinning and investigation of imprint behavior in ferroelectric thin films. *Journal of Applied Physics* **92**, 2734-2739 (2002).

118 Sones, C. L. *et al.* Precision nanoscale domain engineering of lithium niobate via UV laser induced inhibition of poling. *Applied Physics Letters* **92**, 072905 (2008).

119 Shin, J. *et al.* Atomistic Screening Mechanism of Ferroelectric Surfaces: An In Situ Study of the Polar Phase in Ultrathin $BaTiO_3$ Films Exposed to H_2O. *Nano letters* **9**, 6 (2009).

120 Chisholm, M. F., Luo, W., Oxley, M. P., Pantelides, S. T. & Lee, H. N. Atomic-Scale Compensation Phenomena at Polar Interfaces. *Physical Review Letters* **105**, 197602 (2010).

121 Wang, J. L. *et al.* Chemistry and Atomic Distortion at the Surface of an Epitaxial $BaTiO_3$ Thin Film after Dissociative Adsorption of Water. *The Journal of Physical Chemistry C* **116**, 21802-21809 (2012).

122 Koocher, N. Z., Martirez, J. M. P. & Rappe, A. M. Theoretical Model of Oxidative Adsorption of Water on a Highly Reduced Reconstructed Oxide Surface. *The journal of physical chemistry letters* **5**, 3408-3414 (2014).

123 Cao, D. *et al.* Understanding the nature of remnant polarization enhancement, coercive voltage offset and time-dependent photocurrent in ferroelectric films irradiated by ultraviolet light. *Journal of Materials Chemistry* **22**, 12592 (2012).

124 Kim, S., Sinai, O., Lee, C.-W. & Rappe, A. M. Controlling oxide surface dipole and reactivity with intrinsic nonstoichiometric epitaxial reconstructions. *Physical Review B* **92**, 235431 (2015).

125 Liu, F., Fina, I., Bertacco, R. & Fontcuberta, J. Unravelling and controlling hidden imprint fields in ferroelectric capacitors. *Scientific reports* **6**, 25028 (2016).

126 Kan, D. & Shimakawa, Y. Controlled cation stoichiometry in pulsed laser deposition-grown $BaTiO_3$ epitaxial thin films with laser fluence. *Applied Physics Letters* **99**, 081907 (2011).

127 Baniecki, J. D., Ishii, M., Shioga, T., Kurihara, K. & Miyahara, S. Surface core-level shifts of strontium observed in photoemission of barium strontium titanate thin films. *Applied Physics Letters* **89**, 162908 (2006).

128 Miot, C., Husson, E., Proust, C., Erreb, R. & Coutures, J. P. Residual Carbon Evolution in $BaTiO_3$ Ceramics Studied by XPS after Ion Etching. *Journal of the European Ceramic Society* **18**, 5 (1998).

129 Ayouchi, R., Martín, F., Ramos-Barrado, J. R. & Leinen, D. Compositional, structural and electrical characterization of BTO thin films prepared on fused silica and Si(111) by spray pyrolysis. *Surface and Interface Analysis* **30**, 5 (2000).

130 Brown, K. A. *et al.* Giant conductivity switching of $LaAlO_3/SrTiO_3$ heterointerfaces governed by surface protonation. *Nature communications* **7**, 10681 (2016).

131 Melnick, B. M., Scott, J. F., Paz De Araujo, C. A. & McMillan, L. D. Thickness dependence of D.C. leakage current in lead zirconate-titanate (PZT) memories. *Ferroelectrics* **135**, 163-168 (1992).

132 Lunkenheimer, P. *et al.* Origin of apparent colossal dielectric constants. *Physical Review B* **66**, 052105 (2002).

133 Jalaja, M. A. & Dutta, S. Ferroelectrics and multiferroics for next generation photovoltaics. *Advanced Materials Letters*, 17 (2015).

134 Wu, W. & Wang, Z. L. Piezotronics and piezo-phototronics for adaptive electronics and optoelectronics. *Nature Reviews Materials* **1**, 16031 (2016).

135 Butler, K. T., Frost, J. M. & Walsh, A. Ferroelectric materials for solar energy conversion: photoferroics revisited. *Energy Environ. Sci.* **8**, 838-848 (2015).

136 Choi, K. J. *et al.* Enhancement of ferroelectricity in strained $BaTiO_3$ thin films. *Science* **306**, 1005-1009 (2004).

137 Suzuki, T., Nishi, Y. & Fujimoto, M. Analysis of misfit relaxation in heteroepitaxial $BaTiO_3$ thin films. *Philosophical Magazine A* **79**, 2461-2483 (1999).

138 Kawai, M. *et al.* Critical thickness control by deposition rate for epitaxial $BaTiO_3$ thin films grown on $SrTiO_3$(001). *Journal of Applied Physics* **102**, 114311 (2007).

139 Damodaran, A. R., Breckenfeld, E., Chen, Z., Lee, S. & Martin, L. W. Enhancement of ferroelectric Curie temperature in $BaTiO_3$ films via strain-induced defect dipole alignment. *Advanced materials* **26**, 6341-6347 (2014).

140 Schubert, J. *et al.* Structural and optical properties of epitaxial $BaTiO_3$ thin films grown on $GdScO_3$(110). *Applied Physics Letters* **82**, 3460 (2003).

141 Dix, N. *et al.* Large out-of-plane ferroelectric polarization in flat epitaxial $BaTiO_3$ on $CoFe_2O_4$. *Applied Physics Letters* **102**, 172907 (2013).

142 He, J. Q., Vasco, E., Dittmann, R. & Wang, R. H. Growth dynamics and strain relaxation mechanisms in $BaTiO_3$ pulsed laser deposited on $SrRuO_3$/$SrTiO_3$. *Physical Review B* **73**, 125413 (2006).

143 Sun, H. P., Tian, W., Pan, X. Q., Haeni, J. H. & Schlom, D. G. Evolution of dislocation arrays in epitaxial BaTiO3 thin films grown on (100) $SrTiO_3$. *Applied Physics Letters* **84**, 3298-3300 (2004).

144 Naoko Yanase, Kazuhide Abe, Noburu Fukushima & Takashi Kawakubo. Thickness Dependence of Ferroelectricity in Heteroepitaxial $BaTiO_3$ Thin Film Capacitors. *Japanese Journal of Applied Physics* **38**, 5305 (1999).

145 Sinsheimer, J. *et al.* In-situ x-ray diffraction study of the growth of highly strained epitaxial $BaTiO_3$ thin films. *Applied Physics Letters* **103**, 242904

(2013).

146 Warren, W. L. *et al.* Defect‐dipole alignment and tetragonal strain in ferroelectrics. *Journal of Applied Physics* **79**, 9250-9257 (1996).

147 Matthews, J. W. & Blakeslee, A. E. Defects in epitaxial multilayers. *Journal of Crystal Growth* **27**, 118-125 (1974).

148 Nix, W. D. Mechanical properties of thin films. *Metallurgical Transactions A* **20**, 2217 (1989).

149 Chen, Y. B. *et al.* Interface structure and strain relaxation in $BaTiO_3$ thin films grown on $GdScO_3$ and $DyScO_3$ substrates with buried coherent $SrRuO_3$ layer. *Applied Physics Letters* **91**, 252906 (2007).

150 Ederer, C. & Spaldin, N. A. Effect of Epitaxial Strain on the Spontaneous Polarization of Thin Film Ferroelectrics. *Physical Review Letters* **95**, 257601 (2005).

151 Li, Y. L. & Chen, L. Q. Temperature-strain phase diagram for $BaTiO_3$ thin films. *Applied Physics Letters* **88**, 072905 (2006).

152 McCready, D. E., Liang, Y., Shutthanandan, V., Wang, C. M. & Thevuthasan, S. Thermal Lattice Expansion in Epitaxial $SrTiO_3$(100) on Si(100). *JCPDS-International Centre for Diffraction Data*, Newton Square, PA, United States(US); Pacific Northwest National Laboratory (PNNL), Richland, WA (US) (2006).

153 Biegalski, M. D. *et al.* Thermal expansion of the new perovskite substrates $DyScO_3$ and $GdScO_3$. *Journal of Materials Research* **20**, 952-958 (2005).

154 Schlom, D. G. *et al.* Strain Tuning of Ferroelectric Thin Films. *The Annual Review of Materials Research* **37**, 589 (2007).

155 Wang, J. J., Meng, F. Y., Ma, X. Q., Xu, M. X. & Chen, L. Q. Lattice, elastic, polarization, and electrostrictive properties of $BaTiO_3$ from first-principles. *Journal of Applied Physics* **108**, 034107 (2010).

156 Piskunov, S., Heifets, E., Eglitis, R. I. & Borstel, G. Bulk properties and electronic structure of $SrTiO_3$, $BaTiO_3$, $PbTiO_3$ perovskites: an ab initio HF/DFT study. *Computational Materials Science* **29**, 165-178 (2004).

157 Yang, X. *et al.* Nitrogen-Doped ZnO Nanowire Arrays for Photoelectrochemical Water Splitting. *Nano letters* **9**, 2331-2336 (2009).

158 Hoang, S., Guo, S., Hahn, N. T., Bard, A. J. & Mullins, C. B. Visible Light Driven Photoelectrochemical Water Oxidation on Nitrogen-Modified TiO_2 Nanowires. *Nano letters* **12**, 26-32 (2012).

159 Wang, Q., Jiang, H., Zang, S., Li, J. & Wang, Q. Gd, C, N and P quaternary doped anatase-TiO_2 nano-photocatalyst for enhanced photocatalytic

degradation of 4-chlorophenol under simulated sunlight irradiation. *Journal of Alloys and Compounds* **586**, 411-419 (2014).

160 Cao, J., Ji, Y., Tian, C. & Yi, Z. Synthesis and enhancement of visible light activities of nitrogen-doped $BaTiO_3$. *Journal of Alloys and Compounds* **615**, 243-248 (2014).

161 Asahi, R., Morikawa, T., Ohwaki, T., Aoki, K. & Taga, Y. Visible-Light Photocatalysis in Nitrogen-Doped Titanium Oxides. *Science* **293**, 269-271 (2001).

162 Bräuniger, T., Müller, T., Pampel, A. & Abicht, H.-P. Study of Oxygen−Nitrogen Replacement in $BaTiO_3$ by 14N Solid-State Nuclear Magnetic Resonance. *Chemistry of Materials* **17**, 4114-4117 (2005).

163 Yajima, T. *et al.* A labile hydride strategy for the synthesis of heavily nitridized $BaTiO_3$. *Nat Chem* **7**, 1017-1023 (2015).

164 Masuda, N. *et al.* Hydride in $BaTiO_{2.5}H_{0.5}$: A Labile Ligand in Solid State Chemistry. *Journal of the American Chemical Society* **137**, 15315-15321 (2015).

165 Tavares, C. J. *et al.* Enhancement in the photocatalytic nature of nitrogen-doped PVD-grown titanium dioxide thin films. *Journal of Applied Physics* **106**, 113535 (2009).

166 Saha, N. C. & Tompkins, H. G. Titanium nitride oxidation chemistry: An X-ray photoelectron spectroscopy study. *Journal of Applied Physics* **72**, 3072-3079 (1992).

167 Michalow, K. A. *et al.* Synthesis, characterization and electronic structure of nitrogen-doped TiO_2 nanopowder. *Catalysis Today* **144**, 7-12 (2009).

168 Zhao, H. *et al.* Effects of oxygen vacancy on the electronic structure and multiferroics in sol-gel derived $Pb_{0.8}Co_{0.2}TiO_3$ thin films. *Dalton Transactions* **42**, 10358-10364 (2013).

169 Rault, J. E. *et al.* Polarization sensitive surface band structure of doped $BaTiO_3$(001). *Phys Rev Lett* **111**, 127602 (2013).

170 Xing, J. *et al.* Photovoltaic effects and its oxygen content dependence in $BaTiO_{3-\delta}$/Si heterojunctions. *Applied Physics Letters* **92**, 071113 (2008).

Appendix

A.1 Carbon contamination detected in XPS spectra

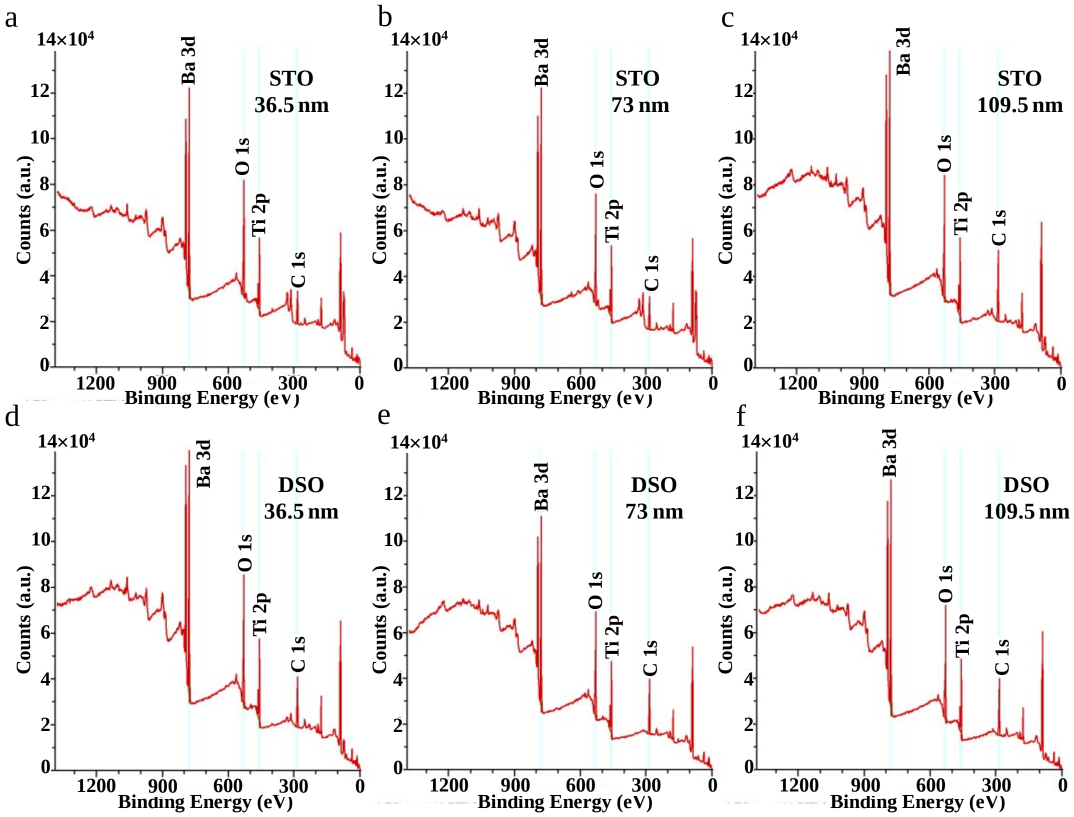

Figure A-1. XPS spectra of the six samples used in chapter 5 showing the presence C peaks. (a,b,c) BTO/LSMO//STO. (d,e,f) BTO/LSMO//DSO.

A.2 Condition of Pt electrodes and its influence on *Stream-treatment*

Learning from the discussion in chapter 5, section 5.3.3, condition of Pt electrodes may play an important role in the results of *stream-treatment*, since it is crucial whether the Pt electrode can tightly cap the BTO surface and prevent H_2O/ OH^- from penetrating or not. To testify the possible variation of the quality of Pt electrodes, three groups of Pt were sputtered on a 109.5 nm BTO/LSMO//DSO sample with 3 different sputtering power: 5, 10 and 20 W, after the sample was exposed to ambient, as the sketch in Figure A-2 shows. 109.5 nm BTO/LSMO//DSO structure is chosen due to its relative high

H_2O/ OH^- adsorption on the surface, learn from the results in chapter 5. An enhancement of ΔP_r along with sputtering power increasing is clearly seen in the plot. It indicates that H_2O/OH^- can penetrate Pt and reach BTO surface easier to screen P under illumination, in Pt sputtered with higher energy. Possible explanation is that with higher sputtering power, the bombardment of Pt atoms on BTO surface is more intense, leading to more defects such as micro cracks and hole into the sputtered Pt, which behaves as tunnels for H_2O/ OH^-. Further study is needed to examine it.

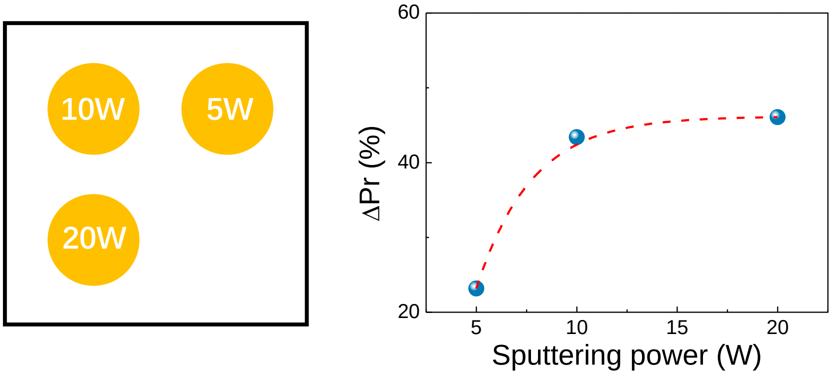

Figure A-2. Left: sketch of the 3 groups of Pt electrodes sputtered on a 109.5 nm BTO/LSMO//DSO sample with different power. Right: Tendency of ΔP_r extracted from *P-E* loops measured in *t-t* to the Pt sputtering power. The red dashed line is plotted to guide the view.

As an inspiration of previous result, a 73 nm BTO/LSMO//STO sample was prepared. Subsequently, Pt was sputtered on BTO with 20 W power, creating electrodes on purpose that may allow H_2O/OH^- to penetrate easily. $\Delta P_r \approx 0$ was measured in as-grown state, being coherent with the result of similar sample in chapter 5, as Figure A-3a shows. Afterwards, the sample was performed a series of *steam-treatment* varying from 20 min to 10 h. Evident enhancement of ΔP_r is observed in *P-E* loops measured after 10 h *steam-treatment*, as Figure A-3b shows. Figure A-3c displays a linear increasing of ΔP_r with logarithmically extending of treating time. These results indirectly confirmed that H_2O/OH^- can penetrate Pt electrodes grown on purpose and change the property of photo-induced polarization screening during the *steam-treatment*. After 10 h *steam-*

treatment, additional *P-E* loops test underwent in vacuum (room temperature) and results are plotted in Figure A-3d. The measurement environment was evacuated up to 1×10^{-5} mbar (see chapter 2, section 2.2.6 for details) and *P-E* loops were recorded 1 h after this pressure was reached. $\Delta P_r \approx 0$ is observed in the results, and moreover, once the sample was exposed to ambient again, *P-E* loops retrieve the same as the ones in Figure A-3b. It is a hint that in the Pt/BTO structure, H_2O/OH^- desorb in vacuum and escape from BTO surface through tunnels in Pt, and reabsorb once vapor partial pressure in the environment recovers.

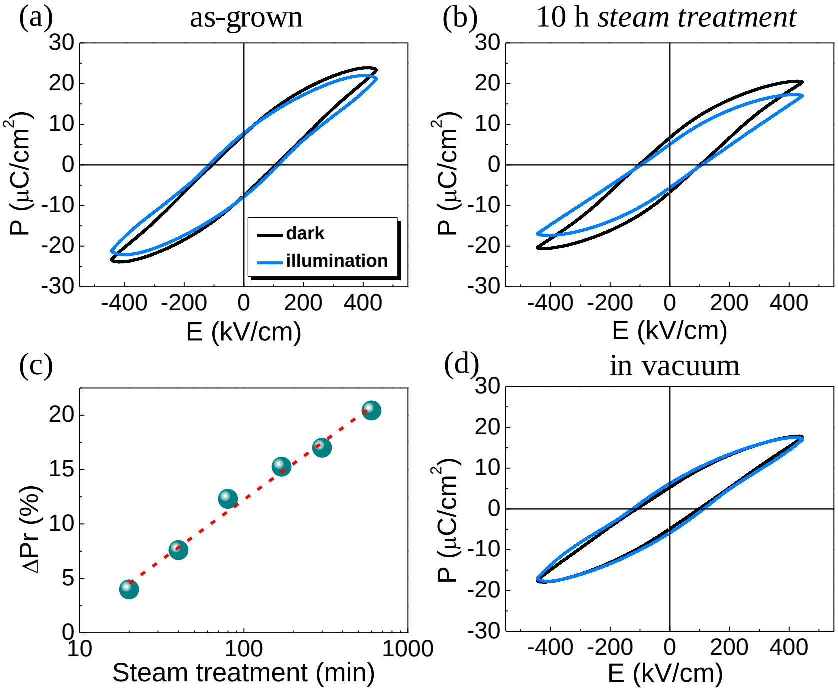

Figure A-3. *P-E* loops of 73 nm BTO/LSMO//STO measured in dark (black curves) and blue laser (405 nm) illumination (blue curves) by *t-t* configuration: (a) as-grown state, (b) after 10 h *steam-treatment*. (c) Variation of ΔP_r with the time of *steam-treatment*. (d) *P-E* loops recorded in vacuum environment with a pressure of 1×10^{-5} mbar.

An interesting phenomenon was noticed during *steam-treatment* of the 73 nm BTO/LSMO//STO sample. The recoded *J-E* loops show a gradually decreasing leakage current at the maximum electric filed (E_{max}) as treating time prolongs, both in the condition of dark and under illumination. Selected *J-E* loops are shown in Figure A-4a,b,c and the decreasing trend of *J* recorded at E_{max} chosen to represent leakage is plotted in Figure A-4d.

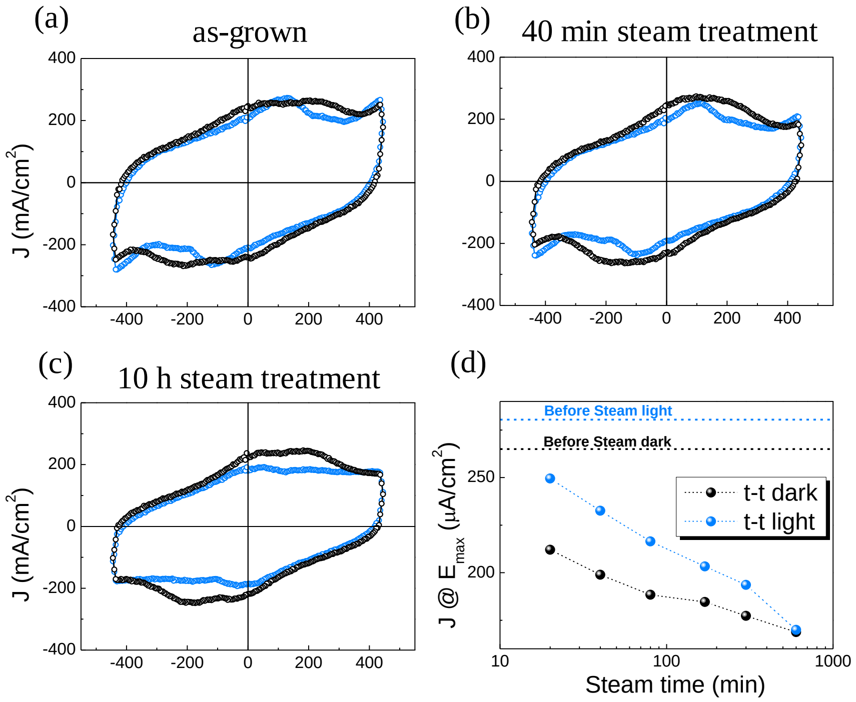

Figure A-4. *J-E* loops measured in dark (black) and under blue laser illumination (blue) of the 73 nm BTO/LSMO//STO sample. (a) As-grown state. (b) After 40 min *steam-treatment*. (c) After 10 h *steam-treatment*. (d) Variation of *J* picked up at E_{max} from *J-E* loops along with the increase of *steam-treatment* time.

Learning from results in Figure 5.13, the microstructure and surface roughness of BTO are not modulated by *steam-treatment*. Thus it is more likely the decrease of leakage is due to the change at Pt/BTO interface instead of BTO itself. A hypothetical scenario that considers the enhancing of Schottky barrier at Pt/BTO interface due to *steam-treatment* is built and the schematics are plotted in Figure A-5. In the as-grown state, partial domains are screened by H_2O/OH^- at Pt/BTO interface. Free electrons in BTO are driven by external electric filed E_{ext} to cross the Schottky barrier and flow into the circuit, presenting as leakage current in *J-E* loops. After *steam-treatment*, the amount of H_2O/OH^- increases and BTO domains are better screened, leading to higher Schottky barrier and making it more difficult for free electrons to cross. At the end presenting as the decreasing of leakage in *J-E* loops.

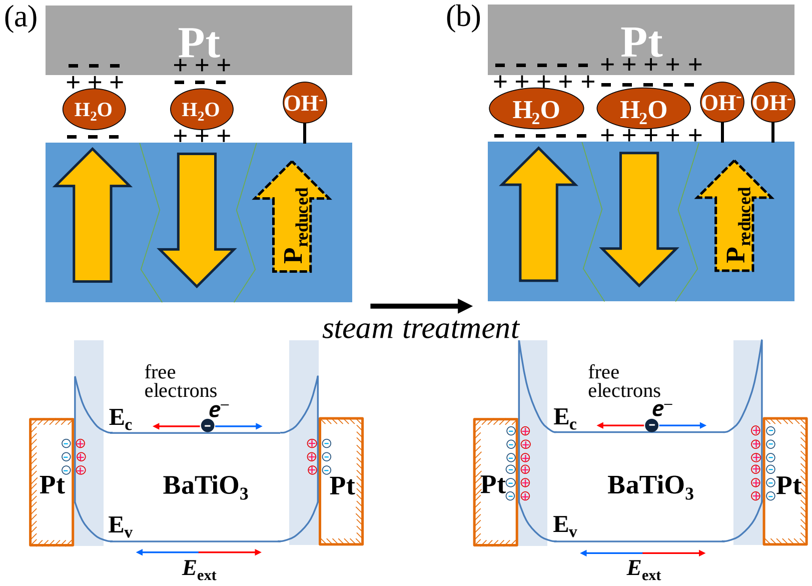

Figure A-5. Schematics of H_2O/OH^- amount (top) and Schottky barriers (bottom) at Pt/BTO interface, *t-t* configuration. (a) As-grown state. (b) After *steam-treatment*. Red and blue arrows point the direction of applied external electric filed (E_{ext}) and corresponding direction of electron migration. To be detected, electrons must cross the Schottky barrier at Pt/BTO interface and flow into the circuit.

A.3 Coexisting of strained and relaxed phases in $BaTiO_3$ thin films

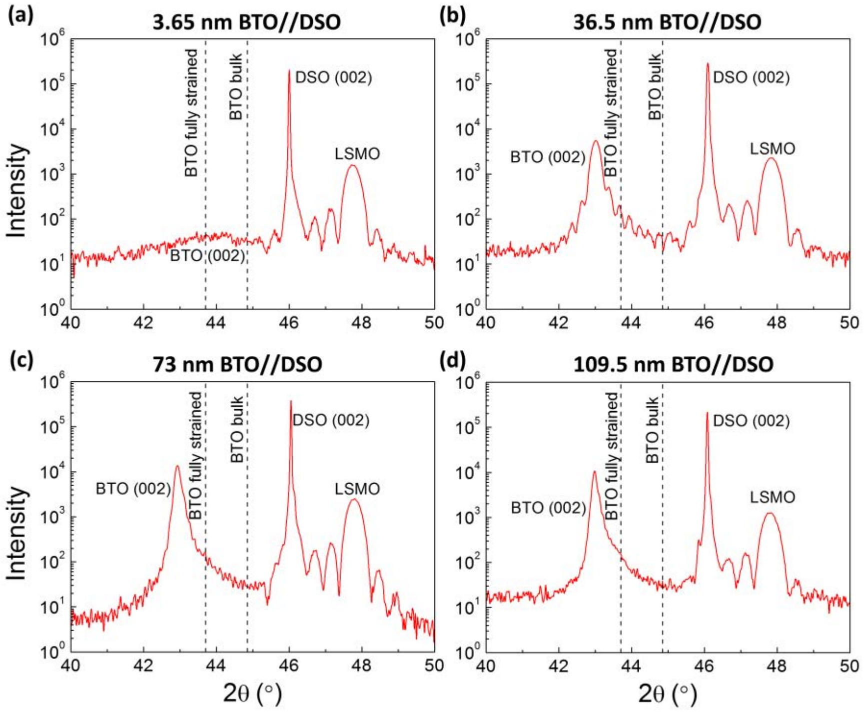

Figure A-6. XRD θ-2θ scans around (002) plane of BTO//DSO films. (a) 3.65 nm, (b) 36.5 nm, (c) 73 nm and (d) 109.5 nm thick BTO film on DSO. Annotations mark the position of the STO substrate, the LSMO buffer layer and the BTO film. Two dashed lines indicate the out-of-plane lattice parameters of bulk BTO and fully stained BTO epitaxially grown on STO which considering BTO cells as incompressible.

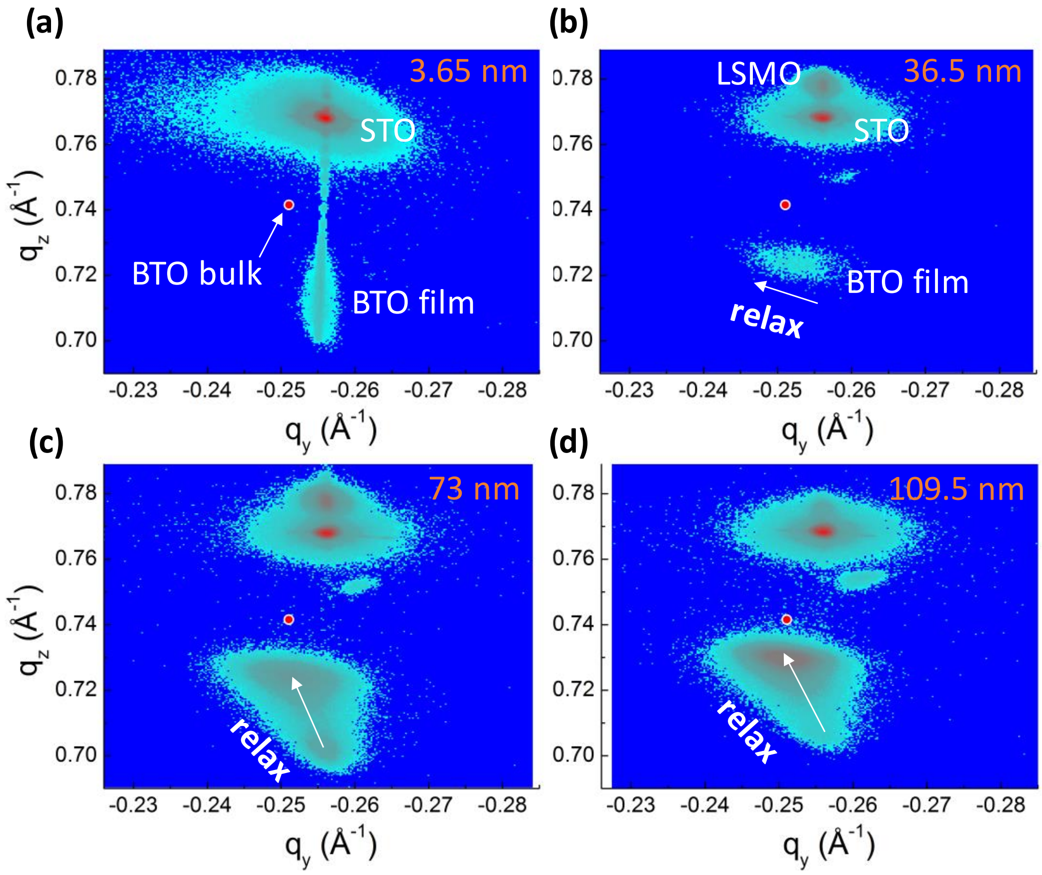

Figure A-7. Projections of 3D RSMs of $(\bar{1}11)$ plane on q_z-q_y reciprocal plane. RSMs are from BTO//STO films with t = (a) 3.65 nm, (b) 36.5 nm, (c) 73 nm and (d) 109.5 nm. Color transition from blue to cyan to purple and to red indicates the increasing of intensity in logarithmic scale. Regions of BTO, STO and LSMO are marked in (a) and (b), also the directions of relaxation are marked by the white arrows in (b), (c) and (d). A red circle in each sub-figure points the lattice parameters of bulk $BaTiO_3$.

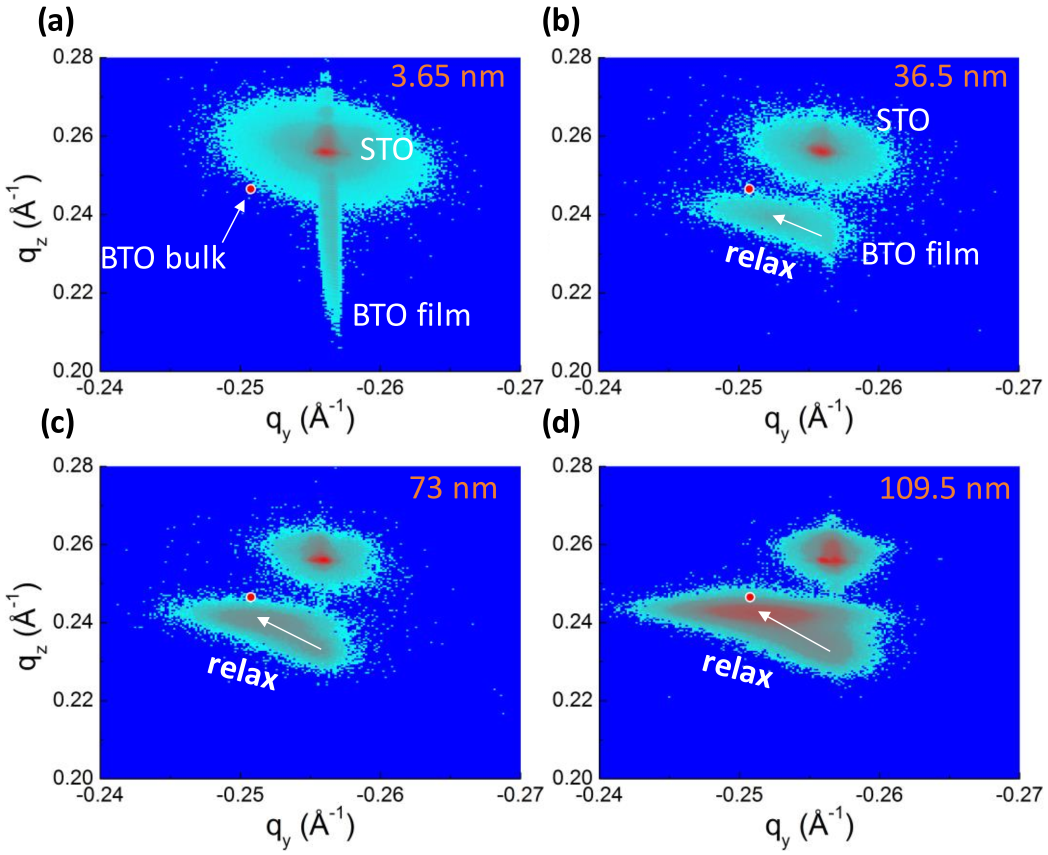

Figure A-8. Projections of 3D RSMs of $(\bar{1}03)$ plane on q_z-q_y reciprocal plane. RSMs are from BTO//STO films with t = (a) 3.65 nm, (b) 36.5 nm, (c) 73 nm and (d) 109.5 nm. Interpretation of colors, marks and annotations are the same as Figure A-7.

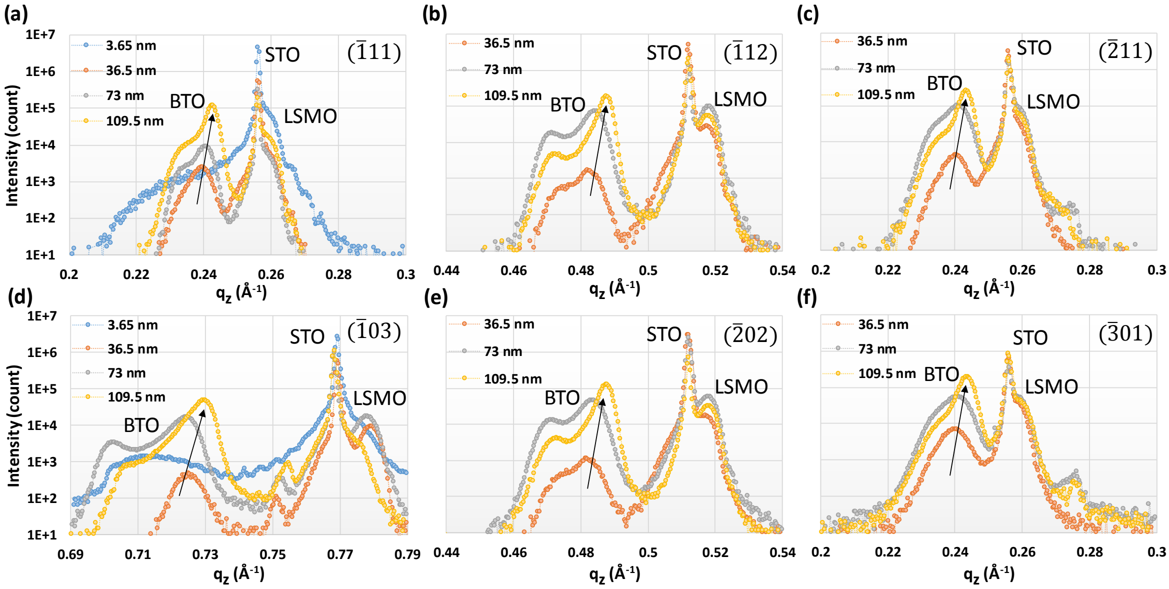

Figure A-9. Projections of 2D RSMs on q_z of BTO//STO films with different thickness. Projection on q_z of **(a)** $(\bar{1}11)$, **(b)** $(\bar{1}12)$, **(c)** $(\bar{2}11)$, **(d)** $(\bar{1}03)$, **(e)** $(\bar{2}02)$ and **(f)** $(\bar{3}01)$

plane. The black arrows guide the view of increasing of q_z value, namely the out-of-plane relaxation, along with the increasing of thickness.

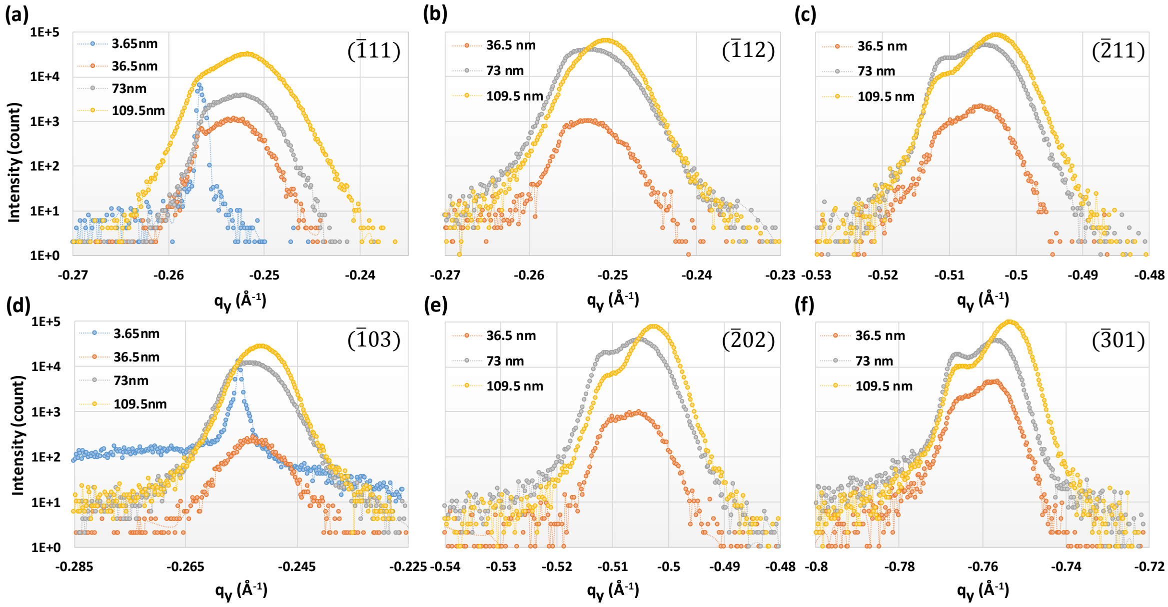

Figure A-10. Projections of 2D RSMs on q_y of BTO//STO films with different thickness. Projection on q_y of **(a)** $(\bar{1}11)$, **(b)** $(\bar{1}12)$, **(c)** $(\bar{2}11)$, **(d)** $(\bar{1}03)$, **(e)** $(\bar{2}02)$ and **(f)** $(\bar{3}01)$ plane.

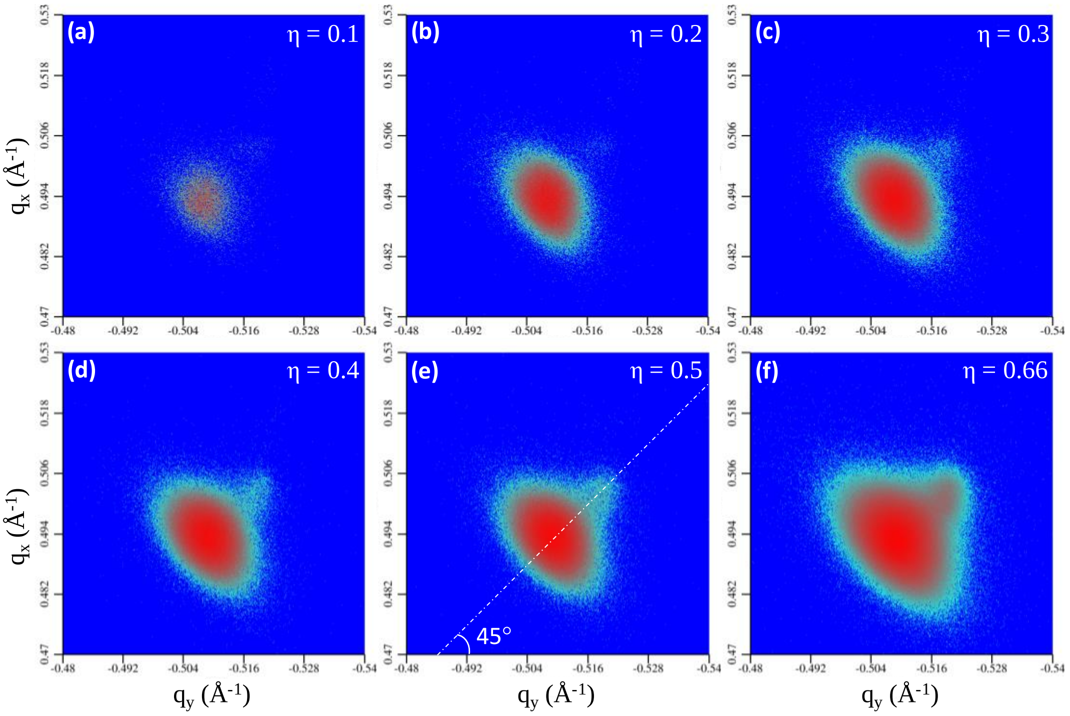

Figure A-11. q_x-q_y projection of RSMs obtained by grazing incidence diffraction geometry at $(\bar{2}22)$ plane of 109.5 nm-thick BTO//STO film. **(a-f)** q_x-

q_y projected RSMs at different incident angle, with η = 0.1°, 0.2°, 0.3°, 0.4°, 0.5°, 0.66°, respectively in the incidence geometry. Logarithmically intensity increasing is expressed by color transition from blue to cyan to purple and to red. The regions with higher intensity (red ovals) occupy positions with smaller q_x and q_y (absolute value), representing the relaxed BTO phase. While the "tails" in cyan and purple stands for the more strained BTO due to their larger q_x and q_y absolute values. Owing to same scale of q_x-q_y and the square dimension of images, the 45° auxiliary line in (e) reveals the symmetry in the two in-plane direction, q_x and q_y, during relaxing from strained to relaxed phase. It implies that the tetragonality of BTO cells is maintains to a certain extent in the relaxation process.

List of symbols and abbreviations

Materials

BTO	$BaTiO_3$
DSO	$DyScO_3$
LSAT	$La_{2/3}Sr_{1/3}MnO_3$
LSMO	$(LaAlO_3)_{0.3}(SrAl_{0.5}Ta_{0.5}O_3)_{0.7}$
SRO	$SrRuO_3$
STO	$SrTiO_3$

Methodologies

AFM	atomic force microscopy
b-t	bottom-top electrodes configuration
DHM	dynamic hysteresis measurement
GIXD	grazing incidence X-ray diffraction
PLD	pulsed laser deposition
PUND	pulse measurement (positive up negative down)
RF	radio frequency
RMS	root mean square
RSM	reciprocal space map
RT	room temperature
t-t	top-top electrodes configuration
XRD	X-ray diffraction
XRR	X-ray reflectometry
XPS	X-ray photoelectron spectroscopy

Variables

a	in-plane lattice parameter
c	out-of-plane lattice parameter
f	lattice mismatch
t, t_c	layer thickness, critical thickness

ε	permittivity (chap 4) / biaxial strain (chap. 6)
ε_r	relative permittivity
λ	wavelength
ν	frequency
ρ	resistivity
τ	time / delay time / time constant
ϕ	work function
E, E_c	electric field, coercive electric field
E_{imp}, E_{dep}	imprint field, depolarization field
E_k, E_B	kinetic energy, bonding energy
J, J_p	current density, photocurrent density
P, P_r, P_{max}	polarization, remanent polarization, saturated polarization
Q	charge (chap. 2-4) / volume flow rate (chap. 7)
T_c	curie temperature / phase transition temperature
V, V_c	voltage, coercive voltage

Others

S	strained $BaTiO_3$ phase
R	relaxed $BaTiO_3$ phase

Publications

Published works

F. Liu, I. Fina, R. Bertacco, J. Fontcuberta. Unravelling and Controlling Hidden Imprint Fields in Ferroelectric Capacitors. *Scientific Reports*, 2016, 6: 25028.

F. Liu, I. Fina, D. Gutiérrez, G. Radaelli, R. Bertacco, J. Fontcuberta. Selecting Steady and Transient Photocurrent Response in $BaTiO_3$ Films. *Advanced Electronic Materials*, 2015, 1: 1500171.

In preparation works

F. Liu, I. Fina, F. Sánchez, G. Sauthier, J. Fontcuberta. Ferroelectric polarization of $BaTiO_3$ films controlled by photoreactive adsorbates. *To be Submit*.

F. Liu, C. Frontera, I. Fina, F. Sánchez, J. Fontcuberta. Structural characterization of double strain states of $BaTiO_3$ thin films by synchrotron radiation. *In preparation.*

F. Liu, I. Fina, A. Black, A. Fuertes, J. Fraxedas, F. Sánchez, J. Fontcuberta. Band-gap Modification by Ammonia Annealing – the Route Toward Extensive Applications of $BaTiO_3$ Thin Films. *In preparation*.

Contributions to conferences

F. Liu, I. Fina, F. Sánchez, J. Fontcuberta. Tuning Light-induced Polarization Screening of Ferroelectric Materials by Water. *2017 E-MRS Spring Meeting*, Strasbourg France, May 2017.

F. Liu, I. Fina, F. Sánchez, J. Fontcuberta. Tuning Light-induced Polarization Screening of Ferroelectric Materials by Water. *2017 Joint IEEE ISAF-IWATMD-PFM Conference*, Atlanta USA, May 2017.

F. Liu. Deep Learning on the Photo-responses on $BaTiO_3$ Thin Film. *Invited talk*. Key Laboratory of Electronic Ceramics and Devices, Xi'an Jiaotong University, Xian China, Dec. 2016.

I. Fina, F. Liu, F. Sanchez, J. Fontcuberta. On the Origin of Shortcircuit Photocurrent on $BaTiO_3$ Films. *20th International Conference on Ternary and Multinary Compounds*, Halle Germany, Sep. 2016.

F. Liu, I. Fina, F. Sánchez, R. Bertacco, J. Fontcuberta. Role of Surface States on the Photoresponse of $BaTiO_3$ Thin Films. *2016 Joint ISAF/ECAPD/PFM Conference*, Darmstadt Germany, Aug. 2016.

F. Liu, I. Fina, J. Fontcuberta. Unravelling Hidden Imprint in Ferroelectric Capacitors by Light. *NANOSELECT NOE Annual Meeting*, Sant Feliu de Guíxols Spain, June. 2016.

I. Fina, F. Liu, J. Fontcuberta. Role of the Surface States on the Photoresponse of $BaTiO_3$ Thin Films. *To-Be Meeting Spring 2016*, Coventry United Kingdom, Apr. 2016.

F. Liu, I. Fina, G. Radaelli, R. Bertacco, D. Gutiérrez, D. Gutiérrez, F. Sánchez, J. Fontcuberta. Selecting Steady or Transient Photoresponses in $BaTiO_3$ Films and the Role of Defects. *13th European Meeting on Ferroelectricity*, Porto Portugal, Jul. 2015.

I. Fina, F. Liu, D. Gutiérrez, G. Radaelli, R. Bertacco, J. Fontcuberta. Relation between Short-circuit Photocurrent and Ferroelectric Retention in $BaTiO_3$ Thin Films. *E-MRS 2015 Spring Meeting: Symposium M*, Lille France, May 2015.

I. Fina, F. Liu, D. Gutiérrez, G. Radaelli, R. Bertacco, J. Fontcuberta. Relation between Short-circuit Photocurrent and Ferroelectric Retention in $BaTiO_3$ Thin Films. *TO-BE Spring Meeting 2015*, Aveiro Portugal, Mar. 2015.

F. Liu, D. Gutiérrez, I. Fina, J. Fontcuberta. Photoinduced Effects in Metal-ferroelectric-metal Heterostructures. *NANOSELECT - Annual Meeting 2014*, Sant Feliu de Guíxols Spain, Jun. 2014.

Honors

Student paper competition finalist, the 2017 Joint IEEE ISAF-IWATMD-PFM Conference.